LUMINESCENT RUTHENIUM NANOPROBES FOR APPLICATIONS IN DYE SENSITIZED SOLAR CELLS

By

SHANI ANN MARIE OSBORNE

A Thesis submitted to
The University of Birmingham
For the degree of
DOCTOR OF PHILOSOPHY

UNIVERSITY OF
BIRMINGHAM

University of Birmingham Research Archive

e-theses repository

This unpublished thesis/dissertation is copyright of the author and/or third parties. The intellectual property rights of the author or third parties in respect of this work are as defined by The Copyright Designs and Patents Act 1988 or as modified by any successor legislation.

Any use made of information contained in this thesis/dissertation must be in accordance with that legislation and must be properly acknowledged. Further distribution or reproduction in any format is prohibited without the permission of the copyright holder.

Abstract

Luminescent nanoprobes have been widely researched for applications in areas such as biological imaging, sensing and photonics. Developing a nanoprobe that adopts the properties of a molecular probe has great difficulty due to quenching of the luminescence of the probe upon attachment to the nanoparticle. Luminescent polypyridyl ruthenium complexes were efficiently labelled on gold nanoparticles to produce a nanoprobe with enhanced photophysical properties compared to the molecular probe. Gold nanoparticles with diameter 13, 50 and 100 nm were employed to investigate the effect of the size of the nanoparticle and it was found that this has no effect on the photophysical properties of the nanoprobe. The distance between the photoactive ruthenium centre and nanoparticle surface was varied through an organic chain to investigate the effect of distance and it was found that increasing the distance increases the photophysical enhancement. Ruthenium molecular probes with optimised photophysical properties were designed and synthesised for development of further enhanced nanoprobes. Upon attaching a bis-phenanthroline ruthenium probe (RuphenS12) to gold nanoparticles, a luminescent lifetime of 1.7 μs was demonstrated. This is competitive with tris-phenanthroline ruthenium complexes seen in the literature. Solid state photophysical properties of all developed molecular probes and nanoprobes were investigated. The molecular probes and nanoprobes were investigated in applications for Dye Sensitized Solar Cells.

Acknowledgements

Thank you for reading my Thesis, I hope you enjoy it ☺

Firstly I would like to thank my supervisor, Professor Zoe Pikramenou and my second supervisor, Dr Sarah Horswell. Their support and guidance over the past few years has been highly appreciated and I am grateful that I was warmly welcomed as a member of the ZP group.

Thanks go to the ZP group past and present, for becoming my friends and making me laugh through the past few years: John Lilley; Siobhan King; Sunil Claire; Sam Adams; Sully Khan; Sajni Haria; Andrew Carrod; John Ddungu; Freya Bell; Cristiano Matricardi; Rodolfo Teixeira; Meng Lyu; Olly Francis; Luke Woodbridge; Tom Deo; Hannah Mather; Kim Dunne and Li Guangjing. Special thanks go to John Lilley for being my best friend and my rock, Sam Adams for helping me throughout my transition to a postgraduate researcher and Sunil Claire for baking amazing cakes.

I wish to acknowledge EPSRC, The Leverhulme Trust (ZP) and the School of Chemistry, University of Birmingham for financial support. Some of the spectrometers used in this research were obtained through Birmingham Science City: Innovative Uses for Advanced Materials in the Modern World (West Midlands Centre for Advanced Materials Project 2), with support from Advantage West Midlands (AWM) and partial funding from the European Regional Development Fund (ERDF).

I would like to acknowledge the analytical facility in the school of chemistry: Jackie Deans with her help on the RAMAN instrument; Chi Tsang and Philip Ashton for their help with MS; Cecile Le Duff and Neil Spenser for their help with NMR; Ashleigh Danks and Dr Zoe Schnepp for their training on the Nitrogen Sorption and Louise Male. I would like to thank Theresa Morris and Paul Stanley from the Metallurgy and Materials department for their help

with the TEM and SEM instruments and Nasim Mahmoodi from the Electrical Engineering department for her help with the gold evaporator. From the University of Warwick I would like to thank Dr Michael Hornbury and Dr Vasilios Stavros for running the transient absorption experiments and Philip Ashton and Lijiang Song for running the ICP-MS experiments. From Queen Mary London, I would like to thank: Prof William Gillin and Dr Theo Kreouzis for supervision; Dr Ken Scott for help with the gold evaporator; Xuan Li for help with the preparation of electrodes and most of all Dr Joe Briscoe for all of his help and guidance throughout my visits. I would like to thank NEXUS from Newcastle University for running the XPS.

Thanks go to all of the support staff in the chemistry department: Bernard Tudor; Ian Bodfish; Stuart Arkless; Helen Vahey; Lynn Blake; Terry Green and Iain Wilkinson. They have all made my time here at Birmingham University pleasant and enjoyable and I will be sad to leave. Thank you to Adrian Wright who was supportive during AVD and Open days. Thanks go to Alan from the biochemistry stores who would always make me laugh and brighten up my Monday morning.

I would also like to thank my fellow PhD students in the department: Greg O'Callaghan; Will Brittain; Francia Allibush; Owen Jones; Ashleigh Danks; Phil Jemmett and Dennis Zheo. They all made lunchtime exciting and helped me relax. My friends outside of university are always there for me and even though they don't understand what I am doing, their support to get me through has been immense: Emma Dyson; Natalie Wellham; Maddie Meyer; Joanne Lovell and Ally Beckett. Thank you to both my current and future family, they have all been brilliant and have believed in me from the start: Catharine Clarke; Steve Clarke; Jake Osborne; Logan Clarke; Sydnee Clarke; Brian Osborne; Marlei Osborne; Zak Osborne; Violet Michel; John Michel; Lisa Michel and Julie Michel.

Most of all I would like to thank my fiancé Colin Michel. He has been amazing and has had to put up with me at my lowest points but would always find a way to cheer me up. Thank you so much for being the greatest.

Contents

Abbreviations

^{13}C NMR	Carbon Nuclear Magnetic Resonance
^{1}H NMR	Proton Nuclear Magnetic Resonance
AuNP	Gold nanoparticle
bpy	2,2'-bipyridine
CB	Conduction Band
CD	Cyclodextrin
COSY	Correlation Spectroscopy
CTTS	Charge Transfer to Solvent transitions
DCE	Dichlroethane
DCM	Dichloromethane
DLS	Dynamic light scattering
DMF	Dimethyl Formaldehyde
DMSO	Dimethyl Sulfoxide
DSC	Dye Sensitized Solar Cell
e^-	Electron
EDC	1-Ethyl-3-(3-dimethylaminopropyl)carbodiimide
EDTA	Ethylenediaminetetraacetic acid
FF	Fill Factor
h^+	Positive Hole
HMBC	Heteronuclear multiple-bond correlation spectroscopy
HOMO	Highest Occupied Molecular Orbital
HSQC	Heteronuclear single-quantum correlation spectroscopy
IC	Internal conversion
ICPE	Incident Photon to Current Efficiency
ICP-MS	Inductively coupled plasma mass spectrometry
IR	Infrared Spectroscopy

ISC	Intersystem crossing
J_{max}	Maximum current
J_{sc}	Short-Circuit Photocurrent density
K_n	Rate of radiative decay
K_{nr}	Rate of non-radiative decay
K_q	Rate of quenching
LC	Ligand Centre Transfer
LUMO	Lowest Unoccupied Molecular Orbital
MALDI	Matrix assisted laser desorption ionisation
MLCT	Metal to Ligand Charge Transfer
MS	Mass Spectrometry
η	Efficiency of DSC
N-EM	N-ethylmaleimide
PDI	Polydispersity index
phen	1,10-phenanthroline
P_{max}	Maximum power
PMT	Photomultiplier tube
P_s	Power Density of Incident Light
SEM	Scanning electron microscopy
SPR	Surface Plasmon Resonance
TA	Transient absorption
TEA	Triethylamine
TEM	Transmission electron microscopy
TFA	Trifluoroacetic Acid
THF	Tetrahydrofuran
TOF	Time of flight
UV	Ultraviolet

Vis	Visible Spectrum
V_{max}	Maximum voltage
V_{oc}	Open-Circuit Photovoltage
XPS	X-ray photoelectron spectroscopy
ε	Molar Absorptivity
ζ-potential	Zeta potential
λ_{max}	Wavelength with Maximum Intensity
τ	Luminescence lifetime
Φ	Luminescence quantum Yield

1 Introduction

1.1 Properties of ruthenium (II) polypyridyl complexes

In the field of inorganic photochemistry, ruthenium(II) complexes with 2,2'-bipyridine ligands have attracted intense research. They have been widely used due to favourable properties including strong luminescence in the visible region at room temperature in solution, long excited state lifetimes in the nano-seconds, good photostability, easy functionalisation and the ability to undergo photo-induced electron and energy transfer processes.[1, 2]

Ruthenium(II) bipyridine complexes have a large absorption range in the blue due to excitation of the singlet Metal Ligand Charge Transfer (^{1}MLCT) state or higher energy Metal Centre (MC) or Ligand Centre (LC) bands (Figure 1.2.a). Upon irradiation of the ^{1}MLCT state, fast intersystem crossing (ISC) (50 fs), followed by vibrational relaxation (5-10 ps) leads to population of the lowest level ^{3}MLCT state (Figure 1.2.b).[3]

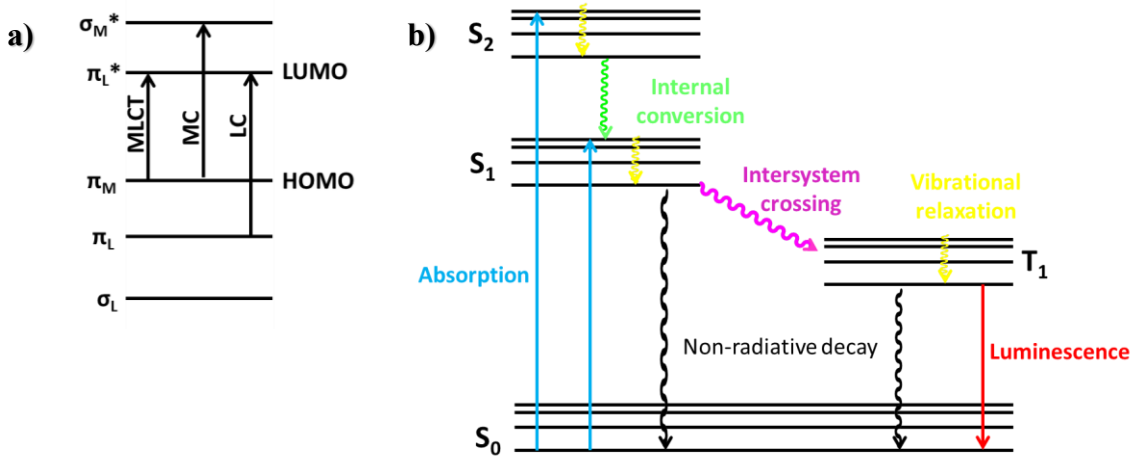

Figure 1.1: Molecular orbital diagram (a) and the energy state diagram (b) for $[Ru(L)_3]^{2+}$. HOMO is the highest occupied molecular orbital and LUMO is the lowest unoccupied molecular orbital. Adapted from reference.[1]

This state formed is high energy and unstable so must undergo a process to return back to the ground state (Figure 1.2).[1] Excited state deactivation can occur *via* 1. Reaction of the original molecule to form different products (Photochemical reaction), 2. Emission of light

(Luminescence), 3. Degradation of the excess energy into heat (Non-radiative decay) and 4. Interaction with another species (Quenching).

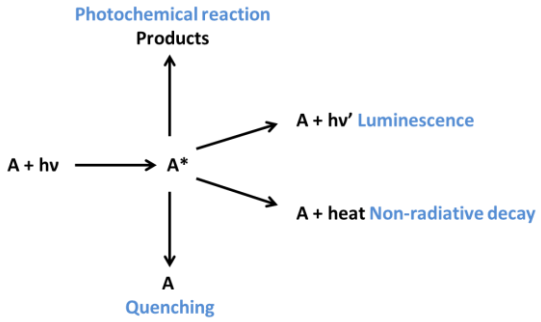

Figure 1.2: Schematic to show excited state deactivation processes. Adapted from reference.[1]

The ^{1}MLCT absorption is typically in the blue and the broad ^{3}MLCT emission is in the red. This large stokes shift (shift between emission and excitation wavelength of the same transition) ensures that none of the emitting light is reabsorbed, leading to a more efficient process. The relaxation of the ^{3}MLCT is spin-forbidden, allowing for emission with a long lifetime to occur, providing that there are no low-lying triplet Metal Centre (^{3}MC) states that can deactivate the ^{3}MLCT (Figure 1.3).

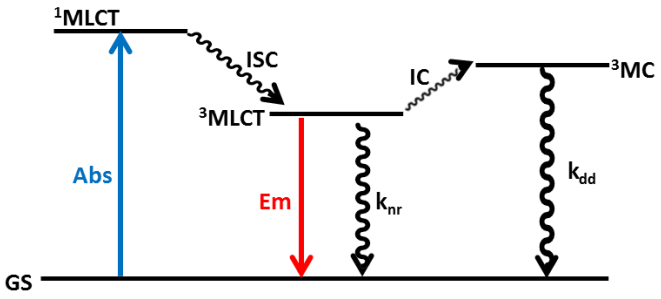

Figure 1.3: Jablonski diagram to show the quenching by ^{3}MC states.

The luminescent lifetime (τ) and quantum yield (Φ) are related to the non-radiative (k_{nr}) and radiative (k_r) decay of the excited state (Equation 1.1 & 1.2).[4, 5]

$$\tau = \frac{1}{k_r + k_{nr}} \qquad \textbf{Equation 1.1}$$

$$\Phi = \frac{k_r}{k_r + k_{nr}} \qquad \textbf{Equation 1.2}$$

A large number of bipyridine based ruthenium(II) complexes have been synthesised and studied by spectroscopic and electrochemical techniques.[6-9] The most famous example of a polypyridyl ruthenium complex is $[Ru(bpy)_3]^{2+}$.[1, 10-12] Ru^{2+} is a low spin d^6 metal ion and has octahedral microsymmetry (D_3).[2] The 2,2'-bipyridine ligands have σ-donors localised on the nitrogen atoms and have π-donating and π*-accepting orbitals located on the aromatic rings.[1] There is a low rate of ligand exchange for low-spin d^6 complexes, which make them relatively unreactive and stable. $[Ru(bpy)_3]^{2+}$ has a strong absorption ($\varepsilon = 13000\ mol^{-1}\ cm^{-1}$) at 450 nm, assigned to the lowest ^{1}MLCT (Figure 1.4). Excitation of the ^{1}MLCT leads to ^{3}MLCT emission at 650 nm with a quantum yield of 2.8% and luminescent lifetime of 390 ns in an oxygen environment at room temperature in water.

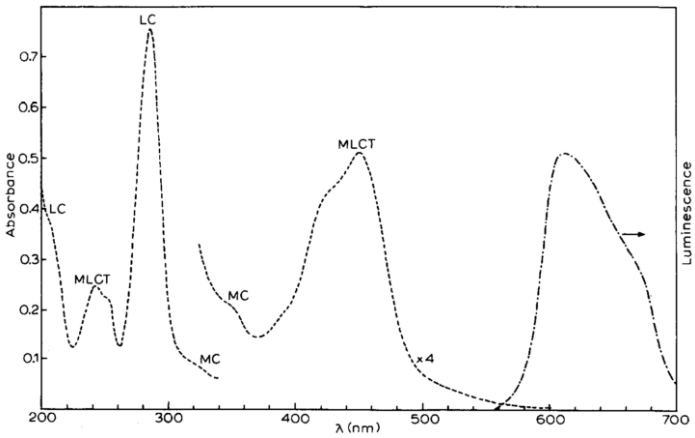

Figure 1.4: Assigned absorption and emission spectrum of $[Ru(bpy)_3]^{2+}$ in aqueous solution at room temperature. Taken from reference.[2]

Excitation of the MLCT state leads to delocalisation of the electron, but there has been some debate over whether the electron is delocalised over all of the ligands to form $[Ru^{3+}(bpy)_3^-]$ or if it is localised to one ligand to form $[Ru^{3+}(bpy)^-(bpy)_2]$ (Figure 1.5.a). This was solved using a combination of cyclic voltammetry and resonance Raman spectroscopy, suggesting the electron is delocalised on one orbital. Wrighton *et al.* have demonstrated the appearance of new bands in the Raman of the excited state of $[Ru(bpy)_3]^{2+}$, compared to the ground state, corresponding to the presence of a bpy^- species (Figure 1.5.b).[13] Hopkins *et al.* have shown

that when substituting a 2,2'-bipyridine ligand for 1,10-phenanthroline in $[Ru(bpy)_3]^{2+}$, to form both $[Ru(bpy)_2(phen)]^{2+}$ and $[Ru(bpy)(phen)_2]^{2+}$, there is no change in the excited state Raman compared to $[Ru(bpy)_3]^{2+}$. There is however a change seen when substituting all of the bpy ligands for phen.[14, 15] This suggests that the electron is localised on one ligand to form $[Ru^{3+}(bpy)^{-}(bpy)_2]$ and in the case of $[Ru(bpy)_2(phen)]^{2+}$ and $[Ru(bpy)(phen)_2]^{2+}$ the electron is localised to the bpy ligand.

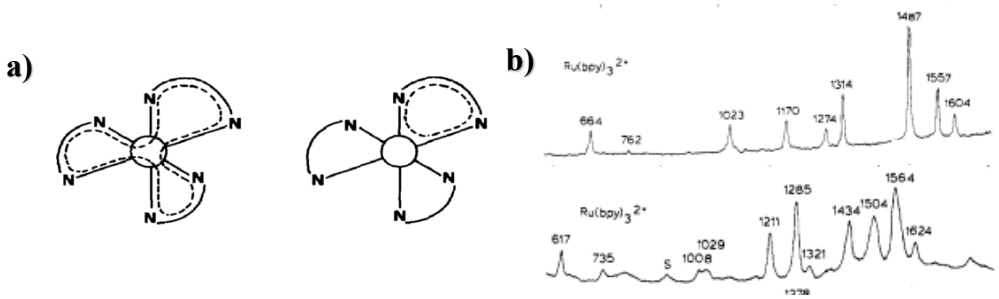

Figure 1.5: Schematic to show localisation across all three bipyridine rings (left) and localisation of one bipyridine ring (right) (a). Taken from reference.[1] Raman spectroscopy of ground state (top) and excited state (bottom) of $[Ru(bpy)_3]^{2+}$ (b). Taken from reference.[13]

There is a shift in emission maxima for $[Ru(bpy)_3]^{2+}$ in different solvents, and a change in the luminescence lifetime and quantum yield.[16-18] This is due to the charge transfer nature of the transition and arises from the interaction of the solvent dipole with the excited and ground state. The solvent molecules distribute themselves around the solute molecules for stability and the energy of the system is determined by the electrostatic forces. The excited state has a larger dipole than the ground state so is more stabilised. States with small dipoles are less sensitive to solvent effects. The solvent molecules rearrange to minimise energy and the more polar molecules cause an increased stability of the excited state, leading to a red shift in emission (Figure 1.6).[19, 20] Solvent relaxation is on the time scale of 10 – 100 ps, which is too fast to affect the absorption to great extent. For some molecules there can also be quenching of the excited state from the solvent molecules through Charge Transfer to Solvent transitions (CTTS).[2, 16]

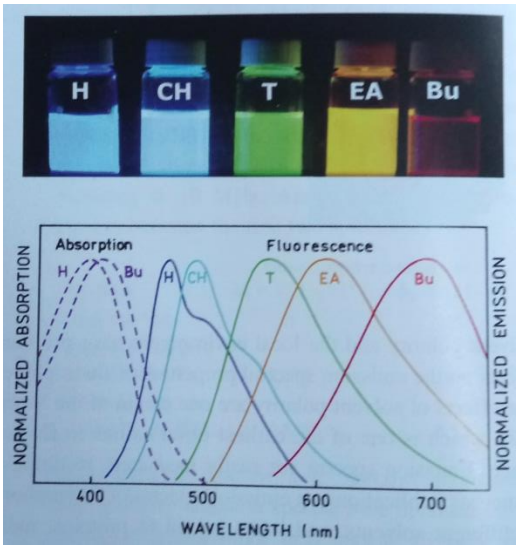

Figure 1.6: Photo (top) and absorption and emission graph (bottom) of 4-dimethylamino-4'-nitrostilbene in solvents with increasing polarity: hexane (H), cyclohexane (CH), toluene (T), ethyl acetate (EA) and n-butanol (Bu). Taken from reference.[20]

The largest quencher of the ruthenium excited state is triplet oxygen. It has been shown that oxygen has a rate of quenching (k_q) of 3.3 x 10^9 M^{-1} s^{-1} for $[Ru(bpy)_3]^{2+\bullet}$ in water.[21, 22] Adams *et al.* show the lifetime of $Ru(bpy)_3Cl_2$ increases 5-fold when in a deaerated environment (170 to 840 ns in acetonitrile).[8] This is due to its long lifetime and triplet character of the excited state (Figure 1.7). Quenching can occur through electron or energy transfer but the mechanism here is unknown. Sutin *et al.* suggests it goes *via* an electron transfer process to yield $[Ru(bpy)_3]^{3+}$ and O_2^-, however Olmsted *et al.* suggest energy transfer.[23, 24]

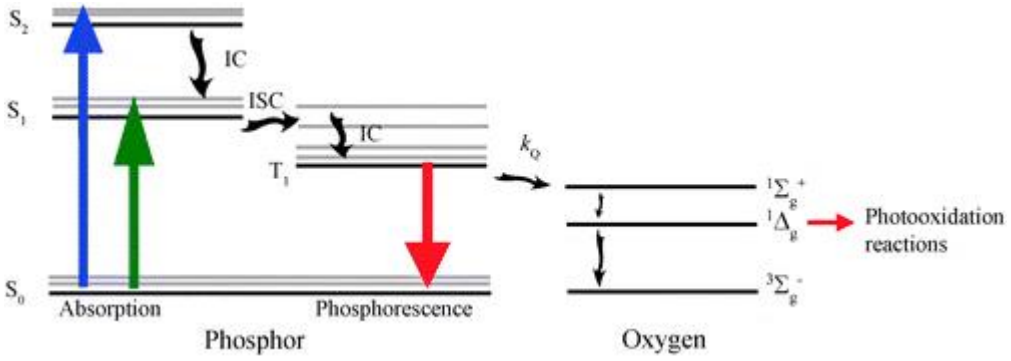

Figure 1.7: Schematic to show the process of oxygen quenching. Image taken from reference.[25]

1.2 Properties of gold nanoparticles

Gold nanoparticles (AuNP) are widely used in research areas such as nanomedicine,[26-28] catalysis,[29-31] sensors[32-34] and photovoltaics.[35-37] This is due to ease of synthesis and surface functionalisation, and can be made water soluble, inert and non-toxic.

Different shapes and sizes of AuNP can be easily synthesised. They can be formed through either the bottom-up method or the top-down method. The top-down method involves formation of the particles from the bulk material through laser ablation[38-40] or lithography.[41-43] The bottom-up method is more widely used and involves the reduction of gold atoms. This was reported in 1951 by Turkevitch, through reduction with citrate ions to produce citrate stabilised AuNP.[44] The size and shape of the nanoparticles are determined by the ratio of gold salt and citrate ions, temperature, and order of addition; so changing these can alter the properties.[45] Other reduction methods using $NaBH_4$[46-48] and thiols,[49-51] as well as other ligands[52-55] have been demonstrated.

AuNP possess localised surface plasmon resonance (SPR) due to oscillation of surface electrons (Figure 1.8).[56-59] The surface electrons oscillate in resonance with light waves and cause polarisation to one surface.[60, 61] This SPR is responsible for the electromagnetic field seen for the AuNP, which can cause interaction with the environment and has been seen to lead to enhancements in Raman scattering and luminescence.[61, 62]

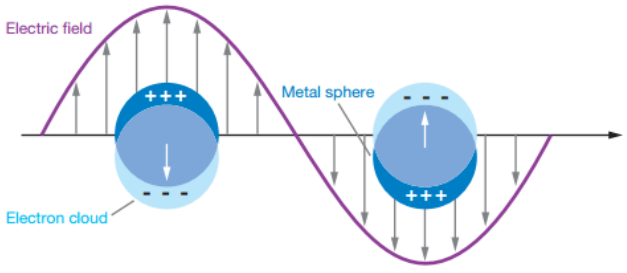

Figure 1.8: Localised surface plasmon resonance. Taken from reference.[61]

The SPR can be monitored using UV-vis, and changes depending on the size[63-65] and shape[66-68] of the nanoparticle (Figure 1.9). As the size or shape changes, the surface geometry changes causing a shift in the electric field density on the surface.[60] The change in optical properties and absorption maximum arises from a change in oscillation. Wang *et al.* have shown the absorption maximum of AuNP with diameter between 8 to 180 nm increase from 518 to 720 nm[63] and Puntes *et al.* have shown an increase from 525 to 835 nm for particles with diameter 32 to 216 nm.[65]

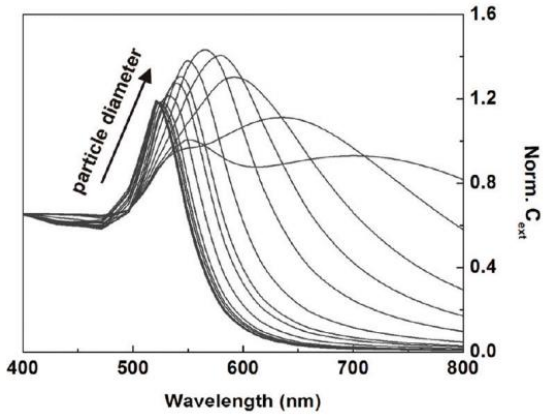

Figure 1.9: Calculated extinction coefficient of AuNP with diameter between 8 – 180 nm. Taken from reference.[65]

This SPR allows for scattering and absorption of light. It has been shown that smaller particles have a larger contribution of absorbance to the molar absorptivity and larger particles show a larger contribution from scattering (Figure 1.10).[69] Electrons are free to travel through the material and the mean free path of gold is 50 nm, so particles smaller than this will have little scattering.[60]

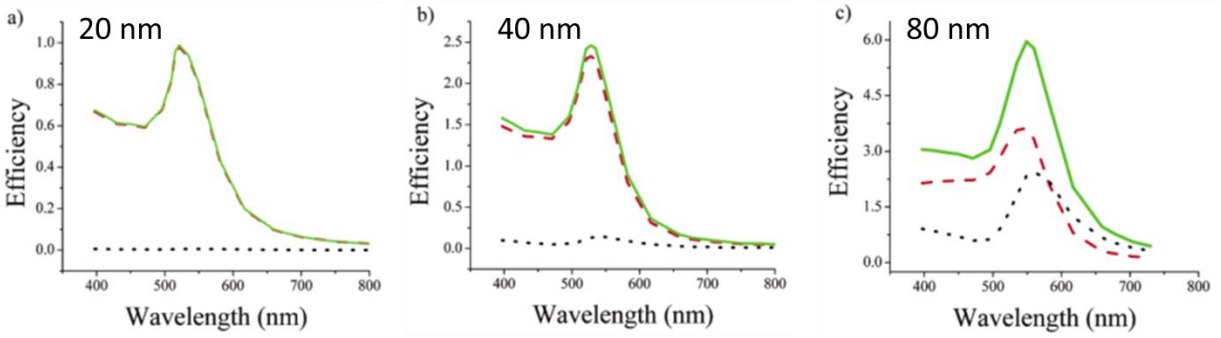

Figure 1.10: Calculated spectra of the absorption (red dash), scatter (black dash) and molar absorptivity (green) for 20 nm (a), 40 nm (b) and 80 nm (c) diameter AuNP. Taken from reference.[69]

AuNP can be easily labelled using a sulfur ligand.[8, 70] The Au-S is an easy, strong and stable bond. It can exchange with other ligands on the surface, meaning a clean surface is not required for functionalisation, and the strong bond will prevent leaching of the ligand into the environment.[71] Attaching a luminophore to AuNP can change its properties through quenching or enhancement of photophysical and electronic properties arising from the particles magnetic field.[60] Ruthenium complexes have been attached to AuNP and are researched in areas such as sensing and biological imaging.[72-75] Yam *et al.* have attached a photoactive ruthenium complex with a lipoic acid linker to AuNP for use as an esterase detector (Figure 1.11.a).[76] Kamat *et al.* have attached photoactive ruthenium complexes to AuNP through a thiol linker (Figure 1.11.b&c).[77, 78] Pikramenou *et al.* and Gunnlaugsson *et al.* have attached photoactive ruthenium centres to AuNP through one or two thiol legs for use in biological imaging (Figure 1.11.d&e).[7, 79] McDonagh *et al.* have shown stable ruthenium coated AuNP at high temperatures (Figure 1.11.f).[80]

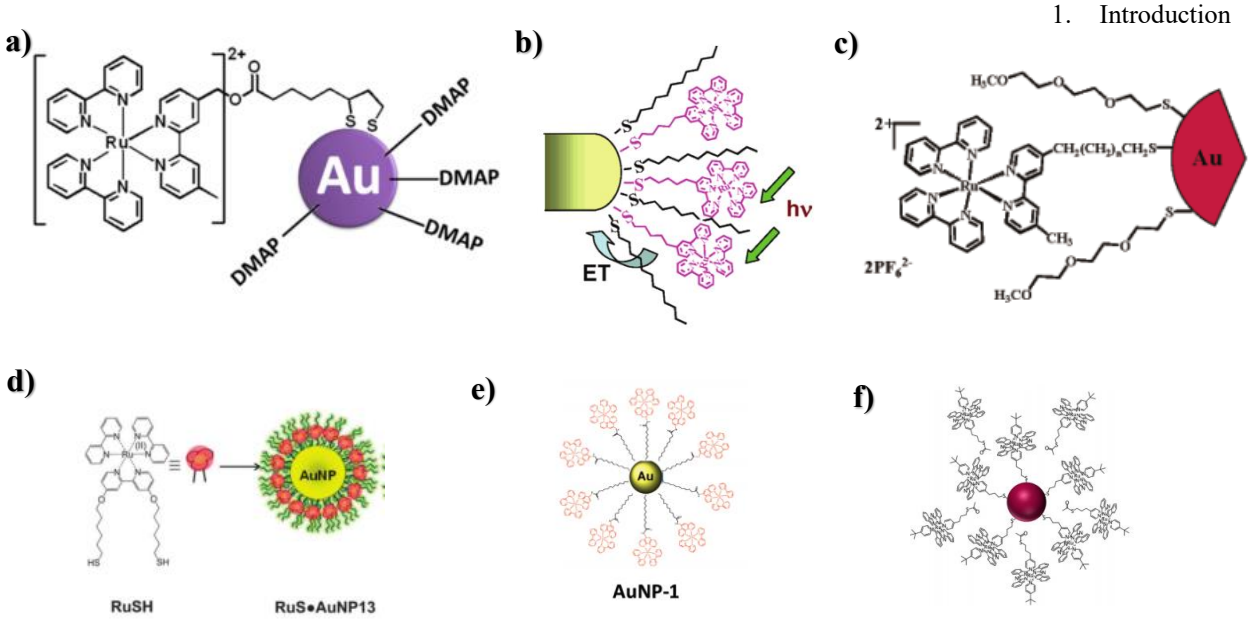

Figure 1.11: Ruthenium coated nanoparticles with thiol linkers. Taken from reference.[7, 76-80]

1.3 Dye Sensitized Solar Cells

Recently, the world wide acknowledgement towards depleting fossil fuels has escalated and together with the drastic increase of fuel prices, the communal support towards finding economical alternative fuels has improved. Nobel Laureate Richard Smalley outlined humanity's top 10 problems for the next 50 years, with energy being top of the list.[81] Forecasts predict that human energy needs are likely to double over the next 50 years due to an increase in population and emerging economy's such as India and China, while fossil fuel reserves shrink.[82, 83] Calculations predict that after 2042 the only form of fossil fuels will be coal and by 2112 the coal reserves will be empty,[84] with fuel costs currently increasing at 4% a year.[85] Utilisation of green energy is important due to the fossil fuel crisis in combination with carbon dioxide reduction. Scientists and engineers around the world are currently researching into improving the efficiency, production and lifetimes of solar cells, wind turbines, hydro power, geothermal and tidal power, as well as trying to make nuclear safer.[86] Solar energy is a promising technology as 3 x 10^{24} joules of energy per year are supplied to the earth from the sun. That is ten thousand times more than the earth needs to meet its global

energy needs. In other words, enough energy hits the earth in one hour to meet the global consumption for a year.[87, 88]

Currently, solar cells are made mainly of silicon and are based on a *p*-*n* junction; an electron is excited across the junction, creating a circuit (Figure 1.12).[89] The p-type material is doped with an electron poor material, creating holes (h^+) and making it overall positive. The n-type material is doped with an electron rich material, creating additional electrons (e^-) and making it overall negative. Light hits the electron in the *p*-*n* junction and gives it enough energy to excite it across the junction, giving it potential to flow around the circuit.

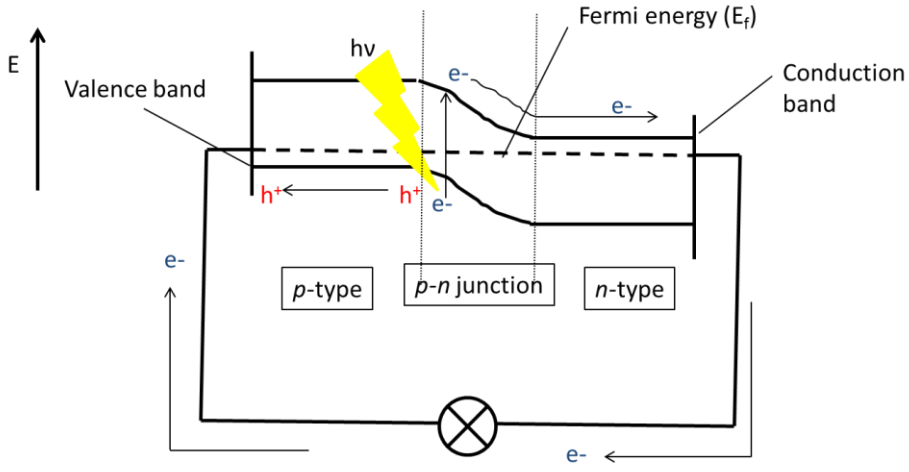

Figure 1.12: Schematic to show the structure of a silicon solar cell. Adapted from reference.[89]

Preparation of silicon solar cells is expensive as they require high purity crystals and need to be fabricated under vacuum. Circuits are only created at the *p*-*n* junction, so many junctions per area need to be manufactured to get typical efficiencies (26%), thus these lead to high production costs and low throughputs.[90] In addition, the solar panels are bulky and have applications for stationary purposes only (Figure 1.13). An inexpensive and more applicable alternative must be found.

Figure 1.13: Photograph of silicon solar panels.

Recently, examples of solar cells for a wide range of applications have been demonstrated, from stationary to wearable (Figure 1.14). In the development of solar windows, Lunt *et al.* have gained efficiencies of 10% using organic luminescent salts[91] and Snaith *et al.* have demonstrated the use of perovskite materials in a Thin Film solar cell, to reach efficiencies of 20%.[92] Both Solaria and Solar Windows Technologies have gone into commercial production of solar windows.[93, 94] In 2009 G24 Innovations announced the sale of a solar backpack and in 2015 Tommy Hilfiger and Pvilion released a solar jacket that can charge your phone.[95, 96] These applications have been developed through the use of new solar technologies such as Thin Film and Dye Sensitized Solar Cells (DSCs).

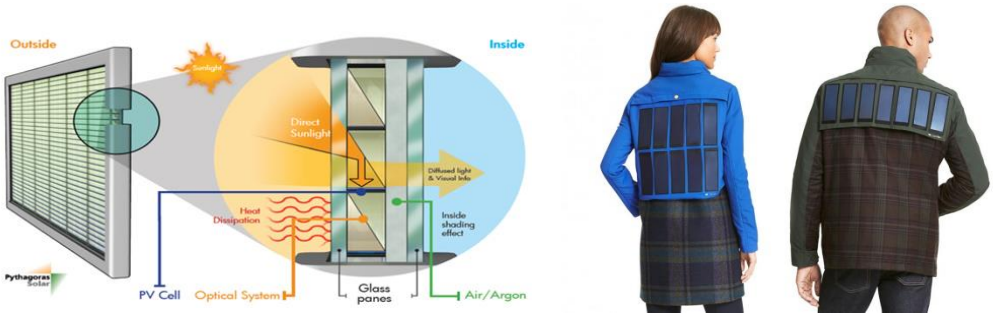

Figure 1.14: Applications of solar cells in solar windows (left) and solar jackets (right). Taken from references.[96, 97]

DSCs were refined by Grätzel and O'Regan in 1991.[98] A typical DSC is formed of two glass slides coated with conductive material (fluorine or indium doped tin oxide). The anode is

coated with TiO_2 nanoparticles (typically Degussa P-25 anatase) and a sensitizer. The counter electrode is coated with a catalyst (typically carbon or platinum). The two electrodes are sandwiched together and the gap is filled with an electrolyte (redox material). The principle operation of a DSC is different compared to the commercial silicon solar cells. The sensitizer absorbs photons of light which causes an electron to be excited from the HOMO to the LUMO. This electron is transferred to the TiO_2 conduction band and passes through an outer circuit to reach the counter electrode. The sensitizer is regenerated by reduction from the electrolyte, which itself is reduced from the counter electrode (cathode). This creates a complete circuit (Figure 1.15). The current can be disrupted through charge recombination from the TiO_2 CB with the dye or electrolyte, or electron back transfer.[99-102]

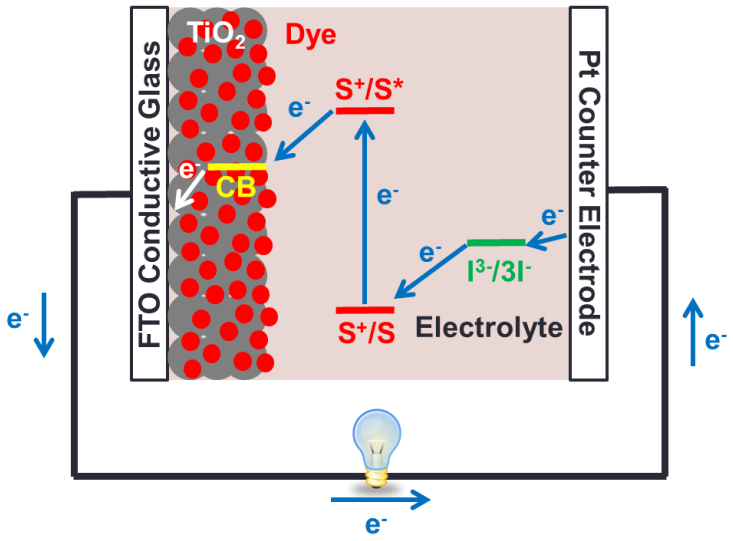

Figure 1.15: Schematic to show the operation of a DSC.

DSCs lead to benefits over silicon solar cells in areas such as cost and time of production, optimal operation, and range of applications. If successful in mass commercialisation, DSCs will reduce the cost of solar energy by a fifth, as they do not require ultra-pure materials, making it more financially viable for household consumption.[103] It has been shown that DSCs still function with high efficiencies in the presence of diffuse light and increased temperatures, whereas the performance of silicon solar cells reduces (Figure 1.16).[104-106] This, with the

ability to develop transparent cells, allows for indoor and window panel applications.[91, 92] In addition, the cells can be made on flexible substrates leading to applications on curved surfaces.[107-109]

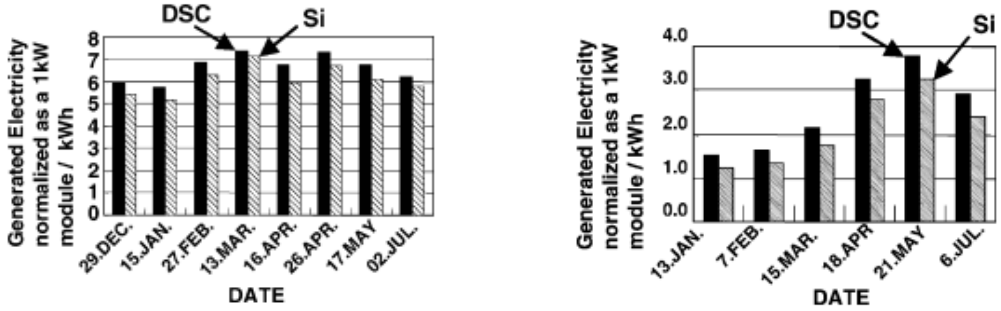

Figure 1.16: Generated electricity for clear and sunny (left) and cloudy (right) days for DSC and silicon solar cells. Taken from reference.[104]

For the DSC to be competitive with silicon solar cells, they must have good efficiencies (amount of electrical energy generated from incident photons (Equation 1.3)) and stability (lifetime of the cell), however currently they are ten times more expensive to produce than silicon solar cells (based on only a 5% efficiency and 5 year lifetime).[110] DSC efficiencies have reached 15%[111] (ranging typically from 5%) with theoretical maximum efficiency of 30%.[112] This is competitive with the silicon solar cell efficiencies of 26%,[113] with theoretical maximum efficiency of 30%.[114]

$$\eta = \frac{FF \, x \, J_{max} \, x \, V_{max}}{P_S} \text{ x } 100 \qquad \textbf{Equation 1.3}$$

Where η is efficiency, FF is the fill factor, J_{max} is the maximum current, V_{max} is the maximum voltage and P_s is the input energy.[115]

The efficiency can be improved by: 1. Increasing the packing of the dyes - as the number of dyes per area increases the light absorbed per area increases;[116] 2. Improving the absorbance of the dye - if the dye absorbs a broader spectrum of light or has a higher absorption coefficient then the input of electrons into the system increases; 3. Reducing the quenching

and 4. Improvements with the production of the system.[117] The lifetime of the cell can be improved from both strengthening the dye-anode bond and the stability of the electrolyte. Other factors that affect the performance of the DSC are charge recombination (with the dye or electrolyte), back transfer and degradation of the dye (Figure 1.17).

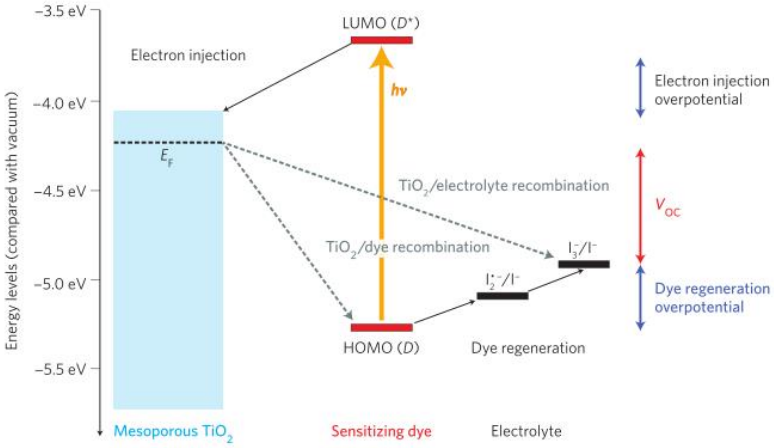

Figure 1.17: Schematic to show recombination in a DSC. Taken from reference.[118]

Different sensitizers have been used in DSCs, such as ruthenium,[119-121] metal-free organic,[122-124] perovskites[125-127] and porphyrins.[128-130] Park *et al.* have reached efficiencies of 16% using a $HC(NH_2)_2PbI_3$ perovskite material and Grätzel *et al.* get efficiencies of 13% with a zinc-porphyrin complex (Figure 1.18).[125, 128] The most established dyes for DSCs are ruthenium complexes. They are desirable due to their optimal photophysical properties and high rate of electron transfer, reaching efficiencies of 12%.[1]

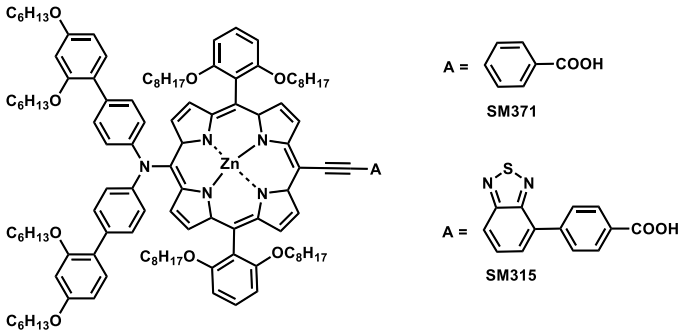

Figure 1.18: Structure of porphyrin sensitizer. Taken from reference.[71]

The dye section of the DSC is the most widely researched.[131] It is absorbed on the TiO_2 anode and its function is to absorb photons of light, and through electron transfer an electron is donated into the TiO_2 conduction band (Figure 1.15). The most famous and widely used ruthenium dyes are the N3,[132] N719[133] and N794 'Black dye'[134] (Figure 1.19).

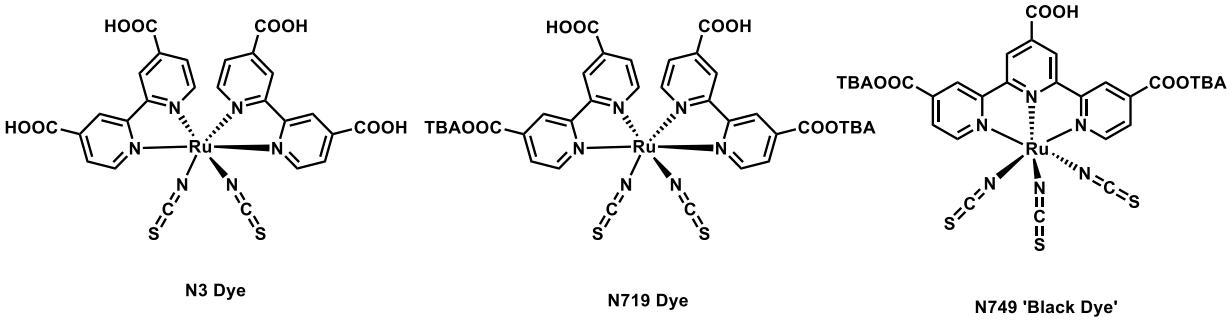

Figure 1.19: Structure of N3, N719 and N749 ruthenium dyes.

For an effective and efficient dye, it requires the following properties:[135]

1. An anchoring ligand which can strongly attach the dye to the TiO_2 surface; current is only produced at a dye-anode interface.
2. The LUMO of the dye must be higher in energy than the CB of TiO_2 for efficient electron transfer from the dye to the anode.
3. The HOMO of the dye must be lower in energy than the electrolyte for efficient regeneration of the dye.
4. The LUMO must be located on the anchoring group, close to the TiO_2 surface.
5. The HOMO must be located near the electrolyte, as far away from the anchor group as possible to avoider non-radiative decay.
6. The dye needs a large absorption coefficient across a broad spectrum to absorb as much light as possible.
7. The dye needs to be photochemically, thermally and electrochemically robust so not to degrade over time.
8. The dye needs to pack efficiently on the TiO_2 surface to produce more current per area.

9. There must be a fast rate of electron transfer from the dye to the TiO_2 CB to avoid quenching by the environment.

Improvement of the sensitizer is a large research field. It is known that increasing the conjugation of the dye increases the absorption coefficient, thus absorbing more energy per photon of light.[136] Cheng *et al.* have demonstrated a 20% increase in efficiency from 8.8 to 10.8% when the conjugation of the system is increased (Figure 1.20).[137]

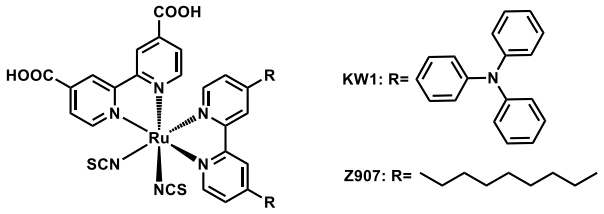

Figure 1.20: Structure of sensitizer KW1 and Z907. Taken from reference.[137]

The dyes C104 and C106 (Figure 1.21) developed by Gratzel *et al.* and Wang *et al.* respectively, show an increase in efficiency through the use of a thiophene system.[138, 139] It has been shown that thiophene causes an increase in photophysical properties of conjugated ruthenium systems due to its polarizability and low resonance energy.[140] They have efficiencies of 10.5% and 11.3% respectively, which are towards the top end for efficiencies of DSCs. C104 and C106 also have an advantage in stability; the long aliphatic chains help separate the electrolyte from the anode in the cell, so prevents quenching of the system through interfacial recombination.[141]

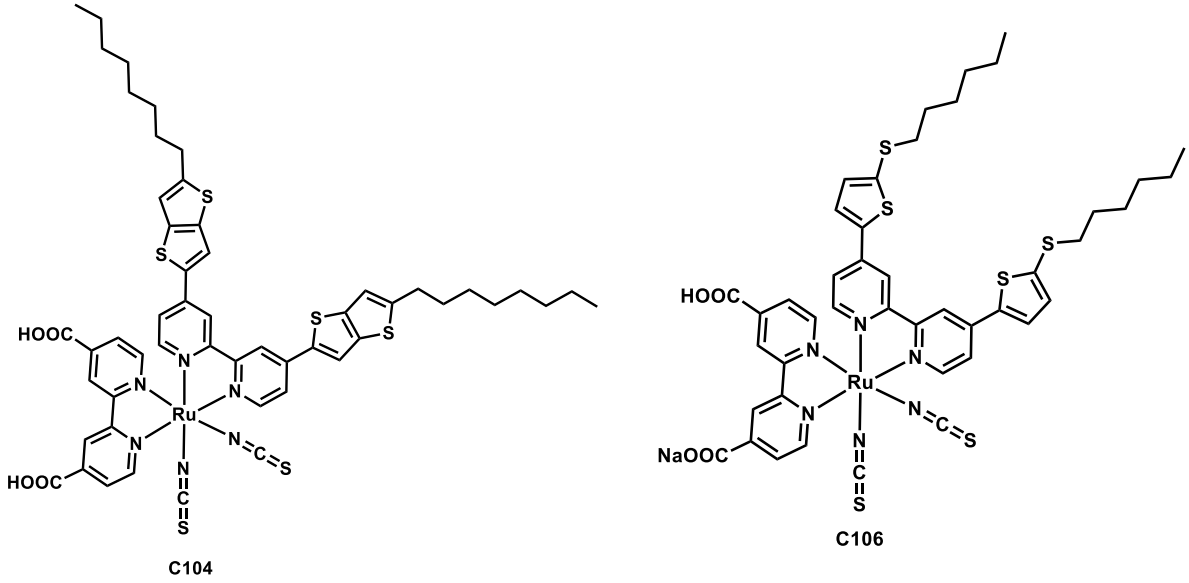

Figure 1.21: Structure of C104 and C106. Adapted from reference.[54, 55]

However, not all dyes that show impressive photophysical properties through increased conjugation are successful as sensitizers in DSCs. 'Star' dyes were developed and showed great absorption due to their increased conjugation, but when put into a DSC system, it was found that the electron injection from the dye into the TiO_2 CB was slower than non-radiative decay, thus making it unsuitable as a dye (Figure 1.22).[142-144]

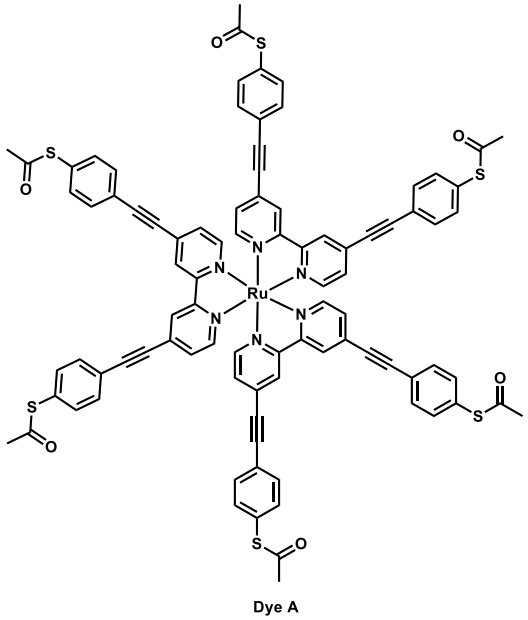

Figure 1.22: Structure of Dye A, an example of a 'star' dye. Taken from reference.[142]

Most dyes seen in the literature have a SCN group. The purpose of this group is to facilitate reduction of the oxidised dye by the electrolyte.[145] However, these SCN groups are unstable and effect the dyes lifetime in the cell due to the fact that the SCN groups can rearrange with themselves and solvent.[146, 147] Grätzel *et al*. have developed a dye, YEO5 (Figure 1.23), which does not have SCN groups present but is competitive with the efficiencies seen for dyes with SCN groups.[148] The advantage to using SCN free dyes is that the lifetime of the cell is increased due to a decrease in degradation of the dye.

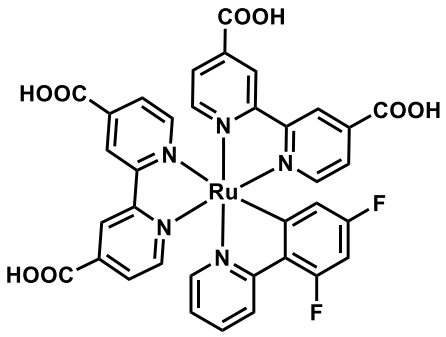

Figure 1.23: Structure of YE05. [148]

An aspect that can affect the stability of the dye on the surface is the linker unit.[149] Current is only produced at the dye-anode interface, so a strong anchor unit is required to prevent dissolution of the sensitizer. Grätzel *et al.* researched into the bonding onto the TiO_2 surface through the carboxylic acid anchors.[150] They noticed that the complex adsorbed *via* two carboxylic acid groups. They bind as carboxylate groups and donate the proton from the acid to the TiO_2 surface, making it positive and decreasing the Fermi energy of the TiO_2 CB.[151] This leads to an increase in photocurrent but a decrease in potential. Theoretically, if the dye has more acidic protons, the photocurrent will increase, thus the efficiency will increase. Three dyes, N3, N719 and N712 have 4, 2 and 0 acidic protons respectively and their adsorptions onto the TiO_2 surface were analysed through IR spectroscopy, and their efficiencies were recorded. As the number of protons increased, the current increased, however the photovoltage decreased, causing similar efficiencies for all three dyes (Table 1.1).

Table 1.1: Performance Characteristics of Photovoltaic Cells.[150]

Sensitizer	Protons	Current / mA cm^{-2}	Potential / mV	η / %
N3	4	19	600	7.4
N719	2	17	730	8.4
N712	1	13	900	8.2

The most widely used linker is a carboxylate, but these bonds are weak, due to the carboxylate-TiO_2 bond breaking in the presence of acid,[152] with an average lifetime in cells of only 24 hours.[153] Linkers such as phosphoric acid,[154-156] silyl[157-159] and many more have been demonstrated for use in DSCs.[160] Zamborini *et al.* have looked into using a silylether as the linker (Figure 1.24) and found an increase in stability of efficiency compared to the COOH linker.[157] The Si-O-Ti covalent bond is stronger,[161, 162] with an average lifetime of greater than 2000 hours.[163] This linker has great potential to increase the stability of the system, so increasing lifetime.

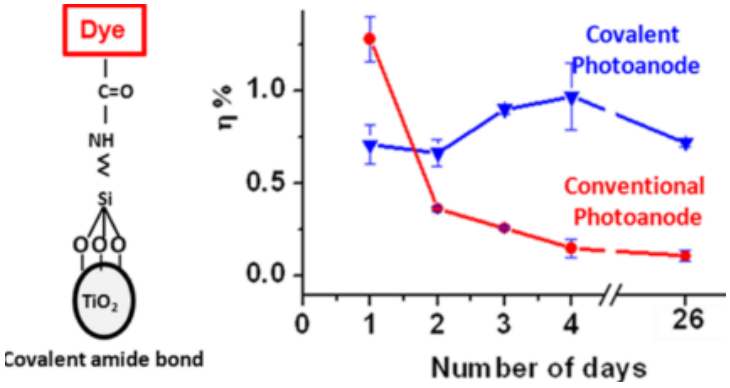

Figure 1.24 : $Si(OEt)_3$ and COOH device linker efficiency over time.[157]

The shape and size of the anode has also been found to be important, with different types of surfaces giving different efficiencies in the system.[164-167] Various semiconductor material such as ZnO and SnO_2 have been researched but TiO_2 is seen as the best due to its stability, low cost and higher power conversion efficiencies.[168] The TiO_2 nanoparticles require a high surface area for attachment of a high concentration of the dye. Mesoporous TiO_2 nanoparticles have been investigated in the use of DSCs for increased surface area.[169-174] The

most widely used material is the P-25, 21 nm anatase nanopowder, produced by Dysol.[175] The small nanoparticle size also helps in reducing recombination.[176, 177] Anatase has been found to be the best material in DSCs, having a photocurrent of 30% higher than the rutile-based cell.[178] High crystallinity of the electrode is required for high efficiency conversion and this can be achieved through high sintering temperatures in the preparation of the electrode.[179] Falaras *et al.* showed production of a higher photocurrent in cells where the films were sintered at 550 °C.[180]

Alteration of the TiO_2 surface, not only by size and shape, but also by addition of a second material, either a metal (such as gold and silver),[181-183] an oxide,[184-186] or quantum dots,[187-189] can lead to changes in the efficiency. The enhancement comes from either plasmonic or charging effects.[190]

There are different types of electrolyte: liquid, quasi-solid and solid electrolyte.[168] The electrolyte plays an important part in the system by regenerating the dye. It has been shown that a large amount of efficiency is lost in this step.[191] The properties of the electrolyte should be: 1. The redox potential should be higher than the HOMO of the sensitizer for efficient regeneration of the sensitizer, 2. It should be highly conductive for efficient electron transfer, 3. It should have stability at high temperatures and over time, and not react with the dye, electrodes or sealant, 4. It should establish good contact between the two electrodes and 5. The absorption should be minimal in the absorption range of the sensitizer.[192, 193] The most widely used electrolyte is the liquid iodide - iodine. Other liquid electrolytes such as bromide - bromine,[194] thiocyanate[195] and cobalt[196, 197] have been investigated.

Pikramenou *et al.* have researched into increasing the efficiency between the electrolyte and dye by addition of a cyclodextrin (CD) on the dye. The liquid iodide - iodine electrolyte fits into the CD cavity and can interact with the dye through supramolecular interactions.[198, 199]

The efficiency increases by 40% (1.17% to 1.64%) when compared to the same dye without the CD cavity (Figure 1.25).[200]

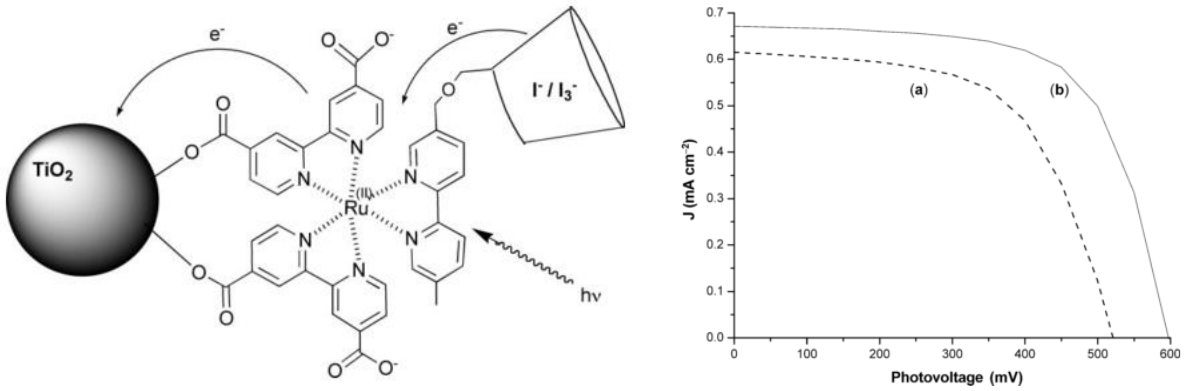

Figure 1.25 : Structure of the Ru dye (left) and photocurrent–photovoltage characteristics of DSCs using Ru dyes without CD (dashed line) and with CD (soid line) under AM 1.5 simulated light (right).[200]

Quasi-solid and solid electrolytes were developed to reduce the volatilization of the electrolyte.[168] Quasi-solid electrolytes can be either polymers or nanopowders and are prepared through gelling liquid electrolytes.[201-203] CuI and solid polymers are examples of solid electrolytes.[204, 205] They reduce recombination from the TiO_2 CB but due to poor contact between the two electrodes they currently only have poor efficiencies of less than 5%.

1.4 Thesis Outline

This thesis focuses on the design of photoactive polypyridyl ruthenium nanoprobes for applications in biological imaging and Dye Sensitized Solar Cells. Thiol functionalised surface active ruthenium complexes are attached to gold nanoparticles and their photophysical properties are investigated.

In chapter 3, three previously developed ruthenium bis-bipyridine complexes with different linker chains are attached to gold nanoparticles.[7, 8, 206] The effect of the distance between the gold surface and the photoactive ruthenium centre on the photophysical properties of the nanoprobe is analysed.[207]

For chapter 4, four novel ruthenium polypyridyl complexes are designed and synthesised for enhanced molecular photophysical properties. The complexes are attached to gold nanoparticles and improvements to the nanoprobes photophysics are studied.

Chapter 5 investigates the solid state photophysical properties of all seven molecular and nanoprobes. Solutions of the samples are dried onto glass and their solid state properties investigated and compared to in solution.

In chapter 6, some of the synthesised ruthenium probes are analysed for applications in Dye Sensitized Solar Cells. The use of gold nanoparticles for enhancement is studied.

1.5 References

1. A. Juris, V. Balzani, F. Barigelletti, S. Campagna, P. Belser and A. Von Zelewsky, *Coord. Chem. Rev.*, 1988, 84, 85-277.
2. K. Kalyanasundaram, *Coord. Chem. Rev.*, 1982, 46, 159-244.
3. S. Campagna, F. Puntoriero, F. Nastasi, G. Bergamini and V. Balzani, in *Photochemistry and Photophysics of Coordination Compounds I*, eds. V. Balzani and S. Campagna, Springer Berlin Heidelberg, 2007.
4. T. Soller, M. Ringler, M. Wunderlich, T. A. Klar, J. Feldmann, H. P. Josel, Y. Markert, A. Nichtl and K. Kürzinger, *Nano Lett.*, 2007, 7, 1941-1946.
5. E. Dulkeith, A. C. Morteani, T. Niedereichholz, T. A. Klar, J. Feldmann, S. A. Levi, F. C. J. M. Veggel, D. N. Reinhoudt, M. Möller and D. I. Gittins, *Phys. Rev. Lett.*, 2002, 89, 203002.
6. C. Kaes, A. Katz and M. W. Hosseini, *Chem. Rev.*, 2000, 100, 3553-3590.
7. N. J. Rogers, S. Claire, R. M. Harris, S. Farabi, G. Zikeli, I. B. Styles, N. J. Hodges and Z. Pikramenou, *Chem. Commun.*, 2014, 50, 617-619.
8. S. J. Adams, D. J. Lewis, J. A. Preece and Z. Pikramenou, *ACS Appl. Mater. Interfaces*, 2014, 6, 11598-11608.
9. J. G. Vos and J. M. Kelly, *Dalton Trans.*, 2006, 4869-4883.
10. M. J. Cook, A. P. Lewis, G. S. G. McAuliffe, V. Skarda, A. J. Thomson, J. L. Glasper and D. J. Robbins, *J. Chem. Soc., Perkin Trans. 2*, 1984, 1293-1301.
11. N. H. Damrauer, G. Cerullo, A. Yeh, T. R. Boussie, C. V. Shank and J. K. McCusker, *Science*, 1997, 275, 54-57.
12. A. Cannizzo, F. van Mourik, W. Gawelda, G. Zgrablic, C. Bressler and M. Chergui, *Angew. Chem.*, 2006, 118, 3246-3248.
13. P. A. Mabrouk and M. S. Wrighton, *Inorg. Chem.*, 1986, 25, 526-531.

14. Y. J. Chang, X. Xu, T. Yabe, S. C. Yu, D. R. Anderson, L. K. Orman and J. B. Hopkins, *J. Phys. Chem*, 1990, 94, 729-736.

15. Y. J. Chang, L. K. Orman, D. R. Anderson, T. Yabe and J. B. Hopkins, *J. Chem. Phys.*, 1987, 87, 3249-3250.

16. J. Van Houten and R. J. Watts, *J. Am. Chem. Soc.*, 1975, 97, 3843-3844.

17. J. Van Houten and R. J. Watts, *J. Am. Chem. Soc.*, 1976, 98, 4853-4858.

18. A. P. K. Kalyonasundaram, *Polypyridyl complexes of ruthenium, osmium and iron*, 1992, Academic Press, London, 105 - 212.

19. D. Rendall, *Fluorescence and Phosphorescence*, 1987, Thames Polytechnic, London.

20. J. Lakowicz, *Principles of Fluorescence Spectroscopy, 3rd Edition*, 2006, Springer.

21. J. N. Demas, E. W. Harris and R. P. McBride, *J. Am. Chem. Soc.*, 1977, 99, 3547-3551.

22. A. A. Abdel-Shafi, M. D. Ward and R. Schmidt, *Dalton Trans.*, 2007, 2517-2527.

23. N. Sutin and C. Creutz, *Pure Appl. Chem.*, 1980, 52, 2717 - 2738.

24. C. J. Timpson, C. C. Carter and J. Olmsted, *J. Phys. Chem*, 1989, 93, 4116-4120.

25. D. B. Papkovsky and R. I. Dmitriev, *Chem. Soc. Rev.*, 2013, 42, 8700-8732.

26. E. C. Dreaden, A. M. Alkilany, X. Huang, C. J. Murphy and M. A. El-Sayed, *Chem. Soc. Rev.*, 2012, 41, 2740-2779.

27. F. Correard, K. Maximova, M. Estève, C. Villard, M. Roy, A. Al-Kattan, M. Sentis, M. Gingras, A. V. Kabashin and D. Braguer, *Int. J. Nanomedicine*, 2014, 9, 5415-5430.

28. E. Boisselier and D. Astruc, *Chem. Soc. Rev.*, 2009, 38, 1759-1782.

29. D. Astruc, F. Lu and J. R. Aranzaes, *Angew. Chem., Int. Ed.*, 2005, 44, 7852-7872.

30. M. Haruta and M. Daté, *Appl. Catal., A*, 2001, 222, 427-437.

31. C. Lucarelli, A. Lolli, A. Giugni, L. Grazia, S. Albonetti, D. Monticelli and A. Vaccari, *Appl. Catal., B*, 2017, 203, 314-323.

32. N. Verdoodt, C. R. Basso, B. F. Rossi and V. A. Pedrosa, *Food Chem.*, 2017, 221, 1792-1796.

33. K. M. Mayer and J. H. Hafner, *Chem. Rev.*, 2011, 111, 3828-3857.

34. K. S. Lee and M. A. El-Sayed, *J. Phys. Chem. B*, 2006, 110, 19220-19225.

35. Y. Tian and T. Tatsuma, *J. Am. Chem. Soc.*, 2005, 127, 7632-7637.

36. M. D. Brown, T. Suteewong, R. S. S. Kumar, V. D'Innocenzo, A. Petrozza, M. M. Lee, U. Wiesner and H. J. Snaith, *Nano Lett.*, 2011, 11, 438-445.

37. A. Pandikumar, S. Lim, S. Jayabal, N. M. Huang, H. N. Lim and R. Ramaraj, *Renew. Sustainable Energy Rev.*, 2016, 60, 408-420.

38. X. Xu, G. Duan, Y. Li, G. Liu, J. Wang, H. Zhang, Z. Dai and W. Cai, *ACS Appl. Mater. Interfaces*, 2014, 6, 65-71.

39. V. Amendola, S. Polizzi and M. Meneghetti, *J. Phys. Chem. B*, 2006, 110, 7232-7237.

40. H. Wender, M. L. Andreazza, R. R. B. Correia, S. R. Teixeira and J. Dupont, *Nanoscale*, 2011, 3, 1240-1245.

41. B. J. Y. Tan, C. H. Sow, T. S. Koh, K. C. Chin, A. T. S. Wee and C. K. Ong, *J. Phys. Chem. B*, 2005, 109, 11100-11109.

42. M. K. Corbierre, J. Beerens and R. B. Lennox, *Chem. Mater.*, 2005, 17, 5774-5779.

43. C. L. Haynes and R. P. Van Duyne, *J. Phys. Chem. B*, 2001, 105, 5599-5611.

44. J. Turkevich, P. C. Stevenson and J. Hillier, *Farad. Discuss.*, 1951, 11, 55-75.

45. F. Schulz, T. Homolka, N. G. Bastús, V. Puntes, H. Weller and T. Vossmeyer, *Langmuir*, 2014, 30, 10779-10784.

46. N. R. Jana, L. Gearheart and C. J. Murphy, *Langmuir*, 2001, 17, 6782-6786.

47. M. Brust, M. Walker, D. Bethell, D. J. Schiffrin and R. Whyman, *J. Chem. Soc., Chem. Commun.*, 1994, 801-802.

48. I. Hussain, S. Graham, Z. Wang, B. Tan, D. C. Sherrington, S. P. Rannard, A. I. Cooper and M. Brust, *J. Am. Chem. Soc.*, 2005, 127, 16398-16399.

49. A. Frenkel, S. Nemzer, I. Pister, L. Soussan, T. Harris, Y. Sun and M. Rafailovich, *J. Chem. Phys.*, 2005, 123, 184701.

50. M. J. Hostetler, J. E. Wingate, C.-J. Zhong, J. E. Harris, R. W. Vachet, M. R. Clark, J. D. Londono, S. J. Green, J. J. Stokes, G. D. Wignall, G. L. Glish, M. D. Porter, N. D. Evans and R. W. Murray, *Langmuir*, 1998, 14, 17-30.

51. R. G. Nuzzo and D. L. Allara, *J. Am. Chem. Soc.*, 1983, 105, 4481-4483.

52. B. Nikoobakht and M. A. El-Sayed, *Chem. Mater.*, 2003, 15, 1957-1962.

53. J. D. S. Newman and G. J. Blanchard, *Langmuir*, 2006, 22, 5882-5887.

54. T. K. Sau and C. J. Murphy, *J. Am. Chem. Soc.*, 2004, 126, 8648-8649.

55. M. Brust, J. Fink, D. Bethell, D. J. Schiffrin and C. Kiely, *J. Chem. Soc., Chem. Commun.*, 1995, DOI: 10.1039/c39950001655, 1655-1656.

56. S. K. Ghosh and T. Pal, *Chem. Rev.*, 2007, 107, 4797-4862.

57. S. Link and M. A. El-Sayed, *J. Phys. Chem. B*, 1999, 103, 8410-8426.

58. M. C. Daniel and D. Astruc, *Chem. Rev.*, 2004, 104, 293-346.

59. K. L. Kelly, E. Coronado, L. L. Zhao and G. C. Schatz, *J. Phys. Chem. B*, 2003, 107, 668-677.

60. S. Eustis and M. A. El Sayed, *Chem. Soc. Rev.*, 2006, 35, 209-217.

61. K. A. Willets and R. P. Van Duyne, *Annu. Rev. Phys. Chem.*, 2007, 58, 267-297.

62. N. L. Gruenke, M. F. Cardinal, M. O. McAnally, R. R. Frontiera, G. C. Schatz and R. P. Van Duyne, *Chem. Soc. Rev.*, 2016, 45, 2263-2290.

63. X. Liu, H. Xu, H. Xia and D. Wang, *Langmuir*, 2012, 28, 13720-13726.

64. Y. Qiao, H. Chen, Y. Lin and J. Huang, *Langmuir*, 2011, 27, 11090-11097.

65. N. G. Bastús, J. Comenge and V. Puntes, *Langmuir*, 2011, 27, 11098-11105.

66. N. Khee Chaw and C. Wenlong, *Nanotechnology*, 2012, 23, 105602.

67. F. Kim, J. H. Song and P. Yang, *J. Am. Chem. Soc.*, 2002, 124, 14316-14317.

68. A. Gole and C. J. Murphy, *Chem. Mater.*, 2004, 16, 3633-3640.

69. P. K. Jain, K. S. Lee, I. H. El-Sayed and M. A. El-Sayed, *J. Phys. Chem. B*, 2006, 110, 7238-7248.

70. E. Pensa, E. Cortés, G. Corthey, P. Carro, C. Vericat, M. H. Fonticelli, G. Benítez, A. A. Rubert and R. C. Salvarezza, *Acc. Chem. Res.*, 2012, 45, 1183-1192.

71. G. H. Woehrle, L. O. Brown and J. E. Hutchison, *J. Am. Chem. Soc.*, 2005, 127, 2172-2183.

72. Y. Kuwahara, T. Akiyama and S. Yamada, *Thin Solid Films*, 2001, 393, 273-277.

73. Y. Li, H. Qi, J. Yang and C. Zhang, *Microchim. Acta*, 2008, 164, 69.

74. T. Akiyama, K. Inoue, Y. Kuwahara, N. Terasaki, Y. Niidome and S. Yamada, *J. Electroanal. Chem.*, 2003, 550–551, 303-307.

75. N. Terasaki, K. Otsuka, T. Akiyama and S. Yamada, *Jpn. J. Appl. Phys.*, 2004, 43, 2372.

76. F. C. Leung, A. Y. Tam, V. K. Au, M. Li and V. W. Yam, *ACS Appl. Mater. Interfaces*, 2014, 6, 6644-6653.

77. M. Jebb, P. K. Sudeep, P. Pramod, K. G. Thomas and P. V. Kamat, *J. Phys. Chem. B*, 2007, 111, 6839-6844.

78. P. Pramod, P. K. Sudeep, K. G. Thomas and P. V. Kamat, *J. Phys. Chem. B*, 2006, 110, 20737-20741.

79. R. B. P. Elmes, K. N. Orange, S. M. Cloonan, D. C. Williams and T. Gunnlaugsson, *J. Am. Chem. Soc.*, 2011, 133, 15862-15865.

80. S. R. King, S. Shimmon, A. R. Gentle, M. T. Westerhausen, A. Dowd and A. M. McDonagh, *Nanotechnology*, 2016, 27, 215702.

81. R. E. Smalley, *American Chemical Society: Washington, DC*, 2003, U24.

82. A. Adeloye and P. Ajibade, *Molecules*, 2014, 19, 12421.

83. J. Conti, *International Energy Outlook 2011; U.S. Energy Administration: Washington, DC*, 2011.

84. S. Shafiee and E. Topal, *Energy Policy*, 2009, 37, 181-189.

85. www.gov.co.uk, 2013.

86. http://www.renewableenergyworld.com/rea/news/hydropower/research.

87. J. Wu, Z. Lan, J. Lin, M. Huang, Y. Huang, L. Fan and G. Luo, *Chem. Rev.*, 2015, 115, 2136-2173.

88. W. Wong, *J. Organomet. Chem.*, 2009, 694, 2644-2647.

89. S. Chih-Tang, R. N. Noyce and W. Shockley, *Proc. IRE*, 1957, 45, 1228-1243.

90. A. V. Shah, J. Meier, E. Vallat-Sauvain, N. Wyrsch, U. Kroll, C. Droz and U. Graf, *Sol. Energy Mater. Sol. Cells*, 2003, 78, 469-491.

91. Y. Zhao, G. A. Meek, B. G. Levine and R. R. Lunt, *Adv. Opt. Mater.*, 2014, 2, 606-611.

92. G. E. Eperon, V. M. Burlakov, A. Goriely and H. J. Snaith, *ACS Nano*, 2014, 8, 591-598.

93. *http://www.solaria.com/*.

94. *http://solarwindow.com/*.

95. *http://gcell.com/product/gratzel-solar-backpack*.

96. *http://www.pvilion.com/index#/solar-clothing/*.

97. *www.greenbiz.com*.

98. B. O'Regan and M. Gratzel, *Nature*, 1991, 353, 734.

99. F. Fabregat-Santiago, J. Bisquert, G. Garcia-Belmonte, G. Boschloo and A. Hagfeldt, *Sol. Energy Mater. Sol. Cells*, 2005, 87, 117-131.

100. E. Palomares, J. N. Clifford, S. A. Haque, T. Lutz and J. R. Durrant, *J. Am. Chem. Soc.*, 2003, 125, 475-482.

101. S. Y. Huang, G. Schlichthörl, A. J. Nozik, M. Grätzel and A. J. Frank, *J. Phys. Chem. B*, 1997, 101, 2576-2582.

102. J. Luo, Z. Wan, C. Jia, Y. Wang and X. Wu, *Electrochim. Acta*, 2016, 215, 506-514.

103. A. D. Carlo, *http://portal.ictp.it/energynet/material/DiCarlo.pdf*, 2008.

104. T. Toyoda, T. Sano, J. Nakajima, S. Doi, S. Fukumoto, A. Ito, T. Tohyama, M. Yoshida, T. Kanagawa, T. Motohiro, T. Shiga, K. Higuchi, H. Tanaka, Y. Takeda, T. Fukano, N. Katoh, A. Takeichi, K. Takechi and M. Shiozawa, *J. Photochem. Photobiol. A*, 2004, 164, 203-207.

105. T. Toyoda, T. Sano, J. Nakajima, S. Doi, S. Fukumoto, A. Ito, T. Tohyama, M. Yoshida, T. Kanagawa, T. Motohiro, T. Shiga, K. Higuchi, H. Tanaka, Y. Takeda, T. Fukano, N. Katoh, A. Takeichi, K. Takechi and M. Shiozawa, *J. Photochem. Photobiol. A*, 2004, 203-207.

106. M. Berginc, U. O. Krašovec, M. Jankovec and M. Topiè, *Sol. Energy Mater. Sol. Cells*, 2007, 91, 821-828.

107. M. Durr, A. Schmid, M. Obermaier, S. Rosselli, A. Yasuda and G. Nelles, *Nat. Mater*, 2005, 607-611.

108. F. O. Pichot, J. R. Pitts and B. A. Gregg, *Langmuir*, 2000, 5626-5630.

109. C. Chen, M. Wang, J. Li, N. Pootrakulchote, L. Alibabaei, C. Ngoc-le, J. Decoppet, J. Tsai, C. Grätzel, C. Wu, S. M. Zakeeruddin and M. Grätzel, *ACS Nano*, 2009, 3, 3103-3109.

110. J. Kalowekamo and E. Baker, *Sol Energy*, 2009, 83, 1224-1231.

111. N. P. J. Burschka, S. Moon, R. Humphry-Baker, P. Gao, M. Nazeeruddin, M. Grätzel, *Nature*, 2013, 316-319.

112. H. J. Snaith, *Adv. Funct. Mater.*, 2010, 20, 13-19.

113. M. A. Green, K. Emery, Y. Hishikawa, W. Warta and E. D. Dunlop, *Prog. Photovolt. Res. Appl.*, 2012, 20, 12-20.

114. W. Shockley and H. J. Queisser, *J. Appl. Phys.*, 1961, 32, 510-519.

115. J. Nelson, *The Physics of Solar Cells*, 2003, Imperial College Press, London.

116. P. A. Antunes, C. J. L. Constantino, R. F. Aroca and J. Duff, *Langmuir*, 2001, 17, 2958-2964.

117. S. E. Koops, B. C. O'Regan, P. R. F. Barnes and J. R. Durrant, *J. Am. Chem. Soc.*, 2009, 131, 4808-4818.

118. B. E. Hardin, H. J. Snaith and M. D. McGehee, *Nat Photon*, 2012, 6, 162-169.

119. Q. Yu, Y. Wang, Z. Yi, N. Zu, J. Zhang, M. Zhang and P. Wang, *ACS Nano*, 2010, 4, 6032-6038.

120. T. W. Rees and E. Baranoff, *Polyhedron*, 2014, 82, 37-49.

121. C. Chen, S. Wu, C. Wu, J. Chen and K. Ho, *Angew. Chem.*, 2006, 118, 5954-5957.

122. S. Ito, H. Miura, S. Uchida, M. Takata, K. Sumioka, P. Liska, P. Comte, P. Pechy and M. Gratzel, *Chem. Commun.*, 2008, DOI: 10.1039/b809093a, 5194-5196.

123. L. Schmidt-Mende, U. Bach, R. Humphry-Baker, T. Horiuchi, H. Miura, S. Ito, S. Uchida and M. Grätzel, *Adv. Mater.*, 2005, 17, 813-815.

124. A. Mahmood, *Sol Energy*, 2016, 123, 127-144.

125. J. Lee, D. Seol, A. Cho and N. Park, *Adv. Mater.*, 2014, 26, 4991-4998.

126. S. S. Shin, J. S. Kim, J. H. Suk, K. D. Lee, D. W. Kim, J. H. Park, I. S. Cho, K. S. Hong and J. Y. Kim, *ACS Nano*, 2013, 7, 1027-1035.

127. L. Chen and Y. Chen, *Sci. Adv. Mater.*, 2015, 7, 1636-1639.

128. S. Mathew, A. Yella, P. Gao, R. Humphry-Baker, F. E. CurchodBasile, N. Ashari-Astani, I. Tavernelli, U. Rothlisberger, K. NazeeruddinMd and M. Grätzel, *Nat Chem*, 2014, 6, 242-247.

129. X. Qian, R. Yan, L. Shao, H. Li, X. Wang and L. Hou, *Dyes Pigm.*, 2016, 134, 434-441.

130. H. Dong, X. Zhou and C. Jiang, *Theor. Chem. Acc.*, 2012, 131, 1102.

131. Z. Ning, Y. Fu and H. Tian, *Energ Environ Sci*, 2010, 3, 1170-1181.

132. R. Katoh, A. Furube, T. Yoshihara, K. Hara, G. Fujihashi, S. Takano, S. Murata, H. Arakawa and M. Tachiya, *J. Phys. Chem. B*, 2004, 108, 4818-4822.

133. K. E. Lee, M. A. Gomez, S. Elouatik and G. P. Demopoulos, *Langmuir*, 2010, 26, 9575-9583.

134. M. K. Nazeeruddin, P. Pechy and M. Gratzel, *Chem. Commun.*, 1997, 18, 1705-1706.

135. P. G. Bomben, K. C. D. Robson, B. D. Koivisto and C. P. Berlinguette, *Coord. Chem. Rev.*, 2012, 256, 1438-1450.

136. D. S. Tyson and F. N. Castellano, *J. Phys. Chem. A*, 1999, 103, 10955-10960.

137. K. Cao, J. Lu, J. Cui, Y. Shen, W. Chen, G. Alemu, Z. Wang, H. Yuan, J. Xu, M. Wang and Y. Cheng, *J. Mater. Chem. A.*, 2014, 2, 4945-4953.

138. F. Gao, Y. Wang, J. Zhang, D. Shi, M. Wang, R. Humphry-Baker, P. Wang, S. M. Zakeeruddin and M. Gratzel, *Chem. Commun.*, 2008, 23, 2635-2637.

139. Y. Cao, Y. Bai, Q. Yu, Y. Cheng, S. Liu, D. Shi, F. Gao and P. Wang, *J. Phys. Chem. C*, 2009, 113, 6290-6297.

140. K. C. D. Robson, B. D. Koivisto, T. J. Gordon, T. Baumgartner and C. P. Berlinguette, *Inorg. Chem.*, 2010, 49, 5335-5337.

141. S. Ko, A. Cho, M. Kim, C. Lee and N. Park, *Dyes Pigm.*, 2012, 94, 88-98.

142. J. Otsuki, H. Kameda, S. Tomihira, H. Sakaguchi and T. Takido, *Chem. Lett.*, 2002, 31, 610-611.

143. P. G. Johansson, Y. Zhang, G. J. Meyer and E. Galoppini, *Inorg. Chem.*, 2013, 52, 7947-7957.

144. Y. Zhang, E. Galoppini, P. G. Johansson and G. J. Meyer, *Pure Appl. Chem*, 2011, 83, 861-868.

145. H. Greijer, J. Lindgren and A. Hagfeldt, *J. Phys. Chem. B*, 2001, 105, 6314-6320.

146. T. P. Brewster, W. Ding, N. D. Schley, N. Hazari, V. S. Batista and R. H. Crabtree, *Inorg. Chem.*, 2011, 50, 11938-11946.

147. P. Tuyet Nguyen, R. Degn, H. Thai Nguyen and T. Lund, *Sol. Energy Mater. Sol. Cells*, 2009, 93, 1939-1945.

148. T. Bessho, E. Yoneda, J. Yum, M. Guglielmi, I. Tavernelli, H. Imai, U. Rothlisberger, M. K. Nazeeruddin and M. Grätzel, *J. Am. Chem. Soc.*, 2009, 131, 5930-5934.

149. J. Mao, N. He, Z. Ning, Q. Zhang, F. Guo, L. Chen, W. Wu, J. Hua and H. Tian, *Angew. Chem., Int. Ed.*, 2012, 51, 9873-9876.

150. M. K. Nazeeruddin, R. Humphry-Baker, P. Liska and M. Grätzel, *J. Phys. Chem. B*, 2003, 107, 8981-8987.

151. S. G. Yan and J. T. Hupp, *J. Phys. Chem*, 1996, 100, 6867-6870.

152. Y. Guo, G. Xue, T. Yu, J. Guan, X. Yu, J. Zhang, J. Liu and Z. Zou, *Int. J. Electrochem. Sci.*, 2012, 1496-1511.

153. M. Turrion, B. Macht, P. Salvador and H. Tributsch, *Z. Phys. Chem*, 1999, 51-57.

154. D. F. Zigler, Z. A. Morseth, L. Wang, D. L. Ashford, M. K. Brennaman, E. M. Grumstrup, E. C. Brigham, M. K. Gish, R. J. Dillon, L. Alibabaei, G. J. Meyer, T. J. Meyer and J. M. Papanikolas, *J. Am. Chem. Soc.*, 2016, 138, 4426-4438.

155. A. Abate, R. Perez-Tejada, K. Wojciechowski, J. M. Foster, A. Sadhanala, U. Steiner, H. J. Snaith, S. Franco and J. Orduna, *Phys. Chem. Chem. Phys.*, 2015, 17, 18780-18789.

156. E. Bae and W. Choi, *J. Phys. Chem. B*, 2006, 110, 14792-14799.

157. T. Luitel and F. P. Zamborini, *Langmuir*, 2013, 29, 13582-13594.

158. J. Font, P. de March, F. Busque, E. Casas, M. Benitez, L. Teruel and H. Garcia, *J. Mater. Chem.*, 2007, 17, 2336-2343.

159. K. Kakiage, Y. Aoyama, T. Yano, K. Oya, J. Fujisawa and M. Hanaya, *Chem. Commun.*, 2015, 51, 15894-15897.

160. L. Zhang and J. M. Cole, *ACS Appl. Mater. Interfaces*, 2015, 7, 3427-3455.

161. N. Iguchi, C. Cady, R. Snoeberger, B. Hunter, E. Sproviero, C. Schmuttenmaer, R. Crabtree, G. Brudvig and V. Batista, *Physical Chemistry of Interfaces and Nanomaterials VII*, 2008, DOI: 10.1117/12.798938.

162. L. Gamble, L. S. Jung and C. T. Campbell, *Langmuir*, 1995, 11, 4505-4514.

163. K. Kakiage, M. Yamamura, E. Fujimura, T. Kyomen, M. Unno and M. Hanaya, *Chem. Lett.*, 2010, 39, 260-262.

164. N. Huang, B. Sebo, M. M. Pan, Y. M. Liu, T. Peng, W. W. Sun, C. H. Bu and X. Z. Zhao, *Sol Energy*, 2013, 97, 266-272.

165. X. Feng, K. Zhu, A. J. Frank, C. A. Grimes and T. E. Mallouk, *Angew. Chem.*, 2012, 124, 2781-2784.

166. V. Dhas, S. Muduli, S. Agarkar, A. Rana, B. Hannoyer, R. Banerjee and S. Ogale, *Sol Energy*, 2011, 85, 1213-1219.

167. U. Diebold, *Surf. Sci. Rep.*, 2003, 48, 53-229.

168. A. Jena, S. P. Mohanty, P. Kumar, J. Naduvath, V. Gondane, P. Lekha, J. Das, H. K. Narula, S. Mallick and P. Bhargava, *Trans. Indian Ceram. Soc.*, 2012, 71, 1-16.

169. Y. Liu, S. Wang, Z. Shan, X. Li, J. Tian, Y. Mei, H. Ma and K. Zhu, *Electrochim. Acta*, 2012, 60, 422-427.

170. M. A. Abdolahi Sadatlu and N. Mozaffari, *Sol Energy*, 2016, 133, 24-34.

171. H. Li, Z. Bian, J. Zhu, D. Zhang, G. Li, Y. Huo, H. Li and Y. Lu, *J. Am. Chem. Soc.*, 2007, 129, 8406-8407.

172. M. Meire, S. W. Verbruggen, S. Lenaerts, P. Lommens, P. Van Der Voort and I. Van Driessche, *J. Mater. Sci.*, 2016, 51, 9822-9829.

173. M. Zukalová, A. Zukal, L. Kavan, M. K. Nazeeruddin, P. Liska and M. Grätzel, *Nano Lett.*, 2005, 5, 1789-1792.

174. N. Tasić, Z. Marinković Stanojević, Z. Branković, U. Lačnjevac, V. Ribić, M. Žunić, T. Novaković, M. Podlogar and G. Branković, *Electrochim. Acta*, 2016, 210, 606-614.

175. I. Zumeta, R. Espinosa, J. A. Ayllón, X. Domènech, R. guez-Clemente and E. Vigil, *Sol. Energy Mater. Sol. Cells*, 2003, 76, 15-24.

176. K. Zhu, E. A. Schiff, N. G. Park, J. Lagemaat and A. J. Frank, *Appl. Phys. Lett.*, 2002, 80, 685-687.

177. T. L. Ma, T. Kida, M. Akiyama, K. Inoue, S. J. Tsunematsu, K. Yao, H. Noma and E. Abe, *Electrochem. Commun.*, 2003, 5, 369-372.

178. N. G. Park, J. Van de Lagemaat and A. J. Frank, *J. Phys. Chem. B*, 2000, 104, 8989-8994.

179. S. Ngamsinlapasathian, T. Sreethawong, Y. Suzuki and S. Yoshikawa, *Sol. Energy Mater. Sol. Cells.*, 2005, 86, 269-282.

180. G. Kantonis, T. Stergiopoulos, A. P. Katsoulidis, P. J. Pomonis and P. Falaras, *J. Photochem. Photobiol. A*, 2011, 217, 236-241.

181. S. W. Sheehan, H. Noh, G. W. Brudvig, H. Cao and C. A. Schmuttenmaer, *J. Phys. Chem. C*, 2012, 117, 927-934.

182. H. Chen, M. G. Blaber, S. D. Standridge, E. J. DeMarco, J. T. Hupp, M. A. Ratner and G. C. Schatz, *J. Phys. Chem. C*, 2012, 116, 10215-10221.

183. S. Chang, Q. Li, X. Xiao, K. Y. Wong and T. Chen, *Energ Environ Sci*, 2012, 5, 9444-9448.

184. H. S. Jung, J. K. Lee, M. Nastasi, S. W. Lee, J. Y. Kim, J. S. Park, K. S. Hong and H. Shin, *Langmuir*, 2005, 21, 10332-10335.

185. Z. S. Wang, M. Yanagida, K. Sayama and H. Sugihara, *Chem. Mater.*, 2006, 18, 2912-2916.

186. S. Chappel, S. G. Chen and A. Zaban, *Langmuir*, 2002, 18, 3336-3342.

187. P. K. Santra and P. V. Kamat, *J. Am. Chem. Soc.*, 2012, 135, 877-885.

188. A. Kathalingam, J. Rhee and S. Han, *Int. J. Energy Res*, 2014, 38, 674-682.

189. J. H. Yum, J. W. Lee, Y. Kim, R. Humphry-Baker, N. G. Park and M. Grätzel, *Sol Energy*, 2014, 109, 183-188.

190. H. Choi, W. T. Chen and P. V. Kamat, *ACS Nano*, 2012, 6, 4418-4427.

191. R. Harikisun and H. Desilvestro, *Sol Energy*, 2011, 85, 1179-1188.

192. Z. Yu, N. Vlachopoulos, M. Gorlov and L. Kloo, *Dalton Trans.*, 2011, 40, 10289-10303.

193. J. Wu, Z. Lan, S. Hao, P. Li, J. Lin, M. Huang, L. Fang and Y. Huang, *Pure Appl. Chem.*, 2008, 80, 2241-2258.

194. Z. S. Wang, K. Sayama and H. Sugihara, *J. Phys. Chem. B*, 2005, 109, 22449-22455.

195. G. Oskam, B. V. Bergeron, G. J. Meyer and P. C. Searson, *J. Phys. Chem. B*, 2001, 105, 6867-6873.

196. D. Song, M. S. Kang, Y. G. Lee, W. Cho, J. H. Lee, T. Son, K. J. Lee, S. Nagarajan, P. Sudhagar, J. H. Yum and Y. S. Kang, *Phys. Chem. Chem. Phys.*, 2012, 14, 469-472.

197. J. H. Yum, E. Baranoff, F. Kessler, T. Moehl, S. Ahmad, T. Bessho, A. Marchioro, E. Ghadiri, J. E. Moser and C. Yi, *Nature Communications*, 2012, 3, 631.

198. J. M. Haider, R. M. Williams, L. De Cola and Z. Pikramenou, *Angew. Chem., Int. Ed.*, 2003, 42, 1830-1833.

199. J. M. Haider, M. Chavarot, S. Weidner, I. Sadler, R. M. Williams, L. De Cola and Z. Pikramenou, *Inorg. Chem.*, 2001, 40, 3912-3921.

200. J. Faiz, A. I. Philippopoulos, A. G. Kontos, P. Falaras and Z. Pikramenou, *Adv. Funct. Mater.*, 2007, 17, 54-58.

201. M. S. Su'ait, M. Y. A. Rahman and A. Ahmad, *Sol Energy*, 2015, 115, 452-470.

202. A. F. Nogueira, C. Longo and M. A. De Paoli, *Coord. Chem. Rev.*, 2004, 248, 1455-1468.

203. S. Yun, J. N. Freitas, A. F. Nogueira, Y. Wang, S. Ahmad and Z. Wang, *Prog. Polym. Sci.*, 2016, 59, 1-40.

204. K. Tennakone, G. R. R. A. Kumara, A. R. Kumarasinghe, K. G. U. Wijayantha and P. Sirimanne, *Semicond. Sci. Technol.*, 1995, 10, 1689-1693.

205. U. Bach, D. Lupo, P. Comte, J. E. Moser, F. Weissortel, J. Salbeck, H. Spreitzer and M. Gratzel, *Nature*, 1998, 398, 583-585.

206. P. Bertoncello, E. T. Kefalas, Z. Pikramenou, P. R. Unwin and R. J. Forster, *J. Phys. Chem. B*, 2006, 110, 10063-10069.

207. S. A. M. Osborne and Z. Pikramenou, *Farad. Discuss.*, 2015, 185, 219-231.

2 General methods

2.1 Materials

Solvents and deuterated solvent for NMR were purchased from Fisher or Sigma Aldrich and anhydrous solvents were dried over 3Å molecular sieves under N_2 for 1 hr (CCl_4, 1,4-dioxane and DMF), or by PureSolv-EN solvent purification system (THF). All compounds synthesised under N_2 were done so using standard Schlenk techniques.

2.2 Synthesis techniques

^{1}H NMR spectroscopy was carried out on a Brüker AVIII300 spectrometer. $^{13}C\{1H\}$ and 2D NMR spectroscopy was carried out on a Brüker AVIII400 spectrometer. Electrospray mass spectra were recorded on a Waters Micromass LCT time of flight mass spectrometer, using a nitrogen laser, and matrix assisted laser desorption ionisation time of flight (MALDI-TOF) mass spectrometry was performed on a Bruker Diflex IV mass spectrometer. Elemental analysis was performed at the London School of Pharmacy, UCL, on an Elemental Analyser, Model 1108 (Carlo-Erba, Milan, Italy) with PC based data system, Eager 200 for WindowsTM and a Sartorious Ultra Micro Balance, 4504MP8. Fourier transform infra-red (FT-IR) spectroscopy was performed on powder samples, using a Perkin Elmer Spectrum 100 FT-IR, with a universal attenuated total reflectance attachment.

2.3 Photophysical characterisation techniques

UV-vis absorption spectroscopy measurements were performed on a Varian Cary 50 or 5000 spectrometer at a 300 nm min^{-1} acquisition rate. Liquid samples were prepared in 1 cm path length quartz cuvettes. Solid state UV-vis spectroscopy was carried out on a Varian Cary 5000 with a diffuse reflectance accessory (DRA) attachment. Samples were dried onto a quartz glass. Steady-state and time-resolved luminescence measurements were executed on an

Edinburgh Instruments FLS920 spectrometer, with a 450 W xenon arc lamp illumination source. Samples were prepared in quartz cuvettes with four transparent faces, and appropriate long-pass filters were employed to eliminate second-order photon scattering. Luminescence lifetimes (τ) were measured with a 445 nm picosecond pulse length diode laser excitation source, using the time-correlated single-photon counting module of the Edinburgh Instruments FLS920 spectrometer set-up, with the Hamamatsu R928 photomultiplier tube (PMT). Lifetimes were tail-fitted using the Edinburgh Instruments F900 or FAST PC software. The quality of the fit results was evaluated by fitting the reduced chi-square (X^2) parameter between 1.0–1.2. All lifetimes were fitted using a Marquardt-Levenberg algorithm. Quantum yield (Φ) measurements were either performed on the spectrometer using an integrating sphere (for nanoprobes reported) or relative to a standard (for molecular probes reported). On the integrating sphere, solution measurements were referenced to the solvent used and nanoparticles were referenced to un-labelled gold nanoparticles. For reference measurements, they were calculated against the standard $Ru(bpy)_3Cl_2$ (2.8% in water) (Equation 2.1).[1]

$$\boldsymbol{\Phi_x = \Phi_r \left(\frac{A_r(\lambda_r)}{A_x(\lambda_x)}\right)\left(\frac{I_r(\lambda_r)}{I_x(\lambda_x)}\right)\left(\frac{n_x^2}{n_r^2}\right)\left(\frac{D_x}{D_r}\right)} \qquad \textbf{Equation 2.1}$$

Where Φ is the quantum yield, A is the absorbance, I is the intensity of the lamp, n is the refractive index of the solvent, D is the integral of the peak, x is the sample and r is the reference. The absorbance is taken form the UV-vis spectrum and was taken at 450 nm, the lamp intensity correction can be discarded if both the sample and reference are excited at the same wavelength, the refractive index of the solvents are 1.3324 for water and 1.4356 for acetonitrile and the integral is taken from the emission spectra.[2]

2.4 Nanoparticle characterisation techniques

Dynamic Light Scattering (DLS) sizing and zeta potential measurements were carried out on a Malvern Zetasizer nano ZSP calibrated with a zeta potential transfer standard (Malvern Instruments) and flow imaging was carried out on a Malvern Nanosight NS300. The Brunauer-Emmett-Teller (BET) surface area and pore size was obtained by nitrogen sorption experiments using a Quantachrome Autosorb Automated Gas Sorption System at 77 K. Transmission electron microscopy (TEM) and Scanning electron microscopy (SEM) imaging were performed at the Centre for Electron Microscopy, University of Birmingham. For TEM a JEOL JEM-1200EX electron microscope was used, fitted with a Gatan camera by drying colloid onto formvar-coated copper grids (Agar Scientific). Images were acquired using Digital Micrograph 1.8 software (Gatan, CA, USA). SEM was performed on the Quanta 3D FEG ESEM. Inductively coupled plasma optical mass spectrometry (ICP-MS) measurements were performed on a 7500cx IPC-MS with an integrated auto-sampler (Agilent) at the University of Warwick. Metal concentrations were determined using PlasmaCal calibration standards (QMX laboratories), with $R^2 > 0.999$ linear calibration curves in all cases. For these experiments, colloidal suspensions were digested in ultrapure aqua-regia and then diluted accordingly. X-ray Photoelectron Spectrometer (XPS) studies were performed at the NEXUS facility at the University of Newcastle on a K-Alpha fully integrated system. The liquid nanoparticle samples were dried onto a silicon wafer and the electrodes were analysed as they are. Transient Absorption (TA) measurements were performed at Warwick University by Dr Michael Hornbury, in collaboration with Dr Vasilios Stavros. The sample was transferred to a 0.1 cm path length low volume quartz cell and excited at 450 nm. Pump–probe delays (up to 2 ns) were created using a motorized optical delay line in the probe beam path. The pump and probe pulses were generated from a commercially available femtosecond Ti-sapphire regenerative amplified laser system operating at 1 kHz and producing 3 mJ pulses. This beam was detected using a fibre coupled UV-vis spectrometer (Avantes, AvaSpec-ULS1650F-

USB2). Probe polarisation was held at the magic angle (54.7°) relative to the pump polarisation.

2.5 Dye Sensitized Solar Cell techniques

Photovoltaic device current-voltage characteristics were performed at Queen Mary University of London in collaboration with Dr Joe Briscoe. They were measured using a Keithley 2400 SMU controlled using NI Labview. Devices were tested with 100 mW cm^{-2} illumination using a Newport Oriel class ABB solar simulator with an AM 1.5 filter. Raman scattering was performed on an inVia confocal Raman microscope with wavelength lasers at 532 and 63 3nm. Gold evaporation was performed on a Denton Metal Evaporator, maintaining the current around 30 amps and a coating rate of 0.3 nm min^{-1}.

2.6 References

1. G. A. Crosby and J. N. Demas, *J. Phys. Chem*, 1971, 75, 991-1024.

2. S. R. Meech and D. Phillips, *J. Photochem.*, 1983, 23, 193-217.

3 Highly luminescent gold nanoparticles: effect of ruthenium distance for nanoprobes with enhanced lifetimes

3.1 Introduction

Ruthenium bipyridine complexes have been highly researched due to their attractive properties of luminescence emission and lifetime, chemical stability, redox properties and excited state reactivity.[1] These properties lend them to play a key role in the research in areas such as artificial photosynthesis,[2-5] Dye Sensitized Solar Cells[6-8] and theranostics.[9-11] It has been shown that certain ruthenium bipyridine complexes are selectively cytotoxic towards tumour cells through inhibiting cell division *via* mitosis[9] and can participate in photocleavage of DNA through intercalation.[11] These properties, together with luminescence imaging give ruthenium complexes a great potential for *in vivo* applications.

Gold nanoparticle, AuNP, use in biology and medicinal chemistry has vastly increased over the past few years due to their easily tuneable size with narrow size distribution, water solubility, low toxicity, high surface area and ease of surface modification through functionalization for drug or probe loading.[12-18] Brown *et al.* have shown successful delivery of the anticancer drug oxaliplatin to lung cancer cells using carboxylated PEG AuNP.[19] Studies into AuNP uptake into tissues and tumours have been reported, both *in vivo* and *in vitro*, but the imaging techniques are either disruptive, such as inductively coupled plasma mass spectrometry (ICP-MS), or utilise scattering properties, such as transmission electron microscopy (TEM), dark field microscopy or confocal reflection microscopy.[20-22] However, when attaching a luminophore onto the surface of the AuNP, it allows for luminescent imaging. This technique is advantageous as it is not disruptive and it allows for imaging of particles in real time with 'live cell imaging'.[23, 24] They are ideal probes for cellular imaging based on their high electron density, which allows multimodal imaging microscopies to be

used, and improved spatial resolution in detection as opposed to molecular probe examples.[25, 26] Ruthenium is seen as a good luminophore due to its ease of synthesis, good photostability and low toxicity when attached to particles.[25, 27, 28] It has been shown that through attaching a ruthenium probe to the AuNP surface it is possible to image single particles which possess the photophysical properties of the ruthenium molecular probe (Figure 3.1).[25] These nanoprobes have also been shown to have applications in protein sensing[29] and optoelectronic devices.[30]

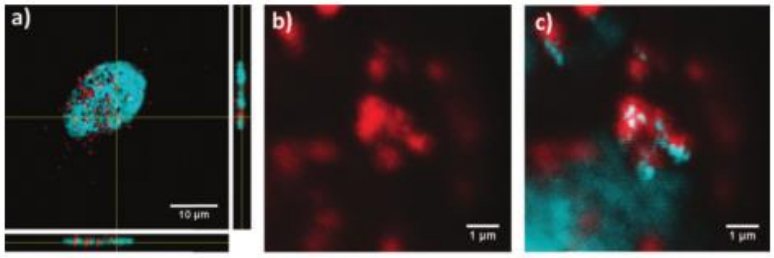

Figure 3.1: 3 Imaging nuclear localisation of RuS•AuNP100 in A549 cells. (a) Orthogonal view of the central z-stack slice (xz plane below, yz plane-right) from a single cell, illustrating ruthenium luminescence from within the central z-planes containing the Hoechst luminescence. (Scale bar 10 mm; acquisition time 75 s). (b) Ruthenium luminescence image and (c) corresponding overlay with Hoechst nuclear stain; acquisition time = 60 s, showing association of chromatin with RuS6•AuNP100 particles inside the nucleus (Scale bar 1 mm; acquisition time = 60 s). Taken from reference.[25]

Although the labelling of AuNP with luminescent probes has been reported for some time, a limitation of their use has been the quenching of the molecular fluorescence by different mechanisms involving the surface plasmon of the gold.[31-34] The quenching of the fluorescence signal by plasmonic nanoparticles in short distances has been attributed to "near-field" effect involving energy or electron transfer non-radiative pathways.[35, 36] In most cases it is shown that if an organic fluorophore is within 5 nm from the AuNP surface, it is close enough to electronically interact with the AuNP and the fluorophore's excited electron is donated to the gold.[31, 37] If the fluorophore is at a great enough distance from the AuNP surface, the nanoparticle is not able to interact directly with the electrons of the fluorophore, so quenching is not seen. At these large distances, the electric field of the AuNP can interact with the fluorophore and enhance fluorescence probability.[31]

The distance of the fluorophore to the gold surface and method of attachment are important factors to the luminescent properties of the particles. Their studies can provide an understanding of the mechanism involved in quenching of the fluorescence as well as can direct future molecular designs. More recently, elegant approaches to examine the effect have involved methods for distancing the fluorophore from the gold surface either through an electrolyte film,[38] using Layer by Layer assemblies,[39] or through formation of silica shells around the gold.[40-42] In many cases it has been shown that organic dyes' fluorescence can be enhanced with increasing the distance from the AuNP, but only achieve lifetimes between the regions of a few ps to 50 ns[43] or an 8-fold overall fluorescence enhancement.[39]

Attachment of metal complexes on AuNP to introduce nanoprobes which bear the distinct optical signature of the metal complex are of interest. Metal complexes have advantages over organic probes due to their large Stokes shift, increased luminescent lifetimes and high photostability.

It has been shown that the luminescence of ruthenium complexes is quenched when attached to AuNP.[29, 30, 44] Yam *et al.* took advantage of this quenching to develop a protein sensor (Figure 3.2).[29] Adsorption of $Ru(bpy)_3Cl_2$ on the surface of 10 nm AuNP has shown a luminescence lifetime decrease from 623 to 0.8 ns.[37] It was found that even at a distance of 2 nm from the gold surface, a tris(bipyridine)ruthenium complex has a highly quenched luminescence lifetime with an enhancement of 4-fold seen at a distance of 50 nm via a silica shell.[45]

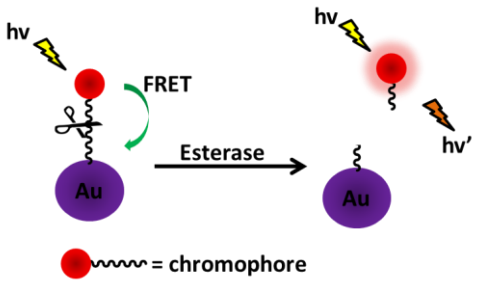

Figure 3.2: Schematic to show a protein sensor system which uses luminescence quenching. Adapted from reference.[29]

Fluorosurfactant coating of the particles has shown to have an effect of protecting the ruthenium probe excited state from quenching by oxygen, increasing the lifetime of the complex on the nanoparticles.[25] The use of surfactant has become increasingly popular for stability of nanoprobes. Meyer *et al.* have shown that by dipping a ruthenium coated TiO_2 surface in poly(methyl methacrylate) (PMMA), there is a 100-fold increase in ruthenium stability (Figure 3.3).[46]

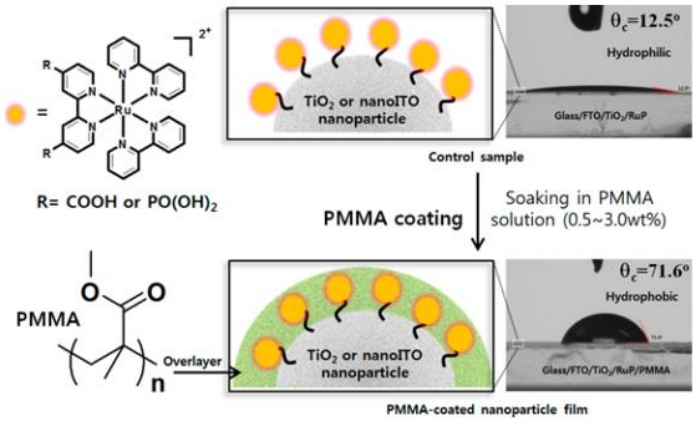

Figure 3.3: Schematic depictions of an added PMMA coating on a metal- oxide surface (TiO_2 or nanoITO) and the results of contact angle measurements of a mesoporous TiO_2 film before and after soaking in a PMMA/DCM coating solution. Also shown are the chemical structures of the RuP^{2+} or RuC^{2+} and PMMA ($n \approx 3500$). Taken from reference.[46]

Although ruthenium coated AuNP have been highly investigated, there are no known examples in the literature of highly luminescent nanoprobes. Most of the literature shows quenching of the luminophore, leading to poor photophysical properties. Optimisation is required to develop a stable and efficient luminescent system where the nanoprobe possesses enhanced photophysical properties of the ruthenium molecular probe.

3.1.1 Chapter summary

In this chapter the effect of the luminescence of the ruthenium probe is examined by varying the distance of the attachment of the probe to the surface of the AuNP. Three ruthenium probes, RuS1, RuS6 and RuS12 are used (Figure 3.4), with different length spacer units between the surface active groups, previously developed in the Pikramenou group.[25, 47, 48] The size of the AuNP is varied to examine if there is an influence on the luminescence lifetime of the probes. An improved method for coating AuNP using fluorosurfactant stabilised AuNP before ruthenium complex addition is described. The effect of the length spacer, together with the fluorosurfactant interactions, for the development of the most efficient design for the ruthenium luminescent nanoparticles is established.

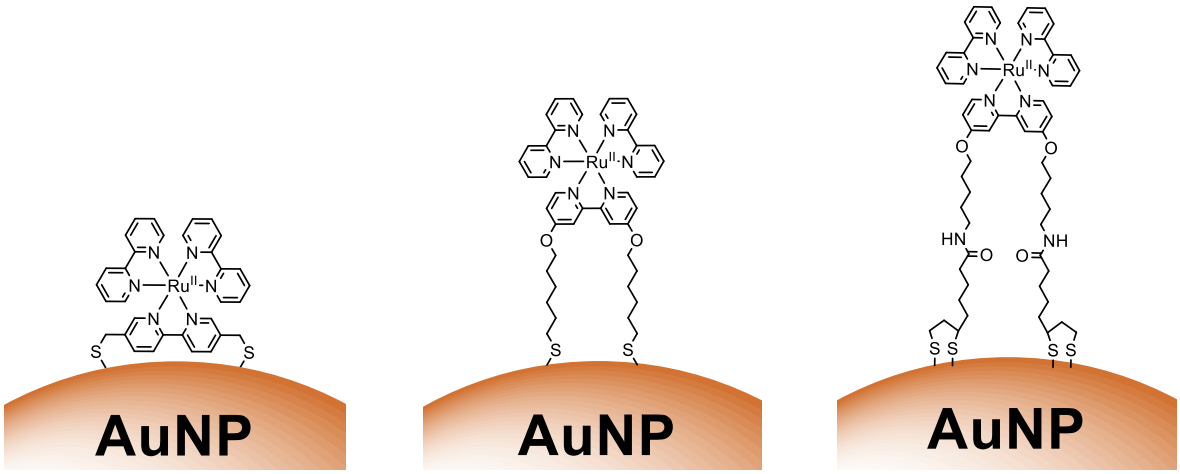

RuS1·AuNP13
RuS1·AuNP50
RuS1·AuNP100

RuS6·AuNP13
RuS6·AuNP50
RuS6·AuNP100

RuS12·AuNP13
RuS12·AuNP50
RuS12·AuNP100

Figure 3.4: Schematic to show the structure of RuS1·AuNP13, RuS1·AuNP50, RuS1·AuNP100, RuS6·AuNP13, RuS6·AuNP50, RuS6·AuNP100, RuS12·AuNP13, RuS12·AuNP50 and RuS12·AuNP100.

3.2 Results and discussion

3.2.1 Ruthenium metal complexes

3.2.1.1 Synthesis

Three ruthenium complexes with different length linker units, RuS1, RuS6 and RuS12 (Figure 3.4) for the attachment to gold were synthesised and fully characterised following previously published methods in the Pikramenou group.[25, 47, 48]

The three ruthenium complexes are based on the tris(bipyridine) luminophore with incorporated surface binding thiols for attachment to AuNP.[49, 50] The complexes are formed by refluxing the ligands with $Ru(bpy)_2Cl_2$ in ethanol and precipitating the hexafluorophosphate salt in water. They were characterised by ^1H NMR, ^{13}C NMR, ES^+ MS and FTIR (Appendix) which are in agreement with previously reported data.[25, 47, 48] The hexafluorophosphate salt was then converted to the chloride through Dowex ion exchange for improved solubility in aqueous solutions, employed in the nanoparticle preparation.

For RuS1, the ligand was synthesised through radical addition of bromine to 5,5'-dimethyl-2,2'-bipyridine, followed by an exchange with thiol (Scheme 3.1). Formation of the complex was confirmed through ES^+ with the m/z at 331.0, corresponding to the $[M\text{-}2PF_6]^{2+}$ ion.

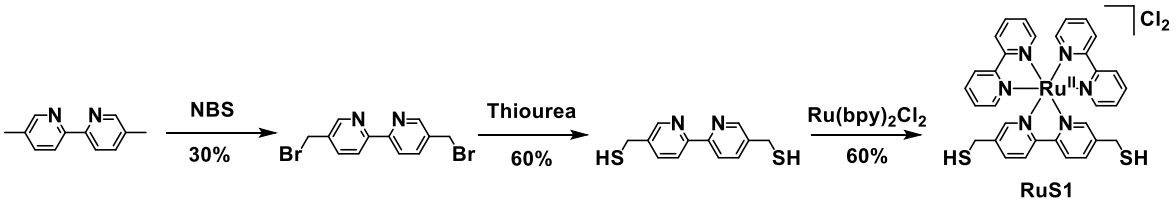

Scheme 3.1: Synthetic route for synthesis of RuS1.

The ligand for RuS6 was synthesised through a Williamson ether reaction of 6-bromohexene with 4,4'-dihydroxy-2,2'-bipyridine, followed by complexation and radical addition of

thioacetic acid (Scheme 3.2). Formation of the complex was confirmed through ES^+ with the m/z at 456.2 corresponding to the $[M\text{-}2PF_6]^{2+}$ ion.

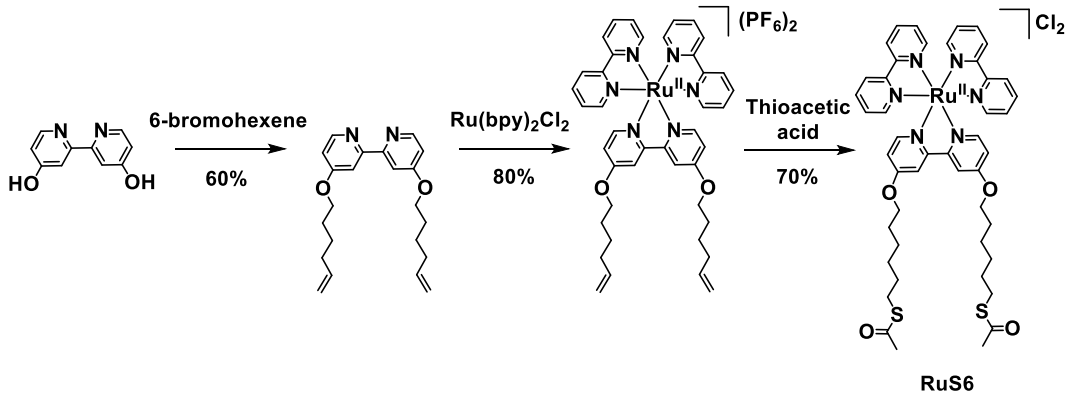

Scheme 3.2: Synthetic route for the synthesis of RuS6.

For RuS12, the ligand was synthesised through a Williamson ether reaction of N-(Boc)-5-amino-1-pentanol with 4,4'-dihydroxy-2,2'-bipyridine, followed by an amide bond formation through reaction with lipoic acid (Scheme 3.3). Formation of the complex was confirmed through ES+ with the m/z at 574.3, corresponding to the $[M\text{-}2PF_6]^{2+}$ ion.

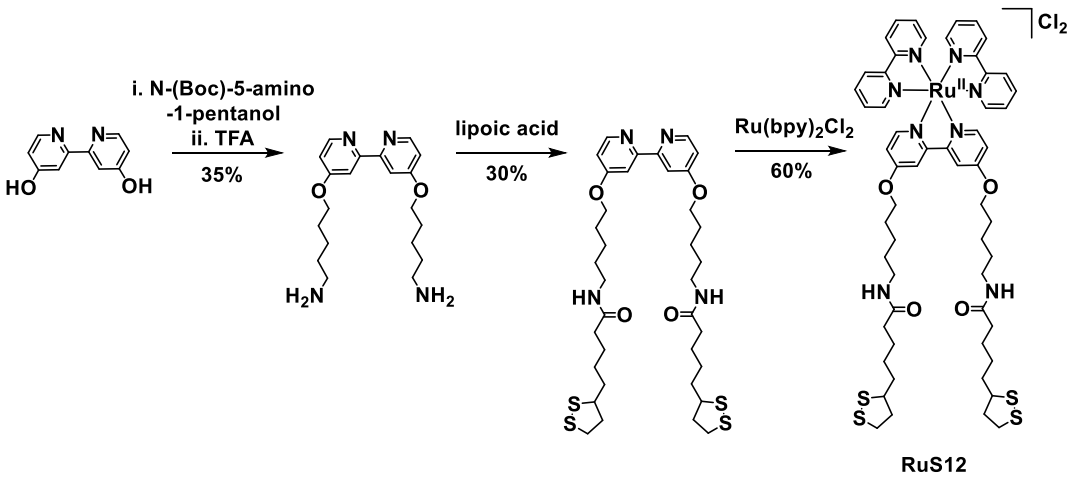

Scheme 3.3: Synthetic route for synthesis of RuS12.

3.2.1.2 Photophysical characterisation

The absorption, steady state emission and excitation were taken for all three complexes in aerated water. The solution based photophysical properties of the complexes have been studied previously in CH_3CN.[25, 47, 48] RuS1, RuS6 and RuS12 were dissolved in methanol to

produce 1.19, 0.95 and 0.87 mM solutions of the chloride ion respectively and diluted with water to produce 11.8, 9.4 and 8.6 μM solutions.

The photophysical properties of all the complexes are similar (Figure 3.5). The absorbance shows the singlet Metal to Ligand Charge Transfer (MLCT) (d - π*) between 400 – 500 nm with the maximum at 450 nm for RuS1, which is similar to the parent $Ru(bpy)_3Cl_2$ complex,[51] and 460 nm for RuS6 and RuS12. This 10 nm red shift for RuS6 and RuS12 is most likely due to the presence of the π electron donating oxygen at the 4,4' position on the bipyridine ring. Electron rich π systems are known to increase the energy of the π_M orbitals.[52] The singlet MLCT molar absorptivity for all of the complexes is approximately 14000 $M^{-1}cm^{-1}$, similar to that of $Ru(bpy)_3Cl_2$ (13000 $M^{-1}cm^{-1}$), showing that the ligands are not affecting the viability of the MLCT. The sharp Ligand Centre (LC) state (π - π*) is present at 290 nm with absorptions also seen at 430 and 240 nm assigned to the Metal Centre (MC) (d - d) and singlet MLCT (d - π*) respectively.[1] The LC molar absorptivity for RuS6 and RuS12 is approximately 70000 $M^{-1}cm^{-1}$, lower than $Ru(bpy)_3Cl_2$ (81000 $M^{-1}cm^{-1}$), showing that the LC transition is less favourable for RuS6 and RuS12. The RuS1 LC molar absorptivity is 92000 $M^{-1}cm^{-1}$, similar to that of $Ru(bpy)_3Cl_2$. The emission is the same for all three complexes, showing the triplet MLCT broad band between 550 - 800 nm with the maximum at 645 nm. This is red shifted 20 nm from the emission of $Ru(bpy)_3Cl_2$, which has a maximum at 625 nm. The excitation spectrum of the complexes mirror the absorbance, with the singlet MLCT between 400 – 500 nm and the LC at 290 nm. There is a decreased contribution of the LC excitation compared to the absorbance.

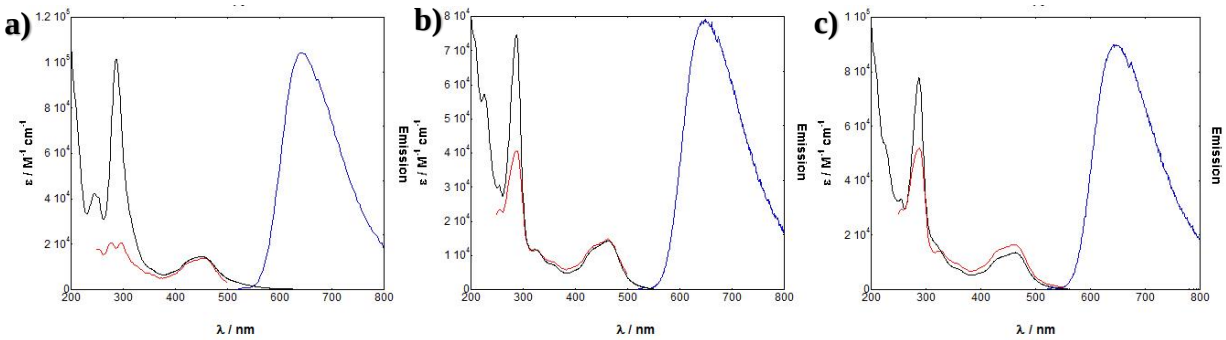

Figure 3.5: Absorption (black), luminescence emission (blue) and excitation (red) data of 11.8 µM RuS1 (a), 9.4 µM RuS6 (b) and 8.6 µM RuS12 (c) in aerated water.

The luminescent lifetimes of RuS1, RuS6 and RuS12 are 420, 240 and 280 ns respectively for the solutions in aerated water (Figure 3.6). RuS1 has a similar lifetime to $Ru(bpy)_3Cl_2$ (380 ns) in water, showing that the addition of the methyl thiols at the 5 position has little effect on the MLCT. The lifetime of RuS6 and RuS12 are approximately half that of $Ru(bpy)_3Cl_2$. This may be due to the oxygens located on the bipyridine ring for RuS6 and RuS12. Triplet oxygen ($^3O_2$) is known to quench luminescence due to the position of the energy levels. The quantum yield of the triplet MLCT (measured at 450 nm) are 2% for all of the complexes, which is slightly lower than $Ru(bpy)_3Cl_2$ (2.8%).

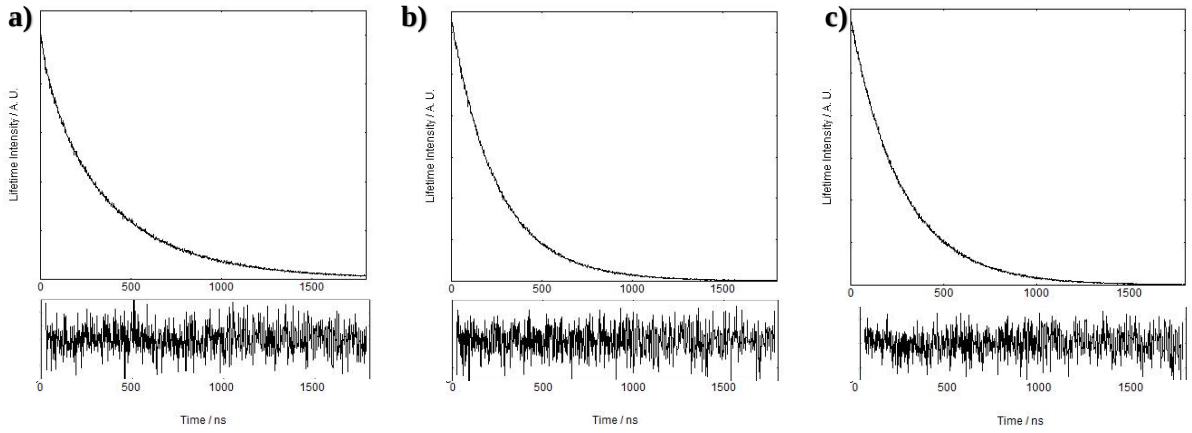

Figure 3.6: Luminescent lifetime decay (top) and fitting (bottom) of RuS1 (a), RuS6 (b), RuS12 (c). λ_{exc} = 445 nm and λ_{det} = 650 nm. X^2 is fitted between 1.0 and 1.2 for all lifetimes.

For all of the photophysical data in solution, RuS1 is similar to $Ru(bpy)_3Cl_2$ due to the negligible effect of the short SH ligands and RuS6 and RuS12 have slightly poorer properties due the presence of oxygen in the π system.

3.2.2 Synthesis of gold nanoparticles

Monodispersed 13 nm AuNP (AuNP13) were synthesised using slight modifications of a previously published method.[53] The protocol involves synthesising AuNP13 seeds and stabilising with citrate anions. Synthesis of citrate stabilised aqueous AuNP13 in the size range 5 - 150 nm was originally developed by Turkevich in 1951[54] and refined by Frens.[55] The Turkevich method has become the most popular synthesis for these nanoparticles due to the straightforward and reproducible synthesis of a large range of sizes of non-toxic and stable AuNP. This method, adapted by Grabar *et al.*[56] consists of reducing the Au^{3+} salt, $HAuCl_4$, in water by adding trisodium citrate to form 9 nM AuNP13. This method has no system to control the environment and although used by previous members of the Pikramenou group, the particles have been found to have a large size distribution and therefore their size is unreliable.[25] Vossmeyer *et al.* have investigated the conditions of the formation of nanoparticles, finding that the size and size distribution can be easily altered by the environment. To gain a better method for a lower size distribution they developed the inverse Turkevich method.[53] The size is mainly determined through the ratio of Au^{3+} salt to citrate ions. The size distribution is dependent on the rate of reaction; the quicker the nucleation, the more narrow the size distribution (Figure 3.7).[57-60] The rate of the reaction is dependent on the formation of the precursors. It has been shown that acetonedicarboxylate, a derivative from citrate, is the species involved in aiding nucleation (Scheme 3.4).[58-60] To increase the rate of reaction, the reactivity or concentration of acetondicarboxylate must be increased. The concentration can be increased by reversing the addition of reagents from the original Turkevich method by adding the Au^{3+} salt mixture into the citrate solution, thus the inverse

method. The rate of reaction can also be increased by controlling the pH; the lower the pH, the faster the reactivity of the precursor Au^{3+}.[59-65] The pH can be controlled by using both sodium citrate and citric acid to produce a buffer solution. Upon nucleation, the nanoparticles will grow with a more narrow size distribution in a diffuse environment, so the concentration should be maintained at a low number (Figure 3.7). The inverse method consists of adding the Au^{3+} salt into a refluxing mixture of sodium citrate, citric acid and ethylenediaminetetraacetic acid (EDTA) (for increased spherical particles) in water to form 2 nM AuNP13. The concentration is an estimation, calculated using the particle size and concentration of Au^{3+} ions (Appendix). With this method the Pikramenou group has found the synthesis is reproducible, forming monodisperse nanoparticles with a consistent polydispersity index (PDI) of less than 0.2.

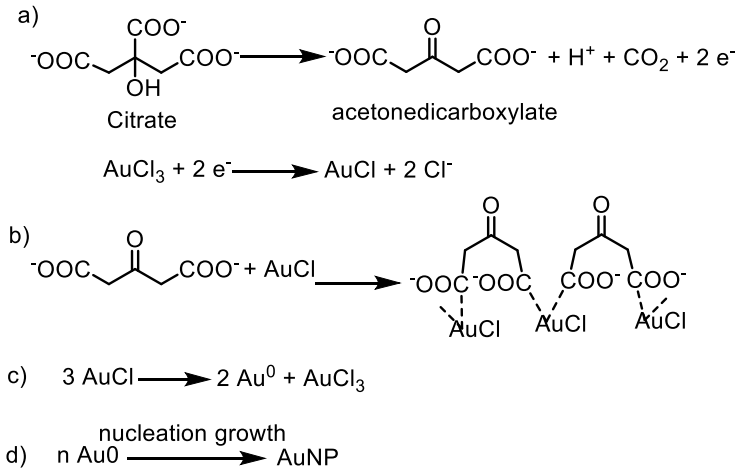

Scheme 3.4: Synthesis of AuNP13 showing the redox reaction of citrate and Au(III) to produce acetonedicarboxylate and Au(I) (a), organisation of Au(I) by acetonedicarboxylate (b), disproportionation of Au(I) to Au(0) and Au(III) (c) and nucleation and growth of Au(0) to AuNP (d).[53]

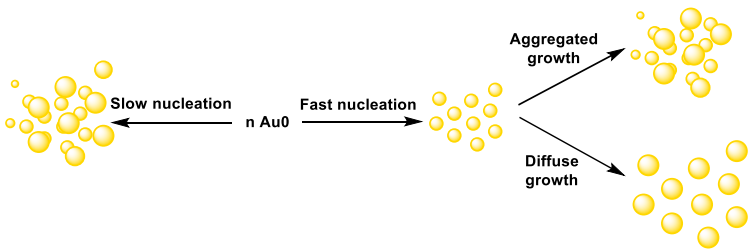

Figure 3.7: Mechanism to show nucleation and growth of AuNP13.[53]

Monodisperse 50 and 100 nm AuNP (AuNP50 and AuNP100) were synthesised using slight modifications from previously published methods.[66] 80 pM AuNP50 and 40 pM AuNP100 were grown through addition of Au^{3+} salt and sodium citrate to AuNP13 seeds (Figure 3.8).

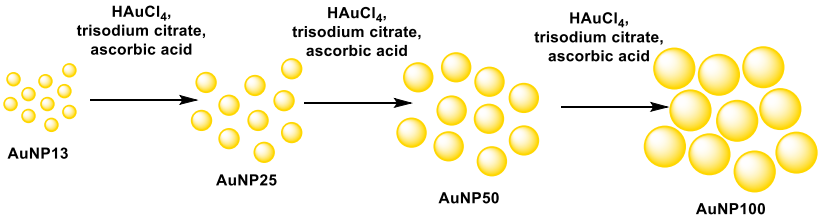

Figure 3.8: Mechanism to show the seeding process to form larger AuNP.

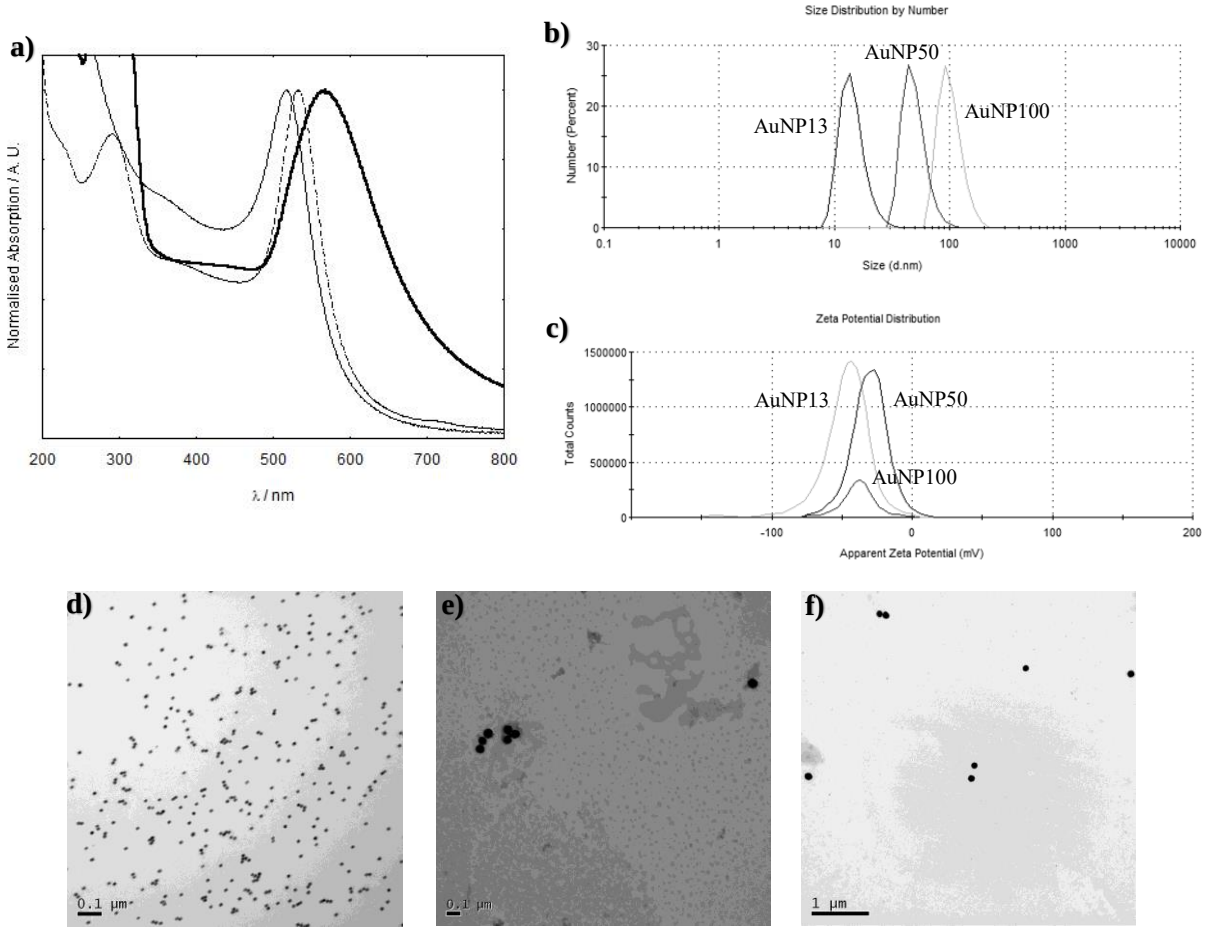

Figure 3.9: UV-vis of the citrate stabilised AuNP13 (thin solid line), AuNP50 (dotted line) and AuNP100 (thick solid line) in water (a). Dynamic light scattering sizing data (b) and zeta potential (c) of citrate stabilised AuNP in water. TEM images of AuNP13 (d), AuNP50 (e) and AuNP100 (f).

The AuNP were characterised by the specific surface plasmon resonance (SPR) band by UV-vis, transmission electron microscopy (TEM), dynamic light scattering (DLS) sizing and zeta potential measurements.

Solutions of AuNP13, AuNP50 and AuNP100 displayed an absorption band with a maximum, λ_{max}, at 517, 532 and 566 nm respectively, characteristic of their SPR band and in agreement with previously published data (Figure 3.9.a).[67, 68] DLS sizing confirmed the AuNP13, AuNP50 and AuNP100 to be 14 ± 4 nm (PDI = 0.09), 50 ± 12 nm (PDI = 0.04) and 100 ± 24 nm (PDI = 0.01) respectively (Figure 3.9.b). The small PDI's show good monodispersed AuNP, suggesting they are all spherical and of similar size. DLS zeta potential are (-) 46 ± 16, (-) 31 ± 13 and (-) 38 ± 12 mV for AuNP13, AuNP50 and AuNP100 respectively (Figure 3.9.c) showing that for all the sizes of nanoparticles the net electrical charge is similar. A negative zeta potential is expected due to the citrate ions stabilising the AuNP. TEM images suggested the sizes of AuNP13, AuNP50 and AuNP100 to be 17, 60 and 120 nm respectively in good agreement with DLS data (Figure 3.9 d-f).

3.2.3 Gold nanoparticle coating with surfactant and metal complex

The ruthenium complexes, RuS1, RuS6 and RuS12 attach to the AuNP *via* a S-Au bond formation between the thiol on the ligand and the gold atoms on the AuNP.[47, 69] Due to the ruthenium complexes being positively charged (2+), and the AuNP being negatively charged, the complex cannot be added directly into the aqueous solution due to electrostatic interactions which cause destabilisation and result in aggregation of the AuNP.[70-73] To prevent this aggregation, a precursor fluorosurfactant, Zonyl FSA, is added to stabilise the particles and allow addition of the ruthenium complexes.[25] Zonyl FSA is used because it has a long fluorinated chain which increases the stability and lipophilicity of the surfactant and has a carboxylic acid group for attachment to the AuNP.

AuNP have a characteristic SPR band in the visible absorption. From this band we can monitor the coating of the AuNP; as the surface changes, the SPR differs and we get a shift in the λ_{max} in the absorption, so as the surfactant and complex attach to the surface, a shift is seen.

Upon addition of the Zonyl surfactant to the AuNP, a shift of 1 nm of the SPR band is observed. The surfactant coated particles, Z·AuNP, were isolated by centrifugation and they were then used for the titration of the ruthenium probe, monitoring the SPR band (Figure 3.10).[25]

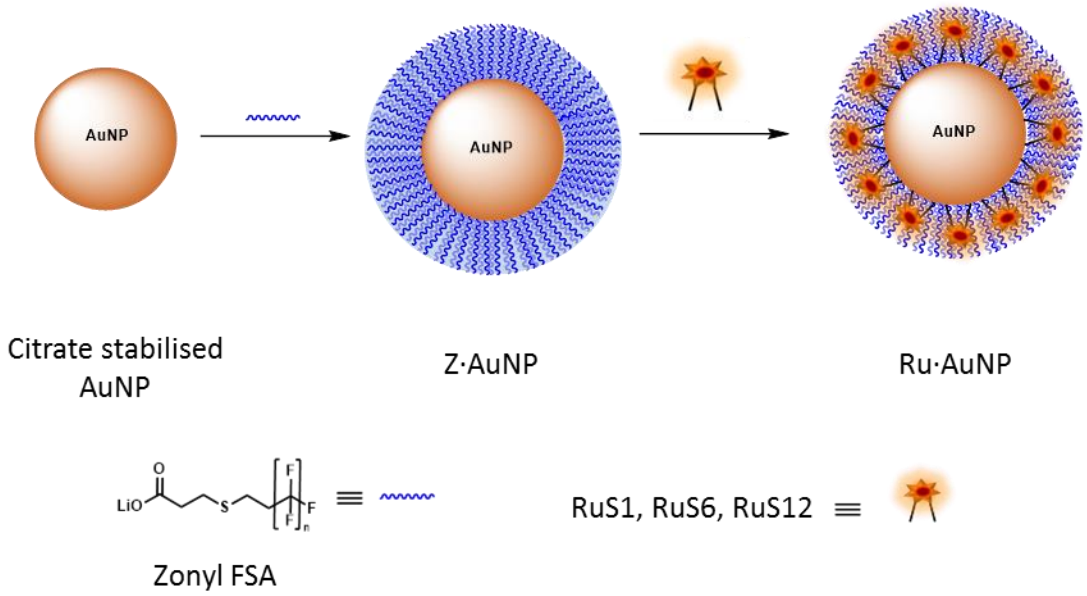

Figure 3.10: Schematic to show the attachment of fluorinated surfactant, Zonyl FSA, and ruthenium complex to AuNP.

For the coating of Z·AuNP13, aliquots (2 µL) of 1.19 mM RuS1, 0.95 mM RuS6 and 0.87 mM RuS12 were titrated into a 4.5 nM solution of Z·AuNP13, and the SPR shift was monitored by the change in λ_{max} to determine the saturation of the AuNP surface (Figure 3.11). As more probe was added, the SPR shifts to the red until optimum coating is achieved and a shift is no longer observed. Addition of 12 µL 1.19 mM RuS1, 16 µL 0.95 mM RuS6 and 20 µL 0.87 mM RuS12 to 4.5 nM Z·AuNP13 result in a 4 (521 nm), 5 (522 nm) and 3 nm (520 nm) shift in λ_{max} respectively (Table 3.1). All three probes cause a similar shift in the

SPR band upon addition to the AuNP. Analyses of the elemental composition of the nanoparticles by inductively coupled plasma mass spectrometry (ICP-MS) reveal a Ru:Au ratio of 1:160, suggesting coating of 600 ruthenium complexes per AuNP13.

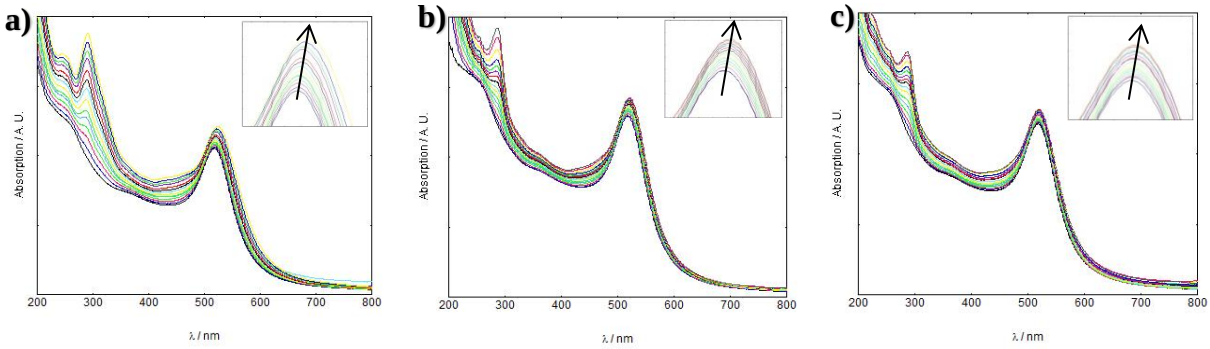

Figure 3.11: UV-vis titration of 1.19 mM RuS1 (a), 0.95 mM RuS6 (b) and 0.87 mM RuS12 (c) into 4.5 nM Z·AuNP13 in water.

Table 3.1: Summary of 13, 50 and 100 nm AuNP SPR shifts upon attachment of Zonyl, RuS1, RuS6 and RuS12.

	λ_{max} / nm	Shift / nm		λ_{max} / nm	Shift / nm		λ_{max} / nm	Shift / nm
AuNP13	517	0	**AuNP50**	532	0	**AuNP100**	566	0
Z·AuNP13	518	1	**Z·AuNP50**	533	1	**Z·AuNP100**	567	1
RuS1·AuNP13	521	4	**RuS1·AuNP50**	537	5	**RuS1·AuNP100**	569	3
RuS6·AuNP13	522	5	**RuS6·AuNP50**	536	4	**RuS6·AuNP100**	569	3
RuS12·AuNP13	520	3	**RuS12·AuNP50**	537	5	**RuS12·AuNP100**	569	3

The isolated particles, following size exclusion chromatography, showed the same λ_{max} as the particles saturated with the ruthenium complex, formed during titration (Figure 3.12). This confirmed that the surface coating of the particles had not changed during isolation and only the excess molecular complex was removed during chromatography.

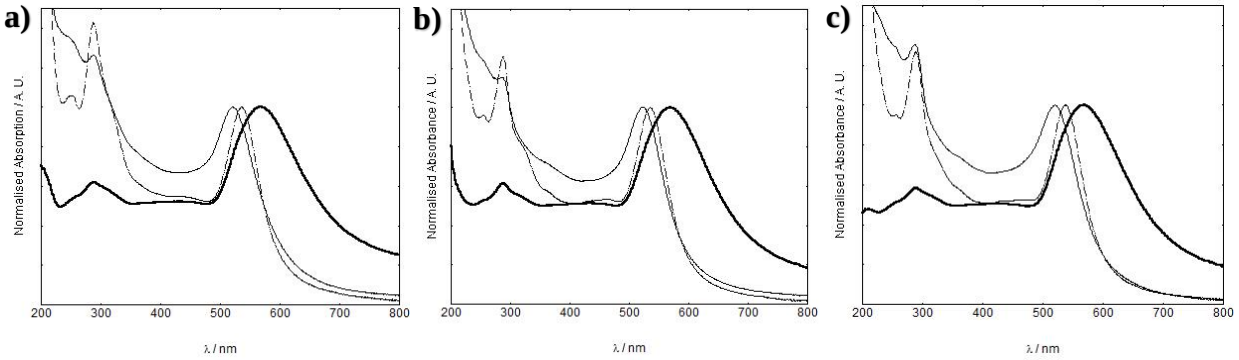

Figure 3.12: UV-vis spectra of 4.5 nM RuS1·AuNP13 (thin solid line), 40 pM RuS1·AuNP50 (dotted line) and 20pM RuS1·AuNP100 (thick solid line) (a), 4.5 nM RuS6·AuNP13, 40 pM RuS6·AuNP50 and 20 pM RuS6·AuNP100 (b) and 4.5 nM RuS12·AuNP13, 40 pM RuS12·AuNP50 and 20 pM RuS12·AuNP100 (c) in water.

TEM and DLS studies show that the sizes of the AuNP have not significantly changed upon coating with the surfactant and the ruthenium complex. Images of the nanoparticles by TEM show monodispersed, uniform particles with estimated sizes from the image of 17 nm for Z•AuNP13, RuS1•AuNP13, RuS6•AuNP13 and RuS12•AuNP13, 60 nm for Z•AuNP50, RuS1•AuNP50, RuS6•AuNP50 and RuS12•AuNP50 and 120 nm for Z•AuNP100, RuS1•AuNP100, RuS6•AuNP100 and RuS12•AuNP100 (Figure 3.13).

Table 3.2: Dynamic Light Scattering of AuNP in water.

	Number distribution / nm	**Intensity distribution / nm**	**PDI**
AuNP13	14 ± 4	23 ± 7	0.09
Z·AuNP13	12 ± 4	40 ± 20	0.19
RuS1·AuNP13	15 ± 6	96 ± 50	0.26
RuS6·AuNP13	24 ± 9	116 ± 57	0.26
RuS12·AuNP13	18 ± 6	48 ± 22	0.14
AuNP50	50 ± 12	68 ± 18	0.04
Z·AuNP50	50 ± 12	70 ± 19	0.04
RuS1·AuNP50	59 ± 17	90 ± 27	0.09
RuS6·AuNP50	54 ± 15	84 ± 26	0.08
RuS12·AuNP50	61 ± 16	86 ± 24	0.04
AuNP100	101 ± 24	120 ± 26	0.01
Z·AuNP100	107 ± 27	130 ± 35	0.02
RuS1·AuNP100	109 ± 28	134 ± 33	0.03
RuS6·AuNP100	107 ± 27	131 ± 31	0.03
RuS12·AuNP100	112 ± 27	133 ± 30	0.02

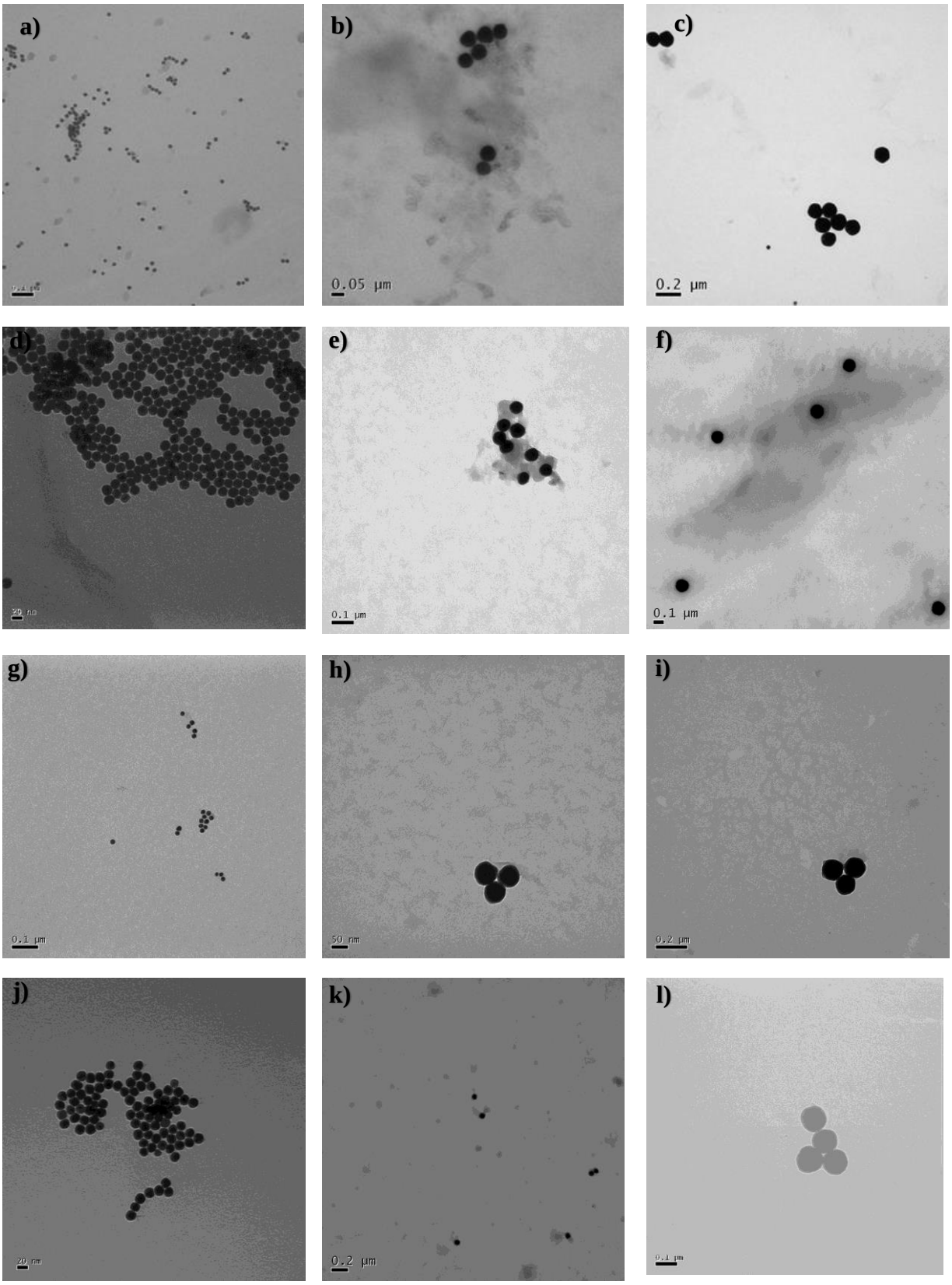

Figure 3.13: TEM images of RuS1·AuNP13 (a), RuS1·AuNP50 (b), RuS1·AuNP100 (c), RuS1·AuNP13 (d), RuS1·AuNP50 (e), RuS1·AuNP100 (f), RuS6·AuNP13 (g), RuS6·AuNP50 (h), RuS6·AuNP100 (i), RuS12·AuNP13 (j), RuS12·AuNP50 (k) and RuS12·AuNP100 (l). Images are taken on the Jeol 1200 EX TEM.

The RuS12·AuNP100 were imaged as single nanoparticles by NanoSight tracking, both through scatter and ruthenium emission detection in the red upon 488 nm excitation (Figure 3.14). The NanoSight emission detection only tracks emission that has been excited at 488 nm and so only the ruthenium will be excited and not the AuNP. From the video cuts it is clear that it is the particles being excited and thus this shows that the complex is attached to the AuNP and not in solution.

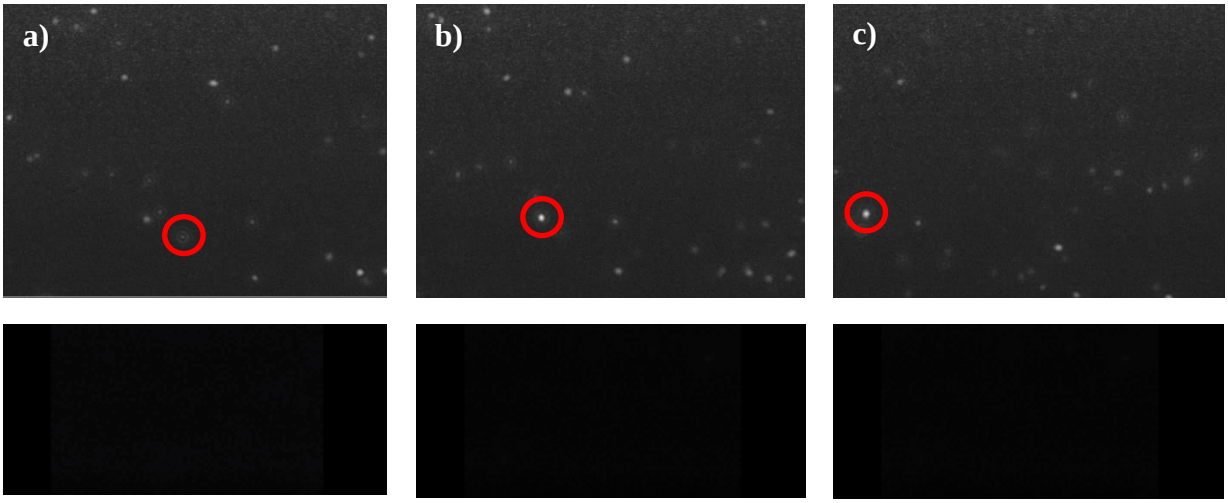

Figure 3.14: Video cuts of RuS12·AuNP100 (top) and AuNP100 (bottom) at 5s (a), 7s (b) and 10s (c) on the NanoSight. λ_{exc} = 488 nm. Filter = 500 nm. Flow rate = 50 mL/h.

X-ray photoelectron spectroscopy (XPS) was used to characterise the surface of the nanoparticle and show that the ruthenium complex was attached to the AuNP (Table 3.3). The three coated AuNP13 were dried onto a silicon wafer and examined for the presence of gold, ruthenium and fluorine to detect the presence of the AuNP, ruthenium complex and fluorosurfactant respectively, and sulfur to analyse attachment of the ruthenium complex to AuNP.

Table 3.3: XPS data analysis of RuS1•AuNP13, RuS6•AuNP13 and RuS12•AuNP13.

	Literature / eV	RuS1•AuNP13 / eV	RuS6•AuNP13 / eV	RuS12•AuNP13 / eV
Au 4f 7/2	84	84.0	84.0	84.1
Au 4f 5/2	88	87.7	87.8	87.8
S 2p 3/2	164	162.7	162.8	162.8
S 2p 1/2	165	163.8	163.9	163.9
Ru 3d 5/2	280	282.4	280.5	280.4
Ru 3d 3/2	284	286.2	284.6	284.4
C 1s	285	286.8	284.9	285.0
C 1s (F)	292	292.5	292.0	290.1
Ru 3p 3/2	461	463.0	463.4	463.2
Ru 3p 1/2	483	485.4	485.8	485.4
F 1s	686	686.0	686.0	686.0

The data for all three coated AuNP are similar and all peaks are present for the examined elements. They are slightly shifted from the literature values which can be caused by the oxidation state of the element and the local chemical and physical environment.[74, 75] For RuS12•AuNP13, the peaks for Ru are weak but present. The peak at 284.4 eV for Ru 3d 3/2 (Figure 3.15.c) is shadowed by a large peak for C 1s, but a small peak at 280.4 eV is seen for Ru 3d 5/2. In the Ru 3p area there are two weak peaks at 463.2 and 485.4 eV for the Ru 3p 3/2 and 1/2 respectively (Figure 3.15.d). The Ru 3p peak is known to be weaker than the 3d due to the increased shielding. There is a peak at 290.1 eV for the C 1s atom with fluorine attached (Figure 3.15.c) and a peak at 686.0 eV for F (Figure 3.15.e), showing that the Zonyl is present. The C 1s shifts by 8 eV for CF_2 compared to CH_2 due to the electronegativity of the fluorine. Higher positive oxidation states exhibit higher binding energy due to increased coulombic interactions between the nucleus and photoemitted electron.[75] The peaks at 162.8 and 163.9 eV for the S 2p 3/2 and 1/2 respectively (Figure 3.15.b) shows chemisorption of a sulfur species on the AuNP.[76, 77] It is not possible to assign this chemisorption to the ruthenium complex as the Zonyl FSA fluorosurfactant also contains sulfur groups which are able to bind to the gold. There is also some contribution to the sulfur peak seen from both unbound sulfur (163.7 and 165.0 eV) and sulphonate (167.4 and 168.6 eV). Similar peaks are seen for RuS1•AuNP13 and RuS6•AuNP13 (Appendix).

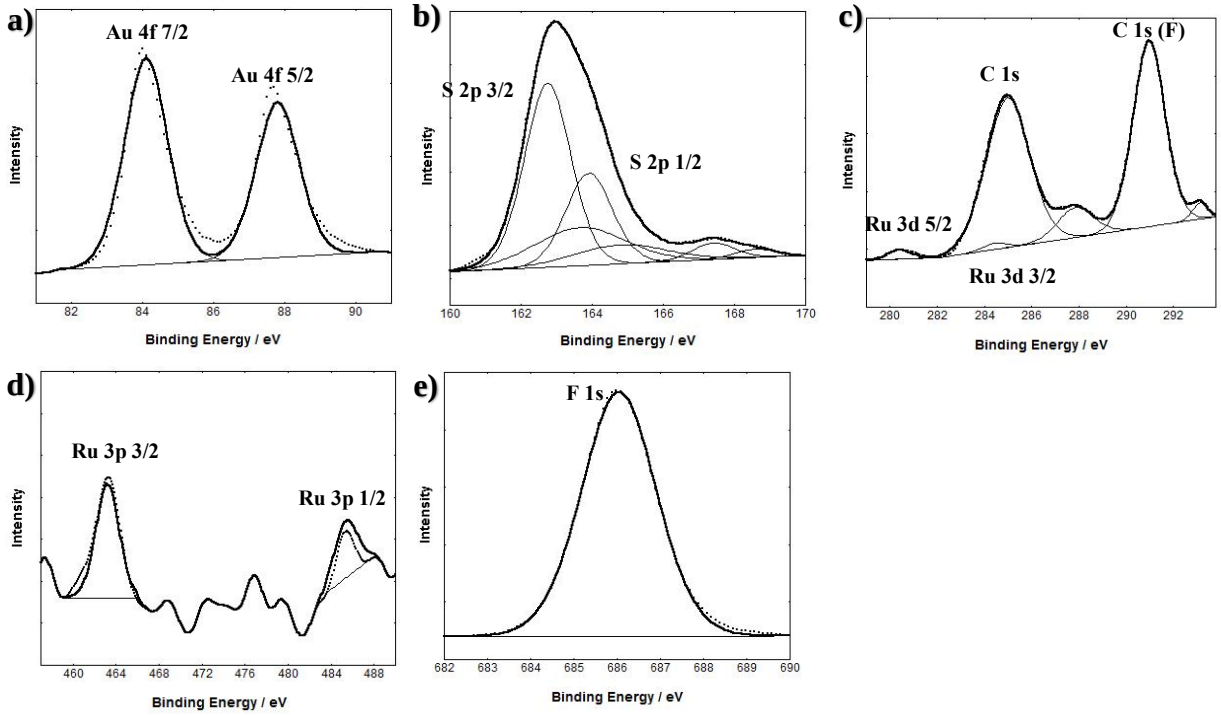

Figure 3.15: XPS binding energy showing the regions of Au 4f (a), S 2p (b), Ru 3d (c), Ru 3p (d) and F 1s (e) for RuS12•AuNP13.

3.2.4 Luminescent studies of ruthenium probes in the presence of the fluorosurfactant and functionalised gold nanoparticle

To characterise the luminescence properties of the probes attached to AuNP, absorption and steady state and time-resolved emission spectroscopy were used. The absorption spectra for all three nanoprobes shows the SPR of the AuNP13, where the excitation spectrum for the luminescence at 650 nm reflects the absorption of the ruthenium complexes (Figure 3.16). In all three cases there is a larger contribution from the LC peak in the excitation when compared to the molecular probes, suggesting that the AuNP is decreasing the viability of the triplet MLCT emission.

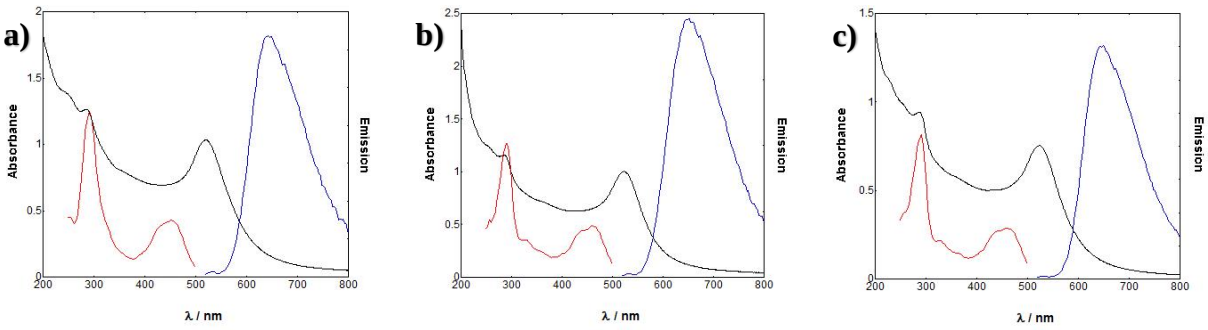

Figure 3.16: Absorption (black), luminescence emission (blue) and excitation (red) data of 4.5 nM RuS1•AuNP13 (a), 4.5 nM RuS6•AuNP13 (b) and 4.5 nM RuS12•AuNP13 (c) in aerated water.

The luminescence spectra and lifetime of the nanoprobes (13, 50 and 100 nm AuNP) were recorded and compared with the molecular complexes in solution, in the presence and absence of the Zonyl surfactant (Figure 3.17). There is no significant shift in λ_{max} of the emission peak upon addition of Zonyl to the complex or upon attachment of the complex to the Z·AuNP, showing that there is negligible effect on the position of the triplet MLCT. The Pikramenou group have previously found that attachment to a gold surface of the RuS12 complex causes a 15 nm blue shift in λ_{max}.[47] This shift may not be present on the AuNP due to the presence of the surfactant or the different probe environment on the gold surface as compared with the nanoparticle.

The luminescence lifetimes of the coated AuNP are summarised in Table 3.4 and comparison of the lifetime decays are presented to illustrate the changes in the lifetimes (Figure 3.17).

Table 3.4: Luminescence lifetimes of the three probes on AuNP and the percentage change in lifetime compared to the free probe in water. The luminescent lifetimes were fitted with a X^2 between 1.0 and 1.2.

	τ /ns	**%**		**τ /ns**	**%**		**τ /ns**	**%**
RuS1	420	0	**RuS6**	240	0	**RuS12**	280	0
RuS1 + Z	420	0	**RuS6 + Z**	400	70	**RuS12 + Z**	350	25
RuS1·AuNP13	470	20	**RuS6·AuNP13**	340	40	**RuS12·AuNP13**	480	70
RuS1·AuNP50	470	20	**RuS6·AuNP50**	340	40	**RuS12·AuNP50**	480	70
RuS1·AuNP100	470	20	**RuS6·AuNP100**	340	40	**RuS12·AuNP100**	480	70

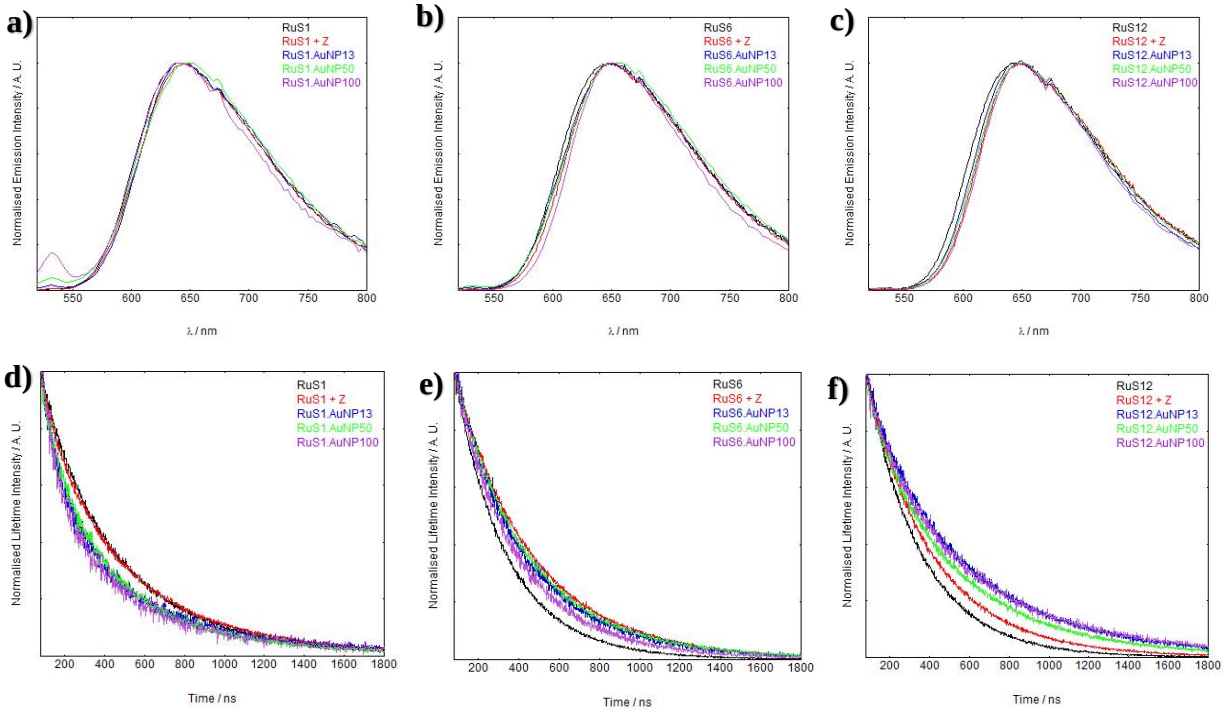

Figure 3.17: Luminescence emission data of RuS1, RuS1·Z, RuS1·AuNP13, RuS1·AuNP50 and RuS1·AuNP100 (a), RuS6, RuS6·Z, RuS6·AuNP13, RuS6·AuNP50 and RuS6·AuNP100 (b) RuS12, RuS12·Z, RuS12·AuNP13, RuS12·AuNP50 and RuS12·AuNP100 (c). λ_{exc} = 450 nm and λ_{det} = 650 nm. The spectra are taken from 520 – 800 nm. Luminescence lifetime data of RuS1, RuS1 + Z, RuS1·AuNP13, RuS1·AuNP50 and RuS1·AuNP100 (d), RuS6, RuS6 + Z, RuS6·AuNP13, RuS6·AuNP50 and RuS6·AuNP100 (e) RuS12, RuS12 + Z, RuS12·AuNP13, RuS12·AuNP50 and RuS12·AuNP100 (f). λ_{exc} = 445 nm and λ_{det} = 650 nm. X^2 is fitted between 1.0 and 1.2 for all lifetimes.

To examine the effect of the Zonyl surfactant on the luminescence properties, the luminescence decays of each ruthenium probe (RuS1, RuS6 and RuS12) were compared upon addition of Zonyl (10 µL of 10% in water). Both the luminescence lifetimes of RuS6 and RuS12 increased upon addition of surfactant by 70% and 25% respectively, compared to the complex in solution (Figure 3.17 e & f). In contrast, the lifetime of RuS1 did not change upon addition of Zonyl surfactant (Figure 3.17.d). This increase in lifetime of RuS6 and RuS12 is attributed to interaction of the surfactant with the molecular complex and consequently protection from $^3O_2$ quenching. Increasing the hydrophobicity of a probe increases interaction with the surfactant and oxygen shielding allows for the largest change in luminescence lifetime upon addition of surfactant. Previous studies have shown that increasing hydrophobicity of the ligands increased ruthenium complex binding to ionic and non-ionic

surfactants.[78-80] It was found that $Ru(phen)_2(CN)_2$ had a 10-fold increase in binding to the anionic sodium dodecyl sulfate surfactant when compared with the less hydrophobic $Ru(bpy)_2(CN)_2$ complex.[79] The lifetime increases significantly more for RuS6 (240 to 400 ns, 70%) than with RuS12 (280 to 350 ns, 25%) in the presence of Zonyl. This is attributed to a less tight interaction of RuS12 with Zonyl, possibly due to the presence of the amide bonds on the aliphatic legs. The lack of increase in lifetime for RuS1 may be attributed to the absence of aliphatic legs for the surfactant to interact with, deeming the complex more polar than RuS6 and RuS12.

To compare the effect of the different sized AuNP on the properties of the ruthenium probe, luminescence lifetime decays were studied for the isolated nanoparticles (AuNP13, AuNP50 and AuNP100) coated with ruthenium. The lifetime decays of RuS1·AuNP13, RuS1·AuNP50 and RuS1·AuNP100 overlap (Figure 3.17.d), showing that there is no difference in the effect of size of AuNP on the luminescence lifetime of the probe (470 ns). Similar observations were made for the luminescence lifetime decays of RuS6·AuNP13, RuS6·AuNP50 and RuS6·AuNP100 (Figure 3.17.e) as well as those of RuS12·AuNP13, RuS12·AuNP50 and RuS12·AuNP100 (Figure 3.17.f). These results show that the size of the nanoparticle does not affect the luminescence lifetime of the three probes, RuS1, RuS6 and RuS12. For all the lifetime fittings of the coated AuNP, a short component was also observed (50 – 100 ns) with small percentage contribution (5 – 20%). This was attributed to be a scattering artefact and only the long component is reported.

The luminescence lifetimes of RuS1, RuS6 and RuS12 upon attachment to the AuNP showed an increase by 20%, 40% and 70% respectively from the free complex (Table 3.4). This is mirrored by an increase in luminescent quantum yield from 2% in solution for all complexes to 2, 5 and 9% for RuS1, RuS6 and RuS12 respectively when attached to AuNP13. These results show that there is an enhancement of the lifetime and quantum yield from the Zonyl

coated AuNP surface, which can be attributed to the interaction with the Zonyl surfactant or to enhancement by AuNP surface. The enhancement of the RuS12 complex on the AuNP is significantly larger than that of RuS1 and RuS6, even though the effect of the Zonyl surfactant is less pronounced than in RuS6. This larger enhancement can be attributed to an interaction of the AuNP electromagnetic field with the luminescent probe dipole, observed more pronounced for RuS12 which is located at a greater distance from the particle surface than the other complexes.

It is expected that the closer the luminescent probe is to the surface, the larger the quenching effect. This agrees with previous research which states that a luminophore close to the gold surface is quenched due to electronically interacting with the surface's strong magnetic field.[31] The effect is attributed to the excited electron being donated to the gold surface, quenching luminescence by non-radiative pathways. For RuS6 and RuS12 there is an increase in radiative decay when attached to the AuNP, compared to in solution, however there is a slight decrease for RuS1 (Table 3.5). This shows that the luminescence is not quenched by non-radiative pathways and in fact is enhanced through radiative pathways. There is a larger increase in radiative decay for RuS12 (0.71 to 1.9) compared to RuS6 (0.83 to 1.5). This is due to the increased distance from the AuNP surface of RuS12.

Table 3.5: Radiative and non-radiative contribution of the decay rate for RuS1·AuNP13, RuS1, RuS6·AuNP13, RuS6, RuS12·AuNP13 and RuS12. τ_N is the natural lifetime, k is the overall decay rate, k_r is the radiative decay rate and k_{nr} is the non-radiative decay rate.

	Φ	τ /s (x 10^{-7})	τ_N /s (x 10^{-6})	k /s^{-1} (x 10^6)	k_r /s^{-1} (x 10^5)	k_{nr} /s^{-1} (x 10^6)
RuS1·AuNP13	0.02	4.7	2.4	2.1 (2.127660)	0.43 (0.42553)	2.1 (2.085107)
RuS1	0.02	4.2	2.1	2.4 (2.380952)	0.48 (4.7619)	2.3 (2.333333)
RuS6·AuNP13	0.05	3.4	6.8	2.9 (2.941176)	1.5 (1.47059)	2.8 (2.794117)
RuS6	0.02	2.4	1.2	4.2 (4.166667)	0.83 (8.3333)	4.1 (4.083334)
RuS12·AuNP13	0.09	4.8	5.3	2.1 (2.083333)	1.9 (1.87500)	1.9 (1.895833)
RuS12	0.02	2.8	1.4	3.6 (3.571429)	0.71 (0.71429)	3.5 (3.500000)

The radiative and non-radiative contributions are calculated from the quantum yield, Φ, and luminescent lifetime, τ (Equation 3.1 – 3.4).[32, 81]

$$\tau_N = \frac{\tau}{\Phi} \quad \textbf{Equation 3.1}$$

$$k = \frac{1}{\tau} \quad \textbf{Equation 3.2}$$

$$k_r = \frac{1}{\tau_N} \quad \textbf{Equation 3.3}$$

$$k = k_r + k_{nr} \quad \textbf{Equation 3.4}$$

To get a greater understanding of the electronic interaction between the ruthenium complexes and the AuNP, femto second transient absorption (TA) was performed at Warwick University in collaboration with Dr Vasilios Stavros and Dr Michael Hornbury. AuNP have been shown to have transient changes of reflectivity and absorption in the picosecond time scale.[82-86] The widely accepted model for the relaxation process is a three stage relaxation. Firstly, surface plasmons are excited and plasmons lose their coherence instantly through electron-electron (e-e) scattering process over a time period of 100 fs. The hot electron system loses energy through electron-phonon (e-p) coupling and forms a quasiequilibriated state over a time period of 10 ps. Finally, over 100 ps, a heat transfer process to the host matrix causes the AuNP to return to the unexcited state. This three lifetime model fits to the data for the citrate stabilised AuNP13 in water, with lifetimes of 5 ± 0.02 and 243 ± 7 ps (Figure 3.18). There is also a shorter lifetime in the fs seen but not quantified. For RuS1•AuNP13, RuS6•AuNP13 and RuS12•AuNP13, no change in the lifetimes were seen compared to AuNP13 (Table 3.6), suggesting that the interaction between the ruthenium complex and AuNP occurs on a longer timescale than 250 ps. The peak around 550 nm is assigned to the SPR bleaching and the peaks around 450 and 650 nm are components of the hot electrons.[84]

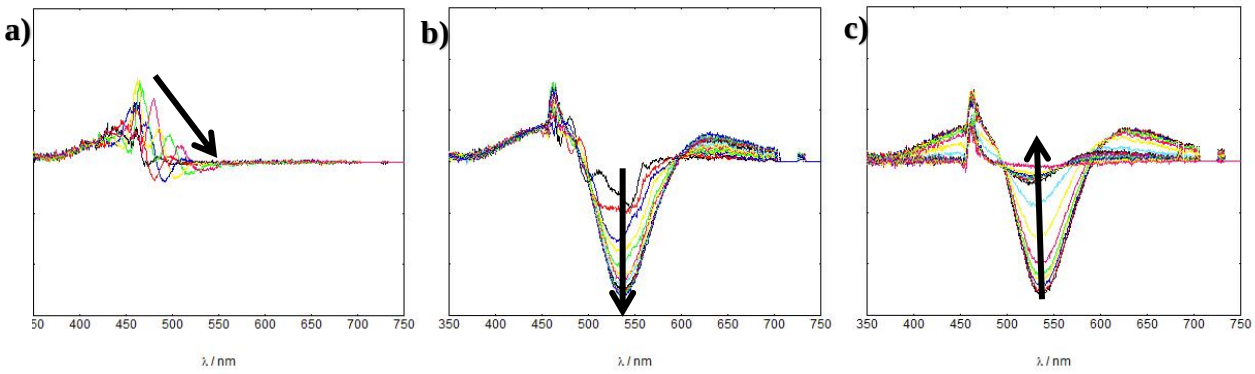

Figure 3.18: Transient Absorption data for RuS12.AuNP13 with initial increase between 80 - 180 fs (a), peak build in 2.5 - 4.0 ps (b) and decay from 9.0 - 5000 ps (c).

Table 3.6: Transient Absorption decay lifetimes of coated AuNP13

	τ_2 / ps	τ_3 / ps
Z.AuNP13	5 ± 0.02	243 ± 7
RuS1.AuNP13	5 ± 0.03	222 ± 8
RuS6.AuNP13	5 ± 0.02	210 ± 9
RuS12.AuNP13	5 ± 0.03	208 ± 7

Yam *et al.* have performed nanosecond TA on ruthenium coated AuNP and see a decrease in lifetime from 535 to 359 ns after attachment of the complex to the probe.[29] They attribute this quenching to a combination of charge transfer and dynamic energy transfer.

In a study of a ruthenium complex with similar chain as the RuS6, a 60% quenching of luminescence was observed when attached to a gold surface.[30] It is clear that the effect of Zonyl is important at this distance from the surface. It is also possible that the induced rigidity upon attachment of the ruthenium complexes to the surfactant functionalised AuNP contributes to the increase in luminescence lifetimes. Although there are examples of luminescence enhancement of luminophores on AuNP, most are at greater than 5 nm distances. No reports have been made of an enhancement in luminescence at these short distances from the surface. Estimated distances of the ruthenium centres in RuS1, RuS6 and RuS12 are 0.7, 1.6 and 2.5 nm from the surface respectively. Rubinstein *et al.* viewed a 4-fold

increase in luminescence at a distance at 50 nm, but at 2 nm from the surface, which is equivalent to the RuS12 distance, they saw a large quenching in luminescence.[45] Our previous studies have shown that the luminescence lifetime of RuS12 is not quenched when the complex is attached to a gold surface, supporting the results that this distance is ideal for gold surfaces.[47]

3.3 Conclusion

There is an effect of the distance of thiol-functionalised ruthenium complexes from the AuNP surface to the luminescence properties of the nanoparticles. The RuS12 complex is shown to display greater enhancement of luminescence upon attachment to AuNP which is significantly higher than those of RuS1 and RuS6 due to its improved distance from the gold surface. Even at these rather close distances to the gold surface, all three probes show an enhancement of luminescence lifetime when attached to the AuNP. The coating with the Zonyl surfactant is important in the enhancement of the luminescence lifetime, especially for the medium chain ruthenium complex, RuS6. The increase of the size of the AuNP from 13 to 50 and 100 nm led to probes with the same lifetimes as AuNP13. This provides an insight to the design of functionalised nanoparticles with luminescent probes which can be adopted for other luminophores.

3.4 Summary of data

Table 3.7: Photophysical characterisation of RuS1, RuS6 and RuS12 in solution with and without Zonyl FSA surfactant and attached to AuNP13

	UV-Vis λ_{max} / nm (ε / $M^{-1}cm^{-1}$)	Emission λ_{max} / nm	τ / ns	Φ / %
RuS1	451 (13000), 430 (sh), 288 (92000), 244 (41000)	645	420	2
RuS1 + Z	451 (13000), 430 (sh), 288 (92000), 244 (sh)	645	420	1
RuS1•AuNP13	521	650	470	2
RuS6	463 (14000), 430 (sh), 287 (75000), 253 (30000)	645	240	2
RuS6 + Z	464 (14000), 430 (sh), 288 (75000), 253 (sh)	645	400	3
RuS6•AuNP13	522	650	340	6
RuS12	460 (13000), 430 (sh), 290 (70000), 230 (sh)	645	280	2
RuS12 + Z	460 (13000), 430 (sh), 290 (70000), 230 (sh)	645	350	2
RuS12•AuNP13	520	650	480	9

Table 3.8: DLS sizing and zeta potential data for the AuNP.

	DLS sizing / nm (PDI)	ζ / mV		DLS sizing / nm (PDI)	ζ / mV		DLS sizing / nm (PDI)	ζ / mV
AuNP13	14 ± 3 (0.09)	- 46 ± 16	AuNP50	50 ± 12 (0.04)	- 31 ± 13	AuNP100	101 ± 24 (0.01)	- 38 ± 12
Z •AuNP13	12 ± 4 (0.19)	-50 ± 8	Z •AuNP50	50 ± 12 (0.04)	- 62 ± 18	Z •AuNP100	107 ± 27 (0.02)	- 53 ± 11
RuS1 •AuNP13	15 ± 6 (0.26)	-49 ± 11	RuS1 •AuNP50	59 ± 17 (0.09)	- 31 ± 10	RuS1 •AuNP100	109 ± 28 (0.03)	- 47 ± 10
RuS6 •AuNP13	24 ± 9 (0.26)	-62 ± 15	RuS6 •AuNP50	54 ± 15 (0.08)	- 44 ± 16	RuS6 •AuNP100	107 ± 27 (0.03)	- 26 ± 9
RuS12 •AuNP13	18 ± 6 (0.14)	-42 ± 13	RuS12 •AuNP50	61 ± 16 (0.04)	- 42 ± 12	RuS12 •AuNP100	112 ± 27 (0.02)	- 36 ± 10

3.5 Experimental

3.5.1 Materials

Starting materials were purchased from Sigma Aldrich or Fisher Scientific.

3.5.2 Synthesis of gold nanoparticles

AuNP13 The protocol for the formation of AuNP13 was based on a previous published method by Vossmeyer *et al*.[53] A solution of trisodium citrate dihydrate (60.3 mg, 0.21 mmol), citric acid (13.6 mg, 0.07 mmol) and ethylenediaminetetraacetic acid (EDTA) (1.6 mg, 0.004 mmol) in deionised water (100 mL) was vigorously stirred and brought to reflux. After 15 minutes of reflux, there was rapid addition of a preheated solution (80 °C) of gold(III) chloride trihydrate ($HAuCl_4.3H_2O$) (8.5 mg, 0.022 mmol) in deionised water (25 mL). After a further 15 minutes reflux, the heat was turned off and the solution was allowed to slowly cool to room temperature to form a 2 nM solution of AuNP13. λ_{max} (H_2O) / nm 517 (SPR). Diameter / nm = 14 ± 3 (DLS number distribution), PDI = 0.09. ζ-potential = - 46 ± 16 mV. Data agreed with previously published. To change the final concentration, AuNP13 were centrifuged at 13000 G for 30 minutes. The supernatant was decanted and the pellet was redispersed in deionised water to form a 9 nM solution of AuNP13.

AuNP50 and AuNP100 The protocol for the formation of AuNP50 and AuNP100 was modified using a previous published method by Ziegler *et al*.[66] Three stock solutions were prepared: 5 mM $HAuCl_4.3H_2O$; 57 mM ascorbic acid and 34 mM trisodium citrate dihydrate in water. AuNP13 (30 mL, 2 nM) were diluted to 40 mL with deionised water and vigorously stirred. The solutions for addition were diluted to 1 mM, 3 mM and 0.75 mM in deionised water to 40 mL for $HAuCl_4.3H_2O$, ascorbic acid and trisodium citrate dihydrate respectively. The two solutions ($HAuCl_4.3H_2O$ and ascorbic acid / trisodium citrate dihydrate) were simultaneously added *via* a peristaltic pump over 45 minutes. The resultant solution was

refluxed for 30 minutes forming a solution of 0.7 nM AuNP25. λ_{max} (H_2O) / nm 520 (SPR). Diameter / nm = 24 ± 6 (DLS number distribution), PDI = 0.09. AuNP25 (9 mL, 0.7 nM) were diluted to 40 mL with deionised water and vigorously stirred. The solutions for addition were diluted to 1 mM, 3 mM and 0.75 mM in deionised water to 40 mL for $HAuCl_4.3H_2O$, ascorbic acid and trisodium citrate dihydrate respectively. The two solutions were simultaneously added *via* a peristaltic pump over 45 minutes. The resultant solution was refluxed for 30 minutes forming a solution of 80 pM AuNP50. λ_{max} (H_2O) / nm 532 (SPR). Diameter / nm = 50 ± 12 (DLS number distribution), PDI = 0.04. ζ-potential = - 31 ± 13 mV. AuNP50 was neutralised with 0.01 M NaOH solution. AuNP50 (40 mL, 80 pM) were vigorously stirred. The solutions for addition were diluted to 4 mM, 12 mM and 3.4 mM in deionised water to 40 mL for $HAuCl_4.3H_2O$, ascorbic acid and trisodium citrate dihydrate respectively. The two solutions were simultaneously added *via* a peristaltic pump over 45 minutes. The resultant solution was refluxed for 30 minutes forming a solution of 40 pM AuNP100. λ_{max} (H_2O) / nm 566 (SPR). Diameter / nm = 102 ± 24 (DLS number distribution), PDI = 0.01. ζ-potential = - 38 ± 12 mV. AuNP100 were taken and centrifuged at 13000 G for 90 s. The supernatant was decanted and the pellet was redispersed in deionised water. Data agreed with previously published.

3.5.3 Ruthenium molecular complexes

The RuS1, RuS6 and RuS12 probes were prepared using previously published methods and all characterisation agreed with previous results.[25, 47, 48] The hexafluorophosphate counterion was exchanged for chlorine using Dowex 1 X 8 ion exchange chromatography and the final solutions to be used for coating were prepared in methanol as 1.19, 0.95 and 0.87 mM solutions of RuS1, RuS6 and RuS12 respectively. RuS6 was sonicated with NH_4OH to produce a 0.63 mM solution.

3.5.3.1 Synthesis of RuS1

5,5'-Dimethylbromide-2,2'-bipyridine[87] A solution of 5,5'-dimethyl-2,2'-bipyridine (0.57 g, 3.09 mmol), N-bromosuccinimide (NBS) (2.90 g, 16.3 mmol) and 1,1'-azobis(cyclohexanecarbonitrile) (ABCN) (120.0 mg, 0.29 mmol) in 40 mL of dry CCl_4 were heated to reflux under N_2 for 90 min and hot filtered. The residual precipitate was washed with 10 mL of CCl_4 and the combined CCl_4 phases were evaporated *in vacuo*. The remaining solid was dissolved in DCM (100 mL) and extracted with $Na_2S_2O_3$ solution (0.5 M, 2 x 150 mL). The combined $Na_2S_2O_3$ fractions were then extracted with DCM (5 x 50 mL) and the combined DCM phases were dried over Na_2SO_4. The crude product was then recrystallized from hot DCM to yield a white solid (0.27g, 0.79 mmol, 26%). δ_H (100 MHz, $CDCl_3$): 4.56 (4H, s, H7); 7.88 (2H, dd, *2.2*, *8.2*, H4); 8.42 (2H, d, *8.2*, H3); 8.71 (2H, d, *2.2*, H6). δ_C (100 MHz, $CDCl_3$): 29.6 (C7); 121.2 (C3); 133.9 (C5); 137.6 (C4); 149.4 (C6); 155.4 (C2). m/z (TOF MS ES^+) 342.9 ($[M+H]^+$). Data agreed with previously published.

5,5'-Dimethylthiol-2,2'-bipyridine[48] 5,5'-Dibromomethyl-2,2'-bipyridine (200 mg, 0.58 mmol) and thiourea (140 mg, 1.83 mmol) were dissolved in dry 1,4-dioxane (30 mL) and the mixture was stirred at reflux under N_2 for 3 hr. NaOH (80 mg, 2 mmol) dissolved in 10 mL of degassed water was added and the mixture and heated at reflux for a further 2 hr. The solvent was removed *in vacuo* to give a pale yellow solid, which was stored in the freezer overnight. Degassed acidified water (25 mL, pH ≈ 4, HCl) was added and the aqueous phase was washed with DCM (5 x 40 mL). The combined DCM phases were evaporated *in vacuo* to yield a yellow solid (90 mg, 0.36 mmol, 63%). δ_H (300 MHz, $CDCl_3$): 3.73 (4H, s, H7); 7.73 (2H, dd, *2.0*, *8.2*, H4); 8.27 (2H, d, *8.2*, H3); 8.53 (2H, d, *2.0*, H6). δ_C

(100 MHz, $CDCl_3$): 25.1 (C7); 120.3 (C3); 136.7 (C4); 137.9 (C5); 148.8 (C6). m/z (TOF MS ES^+) 249 ($[M+H]^+$). Data agreed with previously published.

$Ru(bpy)_2Cl_2$[88] Dichloro(1,5-cyclooctadiene)ruthenium(II) polymer (706 mg, 2.5 mmol) and

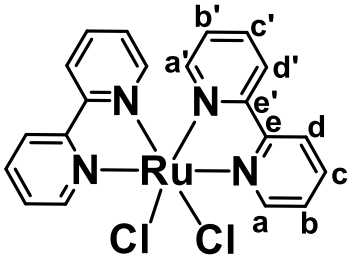

lithium chloride (770 mg, 19.9 mmol) in degassed 2-methoxyethanol (250 mL) was refluxed under N_2. 2,2'-Bipyridine (759 mg, 4.9 mmol) in degassed 2-methoxyethanol (10 mL) was added dropwise over 30 mins and left to stir for 72 hours. The mixture was cooled to rt and filtered. The solvent was reduced *in vacuo* and the thick purple oil was vigorously stirred in ice cold acetone (50 mL) for 5 minutes and then cooled to -5 °C for 24 h. The mixture was filtered and the residue was washed with water (250 mL) and diethyl ether (20 mL) to give a black solid (428 mg, 0.88 mmol, 35%). δ_H (300 MHz; d_6-DMSO): 7.10 (2H, t, *6.0*, Hc'), 7.52 (2H, d, *5.7*, Hd'); 7.68 (2H, t, *8.5*, Hb'); 7.78 (2H, t, *6.0*, Hb); 8.07 (2H, t, *7.8*, Hc); 8.48 (2H, d, *7.8*, Ha'); 8.65 (2H, d, *8.0*, Hd); 9.97 (2H, d, *6.5*, Ha). δ_C (100 MHz; d_6-DMSO): 122.5 (Cd); 122.8 (Cd'); 125.2 (Cb); 125.3 (Cb'); 133.3 (Cc'); 134.5 (Cc); 151.9 (Ca); 153.1 (Ca'); 158.1 (Ce); 160.2 (Ce'). m/z (TOF MS ES^+) 449.1 ($[M-Cl]^+$, 100%): 443.1 (10%); 444.1 (2%); 445.1 (7%); 446.1 (30%); 447.1 (40%); 448.1 (65%); 449.1 (100%); 450.1 (30%); 451.1 (80%); 452.1 (10%); 453.1 (10%); 454.1 (3%); 455.1 (1%); 456.1 (2%). UV-Vis λ_{max} / nm (ε / $M^{-1}cm^{-1}$) /CH_3CN: 551 (7800); 379 (7700); 298 (44000). Data agreed with previously published.

RuS1[48] A suspension of $Ru(bpy)_2Cl_2$ (48.0 mg, 0.10 mmol) and 5,5'-dimethylthiol-2,2'-

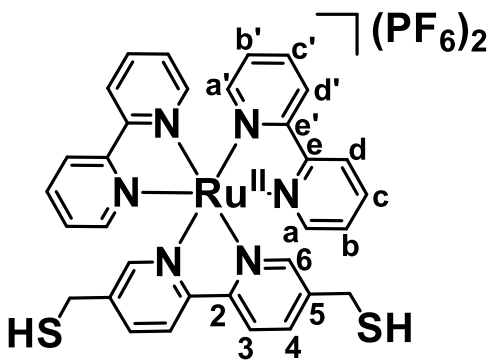

bipyridine (37.0 mg, 0.15 mmol) in degassed ethanol (15 mL) was heated to reflux overnight under N_2. The resulting solution was allowed to cool to room temperature and a saturated methanoic solution of

ammonium hexafluorophosphate (3g in 2 mL MeOH) was added. After cooling the flask in an ice-water bath for 2 hours to promote precipitation, the precipitate was collected by filtration and washed with ethanol (2 x 5mL), water (2 x 5mL) and diethyl ether (5mL) to produce an orange solid as the hexafluorophosphate salt (59.5 mg, 0.063 mmol, 63%). δ_H (300 MHz, CD_3CN): 3.62 (4H, d, *8.3*, H7); 7.42 (4H, m, Hb, Hb'); 7.64 (2H, s, H6); 7.74 (4H, m, Ha, Ha'); 8.09 (6H, m, Hc, Hc', H4); 8.42 (2H, d, *8.2*, H3); 8.52 (4H, d, *8.2*, Hd, Hd'). δ_C (100 MHz, CD_3CN): 24.5 (C7); 123.7 (C3); 124.1 (Cd, Cd'); 127.5 (Cb'); 127.3 (Cb); 137.4 (C4); 137.7 (Cc, Cc'); 141.9 (C5); 150.6 (C6); 151.5 (Ca, Ca'); 157.0 (C2); 157.3 (Ce, Ce'). Data agreed with previously published. All photophysical characterisation is performed as a 12 μM solution in water of the chloride salt, formed from Dowex ion exchange. UV-VIS λ_{max} / nm (ε / $M^{-1}cm^{-1}$): 451 (13000), 430 (sh), 288 (92000), 244 (41000). Emission λ_{max}: 645 nm. τ: 420 ns. Φ: 2%. In the presence of 150 μM Zonyl FSA surfactant. UV-VIS λ_{max} / nm (ε / $M^{-1}cm^{-1}$): 451 (13000), 430 (sh), 288 (92000), 244 (sh). Emission λ_{max}: 645 nm. τ: 420 ns. Φ: 1%.

3.5.3.2 Synthesis of RuS6

4,4'-Dihydroxy-2,2'-bipyridine[89] To a solution of 4,4'-dimethoxy-2,2'-bipyridine (2.4 g, 11.0 mmol) in glacial acetic acid (136 mL) was added hydrogen bromide (8.9 g, 110 mmol) in water (20 mL). The mixture was heated under reflux for 24 h. The mixture was cooled to rt, the solvent was removed *in vacuo* and the white solid was dissolved in water (100 mL) and neutralised with ammonium hydroxide (35% *w/w*). The precipitate was filtered to produce a white solid (1.1 g, 5.8 mmol, 52 %). δ_H (300 MHz; D_2O): 7.04 (2H, dd, *2.5, 6.85*, H5); 7.30 (2H, d, *2.5*, H3); 8.24 (2H, d, *6.9*, H6). δ_C (100 MHz; D_2O): 114.5 (C3), 115.0 (C5), 144.1 (C2), 144.2 (C6), 172.3 (C4). m/z (TOF MS ES^+) 189 ($[M]^+$). Data agreed with previously published.

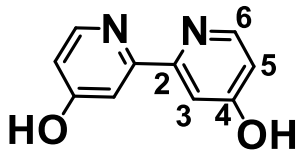

4,4'-Bis(5-hexen-1-yloxy)-2,2'-bipyridine[25] Sodium hydride (5g, 125 mmol, 60% w/w in mineral oil) was added to a solution of 4,4'-dihydroxy-2-2'-bipyridine (2.03 g, 10.8 mmol) in dry DMF and stirred at 60 °C under N_2 for 1 hour. 6-Bromohexene (8.06 g, 49.4 mmol) was added dropwise and the mixture was heated to 60 °C for 20 hours. The reaction was cooled to rt and the sodium hydride was quenched by ice cold ethanol (150 mL). The solvent was removed *in vacuo* and the pale brown residue was extracted with DCM/water and dried over $MgSO_4$. The solvent was removed *in vacuo* and the crude product was purified by recrystallisation from ethanol to yield a white solid (2.32 g, 6.58 mmol, 61 %). δ_H (100 MHz, $CDCl_3$): 1.53–1.65 (4H, m, H10); 1.78–1.90 (4H, m, H8); 2.07–2.20 (4H, m, H9); 4.14 (4H, t, *6.5*, H7); 4.94–5.00 (2H, m, H12); 5.00–5.09 (2H, m, H12'); 5.74–5.91 (2H, m, H11); 6.82 (2H, dd, *5.7, 2.6*, H5); 7.94 (2H, d, *2.5*, H3); 8.45 (2H, d, *5.7*, H6). δ_C (100 MHz, $CDCl_3$): 25.2 (C9); 28.4 (C8); 33.3 (C10); 67.9 (C7); 106.7 (C3); 111.3 (C5); 114.9 (C12); 138.3 (C11); 150.1 (C6); 157.9 (C4); 166.1 (C2). m/z (TOF MS ES^+) 381.2 ($[M+Na]^+$). Data agreed with previously published.

$Ru(bpy)_2Cl_2$ was synthesised as previously discussed (Section 3.5.3.1).

Rubpyhex[25] 4,4'-Bis(5-hexen-1-yloxy)-2,2'-bipyridine (101 mg, 0.29 mmol) and $Ru(bpy)_2Cl_2$ (111 mg, 0.23 mmol) were refluxed in ethanol (20 mL) for 24 hours. The solvent was reduced *in vacuo* (2 mL) and water (35 mL) was added, forming a white precipitate which was filtered out. A saturated solution of ammonium hexafluorophosphate (3g in 2 mL MeOH) was added, forming a red precipitate which was filtered. The residue was washed with water (50 mL) and diethyl ether (50 mL) to form a red solid as the hexafluorophosphate salt (197

mg, 0.187 mmol, 81%). δ_H (300 MHz, CD_3CN): 1.58 (4H, m, H10); 1.85 (4H, m, H8); 2.17 (4H, m, H9); 4.22 (4H, t, *7.0*, H7); 4.95 (2H, m, H12); 5.03 (2H, m, H12'); 5.89 (2H, m, H11); 6.93 (2H, dd, *2.7*, *6.6*, H5); 7.38 (2H, dt, *6.3*, *1.3*, Hb'); 7.44 (2H, dt, *6.3*, *1.3*, Hb); 7.44 (2H, d, *6.6*, H6); 7.74 (2H, dd, *5.3*, *0.7*, Ha'); 7.84 (2H, dd, *5.3*, *0.7*, Ha); 8.00 (2H, d, *2.7*, H3); 8.05 (4H, dq, *8.0*, *1.5*, Hc, Hc'); 8.50 (4H, dd, *3.2*, *8.0*, Hd, Hd'). δ_C (100 MHz, CD_3CN): 25.3 (C10); 28.4 (C9); 33.5 (C8); 70.1 (C7); 111.9 (C3); 114.6 (C5); 115.0 (C11); 124.7 (Cd, Cd'); 128.0 (Cb, Cb'); 137.9 (Cc, Cc'); 139.2 (C12); 152.1 (C6); 152.4 (Ca'); 152.7 (Ca); 157.7 (Ce); 157.9 (Ce'); 158.5 (C4); 167.2 (C2). m/z (TOF MS ES^+) 383.1 ($[M-(PF_6)_2]^{2+}$): 380.2 (10%); 380.7 (5%); 381.2 (5%); 381.7 (50%); 382.2 (60%); 382.7 (70%); 383.1 (100%); 383.7 (45%): 384.2 (60%); 384.7 (25%); 385.2 (5%). Data agreed with previously published.

RuS6[25] Rubpyhex (197 mg, 0.187 mmol) was dissolved in dry THF (4 mL) and pipetted into a solution of thioacetic acid (200 µL, 2.6 mmol) and 1,1'-azobis(cyclohexanecarbonitrile) (ABCN) (240 mg, 0.98 mmol) in dry THF (2 mL) and reacted for 4 days. A saturated aqueous solution of $NaHCO_3$ (10 mL) was added and the solvent was removed *in vacuo*. The solid was dissolved in water (50 mL) and extracted with DCM (2 x 50 mL). The organic layers were dried with $MgSO_4$ and the solvent removed to form a brown solid. The solid was recrystallised in acetonitrile to give a red solid as the hexafluorophosphate salt (153 mg, 0.127 mmol, 68%). δ_H (300 MHz, CD_3CN): 1.46 (8H, m, H9, H10); 1.60 (4H, p, *7.0*, H11); 1.83 (4H, p, *7.0*, H8); 2.30 (4H, s, H14); 2.88 (4H, t, *7.0*, H12); 4.21 (4H, t, *7.0*, H7); 6.93 (2H, dd, *2.7*, *6.6*, H5); 7.38 (2H, dt, *6.3*, *1.3*, Hb'); 7.44 (2H, dt, *6.3*, *1.3*, Hb); 7.44 (2H, d, *6.6*, H6); 7.74 (2H, dd,

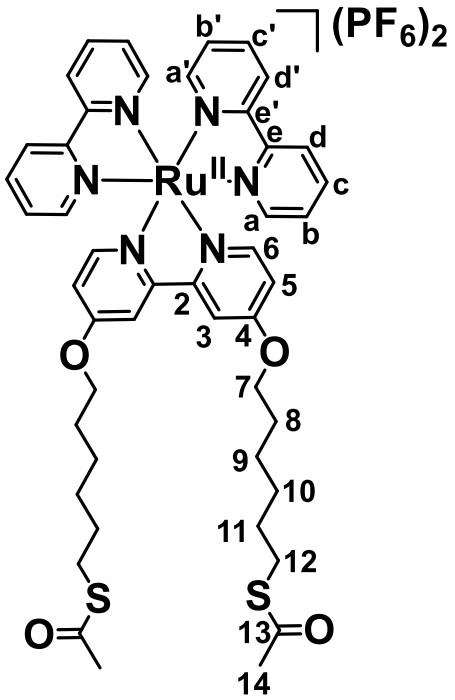

5.3, 0.7, Ha'); 7.84 (2H, dd, *5.3, 0.7*, Ha); 8.00 (2H, d, *2.7*, H3); 8.05 (4H, dq, *8.0, 1.5*, Hc, Hc'); 8.50 (4H, dd, *3.2, 8.0*, Hd, Hd'). δ_C (100 MHz, CD_3CN): 25.5 (C10); 28.5 (C9); 28.7 (C8); 29.0 (C12); 29.8 (C11); 30.4 (C14); 70.2 (C7); 111.9 (C3); 114.7 (C5); 124.7 (Cd, Cd'); 128.0 (Cb, Cb'); 137.9 (Cc, Cc'); 152.1 (C6); 152.3 (Ca'); 152.7 (Ca); 157.7 (Ce); 157.9 (Ce'); 158.5 (C4); 167.2 (C2). m/z (TOF MS ES^+) 459.2 ($[M-(2PF_6)]^{2+}$): 456.2 (7%); 456.7 (5%); 457.2 (5%); 457.7 (25%); 458.2 (40%); 458.7 (50%); 459.2 (100%); 459.7 (40%): 460.2 (50%); 460.7 (25%); 461.2 (5%); 461.7 (2%). Data agreed with previously published. All photophysical characterisation is performed as a 9 µM solution in water of the chloride salt, formed from Dowex ion exchange. UV-VIS λ_{max} / nm (ε / $M^{-1}cm^{-1}$): 463 (14000), 430 (sh), 287 (75000), 253 (30000). Emission λ_{max}: 645 nm. τ: 240 ns. Φ: 2%. In the presence of 150 µM Zonyl FSA surfactant. UV-VIS λ_{max} / nm (ε / $M^{-1}cm^{-1}$): 464 (14000), 430 (sh), 288 (75000), 253 (sh). Emission λ_{max}: 645 nm. τ: 400 ns. Φ: 3%.

3.5.3.3 Synthesis of RuS12

N-Boc-5-amino-1-pentanol[47] Potassium bicarbonate (28.6 g, 286 mmol) was suspended in a solution of 5-amino-1-pentanol (10.9 g, 106 mmol) and THF:water (1:1, 140 mL). Di-tert-butyldicarbonate (22.0 g, 114 mmol) in THF:water (1:1, 160 mL) was added dropwise over 30 mins, maintaining the temperature at 0 – 5 °C. The solution was heated to 50 °C and stirred for 25 hours under N_2. The solution was left to cool to rt, the organic phase reduced *in vacuo* to form a white microsuspension which was dissolved in diethyl ether:water (2:1, 150 mL). The aqueous layer was washed with diethyl ether (50 mL) and the combined organic layers were dried with Na_2SO_4, filtered and the solvent was removed *in vacuo* to produce a clear oil (16.6 g, 81.6 mmol, 77%). δ_H (300 MHz; $CDCl_3$): 1.10-1.40 (6H, m, H2, H3, H4); 1.15 (9H, s, H8); 3.01 (3H, bs, H5, OH); 3.50 (2H, t, *6.5*, H1); 4.83 (1H, bs, NH). δ_C (100 MHz; $CDCl_3$): 22.9

(C2); 28.4 (C8); 29.7 (C3); 32.1 (C4); 40.4 (C1); 62.2 (C5); 79.1 (C7); 156.3 (C6). m/z (TOF MS ES^+) 226 ($[M+Na]^+$). Data agreed with previously published.

N-Boc-5-amino-1-tosylpentane[47] N-Boc-5-amino-1-pentanol (17.8 g, 87.7 mmol) and para-toluene sulfonyl chloride (21.1 g, 110.8 mmol) were dissolved in anhydrous DCM (100 mL). Anhydrous pyridine (23 mL) was added dropwise over 30 mins, maintaining the temperature at 0 – 5 °C. It was stirred for 24 hours at rt. The solvent was reduced *in vacuo* (20 mL) and dissolved in diethyl ether (50 mL). The organic layer was washed with water (50 mL), aqueous $NaHCO_3$ (50 mL) and brine (50 mL) and then dried with Na_2SO_4 and filtered. The solvent was removed *in vacuo* to produce a clear oil, which was trituated in hexane (250 mL) and filtered to produce a white solid (21.0 g, 59.2 mmol, 68%). δ_H (300 MHz; $CDCl_3$): 1.25-1.50 (6H, m, H7, H8, H9); 1.44 (9H, s, H13); 2.46 (3H, s, H1); 3.07 (2H, bt, H10); 4.02 (2H, t, *6.4*, H6); 4.35 (1H, bs, NH); 7.36 (2H, d, *8.1*, H3); 7.80 (2H, d, *8.1*, H4). δ_C (100 MHz; $CDCl_3$): 21.6 (C1); 22.7 (C7); 28.4 (C13); 28.6 (C8); 29.4 (C9); 40.2 (C6); 70.4 (C10); 79.2 (C12); 127.9 (C3); 129.9 (C4); 133.1 (C2); 144.8 (C5); 156.0 (C11). m/z (TOF MS ES^+) 559 ($[M+H]^+$). Data agreed with previously published.

4,4'-Dihydroxy-2,2'-bipyridine was synthesised as previously discussed (Section 3.5.3.2).

4,4'-Di-(N-boc-5-amino-1-pentoxy)-2,2'-bipyridine[47] N-Boc-5-amino-1-tosylpentane (8.42 g, 23.6 mmol) and 4,4'-dihydroxy-2,2'-bipyridine (1.48 g, 7.9 mmol) were suspended in acetone (400 mL) with potassium carbonate (3.27 g, 23.6 mmol) and a catalytic amount of 18-crown-6 and heated to 60 °C for 42 hours. The mixture was hot filtered and the filtrate was cooled to 0 – 5 °C. It was filtered to produce a white solid (1.61 g, 2.9 mmol, 37%). δ_H (300 MHz; $CDCl_3$): 1.46

(18H, s, H14); 1.50-1.60 (8H, m, H8, H9); 1.87 (4H, qu, *10.7*, H10); 3.18 (4H, dd, *4.93*, *10.7*, H11); 4.13 (4H, t, *6.4*, H7); 4.58 (2H, bs, HN); 6.84 (2H, dd, *2.5*, *5.7*, H5); 7.95 (2H, d, *2.5*, H3); 8.47 (2H, d, *5.7*, H6). δ_C (100 MHz; $CDCl_3$): 23.3 (C8); 28.4 (C14); 28.6 (C9); 29.8 (C10); 40.4 (C7); 67.8 (C11); 79.1 (C13); 106.7 (C3); 111.3 (C5); 150.1 (C6); 157.9 (C2); 166.1 (C4). m/z (TOF MS ES^+) 559 ($[M+H]^+$). Data agreed with previously published.

4,4'-Di-(5-amino-1-pentoxy)-2,2'-bipyridine[47] 4,4'-Di-(N-boc-5-amino-1-pentoxy)-2,2'-bipyridine (1.61 mg, 2.89 mmol) was dissolved in trifluoroacetic acid (30 mL) and stirred under N_2 for 90 mins. The solvent was removed *in vacuo* and sodium hydroxide (1 M, 70 mL) was added and the white solid was extracted with chloroform (6 x 50 mL). The organic layers were dried with Na_2SO_4, filtered and the solvent was removed *in vacuo* to produce a yellow oil which was used as is. δ_H (300 MHz; $CDCl_3$): 1.10 (8H, m, H8, H9); 1.40 (4H, m, H10); 2.30 (4H, t, *5.7*, H11); 3.70 (4H, t, *6.3*, H7); 6.43 (2H, dd, *5.7*, *2.5*, H5); 7.59 (2H, d, *2.5*, H3); 8.07 (2H, d, *5.7*, H6). δ_C (100 MHz; $CDCl_3$): 24.0 (C9); 28.9 (C8); 30.6 (C10); 51.0 (C11); 68.0 (C7); 106.7 (C3); 111.3 (C5); 150.1 (C6); 157.9 (C2); 166.1 (C4). m/z (TOF MS ES^+) 381 ($[M+Na]^+$). Data agreed with previously published.

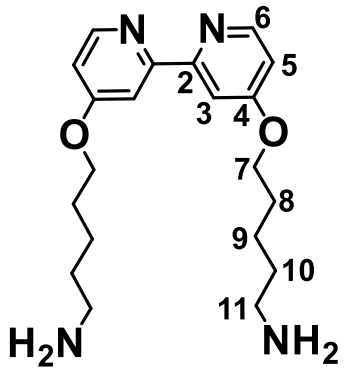

4,4'-Di-(5-lipoamide-1-pentoxy)-2,2'-bipyridine[47]

1-Ethyl-3-(3-dimethylaminopropyl)carbodiimide (EDC) (1.25 g, 8.06 mmol) was added to a mixture of α-lipoic acid (1.29 g, 6.25 mmol) and 1-hydroxybenzotriazol hydrate (1.00 g, 7.41 mmol) in anhydrous DMF (15 mL) and stirred for 1 hour under N_2, maintaining the temperature between 0 - 5 °C. Once the EDC has dissolved it was allowed to warm to rt and stirred for a further 1 hour. A solution of 4,4'-di-(5-amino-1-pentoxy)-2,2'-bipyridine (1.03 g, 2.89 mmol, 1 equiv) and N-ethylmaleimide (0.9 mL, 6.94 mmol) in dry DMF (30 mL) was added and the mixture was left to stir for 16 hours. The white precipitate was filtered and left

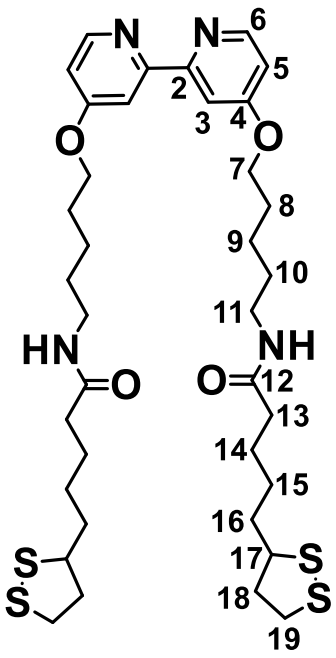

to dry in air over night. It was slurried in DCM and filtered to produce an off-white solid (0.67 g, 0.96 mmol, 33%). δ_H (300 MHz; $CDCl_3$): 1.37-1.80 (22H, m, H8, H9, H14, H15, H16); 1.80-2.00 (6H, m, H10, H18'); 2.19 (4H, t, *7.2*, H13); 2.47 (2H, dt, *6.5*, *12.1*, H18); 3.07-3.35 (4H, m, H19, H19'); 3.31 (4H, dd, *6.6*, *12.7*, H11); 3.54 (2H, dt, *6.4*, *12.9*, H17); 4.15 (4H, t, *6.3*, H7); 5.50 (2H, bt, *4.9*, HN); 6.84 (2H, dd, *2.5*, *5.7*, H5); 7.95 (2H, d, *2.5*, H3); 8.47 (2H, d, *5.7*, H6). δ_C (100 MHz; $CDCl_3$): 23.4 (C9); 25.4 (C14); 28.6 (C15); 28.9 (C8); 29.4 (C10); 34.6 (C16); 36.6 (C13); 38.5 (C19); 39.3 (C11); 40.3 (C18); 56.5 (C17); 67.7 (C7); 106.8 (C3); 111.3 (C5); 150.2 (C6); 157.8 (C2); 166.1 (C4); 172.7 (C12). m/z (TOF MS ES^+) 735 ($[M+H]^+$). Data agreed with previously published.

$Ru(bpy)_2Cl_2$ was synthesised as previously discussed (Section 3.5.3.1).

RuS12[47] $Ru(bpy)_2Cl_2$ (128.7 mg, 0.359 mmol) and 4,4'-di-(5-lipoamide-1-pentoxy)-2,2'-bipyridine (324.5 mg, 0.467 mmol) were heated to 90 °C in ethanol (130 mL) for 24 hours under N_2. The solvent was reduced *in vacuo* (25 mL) and water (35 mL) was added, forming a white precipitate which was filtered out. A saturated solution of ammonium hexafluorophosphate (3g in 2 mL MeOH) is added, forming a red precipitate which was filtered. The residue was washed with water (50 mL) and diethyl ether (50 mL) to form a red solid hexafluorophosphate salt (240.8 mg, 0.210 mmol, 58%). δ_H (300 MHz; CD_3CN): 1.25-1.67 (20H, m, H8, H9, H14, H15, H16); 1.67-1.85 (6H,

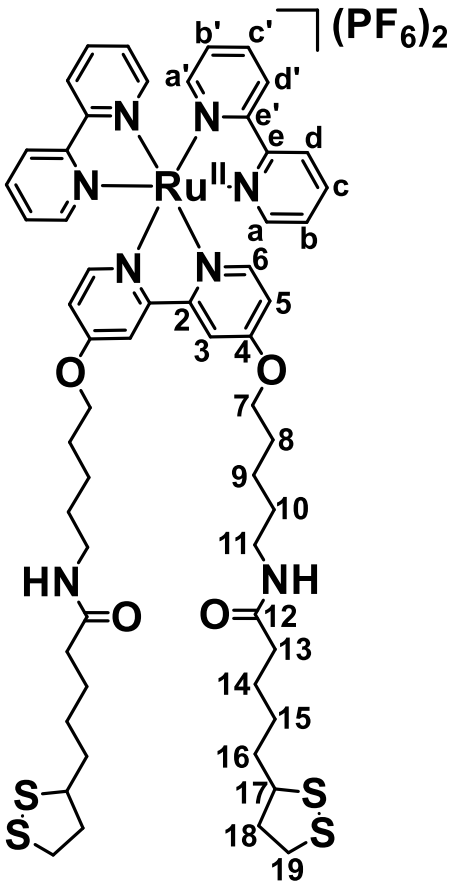

m, H10, H18'); 2.00 (4H, t, H13); 2.30 (2H, td, *6.2, 12.4*, H18); 2.90-3.15 (8H, m, H11, H19, H19'); 3.44 (2H, td, *6.3, 12.6*, H17); 4.10 (4H, t, *6.5*, H7); 6.37 (2H, s, HN); 6.82 (2H, dd, *2.5, 6.5*, H5); 7.26-7.45 (6H, m, H6, Hb, Hb'); 7.75 (2H, d, *5.4*, Ha); 7.64 (2H, d, *5.5*, Ha'); 7.90-8.12 (6H, m, H3, Hc, Hc'); 8.40 (4H, dd, *2.8, 8.1*, Hd, Hd'). δ_C (100 MHz; CD_3CN): 22.4 (C9); 25.0 (C14); 27.6 (C15); 28.2 (C8); 28.6 (C10); 34.0 (C16); 35.3 (C13); 37.9 (C19); 38.1 (C11); 39.8 (C18); 56.1 (C17); 69.3 (C7); 111.1 (C3); 113.9 (C5); 123.8 (Cd, Cd'); 127.1 (Cb, Cb'); 137.0 (Cc, Cc'); 151.2 (Ca); 151.4 (Ca'); 151.7 (C6); 156.8 (Ce); 157.0 (Ce'); 157.6 (C2); 166.3 (C4); 172.2 (C12). m/z (TOF MS ES^+) 574.3 ($[M-2PF_6]^{2+}$, 100%): 571.3 (10%); 571.8 (10%); 572.3 (10%); 572.8 (30%); 573.3 (50%); 573.8 (70%); 574.3 (100%); 574.8 (70%); 575.3 (70%); 575.8 (40%); 576.3. Data agreed with previously published. All photophysical characterisation is a 7 µM solution in water of the chloride salt, formed from Dowex ion exchange. UV-VIS λ_{max} / nm (ε / $M^{-1}cm^{-1}$): 460 (13000), 430 (sh), 290 (70000), 230 (sh). Emission λ_{max}: 645 nm. τ : 280 ns. Φ: 2%. In the presence of 150 µM Zonyl FSA surfactant. UV-VIS λ_{max} / nm (ε / $M^{-1}cm^{-1}$): 460 (13000), 430 (sh), 290 (70000), 230 (sh). Emission λ_{max}: 645 nm. τ: 350 ns. Φ: 2%.

3.5.4 Attachment of probe to gold nanoparticle

Z·AuNP13 10% Zonyl FSA solution in deionised water (10 µL) was added to 9 nM AuNP13 (1 mL) and sonicated for 10 mins. It was centrifuged at 13000 G for 30 mins, the supernatant was decanted and the pellet was resuspended in deionised water (1 mL) to form Z·AuNP13. λ_{max} (H_2O) / nm 518 (SPR). Diameter / nm = 12 ± 4 (DLS number distribution). ζ-potential = - 50 ± 8 mV.

RuS1·AuNP13 RuS1 (12 µL, 1.19 mM) was titrated into a 9 nM solution of Z·AuNP13 with sonication. A Sephadex G-10 size exclusion column was performed and the sample was diluted to 2 mL with deionised water to form a 4.5 nM solution of RuS1·AuNP13. λ_{max} (H_2O) / nm 521 (SPR). Diameter / nm = 15 ± 6 (DLS number distribution). ζ-potential = - 49 ± 11

mV. ICPMS result ratio Ru:Au is 1:180, suggesting 550 complexes per AuNP13. Emission λ_{max}: 650 nm. τ: 470 ns. Φ: 2%.

RuS6·AuNP13 RuS6 (16 µL, 0.63 mM) was titrated into a 9 nM solution of Z·AuNP13 with sonication. A Sephadex G-10 size exclusion column was performed and the sample was diluted to 2 mL with deionised water to form a 4.5 nM solution of RuS6·AuNP13. λ_{max} (H_2O) / nm 522 (SPR). Diameter / nm = 24 ± 9 (DLS number distribution). ζ-potential = - 62 ± 15 mV. ICPMS result ratio Ru:Au is 1:180, suggesting 550 complexes per AuNP13. Emission λ_{max}: 650 nm. τ: 340 ns. Φ: 6%.

RuS12·AuNP13 RuS12 (20 µL, 0.87 mM) was titrated into a 9 nM solution of Z·AuNP13 with sonication. A Sephadex G-10 size exclusion column was performed and the sample was diluted to 2 mL with deionised water to form a 4.5 nM solution of RuS12·AuNP13. λ_{max} (H_2O) / nm 520 (SPR). Diameter / nm = 18 ± 6 (DLS number distribution). ζ-potential = - 42 ± 13 mV. ICPMS result ratio Ru:Au is 1:150, suggesting 690 complexes per AuNP13. Emission λ_{max}: 650 nm. τ: 480 ns. Φ: 9%.

Z·AuNP50 10% Zonyl FSA solution in deionised water (5 µL) was added to 80 pM AuNP50 (1 mL) and sonicated for 10 mins to form Z·AuNP50. λ_{max} (H_2O) / nm 533 (SPR). Diameter / nm = 50 ± 12 (DLS number distribution). ζ-potential = - 62 ± 18 mV.

RuS1·AuNP50 RuS1 (12 µL, 1.19 mM) was titrated into an 80 pM solution of Z·AuNP50 with sonication. A Sephadex G-10 size exclusion column was performed and the sample was diluted to 2 mL with deionised water to form a 40 pM solution of RuS1·AuNP50. λ_{max} (H_2O) / nm 537 (SPR). Diameter / nm = 59 ± 17 (DLS number distribution). ζ-potential = - 31 ± 10 mV. Emission λ_{max}: 650 nm. τ: 470 ns.

RuS6·AuNP50 RuS6 (14 µL, 0.63 mM) was titrated into an 80 pM solution of Z·AuNP50 with sonication. A Sephadex G-10 size exclusion column was performed and the sample was

diluted to 2 mL with deionised water to form a 40 pM solution of RuS6·AuNP50. λ_{max} (H_2O) / nm 536 (SPR). Diameter / nm = 54 ± 15 (DLS number distribution). ζ-potential = - 44 ± 16 mV. Emission λ_{max}: 650 nm. τ: 340 ns.

RuS12·AuNP50 RuS12 (16 µL, 0.87 mM) was titrated into an 80 pM solution of Z·AuNP50 with sonication. A Sephadex G-10 size exclusion column was performed and the sample was diluted to 2 mL with deionised water to form a 40 pM solution of RuS12·AuNP50. λ_{max} (H_2O) / nm 537 (SPR). Diameter / nm = 61 ± 16 (DLS number distribution). ζ-potential = - 42 ± 12 mV. Emission λ_{max}: 650 nm. τ: 480 ns.

Z·AuNP100 10% Zonyl FSA solution in deionised water (5 µL) was added to 40 pM AuNP100 (1 mL) and sonicated for 10 mins. It was centrifuged at 13000 G for 90 s, the supernatant was decanted and the pellet was resuspended in deionised water (1 mL) to form Z·AuNP100. λ_{max} (H_2O) / nm 567 (SPR). Diameter / nm = 107 ± 27 (DLS number distribution). ζ-potential = - 53 ± 11 mV.

RuS1·AuNP100 RuS1 (1 µL, 1.19 mM) was titrated into a 40 pM solution of Z·AuNP100 with sonication. A Sephadex G-10 size exclusion column was performed and the sample was diluted to 2 mL with deionised water to form a 20 pM solution of RuS1·AuNP100. λ_{max} (H_2O) / nm 569 (SPR). Diameter / nm = 109 ± 28 (DLS number distribution). ζ-potential = - 47 ± 10 mV. Emission λ_{max}: 650 nm. τ: 470 ns.

RuS6·AuNP100 RuS6 (4 µL, 0.63 mM) was titrated into a 40 pM solution of Z·AuNP100 with sonication. A Sephadex G-10 size exclusion column was performed and the sample was diluted to 2 mL with deionised water to form a 20 pM solution of RuS6·AuNP100. λ_{max} (H_2O) / nm 569 (SPR). Diameter / nm = 107 ± 27 (DLS number distribution). ζ-potential = - 26 ± 9 mV. Emission λ_{max}: 650 nm. τ: 340 ns.

RuS12·AuNP100 RuS12 (8 µL, 0.87 mM) was titrated into a 40 pM solution of Z·AuNP100 with sonication. A Sephadex G-10 size exclusion column was performed and the sample was diluted to 2 mL with deionised water to form a 20 pM solution of RuS12·AuNP100. λ_{max} (H_2O) / nm 569 (SPR). Diameter / nm = 112 ± 27 (DLS number distribution). ζ-potential = - 36 ± 10 mV. Emission λ_{max}: 650 nm. τ: 480 ns.

3.5.5 Instrumentation

Transient Absorption (TA) measurements were run at Warwick University by Dr Michael Hornbury, in collaboration with Dr Vasilios Stavros. The sample was transferred to a 0.1 cm path length low volume quartz cell and excited at 450 nm. Pump–probe delays (up to 2 ns) were created using a motorized optical delay line in the probe beam path. The pump and probe pulses were generated from a commercially available femtosecond Ti-sapphire regenerative amplified laser system operating at 1 kHz and producing 3 mJ pulses. This beam was detected using a fibre coupled UV-vis spectrometer (Avantes, AvaSpec-ULS1650F-USB2). Probe polarisation was held at the magic angle (54.7°) relative to the pump polarisation.

3.6 References

1. A. Juris, V. Balzani, F. Barigelletti, S. Campagna, P. Belser and A. Von Zelewsky, *Coord. Chem. Rev.*, 1988, 84, 85-277.
2. K. R. Brereton, C. L. Pitman, T. R. Cundari and A. J. M. Miller, *Inorg. Chem.*, 2016, 55, 12042-12051.
3. D. W. Shaffer, Y. Xie, D. J. Szalda and J. J. Concepcion, *Inorg. Chem.*, 2016, 55, 12024-12035.
4. J. M. Kamdar, D. C. Marelius, C. E. Moore, A. L. Rheingold, D. K. Smith and D. B. Grotjahn, *ChemCatChem*, 2016, 8, 3045-3049.
5. J. M. de Ruiter, R. L. Purchase, A. Monti, C. J. M. van der Ham, M. P. Gullo, K. S. Joya, M. D'Angelantonio, A. Barbieri, D. G. H. Hetterscheid, H. J. M. de Groot and F. Buda, *ACS Catalysis*, 2016, 6, 7340-7349.
6. H. Shahroosvand, L. Najafi, A. Sousaraei, E. Mohajerani, M. Janghouri and F. Bonaccorso, *J. Phys. Chem. C*, 2016, 120, 24965-24972.
7. T. Lu, W. Li, J. Chen, F. Bai, J. Wang, L. He and H. Zhang, *Phys. Chem. Chem. Phys.*, 2016, 18, 29591-29599.
8. A. L. A. Parussulo, T. A. Matias, R. R. Guimaraes, S. H. Toma, K. Araki and H. E. Toma, *Inorg. Chim. Acta*, 2016, 453, 764-770.
9. A. P. Carnizello, M. I. F. Barbosa, M. Martins, N. H. Ferreira, P. F. Oliveira, G. M. Magalhães, A. A. Batista and D. C. Tavares, *J. Inorg. Biochem.*, 2016, 164, 42-48.
10. C. Zeng, C. Zhang, S. Lai, B. Tang, D. Wan and Y. Liu, *Transition Met. Chem. (London)*, 2016, 41, 923-931.
11. Y. P. Kumar, C. S. Devi, A. Srishailam, N. Deepika, V. R. Kumar, P. V. Reddy, K. Nagasuryaprasad, S. S. Singh, P. Nagababu and S. Satyanarayana, *J. Fluoresc.*, 2016, 26, 2119-2132.

12. N. Tlotleng, M. A. Vetten, F. K. Keter, A. Skepu, R. Tshikhudo and M. Gulumian, *Cell. Biol. Toxicol*, 2016, 32, 305-321.

13. N. Lewinski, V. Colvin and R. Drezek, *Small*, 2008, 4, 26-49.

14. C. J. Murphy, A. M. Gole, J. W. Stone, P. N. Sisco, A. M. Alkilany, E. C. Goldsmith and S. C. Baxter, *Acc. Chem. Res.*, 2008, 41, 1721-1730.

15. H. Peng, H. Tang and J. Jiang, *Sci. China. Chem*, 2016, 59, 783-793.

16. K. Weintraub, *Nature*, 2013, 495, S14-S16.

17. J. O. You, P. Guo and D. T. Auguste, *Angew. Chem., Int. Ed.*, 2013, 52, 4141-4146.

18. M. Daniel and D. Astruc, *Chem. Rev.*, 2004, 104, 293-346.

19. S. D. Brown, P. Native, J. Smith, D. Stirling, P. R. Edward and B. Venugopal, *J. Am. Chem. Soc.*, 2010, 132, 4679.

20. G. N. Abdelrasoul, R. Magrassi, S. Dante, M. d'Amora, M. S. d'Abbusco, T. Pellegrino and A. Diaspro, *Nanotechnology*, 2016, 27, 255101.

21. N. Zhao, Y. Pan, Z. Cheng and H. Liu, *J. Innov. Opt. Health. Sci*, 2016, 09, 1630004.

22. X. Liu, N. Huang, H. Li, Q. Jin and J. Ji, *Langmuir*, 2013, 29, 9138-9148.

23. D. J. Stephens and V. J. Allan, *Science*, 2003, 300, 82-86.

24. L. Zhang, R. Zhang, M. Gao and X. Zhang, *Talanta*, 2016, 158, 315-321.

25. N. J. Rogers, S. Claire, R. M. Harris, S. Farabi, G. Zikeli, I. B. Styles, N. J. Hodges and Z. Pikramenou, *Chem. Commun.*, 2014, 50, 617-619.

26. L. Zhao, T. H. Kim, H. W. Kim, J. C. Ahn and S. Y. Kim, *Mat. Sci. Eng. C*, 2016, 67, 611-622.

27. T. S. Tang, H. Liu and K. K. Lo, *Chem. Eur. J.*, 2016, 22, 9649-9659.

28. L. Yang, H. Peng, H. Ding, F. You, L. Hou and F. Teng, *Microchim. Acta*, 2014, 181, 743-749.

29. F. C. Leung, A. Y. Tam, V. K. Au, M. Li and V. W. Yam, *ACS Appl. Mater. Interfaces*, 2014, 6, 6644-6653.

30. M. Jebb, P. K. Sudeep, P. Pramod, K. G. Thomas and P. V. Kamat, *J. Phys. Chem. B*, 2007, 111, 6839-6844.

31. S. Eustis and M. A. El Sayed, *Chem. Soc. Rev.*, 2006, 35, 209-217.

32. E. Dulkeith, A. C. Morteani, T. Niedereichholz, T. A. Klar, J. Feldmann, S. A. Levi, F. C. J. M. Veggel, D. N. Reinhoudt, M. Möller and D. I. Gittins, *Phys. Rev. Lett.*, 2002, 89, 203002.

33. K. G. Thomas and P. V. Kamat, *Acc. Chem. Res.*, 2003, 36, 888-898.

34. K. Saha, S. S. Agasti, C. Kim, X. Li and V. M. Rotello, *Chem. Rev.*, 2012, 112, 2739-2779.

35. F. Liu and J. M. Nunzi, *Appl. Phys. Lett.*, 2011, 99, 123302.

36. J. Kümmerlen, A. Leitner, H. Brunner, F. R. Aussenegg and A. Wokaun, *Mol. Phys.*, 1993, 80, 1031-1046.

37. W. R. Glomm, S. J. Moses, M. K. Brennaman, J. M. Papanikolas and S. Franzen, *J. Phys. Chem. B*, 2004, 109, 804-810.

38. H. Zhang, M. Cao, W. Wu, H. Xu, S. Cheng and L. Fan, *Nanoscale*, 2015, 7, 1374-1382.

39. A. V. Sorokin, A. A. Zabolotskii, N. V. Pereverzev, I. I. Bespalova, S. L. Yefimova, Y. V. Malyukin and A. I. Plekhanov, *J. Phys. Chem. C*, 2015, 119, 2743-2751.

40. I. O. Osorio-Román, A. R. Guerrero, P. Albella and R. F. Aroca, *Anal. Chem.*, 2014, 86, 10246-10251.

41. P. Reineck, D. Gómez, S. H. Ng, M. Karg, T. Bell, P. Mulvaney and U. Bach, *ACS Nano*, 2013, 7, 6636-6648.

42. N. S. Abadeer, M. R. Brennan, W. L. Wilson and C. J. Murphy, *ACS Nano*, 2014, 8, 8392-8406.

43. D. Lee and D. J. Jang, *Polymer*, 2014, 55, 5469-5476.

44. P. Zhang, J. Wang, H. Huang, H. Chen, R. Guan, Y. Chen, L. Ji and H. Chao, *Biomaterials*, 2014, 35, 9003-9011.

45. O. Kedem, W. Wohlleben and I. Rubinstein, *Nanoscale*, 2014, 6, 15134-15143.

46. K. Wee, M. K. Brennaman, L. Alibabaei, B. H. Farnum, B. Sherman, A. M. Lapides and T. J. Meyer, *J. Am. Chem. Soc.*, 2014, 136, 13514-13517.

47. S. J. Adams, D. J. Lewis, J. A. Preece and Z. Pikramenou, *ACS Appl. Mater. Interfaces*, 2014, 6, 11598-11608.

48. P. Bertoncello, E. T. Kefalas, Z. Pikramenou, P. R. Unwin and R. J. Forster, *J. Phys. Chem. B*, 2006, 110, 10063-10069.

49. T. Burgi, *Nanoscale*, 2015, 7, 15553-15567.

50. Y. Dong, S. Abaci, C. Shannon and M. J. Bozack, *Langmuir*, 2003, 19, 8922-8926.

51. B. Durham, J. V. Caspar, J. K. Nagle and T. J. Meyer, *J. Am. Chem. Soc.*, 1982, 104, 4803-4810.

52. V. W. Yam and K. M. Wong, *Chem. Commun.*, 2011, 47, 11579-11592.

53. F. Schulz, T. Homolka, N. G. Bastús, V. Puntes, H. Weller and T. Vossmeyer, *Langmuir*, 2014, 30, 10779-10784.

54. J. Turkevich, P. C. Stevenson and J. Hillier, *Farad. Discuss.*, 1951, 11, 55-75.

55. G. Frens, *Nat. Phys. Sci.*, 1973, 20.

56. K. C. Grabar, R. G. Freeman, M. B. Hommer and M. J. Natan, *Anal. Chem.*, 1995, 67, 735-743.

57. P. Zhao, N. Li and D. Astruc, *Coord. Chem. Rev.*, 2013, 257, 638-665.

58. X. Ji, X. Song, J. Li, Y. Bai, W. Yang and X. Peng, *J. Am. Chem. Soc.*, 2007, 129, 13939-13948.

59. I. OjeaJiménez, N. G. Bastús and V. Puntes, *J. Phys. Chem. C*, 2011, 115, 15752-15757.

60. H. Xia, S. Bai, J. Hartmann and D. Wang, *Langmuir*, 2010, 26, 3585-3589.

61. I. Ojea-Jiménez and J. M. Campanera, *J. Phys. Chem. C*, 2012, 116, 23682-23691.

62. S. Biggs, M. K. Chow, C. F. Zukoski and F. Grieser, *J. Colloid Interface Sci.*, 1993, 160, 511-513.

63. M. K. Chow and C. F. Zukoski, *J. Colloid Interface Sci.*, 1994, 165, 97-109.

64. S. Kumar, K. S. Gandhi and R. Kumar, *Ind. Eng. Chem. Res.*, 2007, 46, 3128-3136.

65. K. Zabetakis, W. E. Ghann, S. Kumar and M. C. Daniel, *Gold Bull.*, 2012, 45, 203-211.

66. C. Ziegler and A. Eychmüller, *J. Phys. Chem. C*, 2011, 115, 4502-4506.

67. W. Haiss, N. T. K. Thanh, J. Aveyard and D. G. Fernig, *Anal. Chem.*, 2007, 79, 4215-4221.

68. S. K. Ghosh and T. Pal, *Chem. Rev.*, 2007, 107, 4797-4862.

69. E. Pensa, E. Cortés, G. Corthey, P. Carro, C. Vericat, M. H. Fonticelli, G. Benítez, A. A. Rubert and R. C. Salvarezza, *Acc. Chem. Res.*, 2012, 45, 1183-1192.

70. Y. Wu, S. Zhan, F. Wang, L. He, W. Zhi and P. Zhou, *Chem. Commun.*, 2012, 48, 4459-4461.

71. H. M. Zakaria, A. Shah, M. Konieczny, J. A. Hoffmann, A. J. Nijdam and M. E. Reeves, *Langmuir*, 2013, 29, 7661-7673.

72. T. Lou, L. Chen, C. Zhang, Q. Kang, H. You, D. Shen and L. Chen, *Anal. Methods*, 2012, 4, 488-491.

73. E. C. Dreaden, A. M. Alkilany, X. Huang, C. J. Murphy and M. A. El-Sayed, *Chem. Soc. Rev.*, 2012, 41, 2740-2779.

74. A. V. Naumkin, A. KrautVass, S. W. Gaarenstroom and C. J. Powell, *NIST Standard Reference Database 20, Version 4.1* 2012.

75. F. C. Krebs, *Polymer Photovoltaics: A Practical Approach*, 2008, In: K. Norrman; S. Cros; R. Bettignies; M. Firon; F. C. Krebs,. *Lifetime and Stability Studies*, SPIE, Washington.

76. C. Battocchio, F. Porcaro, S. Mukherjee, E. Magnano, S. Nappini, I. Fratoddi, M. Quintiliani, M. V. Russo and G. Polzonetti, *J. Phys. Chem. C*, 2014, 118, 8159-8168.

77. D. Grumelli, C. Vericat, G. Benitez, M. E. Vela, R. C. Salvarezza, L. J. Giovanetti, J. M. Ramallo-López, F. G. Requejo, A. F. Craievich and Y. S. Shon, *J. Phys. Chem. C*, 2007, 111, 7179-7184.

78. B. Factor, B. Muegge, S. Workman, E. Bolton, J. Bos and M. M. Richter, *Anal. Chem.*, 2001, 73, 4621-4624.

79. S. W. Snyder, S. L. Buell, J. N. Demas and B. A. DeGraff, *J. Phys. Chem*, 1989, 93, 5265-5271.

80. W. J. Dressick, B. L. Hauenstein, T. B. Gilbert, J. N. Demas and B. A. DeGraff, *J. Phys. Chem*, 1984, 88, 3337-3340.

81. T. Soller, M. Ringler, M. Wunderlich, T. A. Klar, J. Feldmann, H. P. Josel, Y. Markert, A. Nichtl and K. Kürzinger, *Nano Lett.*, 2007, 7, 1941-1946.

82. T. E. Karam, R. A. Khoury and L. H. Haber, *J. Chem. Phys.*, 2016, 144, 124704.

83. T. E. Karam, H. T. Smith and L. H. Haber, *J. Phys. Chem. C*, 2015, 119, 18573-18580.

84. S. Link and M. A. El-Sayed, *J. Phys. Chem. B*, 1999, 103, 8410-8426.

85. H. Inouye, K. Tanaka, I. Tanahashi and K. Hirao, *Phys. Rev. B*, 1998, 57, 11334-11340.

86. K. Puech, F. Z. Henari, W. J. Blau, D. Duff and G. Schmid, *Chem. Phys. Lett.*, 1995, 247, 13-17.

87. U. S. Schubert, C. Eschbaumer and G. Hochwimmer, *Synthesis*, 1999, 1999, 779-782.

88. S. Farabi, *PhD, University of Birmingham*, 2011.

89. Y. Hong and C. B. Gorman, *J. Org. Chem.*, 2003, 68, 9019-9025.

4 Improving the photophysical properties of ruthenium complexes with 2,2'-bipyridine-4,4'-sulfur ligands

4.1 Introduction

Ruthenium probes for attachment to gold nanoparticles, AuNP, have been highly researched.[1-4] Many groups see quenching of the molecular probe photophysical properties when attached to the AuNP, however our group has shown an enhancement (Chapter 3).[1] Adsorption of $Ru(bpy)_3Cl_2$ on the surface of 10 nm AuNP has shown a luminescence lifetime decrease from 623 to 0.8 ns.[5] It was found that even at a distance of 2 nm from the gold surface, a tris(bipyridine)ruthenium complex has a highly quenched luminescence.[4, 6] The greatest enhancement seen from our group was with a bis-bipyridine probe, RuS12, with a long chain for attachment (Figure 4.1). This showed a 70% enhancement in luminescence lifetime as the nanoprobe, compared to the molecular probe. The properties of the molecular probe however are poor, having a luminescent lifetime of 280 ns, which is low when comparing it to the parent molecule $Ru(bpy)_3Cl_2$ (380 ns). Similar molecules such as RuS1 (the short chain probe), $[Ru(bpy)_2(4,4'\text{-dimethyl-}2,2'\text{-bipyridine})]^{2+}$ and $[Ru(bpy)_2(4,4\text{-di-}t\text{-butyl-}2,2'\text{-bipyridine})]^{2+}$ have been shown to have comparable lifetimes to that of $Ru(bpy)_3Cl_2$.[1, 7, 8]

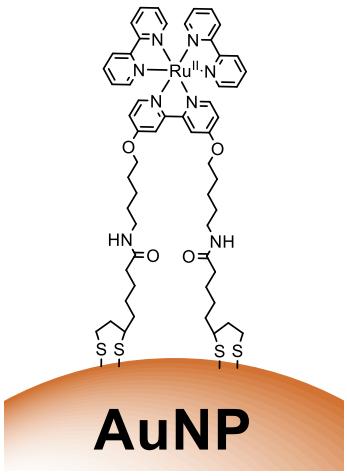

Figure 4.1: Schematic to show the structure of RuS12•AuNP13.

This low lifetime (280 ns) may be attributed to internal oxygen quenching of the ruthenium triplet excited state (Figure 4.2). It has been shown that oxygen is the largest molecular quencher of these excited states, with a rate of quenching (k_q) of 3.3 x 10^9 M^{-1} s^{-1} for $[Ru(bpy)_3]^{2+\bullet}$ in water.[9, 10] In the literature, luminescent lifetimes are presented as both in an air and a deaerated environment, showing the extent of quenching. Adams *et al.* show the lifetime of $Ru(bpy)_3Cl_2$ increases 5-fold when in a deaerated environment (170 to 840 ns in acetonitrile).[11] Quenching can occur through electron or energy transfer but the mechanism here is unknown. Sutin *et al.* suggests it goes *via* an electron transfer process to yield $[Ru(bpy)_3]^{3+}$ and O_2^-, however Olmsted *et al.* suggest energy transfer.[12, 13] Quenching of the luminescent lifetime from internal donor-acceptor systems are seen. Zhang *et al*. investigated the effect of substituents on the photophysical properties of $[Ru(bpy)_3]^{2+}$ (τ = 1150 ns) derivatives and found that there was a 6-fold decrease in luminescent lifetime, attributed to an increase in non-radiative decay, when an oxygen was adjacent to the bipyridine ring ($[Ru(bpy)_2(bpyOMe)]^{2+}$, τ = 176 ns) and only a 40% decrease in lifetime when the oxygen was separated by 1 carbon ($[Ru(bpy)_2(bpyCH_2OH)]^{2+}$, τ = 844 ns).[14] Åkermark *et al.* have attached a naphthalenediimide to $[Ru(bpy)_3]^{2+}$ and found a large quenching of luminescent lifetime when the acceptor and donor are separated by 1 carbon (890 to 0.2 ns).[15] In RuS12, where oxygen is adjacent to the bipyridine ring, a 2-fold decrease in luminescent lifetime is seen compared to similar ruthenium complexes without the oxygen. This decrease in lifetime can be attributed to internal quenching from the oxygen.

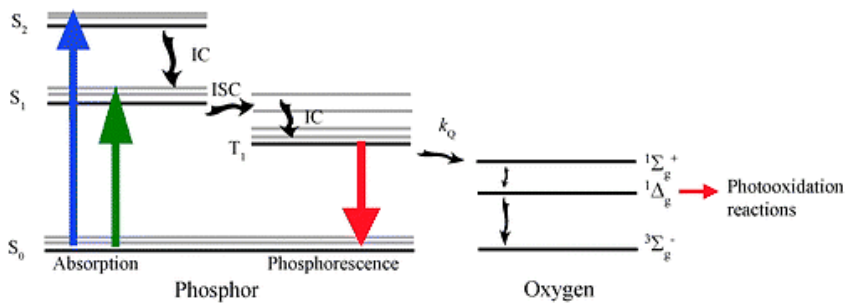

Figure 4.2: Schematic to show the process of oxygen quenching. Image taken from reference.[16]

RuS12 has been shown to be the best molecular probe for enhanced properties when attached to AuNP due to its optimised distance from the surface. Further optimisation of the molecular probe is required to provide improved nanoprobe photophysical properties for imaging compared to the RuS12•AuNP13 system (τ = 480 ns, Φ = 9%).[1] Biological imaging requires long lifetimes and high quantum yields which lead to highly luminescent probes for resolved and clear images. The properties of the ruthenium molecular probe can be easily altered by synthetic manipulation of the ligand.[17, 18] Through enhancing the photophysical properties of the molecular probe, and maintaining the optimal distance between the ruthenium photoactive centre and the surface of the AuNP, further enhancement of the nanoprobe is possible.

It has been shown that increasing the conjugation of ligands lead to improved photophysical properties. Barigelletti *et al.* show an increase in lifetime with increasing conjugation from 1.1 μs for $[Ru(bpy)_3]^{2+}$ to 1.4 and 1.6 μs for $[Ru(bpy)_2(4,4'\text{-diphenylbipyridine})]^{2+}$ and $[Ru(bpy)(4,4'\text{-diphenylbipyridine})_2]^{2+}$ respectively.[19] Ziessel *et al.* have demonstrated a 35 times increase in luminescent lifetime and 7 times increase in molar absorptivity when a pyrene is substituted for a benzene ring in $[Ru(bpy)(5\text{-L-bpy})_2]^{2+}$.[20] Electron rich π systems are known to increase the energy of the π_M orbitals.[21] This arises from a decrease of electron density on the σ-donating nitrogen, leading to a destabilisation of the positive ruthenium centre. This causes a decrease in the energy distance between the highest occupied molecular orbital (HOMO) and lowest unoccupied molecular orbital (LUMO) which causes a red shift in emission maximum.

1,10-Phenanthroline ligands have been shown to have higher luminescent lifetimes and quantum yields for Ru^{2+} complexes compared to 2,2'-bipyridine.[22-24] Contrary to the conjugated systems, phenanthroline ligands have a blue shift in absorption and emission.[10, 23, 25, 26] It has been suggested that this blue shift is due to rigidity of the complex as the

phenanthroline cannot rotate around the 2,2' carbon bond, causing destabilisation and an increase in energy of the π_L^* orbital.[27] This rigidity is said to diminish the non-radiative deactivation, causing an increase in luminescent quantum yield.[28, 29]

The energy gap law states that as the distance between energy levels decrease, the non-radiative rate of decay increases and the radiative rate decreases (Equation 4.1 & 4.2).[30, 31] k_r is the radiative rate, k_{nr} is the non-radiative rate and E_{em} is the energy gap.

$$\boldsymbol{k_r \propto (E_{em})^3} \qquad \textbf{Equation 4.1}$$

$$\boldsymbol{k_{nr} \propto e^{(-E_{em})}} \qquad \textbf{Equation 4.2}$$

Improving the molecular photophysical properties of the probe through elimination of internal oxygen quenching, incorporating conjugation or using the bis-phenanthroline systems should allow for improvement of the molecular probe. This has the potential to provide a highly luminescent nanoprobe with a lifetime longer than 480 ns and a quantum yield greater than 9% (seen for RuS12). A nanoprobe with such properties would be highly sought after in areas such as biological imaging, due to efficient light excitation in the visible region, minimising damage to the cells.[2, 3, 32] Current ruthenium imaging agents have short luminescent lifetimes which give poor imaging quality,[33] leading research into areas such as 2-photon imaging and pH sensitive ruthenium probes.[34, 35] However, some groups have taken high resolution images in cells using ruthenium coated AuNP. Pikramenou *et al.* have imaged single ruthenium coated 100 nm AuNP in cells using the RuS6 probe[2] and Gunnlaugsson *et al.* have images of 3 and 15 nm AuNP coated with a bis-phenanthroline ruthenium complex for DNA targeting (Figure 4.3).[3, 36] The molecular probe has a quantum yield of 5.6%, however when attached to the AuNP, that decreases 30-fold to 0.2%.

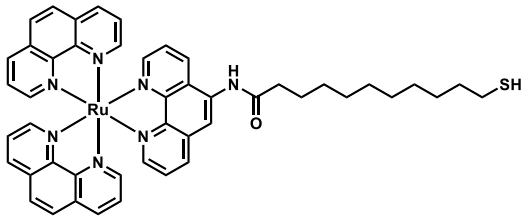

Figure 4.3: Schematic to show the structure of the bis-phenanthroline ruthenium complex. UV-vis / nm (ε / cm^{-1} M^{-1}): 285 (49500), 450 (12500). λ_{max} emission: 605 nm. Taken from reference.[3, 36]

4.1.1 Chapter summary

In this chapter, luminescent bis-bipyridine and bis-phenanthroline ruthenium probes were designed for attachment to AuNP and their properties compared, to deduce the optimal nanoprobe. Four complexes, RuphenS12, RuSconj, RuS8 and RuphenS8 were synthesised and characterised as molecular probes in water and attached to AuNP (Figure 4.4). Optimisation, to develop a probe with a longer lifetime and higher quantum yield, compared to RuS12, was achieved through changing the design of the ligand.

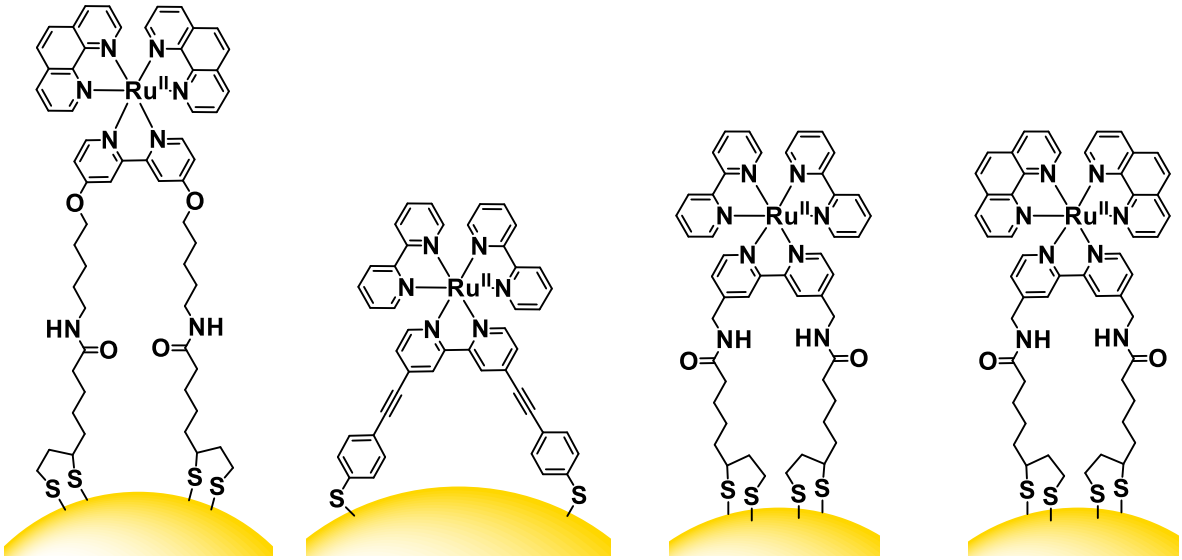

RuphenS12•AuNP13 RuSconj•AuNP13 RuS8•AuNP13 RuphenS8•AuNP13

Figure 4.4: Schematic to show the structure of RuphenS12•AuNP13, RuSconj•AuNP13, RuS8•AuNP13 and RuphenS8•AuNP13.

4.2 Results and discussion

4.2.1 Optimisation of molecular probe

Four complexes were designed for improved photophysical properties when compared to RuS12. It has been shown that substituting the 2,2'-bipyridine ligands for 1,10-phenanthroline leads to enhanced lifetimes and quantum yields. RuphenS12 was designed to contain the same linker as RuS12, but to incorporate the bis-1,10-phenanthroline system for direct comparison between the bipyridine and phenanthroline systems. RuSconj was designed due to its highly conjugated rigid ligand. As the conjugation in the ligand is increased, the molar absorptivity increases. This gives comparison of conjugated and aliphatic ligands with the bis-bipyridyl system. As RuS12 and RuS6 have a lower lifetime and quantum yield when compared to $Ru(bpy)_3Cl_2$ and RuS1, it was suspected that the oxygen adjacent to the π ring was causing quenching, so RuS8 was designed to remove this oxygen and compare two similar ligands with (RuS12) and without (RuS8) the adjacent oxygen. The RuphenS8 was designed similarly to RuphenS12, for the intention to directly compare the bipyridine and phenanthroline systems.

4.2.2 Synthesis of ruthenium metal complexes

Four novel complexes, RuphenS12, RuSconj, RuS8 and RuphenS8 were synthesised and fully characterised by ^{1}H NMR, ^{13}C NMR, ES^{+} MS and FTIR (Appendix).

4.2.2.1 RuphenS12

RuphenS12 is based on RuS12, and the synthesis was adapted from a previously published method in the group.[11] The ligand was synthesised through a Williamson ether reaction of N-(Boc)-5-amino-1-pentanol with 4,4'-dihydroxy-2,2'-bipyridine, followed by an amide bond formation through reaction with lipoic acid (Scheme 4.1), as for RuS12 (Section 3.2.1.1). The

complex is formed through refluxing the ligand with $Ru(phen)_2Cl_2$ in ethanol and isolating as the chloride ion through chromatography.

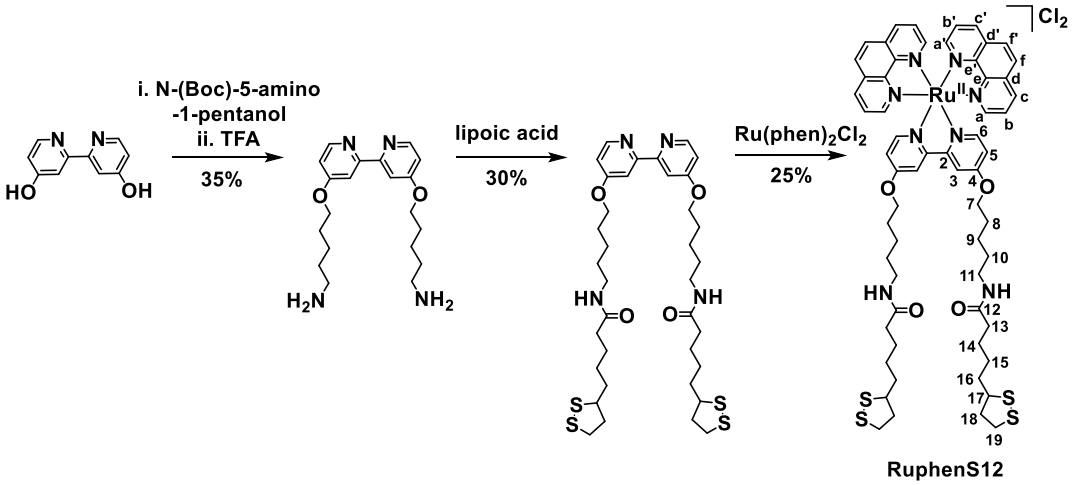

Scheme 4.1: Synthetic route for synthesis of RuphenS12.

The product was characterised by NMR and MS. The ^1H NMR spectrum is similar to that of the ligand, S12, with the aliphatic region having the same shifts (Figure 4.5). In the aromatic region, H3, H5 and H6 from the ligand can be seen at 8.1, 6.8 and 7.4 ppm respectively, similar to RuS12. H6 experiences a large upfield shift upon complexation, from 8.5 ppm, due to shielding from the adjacent bipyridine ligands. This is also seen in RuS6 and RuS12.

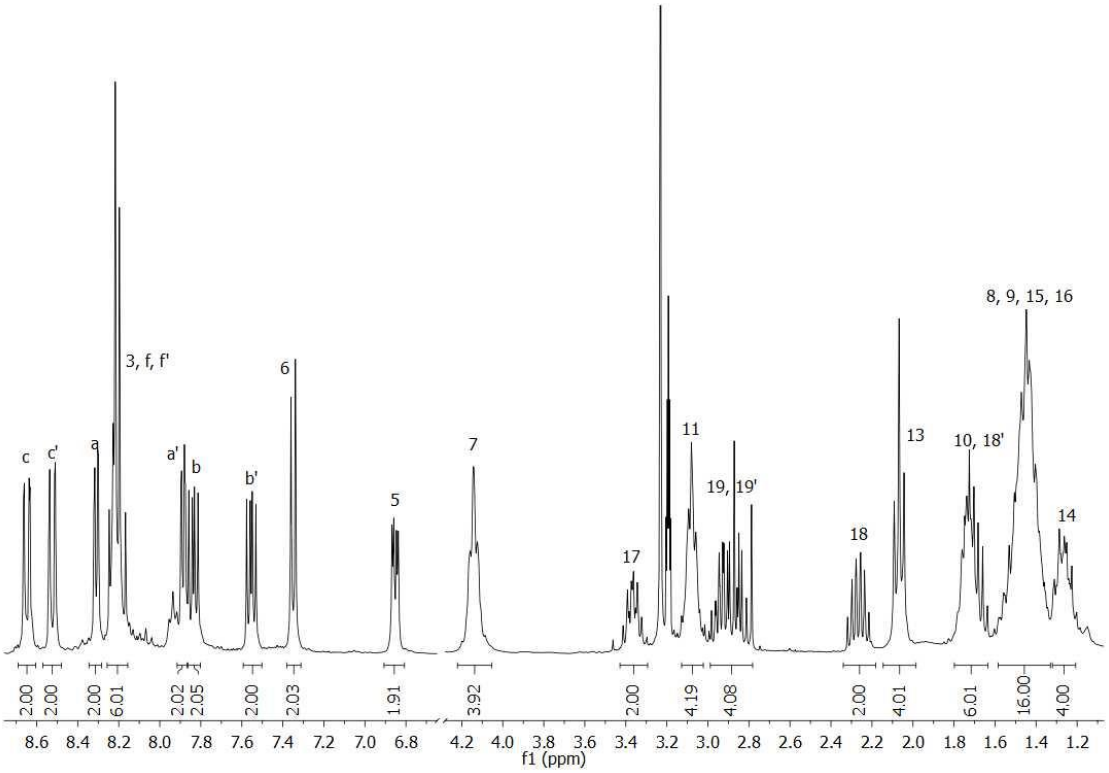

Figure 4.5: ^{1}H NMR of RuphenS12 (δ_4-CD_3OD).

Ha and Hb from the phenanthroline experience a large upfield shift (8.3 and 7.8 ppm) compared to $Ru(phen)_2Cl_2$ (10.3 and 8.3 ppm), whereas the remaining phenanthroline protons (Ha', Hb', Hc', Hc, Hf' and Hf) only shift slightly (Figure 4.6.b). This is because Ha and Hb are closest to the chlorines in $Ru(phen)_2Cl_2$, so feel a stronger deshielding, but upon complexation with the ligand, they feel shielding and shift upfield. In contrast to the bipyridine complexes, a small shift is seen between Ha/b and Ha'/b' for the phenanthroline. This is due to the bipyridine protons being in a different environment to the phenanthroline, causing different shielding for Ha/b and Ha'/b' and thus different shifts.

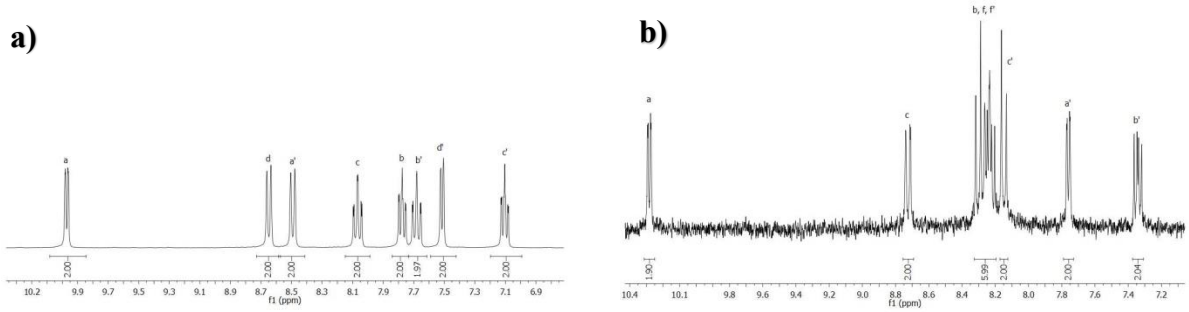

Figure 4.6: ^{1}H NMR of $Ru(bpy)_2Cl_2$ (a) and $Ru(phen)_2Cl_2$ (b) (δ_6-DMSO).

The difference between the NMR of RuS12 and RuphenS12 occur for the bipyridine and phenanthroline protons, which cause shifts and different splitting of the aromatic protons. This can be seen when comparing the ^{1}H NMR of $Ru(bpy)_2Cl_2$ and $Ru(phen)_2Cl_2$ (Figure 4.6). In the $Ru(bpy)_2Cl_2$ NMR, Ha/a', Hb/b' and Hc/c' have splitting of 1.5, 0.1 and 1.0 ppm, whereas for $Ru(phen)_2Cl_2$ Ha/a', Hb/b' and Hc/c' have splitting of 2.5, 0.9 and 0.5 ppm. This larger splitting in the $Ru(phen)_2Cl_2$ NMR is mirrored in the NMR of RuphenS12.

The ^{13}C spectrum of RuphenS12 has the expected peaks (Appendix).The ES^+ MS has a peak with a characteristic ruthenium isotope pattern at 598.2 m/z for the $[M\text{-}2Cl]^{2+}$.

4.2.2.2 RuSconj

The synthesis of RuSconj was adapted from the literature.[37] Takido *et al.* designed and synthesised a ruthenium tris-Sconj, whereas to keep the complex comparable to the $Ru(bpy)_2L$ system the synthesis must be adapted to produces the ruthenium mono-Sconj. The Sconj ligand was synthesised through a double Sonogashira Coupling of 4,4'-dibromo-2,2'-bipyridine with ethynyltrimethylsilane followed by 4-iodo-1-thioacetylbenzene as reported (Scheme 4.2). The complex is formed through refluxing the ligand with $Ru(bpy)_2Cl_2$ in ethanol and precipitating the hexafluorophosphate salt in water. The counterion was exchanged using Dowex 1 x 8 ion exchange to form the chloride salt.

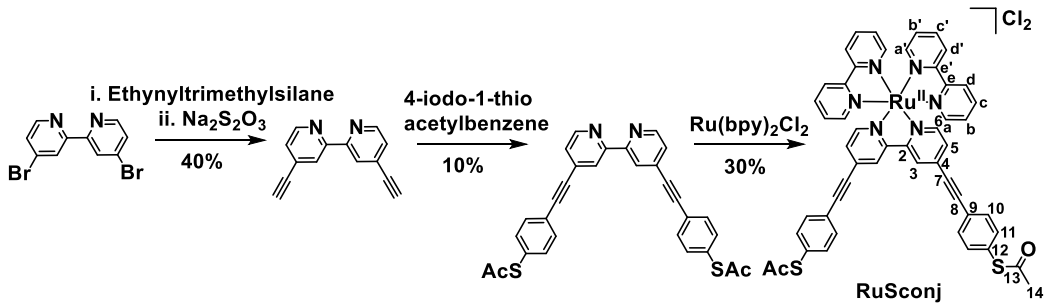

Scheme 4.2: Synthetic route for synthesis of RuSconj.

The identity of RuSconj can be confirmed from its ^{1}H NMR spectrum (Figure 4.7). It was characterised as the hexafluorophosphate salt. The characteristic symmetrical phenyl ring protons can be seen at 7.4 and 7.6 ppm, integrating at 4 protons each. Only a small shift is seen from 7.5 and 7.6 ppm in the ligand and 7.2 and 7.8 ppm in 4-iodo-1-thioacetylbenzene. The singlet at 2.4 ppm represents the 6 protons on the thioacetyl group. The ^{1}H NMR of RuSconj is similar to the ligand (Appendix), however H3 and H6 see a large shift upon complexation from 8.5 and 8.7 ppm to 8.7 and 7.4 ppm respectively. This is due to those protons being closest to the nitrogen binding site so feeling the largest effect on complexation with ruthenium. There is deshielding of all the protons upon complexation (downfield shift) through electron density being donated to the ruthenium centre *via* the σ-N and H6 feels a shielding (upfield shift) from the adjacent bipyridine ligands. H3, H5 and H6 were assigned by the J values.

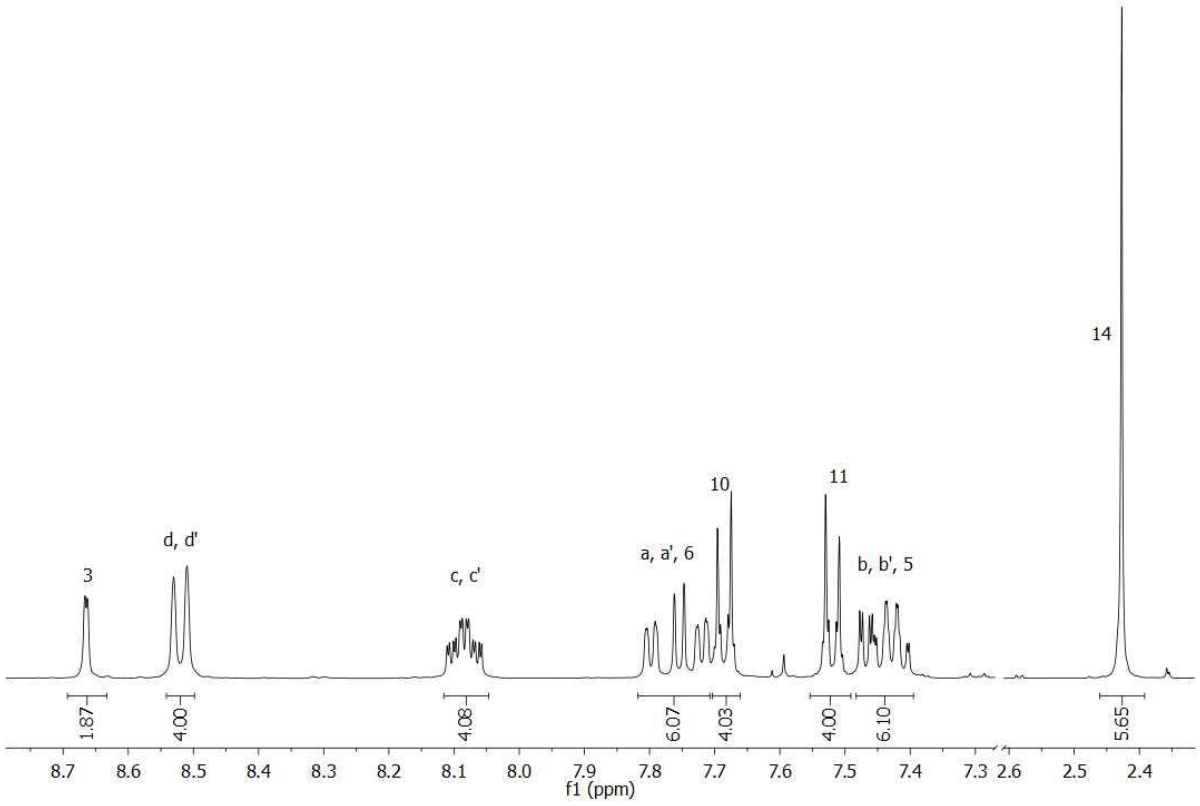

Figure 4.7: ^{1}H NMR of RuSconj (δ_3-CD_3CN).

When comparing this ^{1}H NMR with the aliphatic complexes, RuS6 and RuS12, the shifts of the bipyridine protons are similar, however H3, H5 and H6 on the ligand are seen around 8.1, 6.8 and 7.4 ppm in the aliphatic complexes and are shifted downfield to 8.7, 7.4 and 7.8 ppm in RuSconj due to the increase in conjugation, causing deshielding of the protons.

The ^{13}C NMR (Appendix) shows the expected peaks. The ^{1}H NMR assignments were confirmed using COSY and the ^{13}C NMR was assigned using HSQC 2D analysis (Appendix). The COSY spectrum shows interaction between the peak at 8.1 ppm and at 7.4 and 8.5 ppm, confirming the assignments of Hc/c', Hb/b' and Hd/d' respectively. It also shows interaction between the peak at 7.4 ppm and at 7.8 and 8.7 ppm, confirming the assignments of H5, H6 and H3 respectively. Interaction is also seen between peaks at 7.5 and 7.7 ppm for H10 and H11. The HSQC spectrum shows clear correlation between the assigned ^{1}H NMR and the ^{13}C NMR peaks, allowing for accurate ^{13}C NMR assignment.

The ES^+ MS has a peak with a characteristic ruthenium isotope pattern at 1063.3 m/z for the $[M-(PF_6)]^+$ ion.

4.2.2.3 RuS8 and RuphenS8

The novel S8 ligand was designed to have an aliphatic chain without oxygen adjacent to the π-ring system and to incorporate the lipoic acid attachment into the legs. Through retro-synthesis it was determined that the lipoic acid could be attached through an amide bond, so an amine would need to be present on the methyl attached to the bipyridine ring (Scheme 4.3). It was known that an amine could be formed from bromine, which could be formed from an alcohol. From this the forward synthesis was developed (Scheme 4.4).

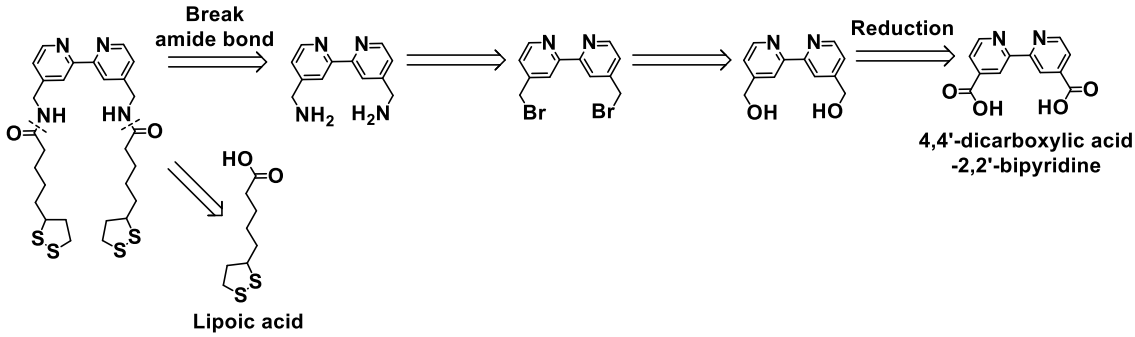

Scheme 4.3: Retrosynthesis of S8 ligand.

The S8 ligand was synthesised through oxidising 4,4'-dicarboxylicacid-2,2'-bipyridine into 4,4'-dimethylester-2,2'-bipyridine, followed by reduction to 4,4'-dimethylalcohol-2,2'-bipyridine and an exchange to form the bromine adduct, 4,4'-dimethylbromine-2,2'-bipyridine. This was then converted to 4,4'-dimethylazide-2,2'-bipyridine, reduced to 4,4'-dimethylamine-2,2'-bipyridine and reacted with lipoic acid to form an amide bond, giving 4,4'-dimethyllipoamide-2,2'-bipyridine (S8). The bpy and phen complexes were formed through refluxing the ligand with $Ru(bpy)_2Cl_2$ and $Ru(phen)_2Cl_2$ respectively in ethanol and isolating as the chloride ion through chromatography (Scheme 4.4).

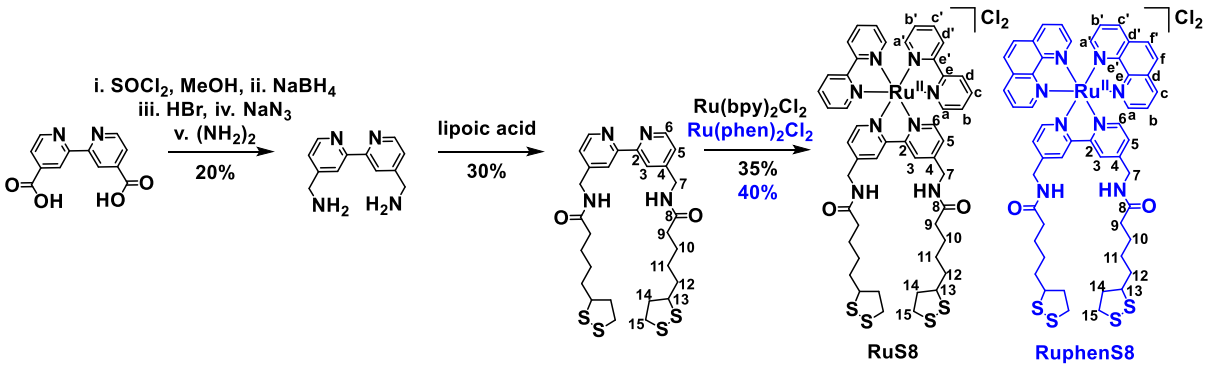

Scheme 4.4: Synthetic scheme for synthesis of RuS8 (black) and RuphenS8 (blue).

The S8 ligand was characterised with ^{1}H (Figure 4.8) and ^{13}C NMR and MS (Appendix). The ^{1}H NMR is similar to that of the S12 ligand (the ligand for RuS12) with the region 1-2 ppm containing the protons in the hydrocarbon chain and the proton adjacent to the carboxylic acid (H9) at 2.2 ppm. The protons in the 5-membered sulfur ring (H13, H14 and H15) are seen at higher ppm, with H14/14' and H15/15' splitting as they are diasteriotopic. The proton closest to the bipyridine ring (H7) is seen downfield at 7.2 ppm and does not shift much between the S8 and S12 ligands, even though in S12 it is adjacent to an oxygen. This shows that the deshielding of the proton is caused by the bipyridine ring and not the oxygen. The bipyridine protons, H3 and H5, are slightly shifted downfield for S8 when compared to S12. In S8 they are seen around 8.2 and 7.2 ppm, shifting from 8.0 and 6.7 ppm respectively in S12. This is due to the electronegative oxygen adjacent to the bipyridine ring in S12, shielding H3 and H5, and causing an upfield shift. H6 remains the same at 8.5 ppm as it is further from the oxygen. This pattern can be seen when comparing the ^{1}H NMR of the starting material with oxygen attached to the bipyridine ring (4,4'-dihydroxy-2,2'-bipyridine: H3= 7.30; H5= 7.05; H6= 8.25 ppm) and without (4,4'-dimethylamine-2,2'-bipyridine: H3= 8.10; H5= 7.20; H6= 8.50 ppm) (Appendix).

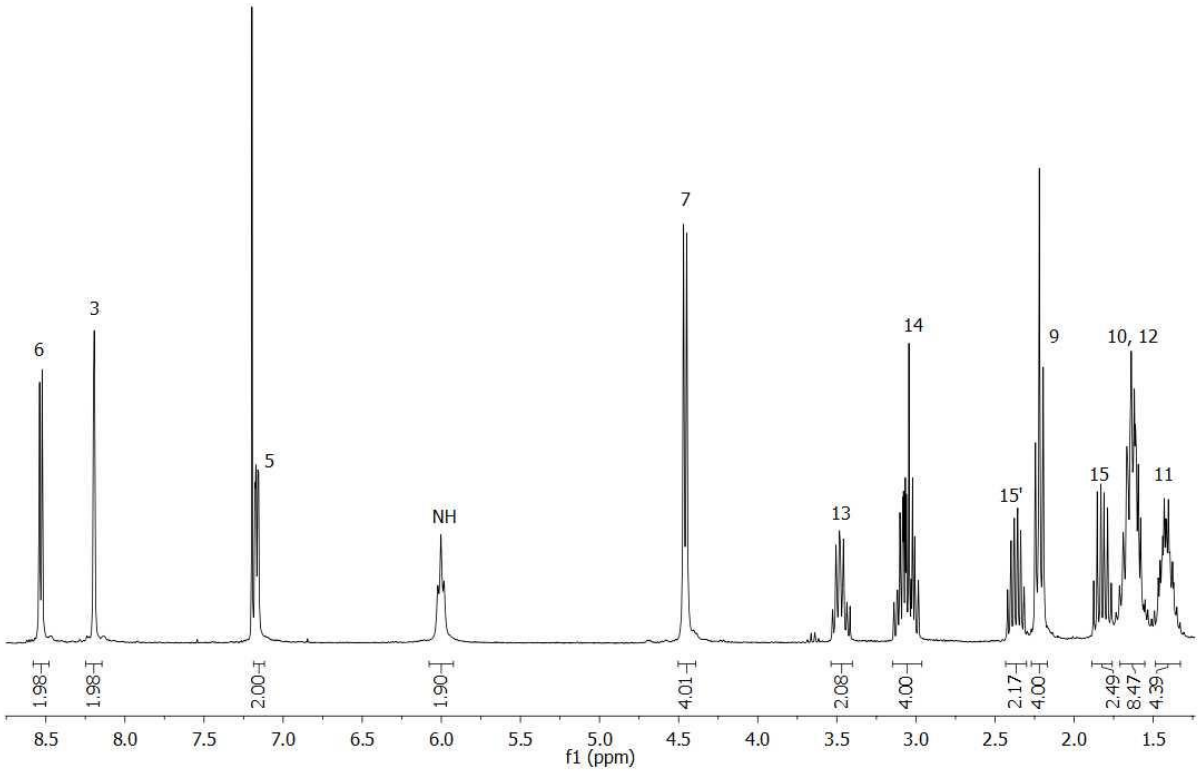

Figure 4.8: ^{1}H NMR of S8 ($CDCl_3$).

The NMR was assigned using COSY and HSQC 2D analysis (Appendix). H3, H5 and H6 were assigned using their J values and were confirmed by COSY as interactions are seen between the peak at 7.2 ppm and those at 8.2 and 8.5 ppm, confirming assignment to H5, H3 and H6 respectively. The peaks at 1.8 and 2.4 ppm with integral of 2 are assigned to the diasteriotopic protons, H15/15'. This is confirmed by COSY, which shows interaction between the 2 peaks. H14 is assigned to 3.1 ppm as interaction is seen in the COSY with both H15 and H15'. The broad peak at 6.0 ppm with integral 2 is characteristic of the NH and the COSY spectra shows interaction to the peak at 4.5 ppm, which is assigned as H7. The peak at 3.5 ppm with integral 2 is assigned to H13. From the COSY there is an interaction with the peak at 1.6 ppm, which can be assigned as H12. The peak at 2.2 ppm is in the region for protons adjacent to a carbonyl, so was assigned as H9 and shows interaction in the COSY with the peak at 1.6 ppm, assigned to H10. The remaining peak at 1.4 ppm is thus H11. The

HSQC spectrum shows clear correlation between the assigned ^{1}H NMR and the ^{13}C NMR peaks, allowing for accurate ^{13}C NMR assignment. The ES^{+} MS has a peak at 591.2 m/z for the $[M+H]^{+}$.

The identity of RuS8 can be confirmed from its ^{1}H NMR spectrum (Figure 4.9). The aliphatic region of the ^{1}H NMR is similar to that of the S8 ligand. As for RuSconj, H3 and H6 shift upon complexation from 8.2 and 8.6 ppm to 8.4 and 7.8 ppm due to being close to the nitrogen binding site and experiencing a change in environment. Unlike RuS12, there is minimal splitting of Ha/a' in RuS8 due to the lack of oxygen adjacent to the benzene ring. Without the oxygen, the three bipyridine rings surrounding the ruthenium are similar so Ha and Ha' are seen as in the same environment. When the oxygen is present, the ligand bipyridine acts as a different environment and causes splitting. This splitting is only seen on Ha/a' as they are the closest to the adjacent bipyridine rings. As seen for the ligands, H3 and H5 on the ligand bipyridine ring are shifted downfield from 8.0 and 6.8 ppm for RuS12 to 8.7 and 7.4 ppm respectively for RuS8. This is again because the oxygen adjacent to the bipyridine ring in RuS12 causes shielding of the protons. For the protons on the bis-bipyridyl ligands, only a small shift of 0.2 ppm is seen when comparing RuS8 and RuS12.

The ^{13}C NMR (Appendix) shows the expected peaks. The NMR was assigned using COSY and HSQC 2D analysis (Appendix).

The ES^{+} MS has a characteristic ruthenium isotope pattern at 502.1 m/z for the $[M-2Cl]^{2+}$ ion (Appendix).

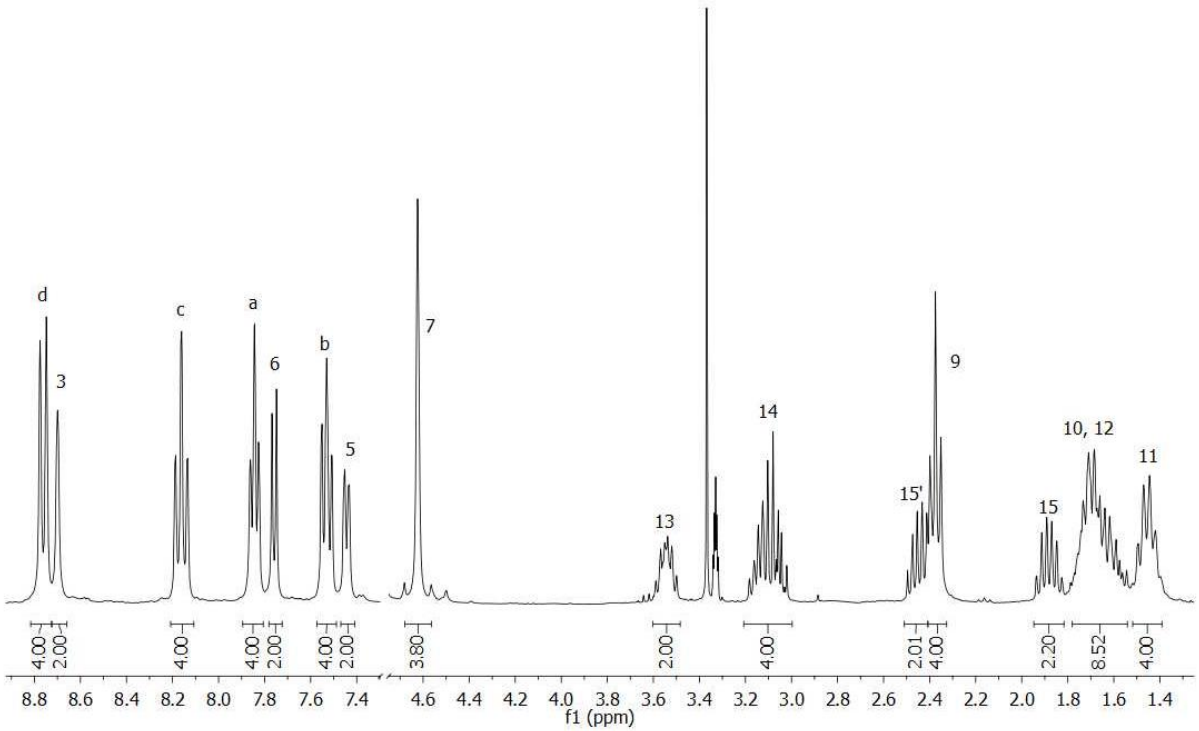

Figure 4.9: ^{1}H NMR RuS8 (δ_4-CD_3OD).

The identity of RuphenS8 can be confirmed from its ^{1}H NMR spectrum (Figure 4.10). As for RuS8, RuphenS8 has a similar ^{1}H NMR to the ligand, with the shifts in the aliphatic region being similar. H3, H5 and H6 are shifted higher than compared to RuphenS12 due to the absence of the oxygen adjacent to the bipyridine ring of the ligand. For the protons on the bis-phenanthroline ligands, only a small shift of 0.2 ppm is seen when comparing RuphenS8 and RuphenS12.

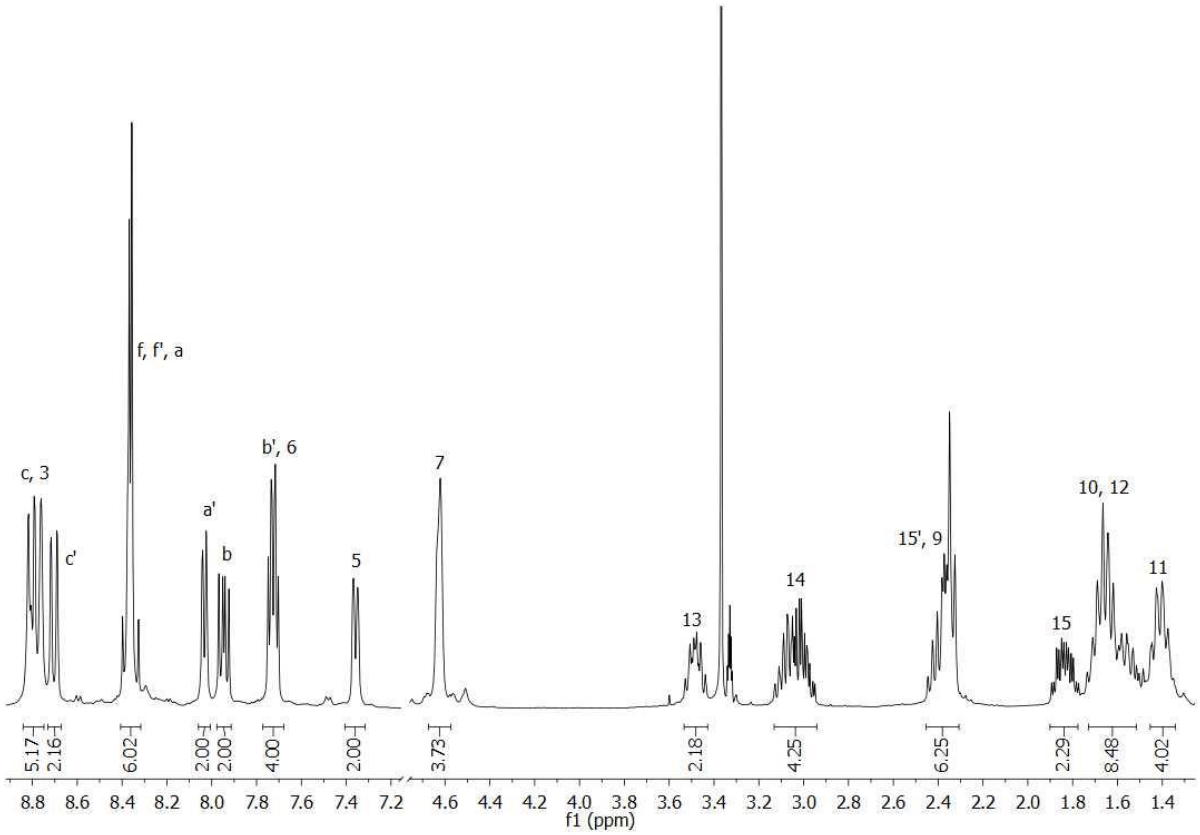

Figure 4.10: ^{1}H NMR of RuphenS8 (δ_4-CD_3OD).

The ^{13}C NMR (Appendix) shows the expected peaks. The NMR was assigned using COSY and HSQC 2D analysis (Appendix). The ES^+ MS has a characteristic ruthenium isotope pattern at 526.1 m/z for the $[M\text{-}2Cl]^{2+}$ ion.

4.2.3 Photophysical characterisation of metal complexes

The absorption, steady state emission and excitation were taken for all the complexes as a solution in aerated water. RuphenS12, RuSconj, RuS8 and RuphenS8 were dissolved in methanol to produce 0.8, 3.7, 0.8 and 1.1 mM solutions of the chloride ion respectively and were diluted with water to produce 7, 25, 8 and 7 µM solutions.

The photophysical properties of all the complexes are similar (Figure 4.11). The absorbance shows the singlet Metal to Ligand Charge Transfer (MLCT) (d-π*) between 400 – 500 nm. For RuphenS12 (Figure 4.11.a) the maximum is around 460 nm, similar to that of its bis-

bipyridine sister complex, RuS12. There is a slight 6 nm blue shift from 463 (RuS12) to 457 nm (RuphenS12). This blue shift from bipyridine to phenanthroline ligands is seen in the literature.[25, 27] This shift is also seen when comparing the bis-phenanthroline and bis-bipyridine complexes of RuphenS8 (Figure 4.11.d) and RuS8 (Figure 4.11.c). The maximum has a 4 nm blue shift from 456 (RuS8) to 452 nm (RuphenS8). RuSconj has a maximum at 480 nm. This is red shifted from the other complexes due to the increased conjugated system and similar to the literature value for [Ru(tris-4,4'-(1-ethynyl-4-thioacetate benzene)-2,2'-bipyridine)]$^{2+}$ (485 nm).[37] Electron rich π systems are known to increase the energy of the π_M orbitals.[38] The singlet MLCT molar absorptivity for RuS8 is 13000 M^{-1} cm^{-1}, which is similar to the bis-bipyridine complexes RuS1, RuS6 and RuS12. This is expected as it was shown that the structure of the ligand does not effect the viability of the MLCT (Section 3.2.1.2). For both the bis-phenanthroline complexes there is a slight increase in molar absorptivity when compared to the bis-bipyridine to 15000 and 16000 M^{-1} cm^{-1} for RuphenS12 and RuphenS8 respectively. It is known that phenanthroline ligands give slightly higher molar absorptivities compared to bipyridine.[39-41] RuSconj has a larger singlet MLCT molar absorptivity at 21000 M^{-1} cm^{-1} due to the increased conjugation, however it is lower than for the [Ru(tris-4,4'-(1-ethynyl-4-thioacetate benzene)-2,2'-bipyridine)]$^{2+}$ (44000 M^{-1} cm^{-1}), which is expected.[37] As for the complexes RuS1, RuS6 and RuS12, all complexes have a Metal Centre (MC) (d-d) absorption at 430 nm and singlet MLCT (d – π*) around 240 nm. The bis-bipyridine complexes have a sharp Ligand Centre (LC) (π - π*) state at 290 nm, whereas the bis-phenanthroline complexes have the LC absorption at 260 nm, blue-shifted by 30 nm. The triplet MLCT emission has a broad band between 550 – 800 nm. RuphenS12 has a maximum emission at 630 nm. This is blue shifted by 15 nm when compared to RuS12 (645 nm). A similar shift is seen when comparing RuphenS8 (625 nm) with RuS8 (635 nm). RuSconj has a maximum emission at 670 nm, similar to the tris-Sconj (680 nm).[37] This large red shift arises

from the highly conjugated system.[21] The excitation spectra at 650 nm mirror the absorbance for all the complexes with a decreased contribution of the LC excitation compared to the absorbance.

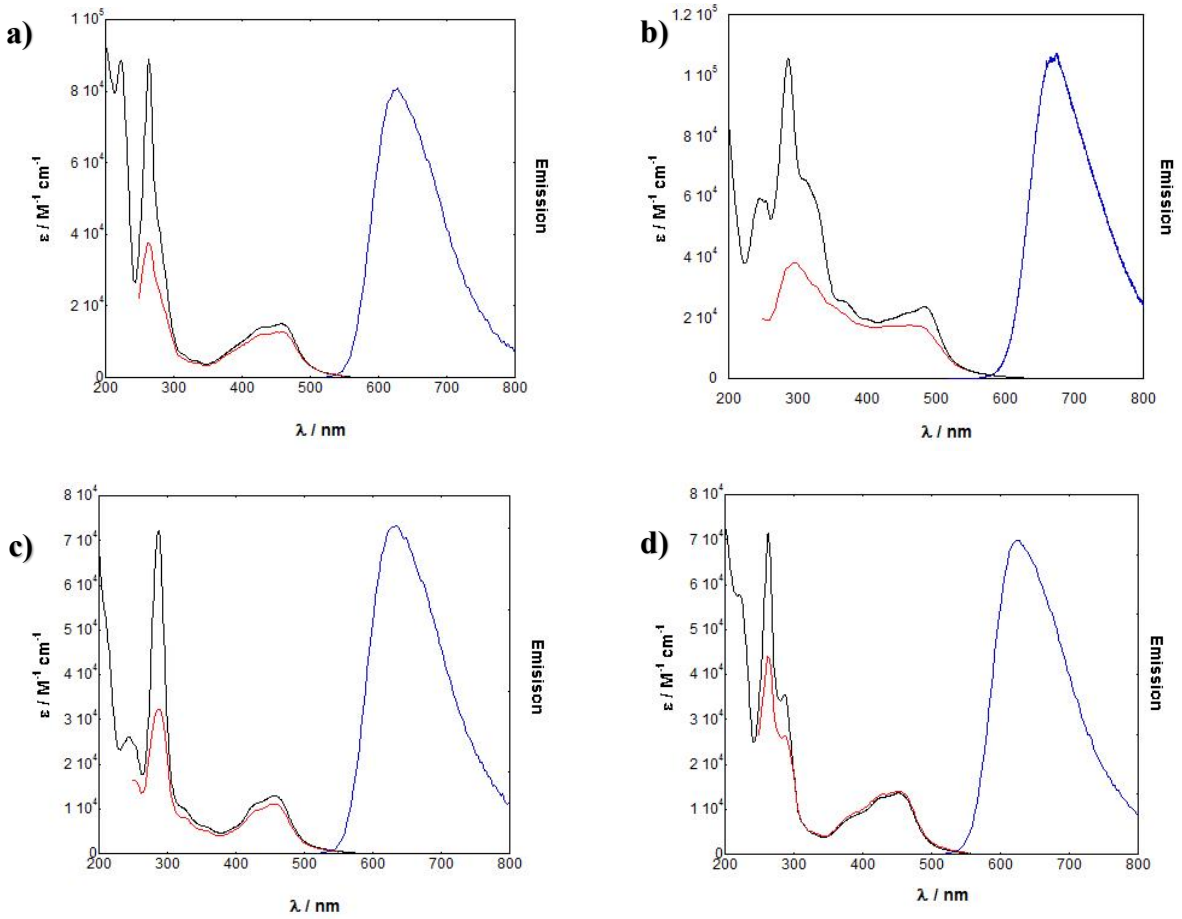

Figure 4.11: Absorption (black), luminescence emission (blue) and excitation (red) data of 7 µM RuphenS12 (a), 25 µM RuSconj (b), 8 µM RuS8 (c) and 7 µM RuphenS8 (d) in aerated water. λ_{exc} = 450 nm and λ_{det} = 640 nm.

The luminescent lifetimes of RuphenS12, RuSconj, RuS8 and RuphenS8 are 550, 440, 430 and 500 ns respectively for the solutions in aerated water (Figure 4.12). RuSconj (440 ns) and RuS8 (430 ns) have similar lifetimes to RuS1 (420 ns) and $Ru(bpy)_3Cl_2$ (380 ns). This is because they all have similar bis-bipyridine structures. This shows that the high conjugation of RuSconj does not have a large contribution to the luminescent lifetime. Both of the bis-phenanthroline complexes show an increase in lifetime when compared to the bis-bipyridine sister complexes. RuphenS12 (550 ns) has a 2-fold increase in lifetime when compared to

RuS12 (280 ns) and RuphenS8 (500 ns) sees a 20% increase when compared to RuS8 (420 ns). It is know that phenanthroline ligands lead to complexes with longer lifetimes than bipyridine.[17] RuphenS12 has a ten times larger increase in lifetime than RuphenS8. This shows that RuphenS12 has a more stable triplet MLCT energy level due to a better combination of ligands. The quantum yields of all complexes are approximately 3%, which is slightly higher than that of RuS1, RuS6 and RuS12 (2%).

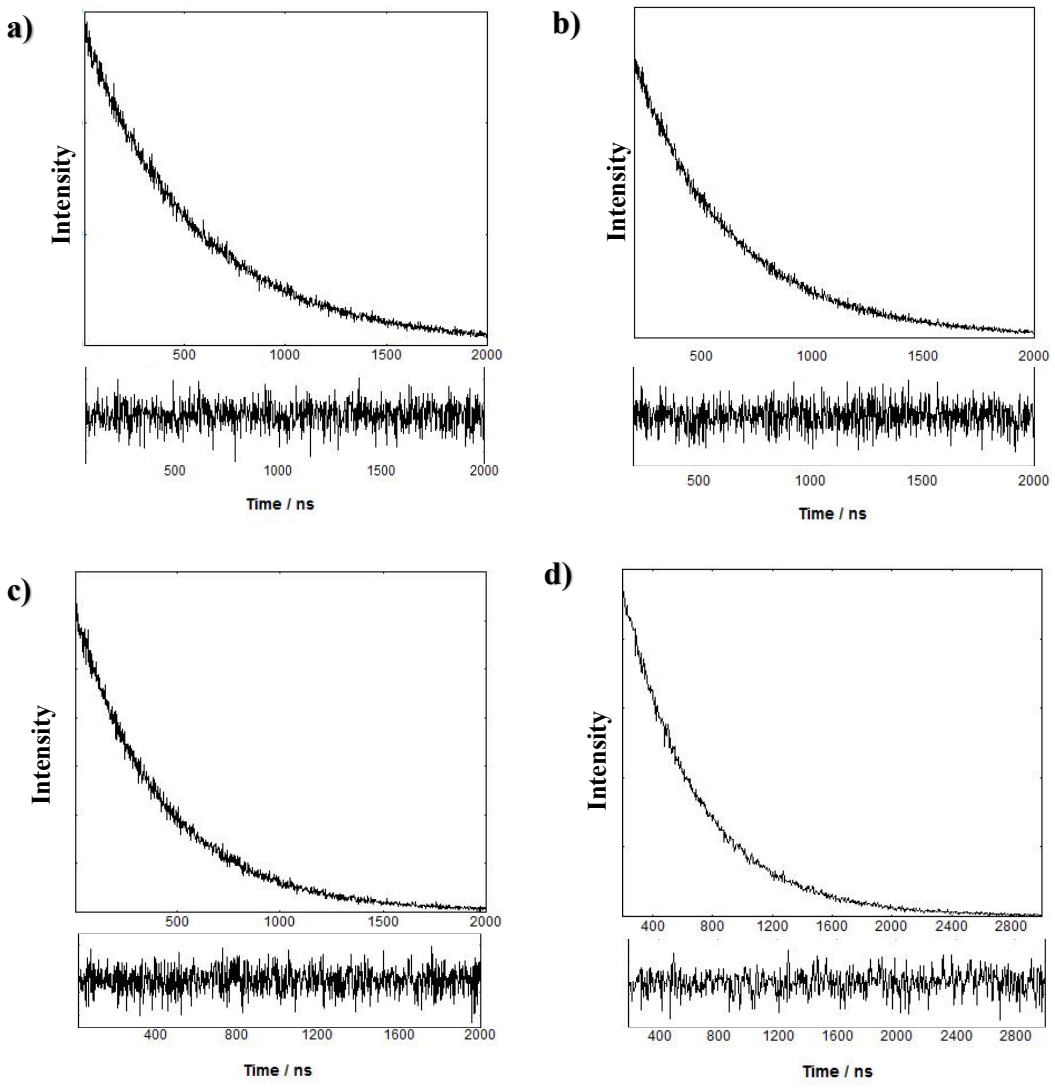

Figure 4.12: Luminescent lifetime decay (top) and fitting (bottom) of RuphenS12 (a), RuSconj (b), RuS8 (c) and RuphenS8 (d). λ_{exc} = 450 nm (480 nm for RuSconj) and λ_{det} = 650 nm (680 nm for RuSconj). X^2 is fitted between 1.0 and 1.2 for all lifetimes.

It is shown that all four complexes have enhanced photophysical properties when compared to RuS1, RuS6 and RuS12. When comparing to the literature, the lifetimes show enhancement compared to some similar compounds - $[Ru(bpy)_2(4,4'\text{-distryly-}2,2'\text{-bipyridine})]^{2+}$ has a lifetime of 300 ns in water and $[Ru(bpy)_2(phen)]^{2+}$ has a lifetime of 400 ns.[42, 43] However the more π–conjugated systems, using groups such as pyrene, are achieving lifetimes greater than 1 μs. Zhao *et al.* have demonstrated lifetimes of 2.4 and 9.2 μs for $[Ru(bpy)_2(3\text{-phenylethynyl-}1,10\text{-phenanthroline})]^{2+}$ and $[Ru(bpy)_2(3\text{-pyrene-}1,10\text{-phenanthroline})]^{2+}$ respectively.[43] McFarland *et al*. show lifetimes of 1.3 and 0.9 μs for $[Ru(bpy)_2(L)]^{2+}$ and $[Ru(phen)_2(L)]^{2+}$ respectively, where L is a ligand based on extended conjugation of 1,10-phenanthroline.[44] Although these groups have long lifetimes, the high conjugation makes them bulky and rigid, causing inefficient packing.

4.2.4 Influence of surfactant on properties of the metal complex

The photophysical properties of the interaction of the complexes with surfactant were studied. Solutions of RuphenS12, RuSconj, RuS8 and RuphenS8 were dissolved in a 150 μM suspension of Zonyl FSA in aerated water to form 7, 25, 8 and 7 μM solutions respectively.

The absorption spectra and molar absorptivity for all of the complexes are similar to without surfactant, showing that the surfactant does not affect the position or viability of the MLCT (Figure 4.13). Small blue-shifts in emission maximum occur for RuphenS12 and RuSconj from 630 and 670 to 635 and 680 nm respectively. RuphenS8 has a 10 nm red-shift from 625 to 615 nm. RuS8 does not undergo any shifting in the presence of surfactant. For all the complexes there is a slight increase in quantum yield when surfactant is present. The excitation at 650 nm mirrors the absorption spectrum with a decrease in LC contribution than compared to the absorption, however the LC has a larger contribution than when surfactant is

not present. This suggests that the increase in luminescence emission and quantum yield in the presence of surfactant is due to an increase in contribution of the LC band to the emission.

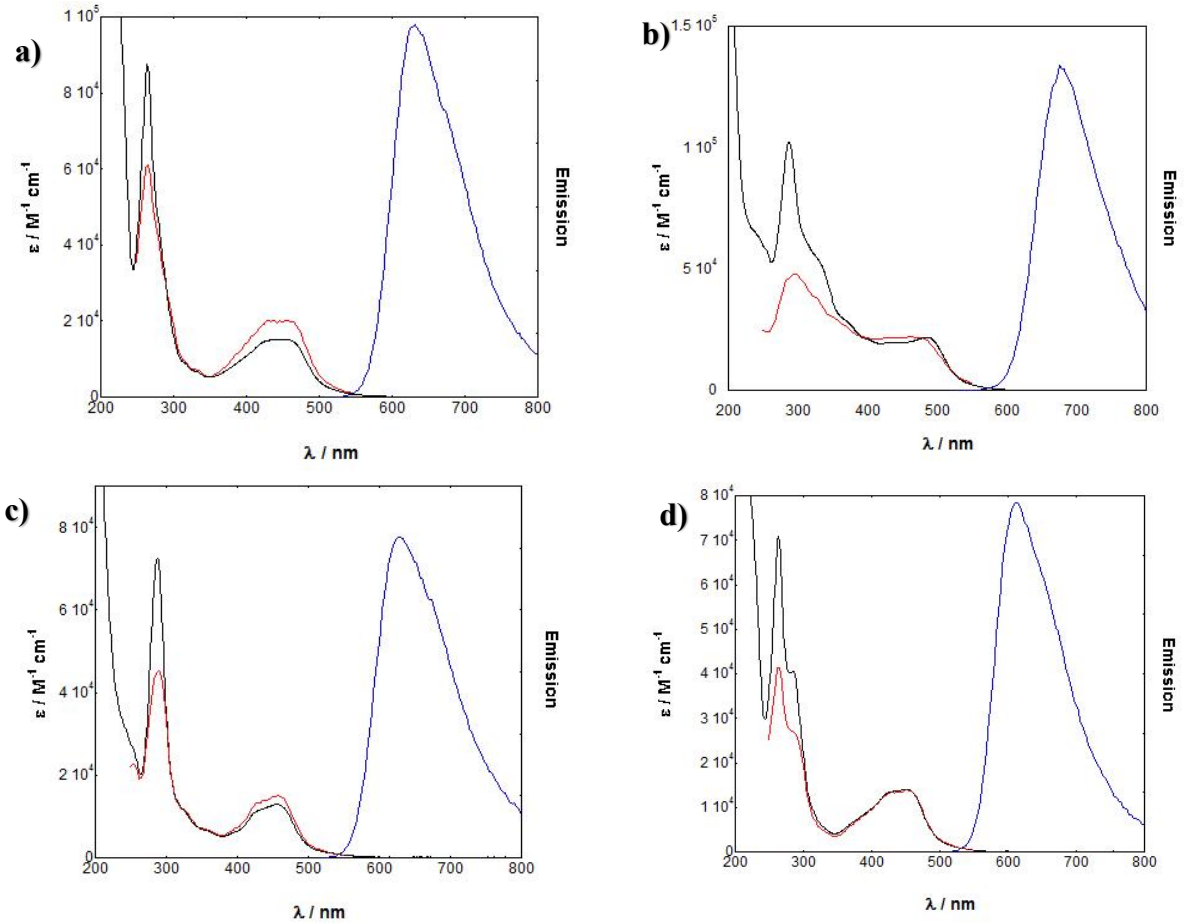

Figure 4.13: Absorption (black), luminescence emission (blue) and excitation (red) data of 7 µM RuphenS12 (a), 25 µM RuSconj (b), 8 µM RuS8 (c) and 7 µM RuphenS8 (d) + 150 µM Zonyl FSA in aerated water. λ_{exc} = 450 nm and λ_{det} = 640 (λ_{exc} = 480 nm and λ_{det} = 680 for RuSconj)

All four complexes see an increase in lifetime when surfactant is present (Figure 4.14). This increase in lifetime seen may be attributed to the interaction of the surfactant with the molecular complex and consequently protection from $^3O_2$ quenching (Section 3.2.4).[45-47] The increase in lifetime depends on the strength of the interaction of the complex with the surfactant. Previous studies have shown that increasing hydrophobicity of the ligands increased ruthenium complex binding to ionic and non-ionic surfactants.[45-47] RuphenS12 + Z (750 ns), RuS8 + Z (600 ns) and RuphenS8 + Z (700 ns) all see an increase in luminescent lifetime of 40% from the complexes without surfactant (550, 430 and 500 ns respectively).

This is similar to RuS12 (25% increase). This is because the strength of interaction, and thus lifetime increase, is dependent on the ligand and all four complexes have similar ligands. RuSconj sees a small increase in lifetime of 10% from 440 to 500 ns. This smaller increase can be attributed to the surfactant not interacting as strongly with the ligand due to the presence of large benzene rings.

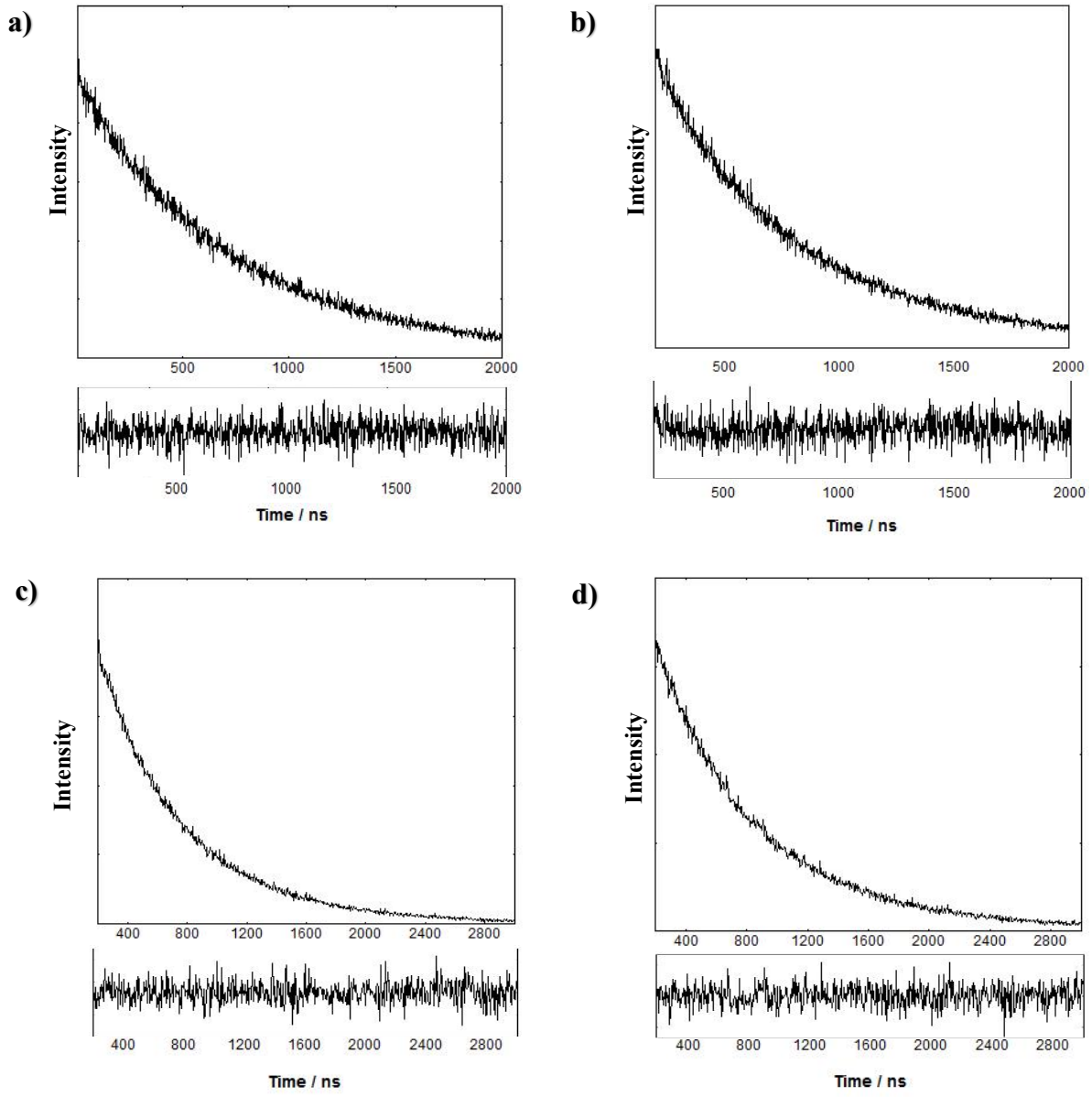

Figure 4.14: Luminescent lifetime decay (top) and fitting (bottom) of RuphenS12 (a), RuSconj (b), RuS8 (c) and RuphenS8 (d) + 150 μM Zonyl FSA in aerated water. λ_{exc} = 445 nm and λ_{det} = 650 nm (λ_{det} = 680 nm for RuSconj). X^2 is fitted between 1.0 and 1.2 for all lifetimes.

4.2.5 Gold nanoparticle coating with surfactant and metal complex

RuphenS12, RuSconj, RuS8 and RuphenS8 are attached to the AuNP through the same method as RuS1, RuS6 and RuS12 (Section 3.2.3). A fluorosurfactant, Zonyl FSA, is added to stabilise the particles, followed by the ruthenium probe (Figure 4.15).[1, 2] The ruthenium complexes attach to the AuNP via a S-Au bond formation between the thiol on the ligand and the gold atoms on the AuNP.[11, 48]

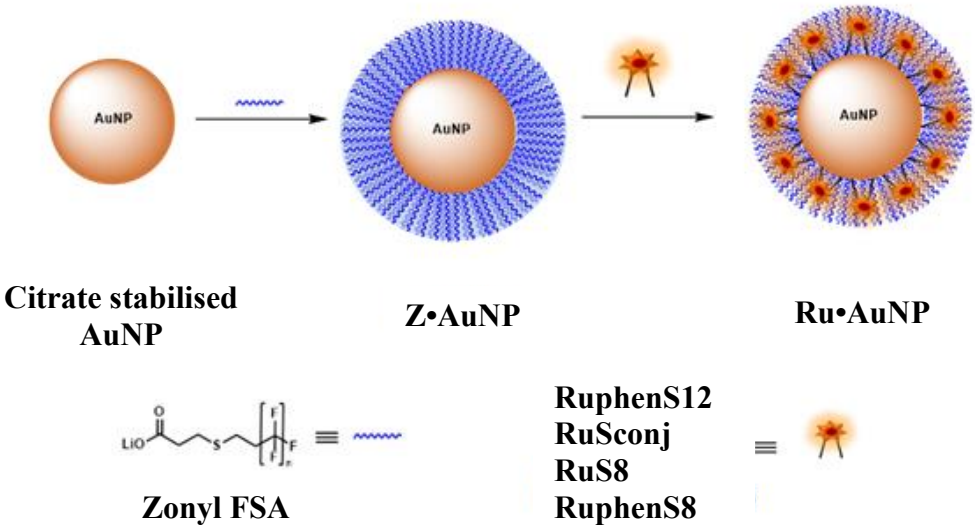

Figure 4.15: Schematic to show the attachment of fluorinated surfactant, Zonyl FSA, and ruthenium complex to AuNP13.

For the coating of Z·AuNP13, aliquots (2 µL) of 0.8 mM RuphenS12, 1.2 mM RuSconj, 0.8 mM RuS8 and 1.1 mM RuphenS8 were titrated into a 9 nM solution of Z·AuNP13 and the SPR shift was monitored by the change in λ_{max} to determine the saturation of the AuNP surface. Addition of 12 µL 0.8 mM RuphenS12, 8 µL 1.2 mM RuSconj, 12 µL 0.8 mM RuS8 and 12 µL 1.1 mM RuphenS8 to 9 nM Z·AuNP13 result in a 4 (521 nm), 4 (521 nm), 2 (519 nm) and 3 nm (520 nm) shift in λ_{max} respectively (Table 4.1, Figure 4.18). All four probes cause a similar shift in the SPR band upon addition to the AuNP and show no change following isolation *via* size exclusion chromatography. This confirmed that only the excess probe has been removed during isolation and the surface of the AuNP has not changed.

Table 4.1: Summary of AuNP13 shifts upon attachment to Zonyl, RuphenS12, RuSconj, RuS8 and RuphenS8.

	λ_{max}/ nm	Shift / nm
AuNP13	517	0
Z·AuNP13	518	1
RuphenS12·AuNP13	521	4
RuSconj·AuNP13	521	4
RuS8·AuNP13	519	2
RuphenS8·AuNP13	520	3

Analysis of the elemental composition of the nanoparticles by inductively coupled plasma mass spectrometry (ICP-MS) reveal a Ru:Au ratio for each of the complexes. The ratio for RuphenS12•AuNP13, RuS8•AuNP13 and RuphenS8•AuNP13 is 1:160, suggesting 600 ruthenium probes per AuNP13. This coating is similar to what was seen for RuS1, RuS6 and RuS12. RuSconj•AuNP13 however has a lower ration of 1:250, suggesting only 400 ruthenium probes per AuNP13. This can be attributed to less close packing of the complex due to the rigidity of the highly conjugated linear legs.

Transmission Electron Microscopy (TEM) and Dynamic Light Scattering (DLS) studies show that upon coating with the ruthenium complex there is little change in size. Images of the nanoparticles by TEM show monodispersed, uniform NPs with estimated diameter from the image of 17 nm (Figure 4.16). DLS results show the number distribution to be around 20 nm (Table 4.2).

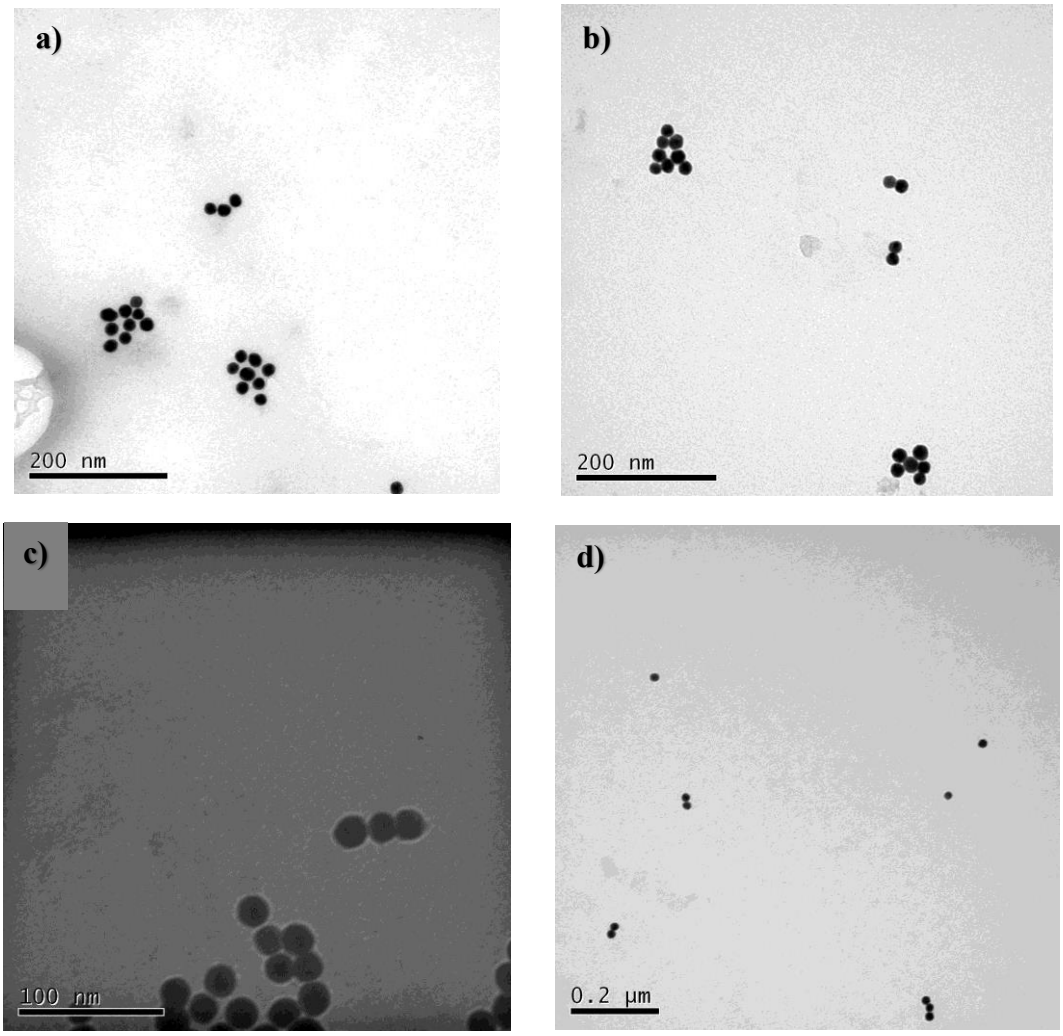

Figure 4.16: TEM images of RuphenS12·AuNP13 (a), RuSconj·AuNP13 (b), RuS8·AuNP13 (c) and RuphenS8·AuNP13 (d). Images are taken on the Jeol 1200 EX TEM.

Table 4.2: Dynamic Light Scattering of AuNP13 in water.

	Number distribution / nm	Intensity distribution / nm	PDI
RuphenS12•AuNP13	17 ± 5	81 ± 52	0.3
RuSconj•AuNP13	20 ± 7	96 ± 65	0.3
RuS8•AuNP13	21 ± 6	81 ± 64	0.4
RuphenS8•AuNP13	20 ± 7	82 ± 64	0.3

X-ray photoelectron spectroscopy (XPS) was used to characterise the surface of the nanoparticle and show that the ruthenium complex was attached to the AuNP (Table 4.3). The four coated AuNP13 were dried onto a silicon wafer and examined for the presence of gold, ruthenium and fluorine to detect the presence of the AuNP, ruthenium complex and

fluorosurfactant respectively, and sulfur to analyse attachment of the ruthenium complex to AuNP.

Table 4.3: XPS data analysis of RuphenS12•AuNP13, RuSconj•AuNP13, RuS8•AuNP13 and RuphenS8•AuNP13.

	Literature / eV	RuphenS12 •AuNP13 / eV	RuSconj •AuNP13 / eV	RuS8 •AuNP13 / eV	RuphenS8 •AuNP13 / eV
Au 4f 7/2	84	84.0	84.0	84.0	84.0
Au 4f 5/2	88	87.7	87.7	87.7	87.8
S 2p 3/2	164	161.9	162.1	161.6	161.7
S 2p 1/2	165	163.1	163.1	162.8	162.8
Ru 3d 5/2	280	281.3	281.2	281.3	280.9
Ru 3d 3/2	284	285.3	284.9	285.3	285.0
C 1s	285	285.0	284.9	284.7	285.0
C 1s (F)	292	291.5	291.4	291.6	291.5
Ru 3p 3/2	461	462.6	462.9	462.9	462.6
Ru 3p 1/2	483	482.6	X	485.2	485.0
F 1s	686	686.0	686.1	685.8	686.0

For all coated AuNP, all peaks are present for the examined elements (Appendix). They are slightly shifted from the accepted values which can be caused by the oxidation state of the element and the local chemical and physical environment.[49, 50] The peaks for ruthenium are weak but present. The data is similar to the XPS for RuS1•AuNP13, RuS6•AuNP13 and RuS12•AuNP13 (Section 3.2.3), showing the presence of the complex and fluorosurfactant (Appendix). From the S 2p peaks, it is clear that there is a mixture of bound and unbound sulfur, as well as the presence of sulfoxide. From analysing the intensity of the Ru 3d and 3p peaks, it appears that there is greater coating of ruthenium complex for the RuS8•AuNP13 and RuphenS8•AuNP13 (Figure 4.17) which agrees with the ICP-MS data (Section 4.5.1). RuSconj•AuNP13 has a very weak peak at 462.9 eV for the Ru 3p 3/2 and no peak is seen at 483 eV for the Ru 3p 1/2.

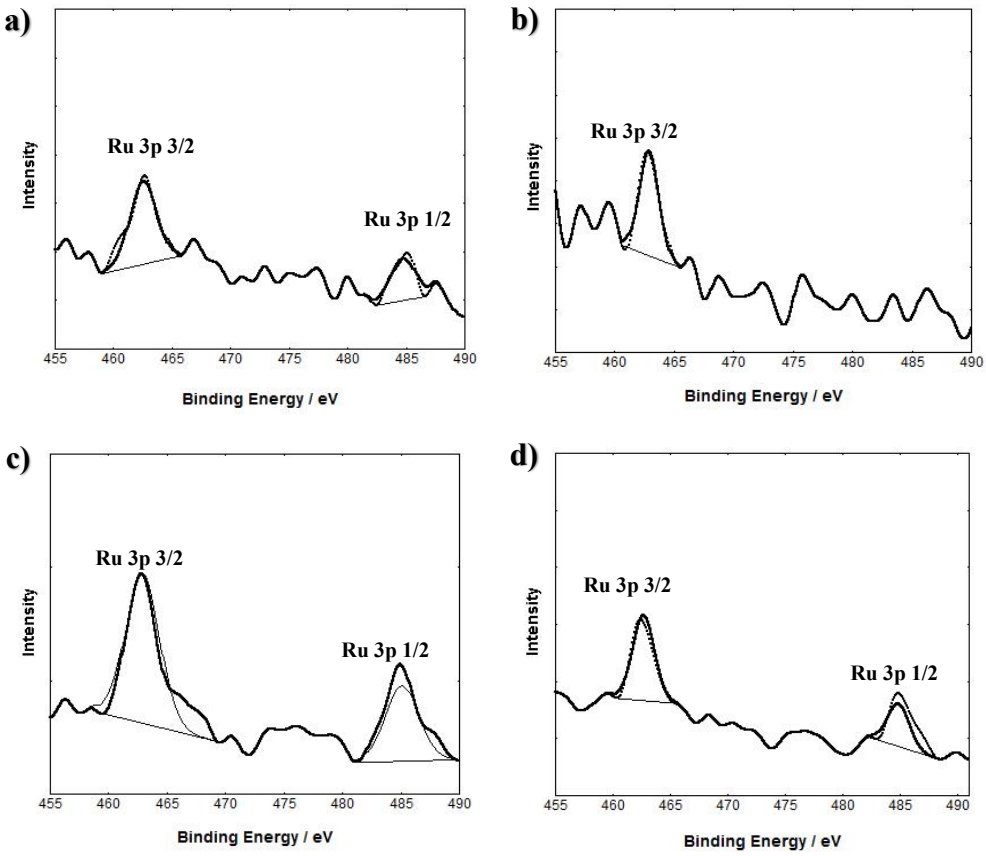

Figure 4.17: XPS data showing the Ru 3p peaks for RuphenS12•AuNP13 (a), RuSconj•AuNP13 (b), RuS8•AuNP13 (c) and RuphenS8•AuNP13 (d).

4.2.6 Luminescent studies of ruthenium probe in the presence of the fluorosurfactant and functionalised gold nanoparticle

Absorption and steady state and time-resolved emission spectroscopy were used to characterise the luminescence properties of the probes attached to AuNP. The absorption spectra for all four nanoprobes shows the SPR of the AuNP13 (Figure 4.18, Table 4.1). The excitation spectrum for the luminescence at 650 nm (RuSconj•AuNP13 at 680 nm) correlates to the absorption of the ruthenium complexes, with a maximum at 450 nm (480 nm for RuSconj•AuNP13). This shows that the emission is arising from excitation of the ruthenium probe and not the AuNP.

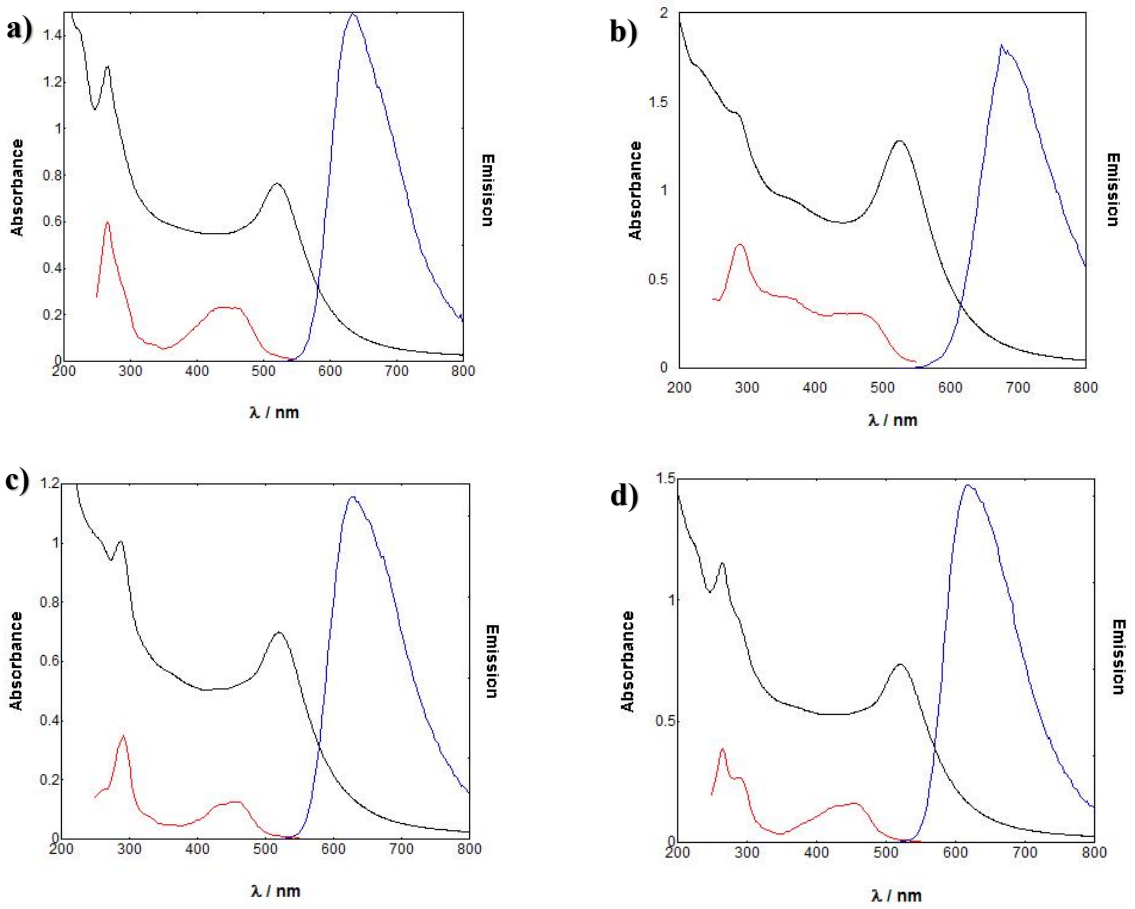

Figure 4.18: Absorption (black), luminescence emission (blue) and excitation (red) data of 4.5 nM RuphenS12•AuNP13 (a), 4.5 nM RuSconj•AuNP13 (b), 4.5 nM RuS8•AuNP13 (c) and 4.5 nM RuphenS8•AuNP13 in aerated water.

The luminescence spectra (Figure 4.19) and lifetime (Figure 4.20) of the nanoprobes were recorded and compared with the molecular complexes in solution, in the presence and absence of the Zonyl surfactant.

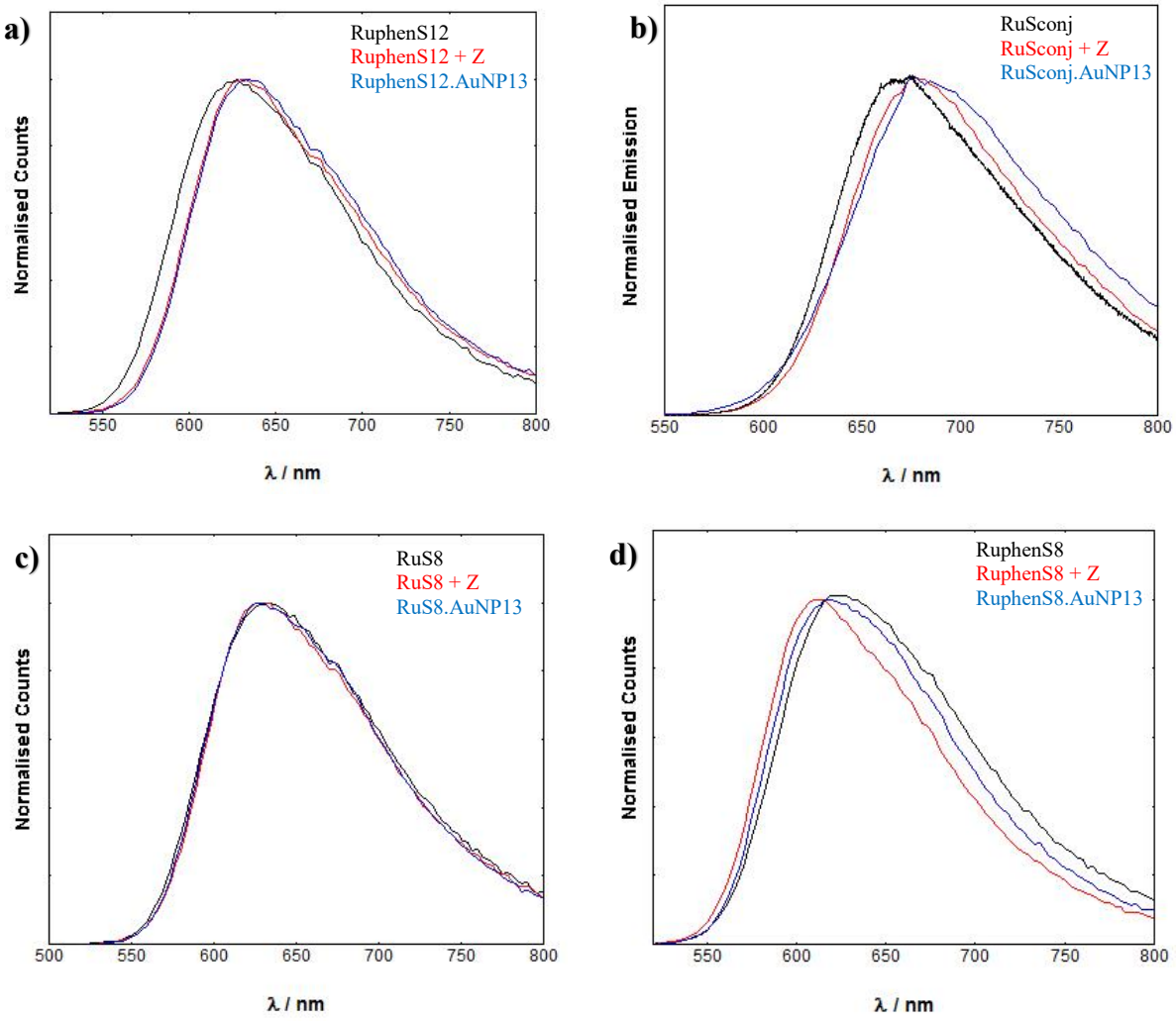

Figure 4.19: Luminescence emission data of RuphenS12, RuphenS12 + Z and RuphenS12·AuNP13 (a), RuSconj, RuSconj + Z and RuSconj·AuNP13 (b), RuS8, RuS8 + Z and RuS8·AuNP13 (c) and RuphenS8, RuphenS8 + Z and RuphenS8·AuNP13 (d). λ_{exc} = 450 nm (480 nm for RuSconj) and λ_{det} = 650 nm (480 nm for RuSconj). The spectra are taken from 550 – 800 nm.

For RuS8 no significant shift in λ_{max} is seen when in the presence of Zonyl surfactant and when attached to AuNP13. This is similar to RuS1, RuS6 and RuS12. The other ruthenium probes do however shift slightly. RuphenS12 and RuSconj see small blue-shifts in the emission of 5 nm when surfactant is present however no further shift is seen when attached to AuNP13. This shows that there is negligible effect on the position of the triplet MLCT upon probe attachment to AuNP13. RuphenS8 undergoes a 10 nm red-shift in the presence of surfactant, followed by a 5 nm blue-shift when attached to AuNP13. This is most likely due to

the interaction of the molecular probe and the surfactant being minimised upon attachment to the AuNP.

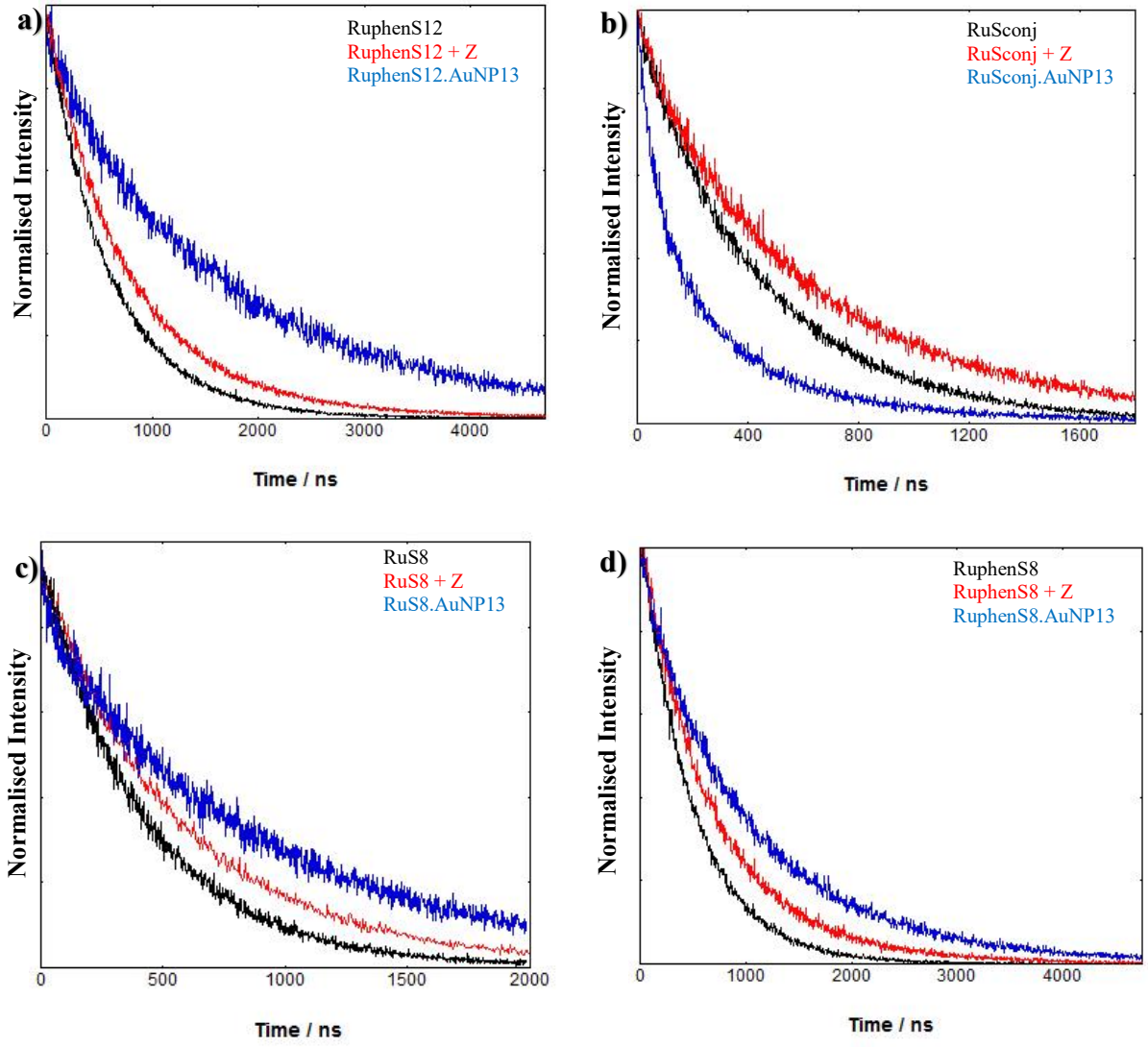

Figure 4.20: Normalised luminescence lifetime data of RuphenS12, RuphenS12 + Z and RuphenS12·AuNP13 (a), RuSconj, RuSconj + Z and RuSconj·AuNP13 (b), RuS8, RuS8 + Z and RuS8·AuNP13 (c) and RuphenS8, RuphenS8 + Z and RuphenS8·AuNP13 (d). λ_{exc} = 445 nm and λ_{det} = 650 nm (680 nm for RuSconj). X^2 is fitted between 1.0 and 1.2 for all lifetimes.

The luminescent lifetimes of the coated AuNP13 are summarised in Table 4.4 and comparison of the lifetime decays are presented to illustrate the changes in lifetime (Figure 4.20).

Table 4.4: Luminescent lifetimes of the four probes in water with and without surfactant and attached to AuNP13. The percentage change in lifetime compared to the free probe is presented. The luminescent lifetimes were fitted with a X^2 between 1.0 and 1.2.

	τ / ns	%
RuphenS12	550	0
RuphenS12 + Z	750	40
RuphenS12•AuNP13	1700	200
RuSconj	440	0
RuSconj + Z	500	10
RuSconj•AuNP13	370	-20
RuS8	430	0
RuS8 + Z	600	40
RuS8•AuNP13	850	100
RuphenS8	500	0
RuphenS8 + Z	700	40
RuphenS8•AuNP13	1100	120

Previous studies have found that thiol-functionalised ruthenium complexes show enhancement when attached to AuNP surface.[1] When comparing photophysical properties of RuS1 (short), RuS6 (medium) and RuS12 (long chain), it was found that the greater the distance from the AuNP, the greater the enhancement in luminescent lifetime (Section 3.2.4). This enhancement is seen for most of the optimised probes (Table 4.4). The enhancement is suspected to arise from interaction of the AuNP electromagnetic field with the luminescent probe dipole as well as simultaneous quenching from electron transfer to the surface of the AuNP.[51] RuSconj•AuNP13 however has a 20% decrease in lifetime (440 to 370 ns). The quenching arises from the presence of the AuNP13 only; in the presence of Zonyl surfactant there is a slight increase in lifetime (440 to 500 ns). Due to the highly conjugated and electron rich ligand of RuSconj, this quenching can be attributed to more efficient electron and energy

transfer to the AuNP surface and thus an increase in non-radiative decay of the excited state ($2.2 \rightarrow 2.6 \times 10^6$ s^{-1}) (Table 4.5).

Table 4.5: Radiative and non-radiative contribution of the decay rate for ruthenium molecular probes and nanoprobes. τ_N is the natural lifetime, k is the overall decay rate, k_r is the radiative decay rate and k_{nr} is the non-radiative decay rate. The radiative and non-radiative contributions are calculated from the quantum yield, Φ, and luminescence lifetime, τ (Equation 3.3 – 3.6).[52, 53]

	Φ	**τ / s (x 10^{-7})**	**τ_N / s (x 10^{-6})**	**k / s^{-1} (x10^6)**	**k_r / s^{-1} (x10^5)**	**k_{nr} / s^{-1} (x10^6)**
RuphenS12•AuNP13	0.30	17.0	5.7	0.6 (0.588235)	1.8 (1.754386)	0.41 (0.411765)
RuphenS12	0.03	5.5	18.3	1.8 (1.818182)	0.55 (0.546448)	1.8 (1.763636)
RuSconj•AuNP13	0.05	3.7	7.4	2.7 (2.702703)	1.4 (1.351351)	2.6 (2.567568)
RuSconj	0.03	4.4	14.7	2.3 (2.272727)	0.68 (0.680272)	2.2 (2.204545)
RuS8•AuNP13	0.10	8.5	8.5	1.2 (1.176471)	1.2 (1.176471)	1.1 (1.058824)
RuS8	0.04	4.3	10.8	2.3 (2.325581)	0.93 (0.925926)	2.2 (2.32558)
RuphenS8•AuNP13	0.20	11.0	5.5	0.9 (0.909091)	1.8 (1.818182)	0.73 (0.727273)
RuphenS8	0.04	5.0	12.5	2.0 (2.0)	0.8 (0.8)	1.9 (1.92)

It was seen that RuS8 has improved photophysical properties than when compared to RuS12 due to the lack of oxygen on the bipyridine ring (Section 4.2.3). RuS12•AuNP13 was shown to have a 70% increase in luminescent lifetime when compared to RuS12 (280 → 480 ns) and RuS8•AuNP13 has a 2-fold increase when compared to RuS8 (430 → 850 ns). The increase is similar for the two probes although RuS8 is closer to the AuNP surface than RuS12, so a larger enhancement for RuS12 would be expected, however it is not seen. However, when analysing the radiative components this is seen; the radiative decay for RuS12 increases by 3-fold ($0.71 \rightarrow 1.9 \times 10^6$ s^{-1}) (Section 3.2.4) whereas for RuS8 it only increases by 30% ($0.93 \rightarrow 1.2 \times 10^6$ s^{-1}) (Table 4.5). This arises from the large quantum yield increase upon attachment to AuNP of five times for RuS12 (2 → 9 %) and only double for RuS8 (4 → 10 %).

RuphenS12 sees a large 3-fold enhancement in lifetime when attached to AuNP13 (550 → 1700 ns). This increase arises from a 3-fold increase in radiative decay (0.55 → 1.8 x 10^6 s^{-1}) and 3-fold decrease in non-radiative decay (1.8 → 0.41 x 10^6 s^{-1}) (Table 4.5) due to a ten times increase in quantum yield (3 → 30 %). This large increase is due to the bis-phenanthroline system and the optimised distance from the AuNP. The long chain, RuS12, was shown to have a greater enhancement in luminescent lifetime upon attachment to AuNP (70 %) compared to the shorter chains RuS6 (40 %) and RuS1 (20 %). The bis-phenanthroline systems are known to have a greater lifetime than the bis-bipyridine. There are few examples in the literature of ruthenium bis-phenanthroline, mono-bipyridine complexes with µs lifetimes. $Ru(phen)_2(bpyC10)$ has a luminescent lifetime of 1.1 µs in Tris or 900 ns in ethanol and $[Ru(phen)_3]^{2+}$ increases from 500 ns to 2.5 µs when intercalated with DNA.[54, 55] To gain longer lifetimes, higher conjugated systems must be used, such as $Ru(dpp)_2$(bpy-OH) which has a lifetime of 5.7 µs in acetonitrile[56] and Ru(4,4'-dmbp)(4,4'-methyl-2,2'-bpy) which has a lifetime of 4 µs in deaerated acetonitrile.[57] The RuphenS12•AuNP13 nanoprobe shows a long lived lifetime for these types of ruthenium complexes which is competitive with the literature.

As both RuS8 and RuphenS12 have been shown to have a greater enhancement when attached to AuNP13 compared to RuS12, a long lifetime was expected for RuphenS8•AuNP13. Although we do see an increase in enhancement (120%) it is only slightly higher than for the bis-bipyridine nanoprobe, RuS8•AuNP13 (100%) and not as high as RuphenS12 (200%). This is most likely because the RuphenS8 photoactive centre is closer to the AuNP surface than RuphenS12, so undergoes a greater quenching. We do however see a larger enhancement in quantum yield, where RuphenS8•AuNP13 has a quantum yield of 20% and RuS8•AuNP13 has a much lower value of 10%.

4.3 Conclusion

Four novel thiol-functionalised ruthenium complexes have been synthesised and their photophysics characterised. All four complexes show enhanced molecular properties compared to RuS1, RuS6 and RuS12. RuphenS12•AuNP13, RuS8•AuNP13 and RuphenS8•AuNP13 show enhanced nanoprobe properties. RuphenS12•AuNP13 has a long lifetime of 1.7 μs, four times that of RuS12•AuNP13, which is competitive with tris-phenanthroline ruthenium complexes. This probe is optimised for applications in imaging due to its high quantum yield and long lifetime. It was shown through the development of a new ligand, S8, that the short lifetime of RuS6 and RuS12 are due to quenching from the oxygen adjacent to the bipyridine ring.

4.4 Summary of data

Table 4.6: Photophysical characterisation of RuphenS12, RuSconj, RuS8 and RuphenS8 in solution with and without Zonyl FSA surfactant and attached to AuNP13.

	UV-Vis λ_{max} / nm (ε / $M^{-1}cm^{-1}$)	Emission λ_{max} / nm	τ / ns	Φ / %
RuphenS12	457 (15000), 430 (sh), 263 (88000), 222 (88000)	630	550	3
RuphenS12 + Z	455 (15000), 264 (88000)	635	750	4
RuphenS12•AuNP13	521	635	1700	30
RuSconj	481 (21000), 320 (sh), 288 (87000), 260 (60000)	670	440	3
RuSconj + Z	481 (21000), 320 (sh), 288 (87000)	680	500	3
RuSconj•AuNP13	521	680	370	5
RuS8	456 (13000), 430 (sh), 287 (72000), 244 (26000)	635	430	4
RuS8 + Z	465 (13000), 430 (sh), 288 (72000)	635	600	5
RuS8•AuNP13	519	635	850	10
RuphenS8	452 (16000), 420 (sh), 390(sh), 286 (42000), 263 (82000), 230 (sh)	625	500	4
RuphenS8 + Z	450 (16000), 420 (sh), 390 (sh), 285 (44000), 263 (70000)	615	700	4
RuphenS8•AuNP13	520	620	1100	20

Table 4.7: DLS sizing and zeta potential data for the AuNP.

	DLS sizing / nm (PDI)	ζ / mV
RuphenS12•AuNP13	17 ± 5	- 42 ± 7
RuSconj•AuNP13	20 ± 7	- 40 ± 8
RuS8•AuNP13	21 ± 6	- 51 ± 7
RuphenS8•AuNP13	20 ± 7	- 47 ± 6

4.5 Experimental

4.5.1 Materials

Starting materials were purchased from Sigma Aldrich or Fisher Scientific.

4.5.2 Synthesis of gold nanoparticles

AuNP13 was synthesised as previously discussed (Section 3.5.2).

4.5.3 Ruthenium molecular complexes

RuphenS12, RuS8 and RuphenS8 were synthesised with the chloride counterion and the final solutions to be used for coating were prepared in methanol as 0.77, 0.76 and 1.1 mM solutions respectively. For RuSconj, the complex was synthesised with the ammonium hexafluorophosphate counterion and it was exchanged for the chloride using Dowex 1 X 8 ion exchange chromatography. The final solution was 3.7 mM in methanol. It was sonicated with NH_4OH to produce a 1.2 mM solution.

4.5.3.1 Synthesis of RuphenS12

4,4'-Di-(5-lipoamide-1-pentoxy)-2,2'-bipyridine was synthesised as previously discussed (Section 3.5.3.3).

$Ru(phen)_2Cl_2$[58] Ruthenium trichloride (0.8 g, 3 mmol), 1,10 phenanthroline (1.1 g, 6 mmol) and lithium chloride (0.8 g, 20 mmol) were dissolved in 5 mL degassed DMF and refluxed under N_2 for 6 hours. Acetone (20 mL) was added and it was cooled to 0 – 5 °C for 24 hours. It was filtered and washed with water (200 mL) and diethyl ether (100 mL) to produce a black compound (0.7 g, 1.3 mmol, 44%). δ_H (300 MHz; DMSO): 7.34 (2H, dd, *5.2, 8.4*, Hb'); 7.76 (2H, d, *5.2*, Ha'); 8.85 (2H, d, *8.4*, Hc'); 8.25 (6H, m, Hb, Hf, Hf'); 8.73 (2H, d, *7.3*, Hc); 10.28 (2H, d, *4.6*, Ha). m/z (TOF MS ES^+) 497.0 ($[M\text{-}Cl]^+$): 491.0

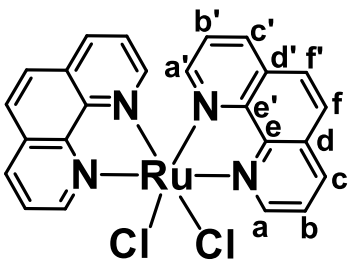

(6%); 492.0 (1%); 493.0 (4%); 494.0 (20%); 495.0 (25%); 496.0 (50%); 497.0 (100%); 498.0 (25%); 499.0 (70%); 500.0 (10%); 501.0 (8%). UV-VIS λ_{max} / nm (DCM) (ε / $M^{-1}cm^{-1}$): 545 (12400); 268 (70000); 228 (50000). Data agreed with previously published.

RuphenS12 Synthesis adapted from reference.[59] $Ru(phen)_2Cl_2$ (49 mg, 0.09 mmol) and 4,4'-dimethyllipoamide-2,2'-bipyridine (100 mg, 0.14 mmol) are refluxed overnight in 40 mL ethanol. The solvent was removed *in vacuo* and the resulting red solid was dissolved in 10 mL of water, cooled to 5 °C and filtered. The solvent was removed and a neutral alumina plug was performed in 2% MeOH in DCM. The product was washed through with MeOH and an LH20 column was performed in MeOH. The solvent was removed *in vacuo* to produce a red solid chloride salt (28 mg, 0.022 mmol, 25%). δ_H (300 MHz; MeOD): 1.27 (4H, m, H4); 1.48 (16H, m, H9, H10, H15, H16); 1.72 (6H, m, H8, H18'); 2.05 (4H, t, *7.2*, H13); 2.26 (2H, tt, *5.5, 11.1*, H18); 2.90 (4H, m, H19); 3.10 (4H, t, *6.3*, H11); 3.36 (2H, dt, *1.6, 3.3*, H17); 4.13 (4H, dt, *6.1, 1.5*, H7); 6.85 (2H, dd, *2.6, 6.5*, H5); 7.35 (2H, d, *6.5*, H6); 7.55 (2H, dd, *5.3, 8.2*, Hb'); 7.82 (2H, dd, *5.3, 8.2*, Hb); 7.88 (2H, dd, *1.1, 5.3*, Ha'); 8.19 (6H, m, H3, Hf, Hf'); 8.31 (2H, dd, *1.1, 5.3*, Ha); 8.52 (2H, dd, *1.1, 8.2*, Hc'); 8.65 (2H, dd, *1.1, 8.2*, Hc). δ_C (100 MHz; MeOD): 22.9 (C9); 25.4 (C15); 28.0 (C8); 28.5 (C14); 28.6 (C10); 34.3 (C16); 35.5 (C13); 38.0 (C19); 38.6 (C11); 40.0 (C18); 56.3 (C17); 69.5 (C7); 111.5 (C3); 114.1 (C5); 125.9 (Cb'); 126.0 (Cb); 128.0 (Cf'); 128.1 (Cf); 131.0 (C4); 136.4 (Cc'); 136.5 (Cc); 147.9 (Cd'); 148.0 (Cd); 152.0 (Ca'); 152.3 (Ca); 152.5 (C6); 158.4 (C2); 166.9 (Ce, Ce'); 174.5 (C12). Assignments by COSY and HSQC. m/z (TOF MS ES^+) 598.2 ($[M-2Cl]^{2+}$): 595.2 (7%); 595.7 (5%); 596.2 (6%); 596.7 (20%): 597.2

(40%); 597.7 (60%); 598.2 (100%); 598.7 (60%); 599.2 (70%); 599.7 (30%); 600.2 (15%); 600.7 (5%). All photophysical characterisation is performed as a 8 μM solution in water as the chloride salt. UV-VIS λ_{max} / nm (ε / $M^{-1}cm^{-1}$): 457 (15000), 430 (sh), 263 (88000), 222 (88000). Emission λ_{max}: 630 nm. τ: 550 ns. Φ: 3%. In the presence of 150 μM Zonyl FSA surfactant. UV-VIS λ_{max} / nm (ε / $M^{-1}cm^{-1}$): 455 (15000), 264 (88000). Emission λ_{max}: 635 nm. τ: 750 ns. Φ: 4%. Attached to AuNP13. UV-VIS λ_{max} / nm: 521. Emission λ_{max}: 640 nm. τ: 1700 ns. Φ: 30%.

4.5.3.2 Synthesis of RuSconj

4,4'-Diacetylene-2,2'-bipyridine[60] Dry THF (50 mL) was degassed with N_2 for 15 mins and

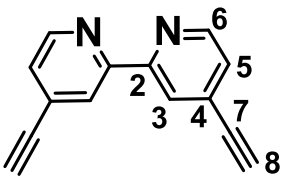

added to 4,4'-dibromo-2,2'-bipyridine (1191 mg, 3.8 mmol), copper iodide (97 mg, 0.5 mmol) and dichlorobis(triphenylphosphine) palladium (91 mg, 0.1 mmol) under N_2. Dipropylamine (20 mL, 142 mmol) and ethylenetrimethylsilane (939 mg, 9.3 mmol) were syringed in and left to stir at rt for 24 hours. The mixture was quenched with water (50 mL) and extracted with DCM (3 x 50 mL). The combined organic layers were washed with sodium thiosulphate (3g in 100 mL water) and the solvent removed *in vacuo*. The solid was dissolved in hexane:ethyl acetate (1:1 100 mL), filtered and the solvent removed *in vacuo*. The solid was dissolved in chloroform (100 mL), filtered and the solvent removed *in vacuo* to yield a yellow solid (296 mg, 1.45 mmol, 38%). δ_H (300 MHz; d_6-DMSO): 4.73 (2H, s, H8); 7.58 (2H, d, *4.4*, H3); 8.36 (2H, s, H5); 8.74 (2H, d, *4.4*, H2). δ_C (100 MHz; d_6-DMSO): 80.89 (C7); 85.94 (C8); 122.38 (C5); 126.34 (C3); 130.92 (C4); 149.93 (C6); 154.67 (C2). m/z (TOF MS ES^+) 226 ($[M+Na]^+$). Data agreed with previously published.

4-Iodo-1-thioacetate benzene[61] 4-Iodo-1-sulfonyl chloride benzene (2.58 g, 8.5 mmol) and dimethylacetamide (2.3 mL, 24.7 mmol) in DCE (10 mL) was added into zinc powder (1.97 g,

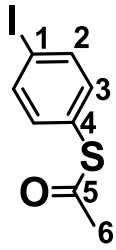

30.1 mmol) and dimethyldichlorosilane (3.5 mL, 28.8 mmol) in DCE (10 mL). It was heated at 75 °C for 4 hours and then cooled to 55 °C. Acetyl chloride (0.8 mL, 11.3 mmol) was added and left to stir for 15 mins. It was quenched with water (50 mL) and extracted with DCM (3 x 50 mL). It was dried with $MgSO_4$, filtered and the solvent removed *in vacuo*. Silica column chromatography was performed (DCM:Petroleum ether 1:4) to produce a white solid (2.08 g, 7.5 mmol, 88%). δ_H (300 MHz; $CDCl_3$): 2.45 (3H, s, H6); 7.15 (2H, d, *8.5*, H2); 7.76 (2H, d, *8.5*, H3). δ_C (100 MHz; $CDCl_3$): 30.3 (C6); 95.9 (C1); 127.8 (C4); 136.0 (C3); 138.4 (C2); 193.2 (C5). m/z (AP^+) 279 ($[M+H]^+$). Data agreed with previously published.

4,4'-Di(4-acetylene-1-thioacetatephenyl)-2,2'-bipyridine[60] Dry THF (20 mL) was degassed

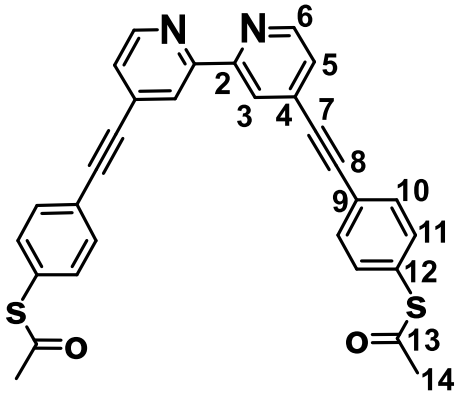

with N_2 for 15 mins and added to 4,4'-diacetylene-2,2'-bipyridine (296 mg, 1.45 mmol), 4-iodo-1-thioacetate benzene (986 mg, 3.6 mmol), copper iodide (36 mg, 0.19 mmol) and dichlorobis(triphenylphosphine) palladium (36 mg, 0.005 mmol) under N_2. Dipropylamine (6 mL) was syringed in and left to stir at rt for 24 hours. The mixture was quenched with water (50 mL) and extracted with DCM (3 x 100 mL). The combined organic layers were washed with water (50 mL), dried with $MgSO_4$ and the solvent removed *in vacuo* to produce a cream solid (90 mg, 0.18 mmol, 12%). δ_H (300 MHz; $CDCl_3$): 2.47 (6H, s, H14); 7.44 (2H, d, *1.5*, H5); 7.46 (4H, d, *8.4*, H11); 7.62 (4H, d, *8.4*, H10); 8.56 (2H, s, H3); 8.71 (2H, d, *5.0*, H6). δ_C (100 MHz; $CDCl_3$): 30.4 (C14); 88.4 (C7); 93.2 (C8); 123.3 (C3); 125.6 (C5); 129.2 (C12); 132.2 (C9); 132.5 (C10); 134.3 (C11); 149.3 (C6); 155.6 (C2); 192.3 (C13). Assignments by COSY and HSQC. m/z (TOF MS ES+): 527 (100%, $[M+Na]^+$): 527 (100%); 528 (40%); 529 (20%).

$Ru(bpy)_2Cl_2$ was synthesised as previously discussed (Section 3.5.3.1).

RuSconj Synthesis adapted from reference.[59] 4,4'-Di(4-acetylene-1-thioacetatephenyl)-2,2'-bipyridine (90 mg, 0.18 mmol) and $Ru(bpy)_2Cl_2$ (144.0 mg, 0.30 mmol) were heated to 90 °C in ethanol (100 mL) for 24 hours. It was cooled to rt then filtered. The solvent was reduced *in vacuo* (25 mL), water (35 mL) was added and it was filtered. A saturated solution of ammonium hexafluorophosphate (1 g in 2 mL MeOH) was added to produce a red precipitate. It was filtered, washed with water (100 mL), hexane (100 mL) and diethyl ether (100 mL). A silica column was performed (95% acetonitrile, 4% water, 1% saturated potassium nitrate in water, increasing up to 70% acetonitrile, 29% water, 1% saturated potassium nitrate in water). The solvent was removed from the fractions and the solid was dissolved in ethanol (5 mL) and water (35 mL). A saturated solution of ammonium hexafluorophosphate (1 g in 2 mL MeOH) was added to produce a red precipitate. It was filtered and washed with water (100 mL) and diethyl ether (100 mL) to produce a red solid hexafluorophosphate salt (61 mg, 0.05 mmol, 28%). δ_H (300 MHz; CD_3CN): 2.43 (6H, s, H14); 7.39-7.48 (6H, m, Hb, Hb', H5); 7.52 (4H, d, *8.5*, H11); 7.69 (4H, d, *8.5*, H10); 7.70-7.81 (6H, m, Ha, Ha', H6); 8.08 (4H, tdd, *1.4, 3.9, 8.1*, Hc, Hc'); 8.52 (4H, d, *8.1*, Hd, Hd'); 8.66 (2H, d, *1.4*, H3). δ_C (100 MHz; CD_3CN): 30.8 (C14); 87.6 (C7); 97.6 (C8); 123.0 (C12); 125.3 (Cd, Cd'); 127.1 (C3); 128.6 (Cb, Cb'); 129.8 (C5); 131.8 (C4); 132.9 (C9); 133.5 (C10); 135.6 (C11); 138.8 (Cc, Cc'); 152.5 (C6); 152.7 (Ca, Ca'); 157.8 (Ce, Ce'); 157.8 (C2); 194.0 (C13). Assignments by COSY and HSQC. m/z (TOF MS ES+): 1063.3 (100%, $[M\text{-}PF_6]^+$): 1057.3 (12%); 1058.3 (9%); 1059.3 (10%); 1060.3 (35%); 1061.3 (50%); 1062.3 (65%); 1063.3 (100%); 1064.3 (55%); 1065.3 (60%); 1066.3 (35%);

1067.3 (12%); 1068.3 (5%). EA: Calculated: C 43.80%, H 2.79%, N 6.13% for RuSconj + PF_6 +H_2O. Observed: C 43.76%, H 2.99%, N 6.03%. All photophysical characterisation is performed as a 25 μM solution in water as the chloride salt, formed from Dowex ion exchange. UV-VIS λ_{max} / nm (ε / $M^{-1}cm^{-1}$): 481 (21000), 320 (sh), 288 (87000), 260 (60000). Emission λ_{max}: 670 nm. τ: 440 ns. Φ: 3%. In the presence of 150 μM Zonyl FSA surfactant. UV-VIS λ_{max} / nm (ε / $M^{-1}cm^{-1}$): 481 (21000), 320 (sh), 288 (87000). Emission λ_{max}: 670 nm. τ: 500 ns. Φ: 3%. Attached to AuNP13. UV-VIS λ_{max} / nm: 521. Emission λ_{max}: 680 nm. τ: 370 ns. Φ: 5%.

4.5.3.3 Synthesis of RuS8

4,4'-Dimethylester-2,2'-bipyridine[62] Thionyl chloride (10 mL) was slowly added to a

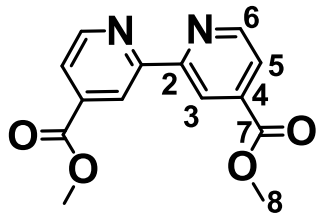

suspension of 4,4'-dicarboxylicacid-2,2'-bipyridine (1.2 g, 5.1 mmol) in MeOH (75 mL) over 5 minutes. The mixture was refluxed overnight and quenched with a saturated solution of $NaHCO_3$ (5 mL). The product was extracted with chloroform (3 x 100 mL), dried over $MgSO_4$ and recrystallized in chloroform/acetone to produce a white solid. δ_H (300 Hz; $CDCl_3$): 4.00 (6H, s, H8); 7.92 (2H, dd, *5.0, 1.6*, H6); 8.88 (2H, dd, *5.0, 0.7*, H5); 8.97 (2H, q, *0.7*, H3). Data agreed with previously published.

4,4'-Dimethylalcohol-2,2'-bipyridine[62] $NaBH_4$ (3.2 g, 85 mmol) was quickly added to a

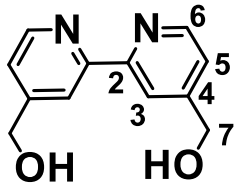

suspension of 4,4'-dimethylester-2,2'-bipyridine (1.5 g, 5.5 mmol) in 75 mL ethanol. The mixture was refluxed for 3 hours and quenched with saturated ammonium chloride (75 mL). The solvent was removed *in vacuo* and the solid was dissolved in 30 mL water and extracted with ethyl acetate (5 x 70 mL) and dried with $NaSO_4$ to produce a white solid (328 mg, 1.52 mmol, 28% over 2-step).

δ_H (300 Hz; $CDCl_3$): 4.87 (2H, d, *5.2*, H7); 7.40 (2H, dquint, *4.5*, *0.8*, H5); 8.40 (2H, q, *0.8*, H3); 8.69 (2H, d, *4.5*, H6). Data agreed with previously published.

4,4'-Dimethylbromine-2,2'-bipyridine[63] 4,4'-Dimethylalcohol-2,2'-bipyridine was taken forward and dissolved in a solution of HBr and H_2SO_4 (25 mL 4:1) and refluxed for 6 hours. The mixture was added to 40 mL water and neutralised with NaOH. The white precipitate was filtered, washed with water and air dried. The white solid was dissolved in 40 mL chloroform, dried with $MgSO_4$ and filtered to produce a white solid (470 mg, 1.37 mmol, 90%). δ_H (300 Hz; $CDCl_3$): 4.50 (4H, s, H7); 7.38 (2H, dd, *1.5*, *5.0*, H5); 8.44 (2H, d, *1.5*, H3); 8.68 (2H, d, *5.0*, H6). Data agreed with previously published.

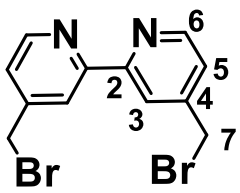

4,4'-Dimethylazide-2,2'-bipyridine[64] Sodium azide (890 mg, 13.7 mmol) is added to a solution of 4,4'-dimethylbromine-2,2'-bipridine (470 mg, 1.37 mmol) in DMSO (5 mL). The mixture was stirred at room temperature for 24 hours. It was poured into water (40 mL) and extracted with diethyl ether (3 x 20 mL), dried with $MgSO_4$ and filtered to produce a white solid (320 mg, 1.2 mmol, 88%). δ_H (300 Hz; $CDCl_3$): 4.50 (4H, s, H7); 7.32 (2H, dt, *0.8*, *5.0*, H5); 8.40 (2H, q, *0.8*, H3); 8.71 (2H, d, *5.0*, H6). m/z (TOF ES^+): 267.1 (100 %), 268.1 (10 %) $[M + H]^+$. Data agreed with previously published.

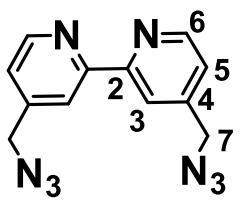

4,4'-Dimethylamine-2,2'-bipyridine[64] A catalytic amount of Pd/C slurried in THF is added to a solution of 4,4'-dimethylazide-2,2'-bipyridine (320 mg, 1.2 mmol) and TEA (200 µL) dissolved in 20 mL THF under N_2. It was left to stir overnight in a H_2 atmosphere. The mixture was put under N_2 atmosphere

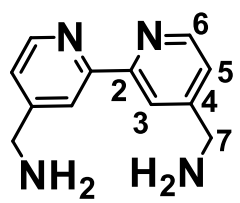

and then filtered through celite. The solvent is removed *in vacuo* to produce a white solid (174 mg, 1.07 mmol, 90%). δ_H (300 Hz; $CDCl_3$): 3.88 (4H, s, H7); 7.19 (2H, dt, *0.8, 5.0*, H5); 8.26 (2H, q, *0.8*, H3); 8.57 (2H, d, *5.0*, H6). Data agreed with previously published.

4,4'-Dimethyllipoamide-2,2'-bipyridine Synthesis adapted from reference.[11] 1-Ethyl-3-(3-

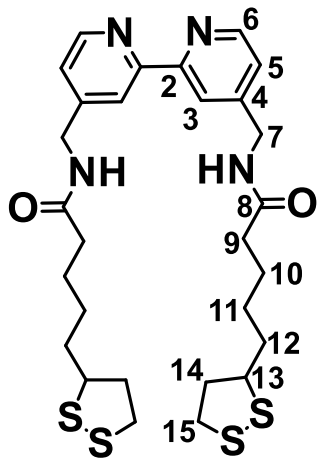

dimethylaminopropyl)carbodiimide (416 mg, 2.7 mmol) is added to a mixture of α-lipoic acid (554 mg, 2.7 mmol) and 1-hydroxybenzotriazol hydrate (363 mg, 2.7 mmol) in dry DMF (20 mL) at 0 °C under N_2. After an hour, it was heated to rt and a solution of 4,4'-dimethylamine-2,2'-bipyridine (174 mg, 1.07 mmol) and N-Ethylmaleimide (285 uL) were added. It was stirred overnight. Water (100 mL) was added and the product was extracted with DCM (3 x 100 mL). The organic phase was taken and the solvent was removed *in vacuo* and the off white solid was suspended in ethanol and filtered to produce a cream solid (181 mg, 0.3 mmol, 29%). δ_H (300 Hz; $CDCl_3$): 1.42 (4H, m, H11); 1.62 (8H, m, H10, H12); 1.81 (2H, m, H15); 2.23 (4H, dd, *7.5, 14.9*, H9); 2.35 (2H, m, H15'); 3.07 (4H, m, H14); 3.47 (2H, tt, *6.2*, *12.5*, H13); 4.46 (4H, d, *6.0*, H7); 6.00 (2H, t, *6.0*, NH); 7.17 (2H, dd, *1.7, 5.0*, H5); 8.18 (2H, t, *9.0*, H3); 8.53 (2H, dd, 0.45, *5.0*, H6). δ_C (400 Hz; $CDCl_3$): 25.4 (C12); 28.9 (C11); 34.6 (C10); 36.3 (C9); 38.5 (C14); 40.2 (C15); 42.6 (C7); 56.4 (C13); 119.7 (C3); 122.7 (C5); 148.6 (C4); 149.5 (C6); 156.2 (C2); 172.9 (C8). Assignments by COSY and HSQC. m/z (TOF ES^+): 591.2 (100 %), 592.2 (25 %), 593.2 (15 %) $[M + H]^+$.

$Ru(bpy)_2Cl_2$ was synthesised as previously discussed (Section 3.5.3.1).

RuS8 Synthesis adapted from reference.[59] $Ru(bpy)_2Cl_2$ (42.4 mg, 0.09 mmol) and 4,4'-dimethyllipoamide-2,2'-bipyridine (60 mg, 0.1 mmol) are refluxed overnight in ethanol (40 mL). The solvent was removed *in vacuo* and a neutral alumina plug was performed in 2% methanol in DCM. The product was stirred with HCl pre-treated Dowex for 2 hours in MeOH and a LH20 column in MeOH was performed. The solvent removed *in vacuo* to produce a red solid chloride salt (35 mg, 0.033 mmol, 36%). δ_H (300 MHz; MeOD): 1.43 (4H, m, H11); 1.5-1.8 (8H, m, H10, H12); 1.88 (2H, m, H15); 2.35 (4H, t, *7.1*, H9); 2.46 (2H, m, H15'); 3.11 (4H, m, H14); 3.55 (2H, m, H13); 4.61 (4H, d, *2.2*, H7); 7.42 (2H, dd, *5.8*, *1.5*, H5); 7.51 (4H, dt, *6.4*, *1.1*, Hb); 7.75 (2H, d, *5.8*, H6); 7.83 (4H, t, *6.4*, Ha); 8.16 (4H, tt, *8.0*, *1.1*, Hc); 8.67 (2H, s, H3); 8.74 (4H, d, *8.0*, Hd). δ_C (100 MHz; MeOD): 25.1 (C12); 28.5 (C11); 34.3 (C10); 35.2 (C9); 38.0 (C14); 40.0 (C15); 41.7 (C7); 56.4 (C13); 122.9 (C3); 124.3 (Cd, Cd'); 125.9 (C5); 127.6 (Cb, Cb'); 137.8 (Cc, Cc'); 151.0 (C6); 151.2 (C4); 151.3 (Ca); 151.4 (Ca'); 156.8 (C2); 157.1 (Ce, Ce'); 175.1 (C8). Assignments by COSY and HSQC. m/z (TOF MS ES^+) 502.1 ($[M-2Cl]^{2+}$): 499.1 (7%); 499.6 (5%); 500.1 (5%); 500.6 (25%); 501.1 35%); 501.6 (55%); 502.1 (100%); 502.6 (50%); 503.1 (60%); 503.6 (25%); 504.1 (15%); 504.6 (5%). All photophysical characterisation is performed as a 8 μM solution in water as the chloride salt. UV-VIS λ_{max} / nm (ε / $M^{-1}cm^{-1}$): 456 (13000), 430 (sh), 287 (72000), 244 (26000). Emission λ_{max}: 635 nm. τ: 430 ns. Φ: 4%. In the presence of 150 μM Zonyl FSA surfactant. UV-VIS λ_{max} / nm (ε / $M^{-1}cm^{-1}$): 465 (13000), 430 (sh), 288 (72000). Emission λ_{max}: 635 nm. τ: 364 (20%), 661 (80%) ns. Φ: 4%. Attached to AuNP13. UV-VIS λ_{max} / nm: 519. Emission λ_{max}: 630 nm. τ: 850 ns. Φ: 10%.

4.5.3.4 Synthesis of RuphenS8

4,4'-Dimethyllipoamide-2,2'-bipyridine was synthesised as previously discussed (Section 4.5.3.3).

$Ru(phen)_2Cl_2$ was synthesised as previously discussed (Section 4.5.3.1).

RuphenS8 Synthesis adapted from reference.[59] $Ru(phen)_2Cl_2$ (46.5 mg, 0.09 mmol) and 4,4'-dimethyllipoamide-2,2'-bipyridine (60 mg, 0.1 mmol) are refluxed overnight in ethanol (40 mL). The solvent was removed *in vacuo* and the resulting red solid was dissolved in water (10 mL), cooled to 5 °C and filtered. The solvent was removed *in vacuo* and a neutral alumina plug was performed in 2% MeOH in DCM. The product was stirred with HCl pre-treated Dowex for 2 hours in MeOH and a Sephadex LH20 column in MeOH was performed. The solvent removed *in vacuo* to produce a red solid chloride salt (43 mg, 0.038 mmol, 43%). δ_H (300 MHz; MeOD): 1.40 (4H, m, H11); 1.5-1.8 (8H, m, H10, H12); 1.82 (2H, m, H15); 2.35 (4H, t, *7.1*, H9); 2.46 (2H, m, H15'); 3.05 (4H, m, H14); 3.49 (2H, m, H13); 4.61 (4H, s, H7); 7.36 (2H, dd, *5.8*, *1.0*, H5); 7.73 (4H, m, Hb', H6); 7.95 (2H, dd, *8.3*, *5.3*, Hb); 8.03 (2H, d, *4.7*, Ha'); 8.36 (5H, m, Hf, Hf', Ha); 8.70 (2H, dd, *8.2*, *1.0*, Hc'); 8.76 (2H, d, H3); 8.80 (2H, dd, *8.2*, *1.0*, Hc). δ_C (100 MHz; MeOD): 25.2 (C12); 28.5 (C11); 34.3 (C10); 35.2 (C9); 38.1 (C14); 40.0 (C15); 41.7 (C7); 56.4 (C13); 122.9 (C3); 125.9 (C5); 126.0 (Cb); 126.2 (Cb'); 128.1 (Cf, Cf'); 131.1 (C4); 136.9 (Cc, Cc'); 147.6 (C2); 147.8 (Cd, Cd'); 151.4 (C6); 125.2 (Ca); 152.5 (Ca'); 157.2 (Ce, Ce'); 175.0 (C8). Assignments by COSY and HSQC. m/z (TOF MS ES^+) 526.1 ($[M-2Cl]^{2+}$): 523.1 (7%); 523.6 (5%); 524.1 (5%); 525.6 (25%); 525.1 (40%); 525.6 (60%); 526.1 (100%); 526.6 (60%);

527.1 (75%); 527.6 (30%); 528.1 (15%); 528.6 (5%). All photophysical characterisation is performed as a 7 μM solution in water as the chloride salt. UV-VIS λ_{max} / nm (ε / $M^{-1}cm^{-1}$): 452 (16000), 420 (sh), 390(sh), 286 (42000), 263 (82000), 230 (sh). Emission λ_{max}: 625 nm. τ: 500 ns. Φ: 4%. In the presence of 150 μM Zonyl FSA surfactant. UV-VIS λ_{max} / nm (ε / $M^{-1}cm^{-1}$): 450 (16000), 420 (sh), 390 (sh), 285 (44000), 263 (70000). Emission λ_{max}: 625 nm. τ: 524 (50%), 954 (50%) ns. Φ: 4%. Attached to AuNP13. UV-VIS λ_{max} / nm: 520. Emission λ_{max}: 620 nm. τ: 1100 ns. Φ: 20%.

4.5.4 Attachment of probe to nanoparticle

Z·AuNP13 was synthesised as previously discussed (Section 3.5.4).

RuphenS12·AuNP13 RuphenS12 (12 μL, 0.8 mM) was titrated into a 9 nM solution of Z·AuNP13 with sonication. A Sephadex G-10 size exclusion column was performed and the sample was diluted to 2 mL with deionised water to form a 4.5 nM solution of RuphenS12·AuNP13. λ_{max} (H_2O) / nm 521 (SPR). Diameter / nm = 17 ± 5 (DLS number distribution). ζ-potential = - 42 ± 7 mV. ICPMS result ratio Ru:Au is 1:180, suggesting 550 complexes per AuNP13.

RuSconj·AuNP13 RuSconj (8 μL, 1.2 mM) was titrated into a 9 nM solution of Z·AuNP13 with sonication. A Sephadex G-10 size exclusion column was performed and the sample was diluted to 2 mL with deionised water to form a 4.5 nM solution of RuSconj·AuNP13. λ_{max} (H_2O) / nm 521 (SPR). Diameter / nm = 20 ± 7 (DLS number distribution). ζ-potential = - 40 ± 8 mV. ICPMS result ratio Ru:Au is 1:250, suggesting 400 complexes per AuNP13.

RuS8·AuNP13 RuS8 (12 μL, 0.8 mM) was titrated into a 9 nM solution of Z·AuNP13 with sonication. A Sephadex G-10 size exclusion column was performed and the sample was diluted to 2 mL with deionised water to form a 4.5 nM solution of RuS8·AuNP13. λ_{max} (H_2O)

/ nm 519 (SPR). Diameter / nm = 21 ± 6 (DLS number distribution). ζ-potential = - 51 ± 7 mV. ICPMS result ratio Ru:Au is 1:180, suggesting 550 complexes per AuNP13.

RuphenS8·AuNP13 RuphenS8 (12 µL, 1.1 mM) was titrated into a 9 nM solution of Z·AuNP13 with sonication. A Sephadex G-10 size exclusion column was performed and the sample was diluted to 2 mL with deionised water to form a 4.5 nM solution of RuphenS8·AuNP13. λ_{max} (H_2O) / nm 520 (SPR). Diameter / nm = 20 ± 7 (DLS number distribution). ζ-potential = - 47 ± 6 mV. ICPMS result ratio Ru:Au is 1:150, suggesting 690 complexes per AuNP13.

4.6 References

1. S. A. M. Osborne and Z. Pikramenou, *Farad. Discuss.*, 2015, 185, 219-231.
2. N. J. Rogers, S. Claire, R. M. Harris, S. Farabi, G. Zikeli, I. B. Styles, N. J. Hodges and Z. Pikramenou, *Chem. Commun.*, 2014, 50, 617-619.
3. M. Martinez-Calvo, K. N. Orange, R. B. P. Elmes, B. la Cour Poulsen, D. C. Williams and T. Gunnlaugsson, *Nanoscale*, 2016, 8, 563-574.
4. F. C. Leung, A. Y. Tam, V. K. Au, M. Li and V. W. Yam, *ACS Appl. Mater. Interfaces*, 2014, 6, 6644-6653.
5. W. R. Glomm, S. J. Moses, M. K. Brennaman, J. M. Papanikolas and S. Franzen, *J. Phys. Chem. B*, 2004, 109, 804-810.
6. O. Kedem, W. Wohlleben and I. Rubinstein, *Nanoscale*, 2014, 6, 15134-15143.
7. A. Ito, N. Kobayashi and Y. Teki, *Inorg. Chem.*, 2017, 56, 3794-3808.
8. A. Juris, V. Balzani, P. Belser and A. von Zelewsky, *Helvetica Chimica Acta*, 1981, 64, 2175-2182.
9. J. N. Demas, E. W. Harris and R. P. McBride, *J. Am. Chem. Soc.*, 1977, 99, 3547-3551.
10. A. A. Abdel-Shafi, M. D. Ward and R. Schmidt, *Dalton Trans.*, 2007, 2517-2527.
11. S. J. Adams, D. J. Lewis, J. A. Preece and Z. Pikramenou, *ACS Appl. Mater. Interfaces*, 2014, 6, 11598-11608.
12. N. Sutin and C. Creutz, *Pure Appl. Chem.*, 1980, 52, 2717 - 2738.
13. C. J. Timpson, C. C. Carter and J. Olmsted, *J. Phys. Chem*, 1989, 93, 4116-4120.
14. Y. Hou, P. Xie, K. Wu, J. Wang, B. Zhang and Y. Cao, *Sol. Energy Mater. Sol. Cells*, 2001, 70, 131-139.
15. O. Johansson, M. Borgström, R. Lomoth, M. Palmblad, J. Bergquist, L. Hammarström, L. Sun and B. Åkermark, *Inorg. Chem.*, 2003, 42, 2908-2918.

16. D. B. Papkovsky and R. I. Dmitriev, *Chem. Soc. Rev.*, 2013, 42, 8700-8732.

17. A. Juris, V. Balzani, F. Barigelletti, S. Campagna, P. Belser and A. Von Zelewsky, *Coord. Chem. Rev.*, 1988, 84, 85-277.

18. V. Balzani and A. Juris, *Coord. Chem. Rev.*, 2001, 211, 97-115.

19. L. De Cola, F. Barigelletti and M. J. Cook, *Helvetica Chimica Acta*, 1988, 71, 733-741.

20. D. V. Kozlov, D. S. Tyson, C. Goze, R. Ziessel and F. N. Castellano, *Inorg. Chem.*, 2004, 43, 6083-6092.

21. V. W. Yam and K. M. Wong, *Chem. Commun.*, 2011, 47, 11579-11592.

22. E. Babu, P. Muthu Mareeswaran, S. Singaravadivel, J. Bhuvaneswari and S. Rajagopal, *Spectrochim. Acta Mol. Biomol. Spectrosc.*, 2014, 130, 553-560.

23. A. M. Pyle, J. P. Rehmann, R. Meshoyrer, C. V. Kumar, N. J. Turro and J. K. Barton, *J. Am. Chem. Soc.*, 1989, 111, 3051-3058.

24. J. N. Demas and J. W. Addington, *J. Am. Chem. Soc.*, 1976, 98, 5800-5806.

25. S. Bernhard, J. A. Barron, P. L. Houston, H. D. Abruña, J. L. Ruglovksy, X. Gao and G. G. Malliaras, *J. Am. Chem. Soc.*, 2002, 124, 13624-13628.

26. N. Katsumi, *Bull. Chem. Soc. Jpn*, 1982, 55, 2697-2705.

27. J. Yin, D. Bhattacharya, P. Thanasekaran, C. Hsu, T. Tseng and K. Lu, *Inorg. Chim. Acta*, 2009, 362, 5064-5072.

28. J. Liu, Z. Diwu, W.-Y. Leung, Y. Lu, B. Patch and R. P. Haugland, *Tetrahedron Lett.*, 2003, 44, 4355-4359.

29. R. F. V. d. Souza and W. F. De Giovani, *Spectrochim. Acta Mol. Biomol. Spectrosc.*, 2005, 61, 1985-1990.

30. G. F. Strouse, J. R. Schoonover, R. Duesing, S. Boyde, W. E. Jones, Jr. and T. J. Meyer, *Inorg. Chem.*, 1995, 34, 473-487.

31. E. M. Kober, J. V. Caspar, R. S. Lumpkin and T. J. Meyer, *J. Phys. Chem*, 1986, 90, 3722-3734.

32. V. Fernandez-Moreira, F. L. Thorp-Greenwood and M. P. Coogan, *Chem. Commun.*, 2010, 46, 186-202.

33. F. Dosio, B. Stella, A. Ferrero, C. Garino, D. Zonari, S. Arpicco, L. Cattel, S. Giordano and R. Gobetto, *Int. J. Pharm.*, 2013, 440, 221-228.

34. R. Zhang, B. Song, Z. Dai, Z. Ye, Y. Xiao, Y. Liu and J. Yuan, *Biosensors and Bioelectronics*, 2013, 50, 1-7.

35. Y. Chen, R. Guan, C. Zhang, J. Huang, L. Ji and H. Chao, *Coord. Chem. Rev.*, 2016, 310, 16-40.

36. R. B. P. Elmes, K. N. Orange, S. M. Cloonan, D. C. Williams and T. Gunnlaugsson, *J. Am. Chem. Soc.*, 2011, 133, 15862-15865.

37. J. Otsuki, H. Kameda, S. Tomihira, H. Sakaguchi and T. Takido, *Chem. Lett.*, 2002, 31, 610-611.

38. P. Bertoncello, E. T. Kefalas, Z. Pikramenou, P. R. Unwin and R. J. Forster, *J. Phys. Chem. B*, 2006, 110, 10063-10069.

39. K. Nakamaru, *Bull. Chem. Soc. Jpn.*, 1982, 55, 2697-2705.

40. K. Kalyanasundaram, *Coord. Chem. Rev.*, 1982, 46, 159-244.

41. L. Tan, H. Chao, H. Li, Y. Liu, B. Sun, W. Wei and L. Ji, *J. Inorg. Biochem.*, 2005, 99, 513-520.

42. D. Patra, A. H. Chaaban, S. Darwish, H. A. Saad, A. S. Nehme and T. H. Ghaddar, *Colloids and Surfaces B: Biointerfaces*, 2016, 138, 32-40.

43. S. Ji, W. Wu, W. Wu, P. Song, K. Han, Z. Wang, S. Liu, H. Guo and J. Zhao, *J. Mater. Chem.*, 2010, 20, 1953-1963.

44. L. Wang, H. Yin, M. A. Jabed, M. Hetu, C. Wang, S. Monro, X. Zhu, S. Kilina, S. A. McFarland and W. Sun, *Inorg. Chem.*, 2017, 56, 3245-3259.

45. B. Factor, B. Muegge, S. Workman, E. Bolton, J. Bos and M. M. Richter, *Anal. Chem.*, 2001, 73, 4621-4624.

46. S. W. Snyder, S. L. Buell, J. N. Demas and B. A. DeGraff, *J. Phys. Chem*, 1989, 93, 5265-5271.

47. W. J. Dressick, B. L. Hauenstein, T. B. Gilbert, J. N. Demas and B. A. DeGraff, *J. Phys. Chem*, 1984, 88, 3337-3340.

48. E. Pensa, E. Cortés, G. Corthey, P. Carro, C. Vericat, M. H. Fonticelli, G. Benítez, A. A. Rubert and R. C. Salvarezza, *Acc. Chem. Res.*, 2012, 45, 1183-1192.

49. A. V. Naumkin, A. KrautVass, S. W. Gaarenstroom and C. J. Powell, *NIST Standard Reference Database 20, Version 4.1* 2012.

50. F. C. Krebs, *Polymer Photovoltaics: A Practical Approach*, 2008, In: K. Norrman; S. Cros; R. Bettignies; M. Firon; F. C. Krebs,. *Lifetime and Stability Studies*, SPIE, Washington.

51. S. Eustis and M. A. El Sayed, *Chem. Soc. Rev.*, 2006, 35, 209-217.

52. T. Soller, M. Ringler, M. Wunderlich, T. A. Klar, J. Feldmann, H. P. Josel, Y. Markert, A. Nichtl and K. Kürzinger, *Nano Lett.*, 2007, 7, 1941-1946.

53. E. Dulkeith, A. C. Morteani, T. Niedereichholz, T. A. Klar, J. Feldmann, S. A. Levi, F. C. J. M. Veggel, D. N. Reinhoudt, M. Möller and D. I. Gittins, *Phys. Rev. Lett.*, 2002, 89, 203002.

54. A. Bouskila, B. Drahi, E. Amouyal, I. Sasaki and A. Gaudemer, *J. Photochem. Photobiol. A*, 2004, 163, 381-388.

55. A. Bouskila, E. Amouyal, C. Verchère-Béaur, I. Sasaki and A. Gaudemer, *J. Photochem. Photobiol., B*, 2004, 76, 69-83.

56. B. W. Chu and V. W. Yam, *Langmuir*, 2006, 22, 7437-7443.

57. C. Goze, J. Chambron, V. Heitz, D. Pomeranc, Xavier J. Salom-Roig, J. Sauvage, Angeles F. Morales and F. Barigelletti, *Eur J Inorg Chem*, 2003, 3752-3758.

58. S. Farabi, *PhD, University of Birmingham*, 2011.

59. B. P. Sullivan, D. J. Salmon and T. J. Meyer, *Inorg. Chem.*, 1978, 17, 3334-3341.

60. R. Ziessel, J. Suffert and M. Youinou, *J. Org. Chem.*, 1996, 61, 6535-6546.

61. Z. Shi, L. Wang, H. Wang, X. Cao and H. Zhang, *Org. Lett.*, 2007, 9, 595-598.

62. T. Prakasam, M. Lusi, M. Elhabiri, C. Platas-Iglesias, J. Olsen, Z. Asfari, S. Cianférani-Sanglier, F. Debaene, L. J. Charbonnière and A. Trabolsi, *Angew. Chem., Int. Ed.*, 2013, 52, 9956-9960.

63. I. Gillaizeau-Gauthier, F. Odobel, M. Alebbi, R. Argazzi, E. Costa, C. A. Bignozzi, P. Qu and G. J. Meyer, *Inorg. Chem.*, 2001, 40, 6073-6079.

64. Google Patents; CN 103896928 A, 2014.

5 Comparison of the solid state photophysics of ruthenium molecular and nanoprobes

5.1 Introduction

Solid state photophysical properties of ruthenium complexes are important for applications in Light Emitting Diodes (LEDs),[1-3] photonic devices[2, 4] and Dye Sensitized Solar Cells (DSCs).[5-7] They have versatile applications due to their widely tuneable electro-optical properties (Figure 5.1). In LEDs, the ruthenium complex emits a certain wavelength of light depending on the energy gap of its energy levels. In a DSC, the ruthenium dye is absorbed on the surface of an electrode and can act as an efficient electron donator to the TiO_2 due to the positioning of the energy levels.

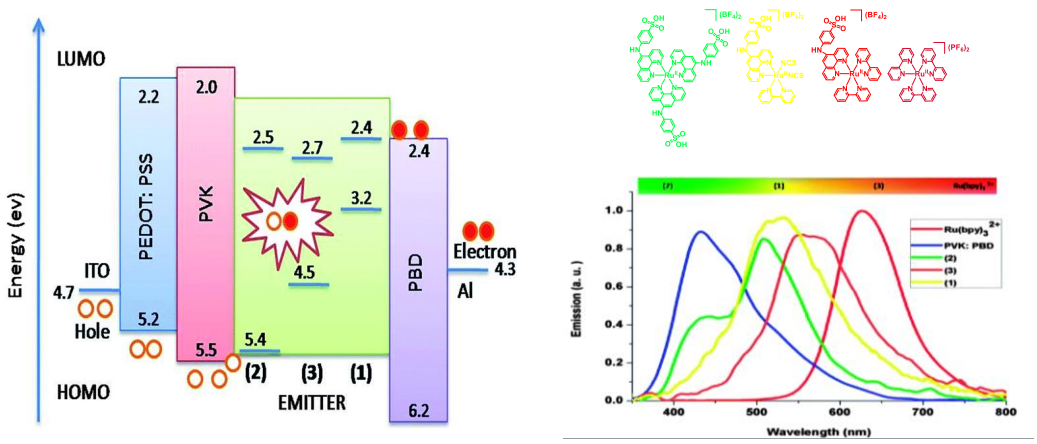

Figure 5.1: Schematic to show the tuneable optical properties of ruthenium complexes. Shown in the image are the energy levels in an LED (left) and emission graphs and structures (right) of $[Ru(bpy)_3]^{2+}$ and three other ruthenium complexes, 1 – 3. Taken from reference.[8]

The solution based photophysical properties of ruthenium complexes are well known and have been highly researched.[9-11] The solid state properties however differ and are less understood. The difference arises from the complexes not being surrounded by solvent molecules and being closely packed together. They lose mobility and become more rigid.[12] This leads to shifts in emission and alterations to the luminescent lifetime and quantum yield.

It has been found that the luminescent lifetime of the complexes decrease when in the solid state due to self-quenching. The complexes are packed together more closely than in solution, which leads to closer interactions between the ruthenium photoactive centres. There are three factors that contribute to the quenching: 1. Non-radiative decay of the triplet Metal Ligand Charge Transfer (MLCT) (k_{decay}), 2. Crossover to the upper d-d state (k_{dd}), 3. Quenching through electron transfer (k_{ET}) (Equation 5.1) (Figure 5.2).[13]

$$k_{nr} = k_{decay} + k_{dd} + k_{ET} \qquad \textbf{Equation 5.1}$$

Electron transfer is the main mechanism responsible for quenching in a solid state environment.[14] The most likely method for this electron transfer is through Dexter.[15] This quenching is distance dependent and can vary depending on the thickness of the film.[16] Malliaras *et al.* have found a 20% increase in lifetime when increasing the film thickness from 17 to 200 nm.[13] Luminescent lifetime can be increased through decreasing the electron transfer. Malliaras *et al.* have demonstrated a decrease in self-quenching through the incorporation of long side chains into the ruthenium structure[17] and Rubnar *et al.* have mixed a polymer, PMMA, with the ruthenium complex, leading to an increase in lifetime.[18, 19] Both of these examples cause inefficient packing of the ruthenium complexes which lead to an increase in distance between the photoactive ruthenium centres and a decrease in the electron transfer.

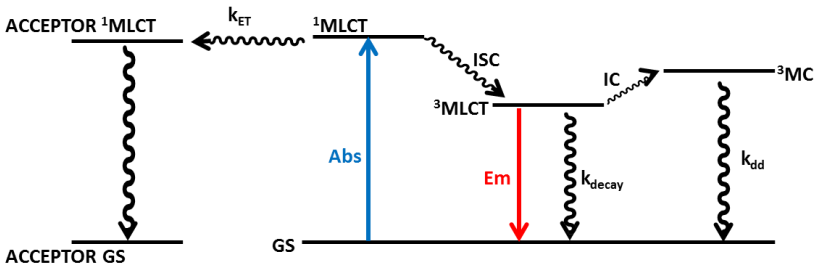

Figure 5.2: Jablonski diagram to show quenching *via* K_{decay}, K_{dd} and K_{ET}.

5.1.1 Chapter summary

In this chapter, solid state photophysical properties were performed on molecular and nanoprobes. Seven complexes, RuS1, RuS6, RuS12, RuphenS12, RuSconj, RuS8 and RuphenS8 (Figure 5.3) were characterised in the solid state through drying onto quartz glass as both molecular probes and attached to AuNP13.

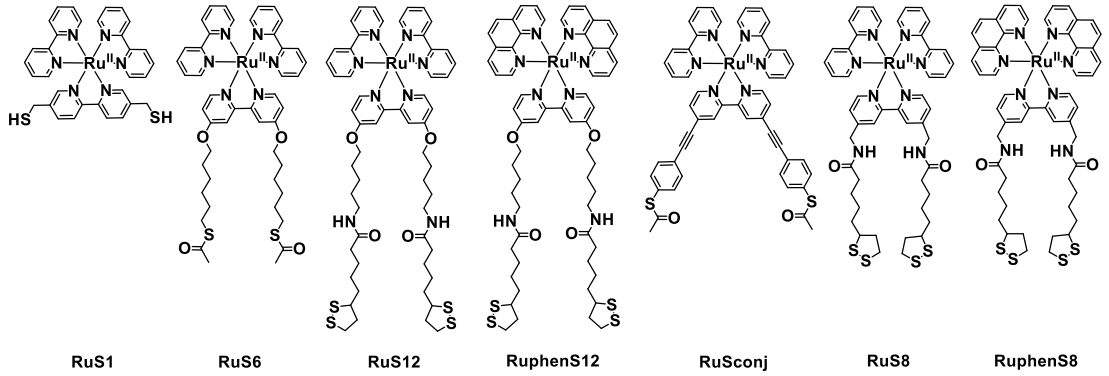

Figure 5.3: Schematic to show the structure of RuS1, RuS6, RuS12, RuphenS12, RuSconj, RuS8 and RuphenS8.

5.2 Results and discussion

5.2.1 Solid state photophysical properties of molecular probe

Seven complexes (RuS1, RuS6, RuS12, RuphenS12, RuSconj, RuS8 and RuphenS8) were dried onto quartz glass to monitor the solid state photophysical properties. The solid state properties of the parent compound, $Ru(bpy)_3Cl_2$, were also monitored for comparison. To characterise the solid state luminescent properties of the molecular probes, solid state absorption and steady state and time resolved emission spectroscopy were taken.

The solid state absorbance shows the singlet Metal Ligand Charge Transfer (MLCT) absorption between 400 – 500 nm (Figure 5.4) which is the same as the absorbance for all the complexes in solution. This is expected as solvent effects have been shown to not alter the absorption.[20, 21] The excitation for all of the complexes mirrors the absorption, with a singlet MLCT peak between 400 – 500 nm. It shows a larger contribution from the singlet MLCT than the Ligand Centre (LC) to the triplet MLCT, unlike in solution. This shows that in the

solid state the singlet MLCT is more viable than in solution. This effect is seen in the literature with other ruthenium complexes in the solid state.[22] The emission shows the triplet MLCT broad band between 550 - 800 nm (Table 5.1). The emission maximum for RuS6, RuS12, RuphenS12 and RuphenS8 are 650, 640, 630 and 630 nm respectively. These complexes in the solid state only have a small shift when compared to in solution (645, 645, 630 and 625 nm respectively). This agrees with previous research in the Pikramenou group, finding a 4 nm blue shift for RuS12 powder and monolayer samples, compared to in solution.[23] In comparison, $Ru(bpy)_3Cl_2$, RuSconj and RuS8 have large blue shifts from solution (625, 670 and 635 nm respectively) to solid state (570, 640 and 620 nm respectively). This blue shift is seen in the literature and can be attributed to an increase in rigidity due to a lack of mobility of the ruthenium probe and suppression of the vibrational deactivation.[12, 24-27] Kuroda *et al.* show $[Ru(bpy)_3]^{2+}$ to have a λ_{max} of 585 nm when absorbed on a C18 surface[28] and Malliaris *et al.* see a blue shift in emission of a 17 nm $Ru(bpy)_3(PF_6)_2$ thin film, compared to in solution.[13] For $Ru(bpy)_3Cl_2$, a shoulder in the emission is seen, which is also seen in the literature by Franville *et al*.[29] RuS1 has a maximum of 670 nm, which is a large red shift from in solution (645 nm).

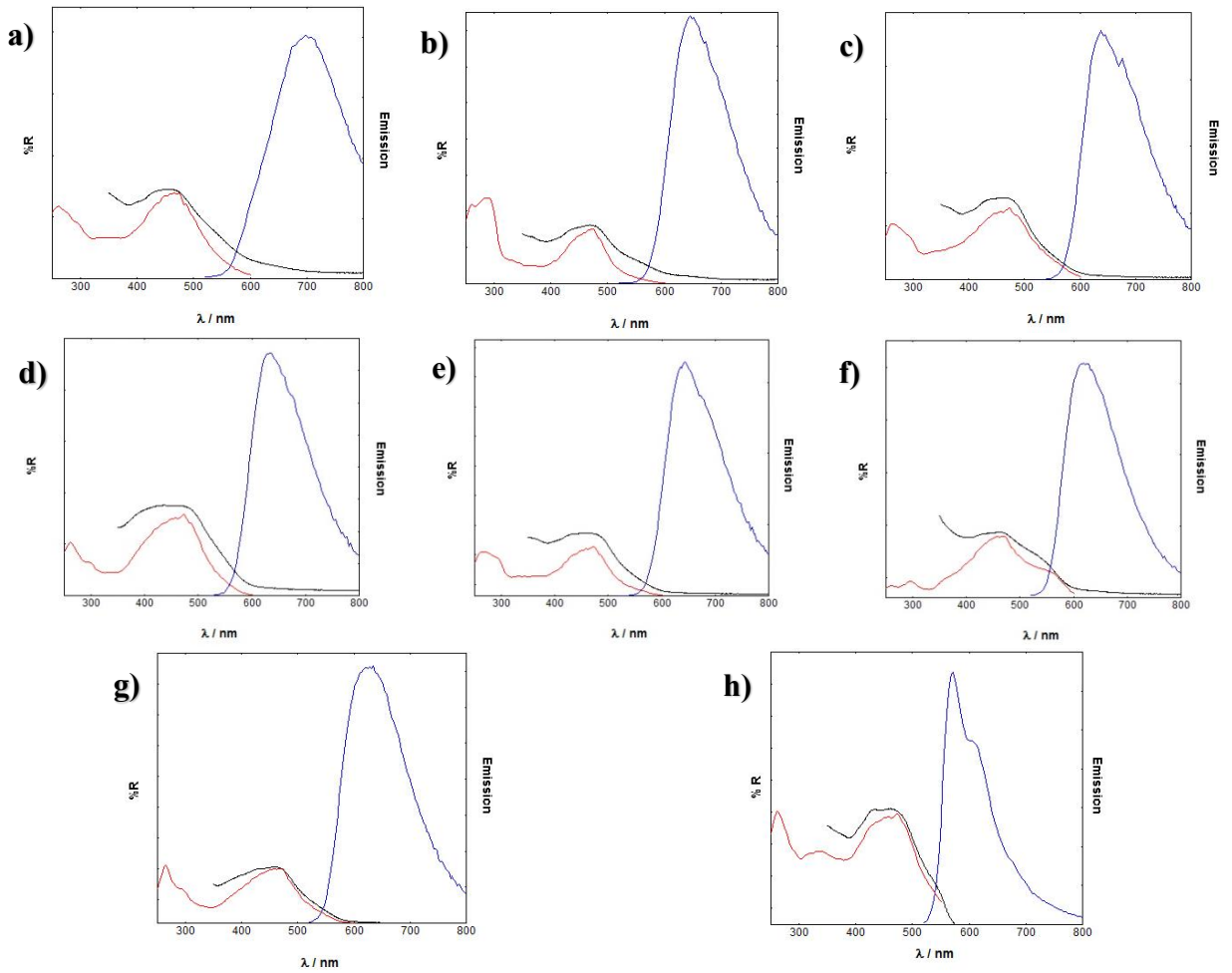

Figure 5.4: Reflectance (black), luminescence emission (blue) and excitation (red) of RuS1 (a), RuS6 (b), RuS12 (c), RuphenS12 (d), RuSconj (e), RuS8 (f), RuphenS8 (g) and $Ru(bpy)_3Cl_2$ (h) dried onto quartz glass. λ_{exc} = 450 nm and λ_{det} = 640 nm (λ_{exc} = 480 nm and λ_{det} = 680 nm for RuSconj).

Table 5.1: Emission maximum for the ruthenium probes.

	λ_{max} / nm	$\lambda_{max\ solution}$ / nm	Shift / nm
$Ru(bpy)_3Cl_2$	570	625	+ 55
RuS1	670	645	- 25
RuS6	650	645	- 5
RuS12	640	645	+ 5
RuphenS12	630	630	0
RuSconj	640	670	+ 30
RuS8	620	635	+ 15
RuphenS8	630	625	- 5

The lifetimes for all complexes as solid state have three components (Table 5.2, Figure 5.5). There is a very short component which has a small percentage (1-20%) that may be attributed to scattering, so will not be discussed.

Table 5.2: Luminescence lifetimes of the ruthenium molecular probes fitted with a X^2 between 1.0 and 1.2.

	τ_1 / ns	τ_2 / ns	τ_3 / ns	$\tau_{solution}$ / ns
$Ru(bpy)_3Cl_2$	17 (11%)	60 (54%)	200 (35%)	380
RuS1	16 (20%)	50 (53%)	260 (27%)	420
RuS6	30 (6%)	150 (37%)	500 (57%)	240
RuS12	30 (5%)	120 (30%)	300 (65%)	280
RuphenS12	43 (3%)	210 (21%)	590 (76%)	550
RuSconj	30 (1%)	170 (15%)	480 (84%)	440
RuS8	20 (1%)	160 (14%)	650 (85%)	430
RuphenS8	30 (2%)	150 (24%)	570 (74%)	500

A short and long component are seen for all of the complexes in the solid state, including $Ru(bpy)_3Cl_2$. The short component arises from quenching of the excited state by non-radiative processes (K_{nr}). This is due an increase in local concentration of the complexes through tighter packing than in solution, which leads to self-quenching of the photoactive ruthenium centres.

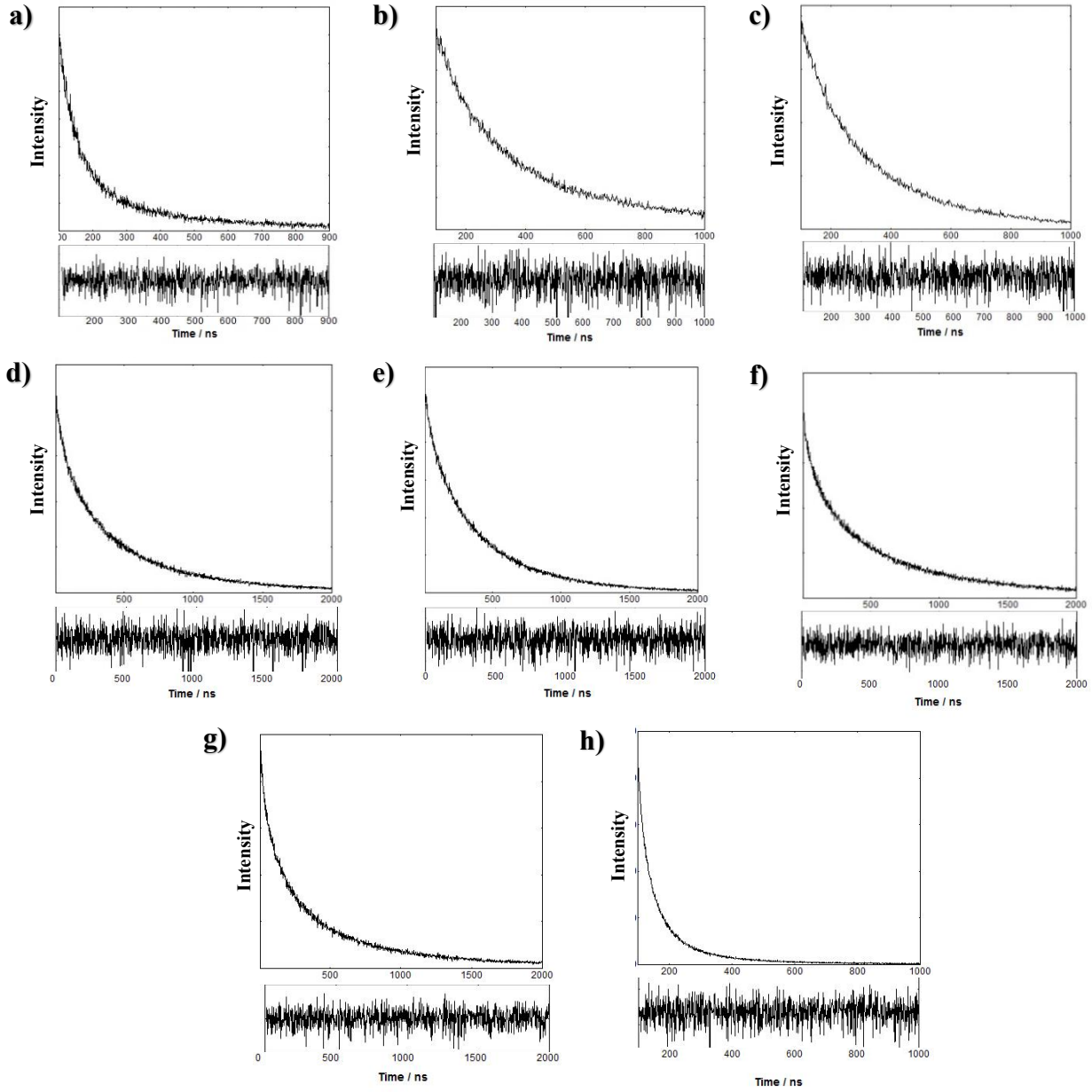

Figure 5.5: Solid state luminescent lifetime decay (top) and fitting (bottom) of RuS1 (a), RuS6 (b), RuS12 (c), RuphenS12 (d), RuSconj (e), RuS8 (f), RuphenS8 (g) and $Ru(bpy)_3Cl_2$ (h). λ_{exc} = 445 nm and λ_{det} = 650 nm (λ_{det} = 680 nm for RuSconj). X^2 is fitted between 1.0 and 1.2 for all the lifetimes.

In the case of RuS1, the long component has decreased with respect to in solution (420 to 260 ns) and the short component is predominant (53%). This pattern is also seen for $Ru(bpy)_3Cl_2$ which decreases from 380 to 200 ns, with the short component predominate (54%). This can be attributed to closer packing in the solid state due to a lack of long legs and therefore an increase in quenching from electron transfer.[17] All of the other complexes see either an increase (RuS6 and RuS8) or little effect (RuS12, RuphenS12, RuSconj and RuphenS8) on

the long lifetime of the solid state compared to in solution, with the short component having a smaller contribution (<30%). This can be attributed to a combination of inefficient packing due to the long legs, reducing electron transfer quenching, and an absence of solvent which will reduce quenching by triplet oxygen. It has been shown that triplet oxygen quenching is reduced in the solid state due to the absence of solvent molecules interacting with the molecule.[13] The long lifetime of RuS12 is similar in solution (280 ns) to solid state (300 ns), which agrees with previous published research in the Pikramenou group that shows the luminescent lifetime of RuS12 similar in solution and as a powder or monolayer.[23]

The quantum yields of the films can be calculated from the lifetimes (Equation 5.2), assuming that the radiative rate is the same in solution as in the solid state.[13] Where Φ is the quantum yield, τ is the lifetime and % is the percentage contribution of the short and long component.

$$\frac{\boldsymbol{\Phi_{film}}}{\boldsymbol{\Phi_{soln}}} = \%_{\boldsymbol{short}}\left(\frac{\boldsymbol{\tau_{shortfilm}}}{\boldsymbol{\tau_{soln}}}\right) + \%_{\boldsymbol{long}}\left(\frac{\boldsymbol{\tau_{longfilm}}}{\boldsymbol{\tau_{soln}}}\right) \qquad \textbf{Equation 5.2}$$

Table 5.3: Quantum yield of the ruthenium probes both as solid state and in solution.

	Φ / %	**$\Phi_{solution}$ / %**
$Ru(bpy)_3Cl_2$	1	2.8
RuS1	1	2
RuS6	3	2
RuS12	2	2
RuphenS12	3	3
RuSconj	3	3
RuS8	5	4
RuphenS8	4	4

The quantum yields follow the pattern of the lifetimes, with a decrease compared to in solution for $Ru(bpy)_3Cl_2$ and RuS1 due to tight packing and high electron transfer quenching. Either an increase (RuS6 and RuS8) or no change (RuS12, RuphenS12, RuSconj and RuphenS8) are seen for the other complexes due to inefficient packing (Table 5.3).

5.2.2 Solid state photophysical properties of gold nanoparticles coated with probe and surfactant

Seven nanoprobes (RuS1•AuNP13, RuS6•AuNP13, RuS12•AuNP13, RuphenS12•AuNP13, RuSconj•AuNP13, RuS8•AuNP13 and RuphenS8•AuNP13) were dried onto quartz glass to monitor the solid state photophysical properties. To characterise the solid state luminescent properties of the nanoprobes, solid state absorption and steady state and time resolved emission spectroscopy were taken.

The solid state absorption for all of the nanoprobes has a peak between 500 – 700 nm for the SPR of the AuNP13 (Figure 5.6). This is also seen for the nanoprobes in solution (Section 3.2.4 & 4.2.6). The excitation for all of the nanoprobes at 650 nm reflects the absorption of the ruthenium probes with a peak between 400 – 500 nm, showing that the emission is arising from excitation of the ruthenium complex and not the AuNP13. There is a larger contribution to the triplet MLCT from the LC than the singlet MLCT compared to the molecular probe solid state excitation. This pattern is also seen in solution; the LC has a larger contribution in the triplet MLCT when the ruthenium probe is attached to AuNP13. This increase in contribution is larger in the solid state than solution for the nanoprobe. This shows that the singlet MLCT viability decreases when attached to AuNP13 and further decreases when in the solid state. Similarly to the molecular probes, either no shift (RuS1, RuS6, RuphenS12 and RuphenS8) or a 20 nm blue shift (RuS12, RuSconj and RuS8) is seen in the solid state emission maximum (Table 5.4). The same complexes appear to blue shift for both the molecular and nanoprobe in the solid state. This shift is attributed to an increase in rigidity.[12]

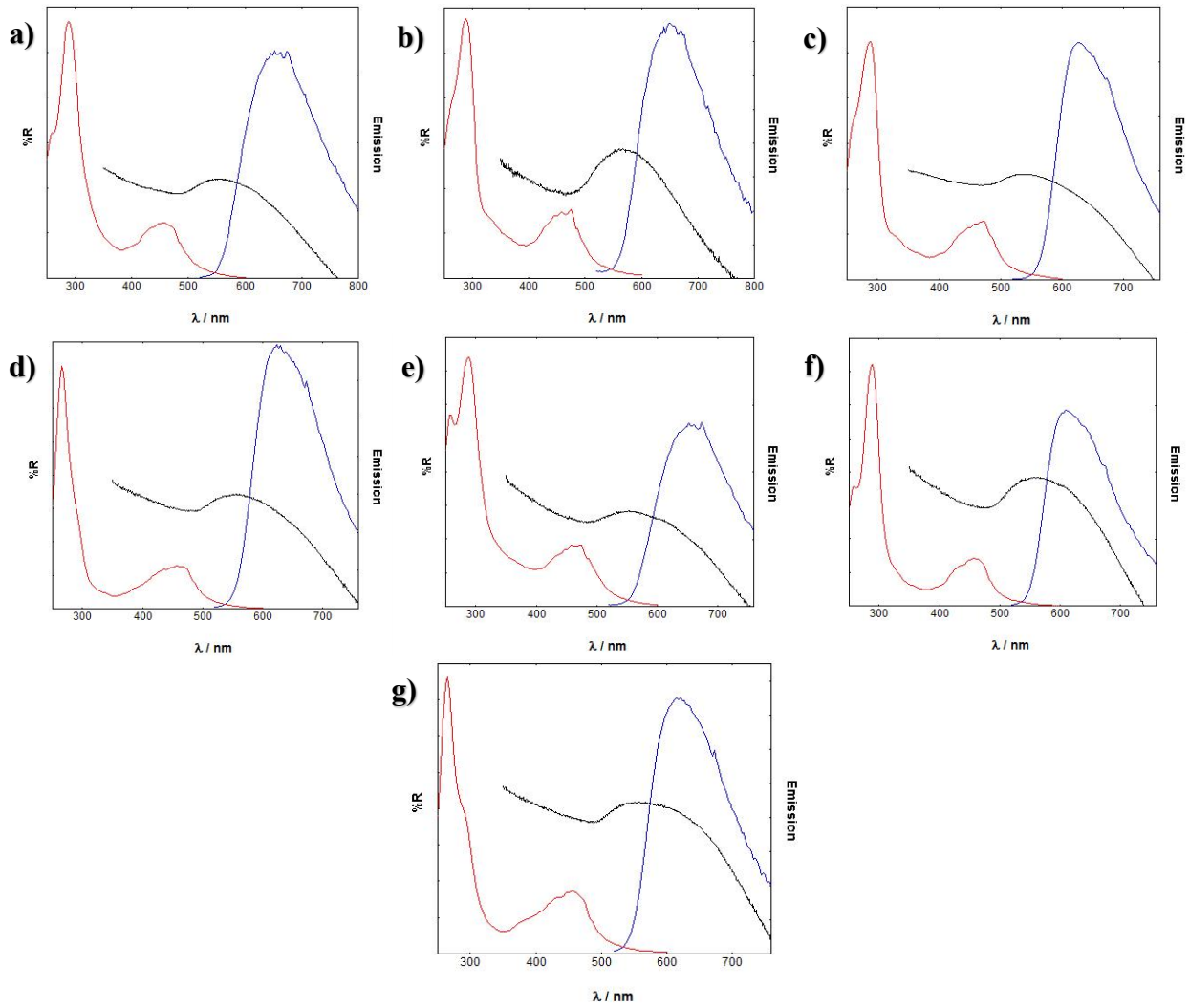

Figure 5.6: Reflectance (black), luminescence emission (blue) and excitation (red) data of RuS1•AuNP13 (a), RuS6•AuNP13 (b), RuS12•AuNP13 (c), RuphenS12•AuNP13 (d), RuSconj•AuNP13 (e), RuS8•AuNP13 (f) and RuphenS8•AuNP13 (g) dried onto quartz glass. λ_{exc} = 450 nm and λ_{det} = 650 nm (λ_{exc} = 480 nm and λ_{det} = 680 nm for RuSconj•AuNP13).

Table 5.4: Emission maximum for the ruthenium nanoprobes both as solid state and in solution.

	λ_{max} / nm	$\lambda_{max\ solution}$ / nm	Shift / nm
RuS1•AuNP13	655	650	- 5
RuS6•AuNP13	650	650	0
RuS12•AuNP13	630	650	+ 20
RuphenS12•AuNP13	630	635	+ 5
RuSconj•AuNP13	655	680	+ 25
RuS8•AuNP13	610	635	+ 25
RuphenS8•AuNP13	620	620	0

The solid state lifetimes for the nanoprobes have three components, as seen for the molecular probes (Table 5.5, Figure 5.7). There is a very short component which has a small percentage (2 - 9%) which may be attributed to scattering so will not be discussed.

Table 5.5: Luminescence lifetimes of the ruthenium nanoprobes both as solid state and in solution. They are fitted with a X^2 between 1.0 and 1.2.

	τ_1 / ns	τ_2 / ns	τ_3 / ns	$\tau_{solution}$ / ns
RuS1•AuNP13	20 (7%)	100 (27%)	470 (66%)	470
RuS6•AuNP13	30 (9%)	170 (48%)	500 (43%)	340
RuS12•AuNP13	25 (2%)	160 (14%)	730 (84%)	480
RuphenS12•AuNP13	20 (3%)	100 (7%)	840 (90%)	1700
RuSconj•AuNP13	30 (3%)	160 (12%)	800 (85%)	370
RuS8•AuNP13	10 (1%)	100 (9%)	710 (90%)	850
RuphenS8•AuNP13	10 (4%)	75 (20%)	475 (76%)	1100

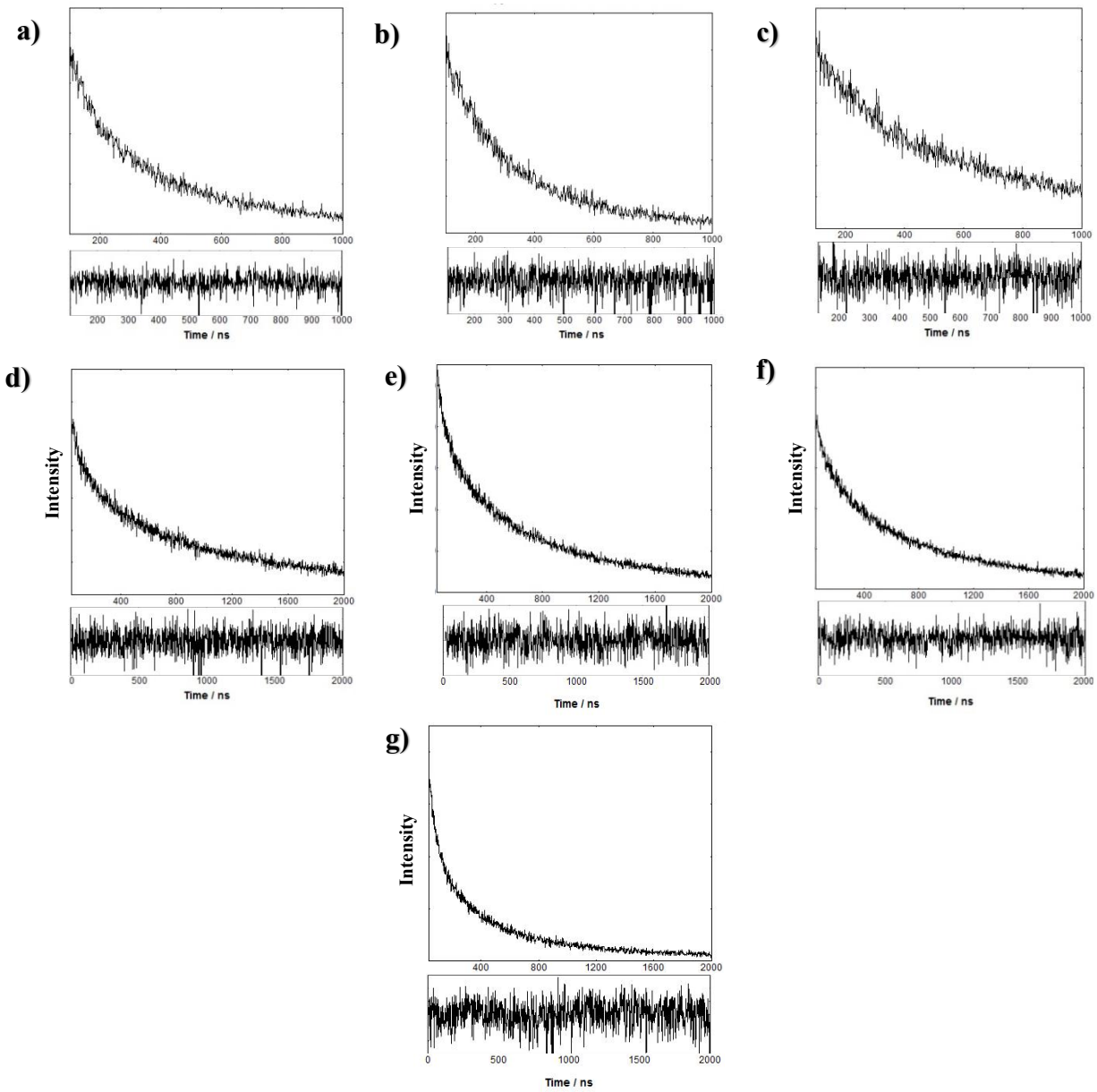

Figure 5.7: Luminescent lifetime decay (top) and fitting (bottom) of RuS1•AuNP13 (a), RuS6•AuNP13 (b), RuS12•AuNP13 (c), RuphenS12•AuNP13 (d), RuSconj•AuNP13 (e), RuS8•AuNP13 (f) and RuphenS8•AuNP13 (g) dried on quartz glass. λ_{exc} = 445 nm and λ_{det} = 650 nm (λ_{det} = 680 nm for RuSconj•AuNP13). X^2 is fitted between 1.0 and 1.2 for all the lifetimes.

As for the molecular probes, the short component arises from quenching of the excited state by non-radiative processes, predominantly electron transfer. For RuS6•AuNP13, RuS12•AuNP13 and RuSconj•AuNP13 there is an increase in the long component lifetime in the solid state (500, 730, 800 ns respectively) when compared to in solution (340, 480, 370 ns respectively). This can be attributed to the absence of solvent and therefore reduction in quenching from triplet oxygen. The long component of RuS1•AuNP13 however does not change (470 ns). This may be due to a more efficient packing of the nanoprobes as the photoactive centre is closer to the gold surface, so self-quenching is more efficient. For RuphenS12•AuNP13 and RuphenS8•AuNP13 there is a 2-fold decrease in the long component in the solid state (840 & 475 ns respectively) compared to in solution (1700 & 1100 ns respectively). This can be attributed to a change in the magnetic field of the AuNP13 in the solid state, which leads to a change in the interaction with the ruthenium bis-phenanthroline complexes and a decrease in enhancement.

Using Equation 5.2, the solid state quantum yields for the nanoprobes have been calculated. They follow a similar trend as the luminescent lifetime long component (Table 5.6). RuS12•AuNP13 and RuSconj•AuNP13 see an increase in quantum yield whereas RuphenS12•AuNP13 and RuphenS8•AuNP13 see a 2-fold decrease.

Table 5.6: Quantum yield of all the ruthenium nanoprobes both as solid state and in solution.

	Φ / %	**$\Phi_{solution}$ / %**
RuS1•AuNP13	1	2
RuS6•AuNP13	5	6
RuS12•AuNP13	12	9
RuphenS12•AuNP13	13	30
RuSconj•AuNP13	10	5
RuS8 •AuNP13	8	10
RuphenS8 •AuNP13	7	20

5.3 Conclusion

Properties of ruthenium complexes in the solid state for both the molecular and nanoprobes have been studied. A blue shift in emission is seen for some of the samples due to increased rigidity of the system. There is addition of a short component of the lifetime when the molecular and nanoprobes are in the solid state. This is due to the photoactive ruthenium centres being in closer proximity compared to in solution and self-quenching occurring through electron transfer. $Ru(bpy)_3Cl_2$ and RuS1 molecular probes show a large quenching of luminescence lifetime and quantum yield through electron transfer due to efficient packing from the absence of long aliphatic or ridged conjugated legs. Increases of the long component of the lifetime were witnessed for some of the molecular and nanoprobes which can be attributed to the reduction of triplet oxygen quenching. A large 2-fold decrease in the long component of the lifetime was seen for the bis-phenanthroline ruthenium nanoprobes. This can be attributed to a change in the magnetic field of the AuNP13 in the solid state, which leads to a change in the interaction with the complexes and decrease in lifetime enhancement. The molecular probe RuS8, and the nanoprobes RuS12•AuNP13, RuphenS12•AuNP13, RuSconj•AuNP13 and RuS8•AuNP13 show potential for use in solid state luminescent applications due to their long luminescent lifetimes (over 600 ns) compared to the literature.[13]

5.4 Summary of results

Table 5.7: Solid state emission, luminescent lifetime and quantum yield data for RuS1, RuS1•AuNP13, RuS6, RuS6•AuNP13, RuS12, RuS12•AuNP13, RuphenS12, RuphenS12•AuNP13, RuSconj, RuSconj•AuNP13, RuS8, RuS8•AuNP13, RuphenS8 and RuphenS8•AuNP13.

	Emission λ_{max} / nm	**τ_1 / ns**	**τ_2 / ns**	**τ_3 / ns**	**Φ / %**
RuS1	670	16 (20%)	50 (53%)	260 (27%)	1
RuS1•AuNP13	655	20 (7%)	100 (27%)	470 (66%)	1
RuS6	650	30 (6%)	150 (37%)	500 (57%)	3
RuS6•AuNP13	650	30 (9%)	170 (48%)	500 (43%)	5
RuS12	640	30 (5%)	120 (30%)	300 (65%)	2
RuS12•AuNP13	630	25 (2%)	160 (14%)	730 (84%)	12
RuphenS12	630	43 (3%)	210 (21%)	590 (76%)	3
RuphenS12•AuNP13	630	20 (3%)	100 (7%)	840 (90%)	13
RuSconj	640	30 (1%)	170 (15%)	480 (84%)	3
RuSconj•AuNP13	655	30 (3%)	160 (12%)	800 (85%)	10
RuS8	620	20 (1%)	160 (14%)	650 (85%)	5
RuS8•AuNP13	610	10 (1%)	100 (9%)	710 (90%)	8
RuphenS8	630	30 (2%)	150 (24%)	570 (74%)	4
RuphenS8•AuNP13	620	10 (4%)	75 (20%)	475 (76%)	7

5.5 Experimental

5.5.1 Synthesis of gold nanoparticles

AuNP13 was synthesised as previously discussed (Section 3.5.2).

5.5.2 Synthesis of ruthenium probes

RuS1, **RuS6** and **RuS12** were synthesised as previously discussed (Section 3.5.3). **RuphenS12**, **RuSconj**, **RuS8** and **RuphenS8** were synthesised as previously discussed (Section 4.5.3).

5.5.3 Attachment of probes to gold nanoparticle

RuS1•AuNP13, **RuS6•AuNP13** and **RuS12•AuNP13** were prepared as previously discussed (Section 3.5.4). **RuphenS12•AuNP13**, **RuSconj•AuNP13**, **RuS8•AuNP13** and **RuphenS8•AuNP13** were prepared as previously discussed (Section 4.5.4).

5.5.4 Preparation of solid state samples

RuS1 (200 µL, 1.2 mM), **RuS6** (200 µL, 1.0 mM), **RuS12** (200 µL, 0.9 mM), **RuphenS12** (200 µL, 0.8 mM), **RuSconj** (200 µL, 3.7 mM), **RuS8** (200 µL, 0.8 mM) and **RuphenS8** (200 µL, 1.1 mM) methanoic solutions were transferred onto a quatz glass sheet (5 x 10 cm) and heated to 90 °C for 10 minutes to form a dry thin film.

RuS1•AuNP13 (1 mL, 9 nM), **RuS6•AuNP13** (1 mL, 9 nM), **RuS12•AuNP13** (1 mL, 9 nM), **RuphenS12•AuNP13** (1 mL, 9 nM), **RuSconj•AuNP13** (1 mL, 9 nM), **RuS8•AuNP13** (1 mL, 9 nM) and **RuphenS8•AuNP13** (1 mL, 9 nM) aqueous solutions were transferred onto a quatz glass sheet (5 x 10 cm) and heated to 90 °C for 10 minutes to form a dry thin film.

5.6 References

1. H. Shahroosvand, L. Najafi, A. Sousaraei, E. Mohajerani, M. Janghouri and F. Bonaccorso, *J. Phys. Chem. C*, 2016, 120, 24965-24972.
2. J. F. Herrmann, P. S. Popp, A. Winter, U. S. Schubert and C. Höppener, *ACS Photonics*, 2016, 3, 1897-1906.
3. H. Yersin, A. F. Rausch, R. Czerwieniec, T. Hofbeck and T. Fischer, *Coord. Chem. Rev.*, 2011, 255, 2622-2652.
4. C. Ho and W. Wong, *Coord. Chem. Rev.*, 2011, 255, 2469-2502.
5. F. Gao, Y. Wang, D. Shi, J. Zhang, M. Wang, X. Jing, R. Humphry-Baker, P. Wang, S. M. Zakeeruddin and M. Grätzel, *J. Am. Chem. Soc.*, 2008, 130, 10720-10728.
6. D. D. Babu, R. Su, A. El-Shafei and A. V. Adhikari, *Electrochim. Acta*, 2016, 198, 10-21.
7. G. Wu, R. Kaneko, A. Islam, Y. Zhang, K. Sugawa, L. Han, Q. Shen, I. Bedja, R. K. Gupta and J. Otsuki, *J. Power Sources*, 2016, 331, 100-111.
8. H. Shahroosvand, P. Abbasi, A. Faghih, E. Mohajerani, M. Janghouri and M. Mahmoudi, *RSC Adv.*, 2014, 4, 1150-1154.
9. A. Juris, V. Balzani, F. Barigelletti, S. Campagna, P. Belser and A. Von Zelewsky, *Coord. Chem. Rev.*, 1988, 84, 85-277.
10. S. Campagna, F. Puntoriero, F. Nastasi, G. Bergamini and V. Balzani, in *Photochemistry and Photophysics of Coordination Compounds I*, eds. V. Balzani and S. Campagna, Springer Berlin Heidelberg, 2007.
11. S. A. M. Osborne and Z. Pikramenou, *Farad. Discuss.*, 2015, 185, 219-231.
12. J. Yin, D. Bhattacharya, P. Thanasekaran, C. Hsu, T. Tseng and K. Lu, *Inorg. Chim. Acta*, 2009, 362, 5064-5072.

13. K. W. Lee, J. D. Slinker, A. A. Gorodetsky, S. Flores-Torres, H. D. Abruna, P. L. Houston and G. G. Malliaras, *Phys. Chem. Chem. Phys.*, 2003, 5, 2706-2709.

14. D. R. Haynes, K. R. Helwig, N. J. Tro and S. M. George, *J. Chem. Phys.*, 1990, 93, 2836-2847.

15. M. Furue, K. Maruyama, Y. Kanematsu, T. Kushida and M. Kamachi, *Coord. Chem. Rev.*, 1994, 132, 201-208.

16. Y. Kawamura, J. Brooks, J. J. Brown, H. Sasabe and C. Adachi, *Phys. Rev. Lett.*, 2006, 96, 017404.

17. S. Bernhard, J. A. Barron, P. L. Houston, H. D. Abruña, J. L. Ruglovksy, X. Gao and G. G. Malliaras, *J. Am. Chem. Soc.*, 2002, 124, 13624-13628.

18. H. Rudmann, S. Shimada and M. F. Rubner, *J. Am. Chem. Soc.*, 2002, 124, 4918-4921.

19. H. Rudmann and M. F. Rubner, *J. Appl. Phys.*, 2001, 90, 4338-4345.

20. D. Rendall, *Fluorescence and Phosphorescence*, 1987, Thames Polytechnic, London.

21. J. Lakowicz, *Principles of Fluorescence Spectroscopy, 3rd Edition*, 2006, Springer.

22. H. J. Bolink, L. Cappelli, E. Coronado, M. Grätzel and M. K. Nazeeruddin, *J. Am. Chem. Soc.*, 2006, 128, 46-47.

23. S. J. Adams, D. J. Lewis, J. A. Preece and Z. Pikramenou, *ACS Appl. Mater. Interfaces*, 2014, 6, 11598-11608.

24. H. Zhang, B. Li, B. Lei, W. Li and S. Lu, *Sens. Actuator B-Chem.*, 2007, 123, 508-515.

25. M. Wrighton and D. L. Morse, *J. Am. Chem. Soc.*, 1974, 96, 998-1003.

26. P. Innocenzi, H. Kozuka and T. Yoko, *J. Phys. Chem. B*, 1997, 101, 2285-2291.

27. N. W. Alcock, P. R. Barker, J. M. Haider, M. J. Hannon, C. L. Painting, Z. Pikramenou, E. A. Plummer, K. Rissanen and P. Saarenketo, *J. Chem. Soc., Dalton Trans*, 2000, 1447-1462.

28. M. Ogawa, T. Nakamura, J. Mori and K. Kuroda, *J. Phys. Chem. B*, 2000, 104, 8554-8556.

29. P. N. Minoofar, R. Hernandez, S. Chia, B. Dunn, J. I. Zink and A. C. Franville, *J. Am. Chem. Soc.*, 2002, 124, 14388-14396.

6 Using gold nanoparticles to aid the properties of ruthenium complexes in Dye Sensitized Solar Cells

6.1 Introduction

Plasmonic and electron charge effects have been shown to lead to enhancements in Dye Sensitized Solar Cells (DSCs) through the use of semiconductor and metallic nanoparticles. Enhancement has been achieved through the use of quantum dots[1-3] and both gold[4-6] and silver metallic nanoparticles.[7-9] Metallic nanoparticles have been demonstrated to show enhancement in silicon p-n junction,[10] organic[11, 12] and perovskite[13] solar cells as well as DSCs. Gold nanoparticles (AuNP) are widely used in solar cells due to their easily tuneable size and shape and enhancement properties.[14-20] They have been shown to lead to enhancements in DSCs through a combination of three factors:[15, 21-23] 1. The AuNP create a Schottky barrier with the TiO_2 - their localised electromagnetic field can influence charge separation through shifting the Fermi Energy more negative and thus increasing the efficiency of charge transfer (Figure 6.1);[24-27] 2. AuNP of over 20 nm have a large scattering contribution which can increase the light intensity reaching the TiO_2 surface and lead to better photon management;[14, 28, 29] 3. The surface plasmon resonance (SPR) excitation enhances charge carrier generation, resulting in an increase in photocurrent.[30, 31] Komarala *et al.* have demonstrated a 15% increase in DSC efficiency when 36 nm AuNP are mixed into the TiO_2 electrode at 0.24 wt%.[32] There are many methods for attaching AuNP to TiO_2 through bonding with an organic linker,[16, 33] reduction using $NaBH_4$,[34, 35] electrochemically[36] or photocatalytically with UV-light.[37] For use in solar cells, the AuNP are seen to be incorporated into the electrode through drying on the surface,[17, 38] mixing with the TiO_2 nanoparticle,[16, 39] using an organic linker[16] and incorporating into the TiO_2 nanoparticle.[39, 40] Yao *et al*. attach 5 nm AuNP to TiO_2 electrode through the use of a (3-Mercaptopropyl)trimethoxysilane linker.[16]

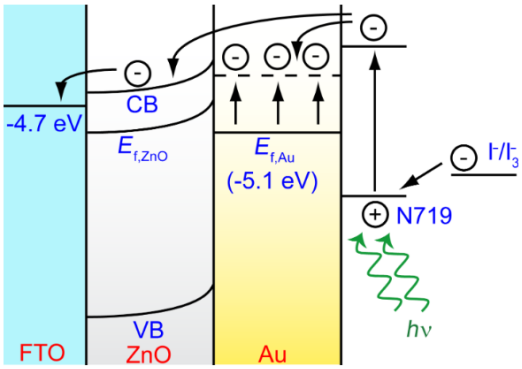

Figure 6.1: Energy-band diagram showing the Schottky barrier and electron-transfer path in a ZnO/Au DSC. Taken from reference.[41]

The most widely used linker for attachment of sensitizer to the TiO_2 is the carboxylate, however there have been questions over its stability on titania. It has been shown that the carboxylate will dissociate from the TiO_2 surface under long irradiation times.[42] Yu *et al.* have demonstrated that for a cell with N719 dye there is a decrease in short – circuit current and thus a decrease in overall efficiency with time.[43] This decrease is attributed to a combination of N719 desorption from the TiO_2 surface through reaction with the iodide – iodine electrolyte[44] and photodegregation of the dye, especially under UV light.[45, 46] It is important to increase the strength of the anchor unit to allow for high stability of the cells. Many other linkers have been investigated such as pyridine,[47] phosphoric acid,[48, 49] 8-hydroxylquinoline[50] and silyl.[39] Zamborini *et al.* have looked into using a silylether as the linker attached to a bis-bipyridine ruthenium dye and found an increase in stability of efficiency over time, compared to the COOH linker, due to the increased strength of the Si-O-Ti covalent bond. [39, 51, 52] Although these groups show strong bonding to the TiO_2, they have poor electron injection, leading to low efficiencies. An anchor unit requires strong binding for long term stability and fast electron injection of the sensitizer for high efficiencies.

The sulfur – gold bond has been highly researched and is known for its strong bonding energies (50-100 kJ mol^{-1}).[53-56] By attaching a gold layer to the TiO_2 surface, it opens up the possibility of using sulfur as the anchor unit, which due to its strong bonding can lead to

improved lifetimes of the cells. Toma *et al.* have attempted to use the sulfur – gold bond to take advantage of plasmonic enhancement in DSCs by attaching a layer of AuNP to the sensitizer, however this does not demonstrated an enhancement (Figure 6.2).[57] Sulfur can be incorporated into ruthenium complexes through easy synthetic steps.[58, 59] It has been shown that ruthenium complexes have efficient electron transfer to AuNP and thus should be sufficient in acting as a sensitizer for Au/TiO_2 DSCs.[60, 61]

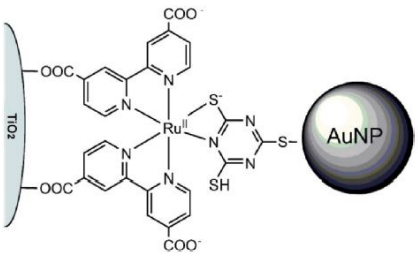

Figure 6.2: Schematic to show a ruthenium dye with the carboxylates bonding to the TiO_2 surface and the sulfur bonding to the AuNP. Taken from reference.[57]

Many papers have used the N719 dye with AuNP to demonstrate enhancement in DSC efficiency.[17-19, 62, 63] Bououdina *et al*. demonstrated a 40% enhancement in efficiency of the N719 TiO_2 solar cell in the presence of pM concentrations of 15 nm AuNP (prepared by laser ablation) mixed in with the N719 dye solution for electrode coverage.[18] Their methods vary between attaching the AuNP before or after the sensitizer. Attaching the sensitizer after the AuNP however does lead to complications due to the fact that both the carboxylate and thiocyanate group can bond to gold. When gold isn't present, the carboxylates of the N719 bind to the TiO_2 surface and the thiocyanate interacts with the electrolyte.[64, 65] When gold is present, it has been shown that the N719 flips and the thiocyanate binds to the gold and the carboxylates faces the electrolyte (Figure 6.3).[40, 65, 66] This will change the position of the highest occupied molecular orbital (HOMO) and the lowest unoccupied molecular orbital (LUMO) and its properties as a sensitizer. Removal of these carboxylate groups to produce a bis-bipyridine system will removed this problem of the orientation of the dye.

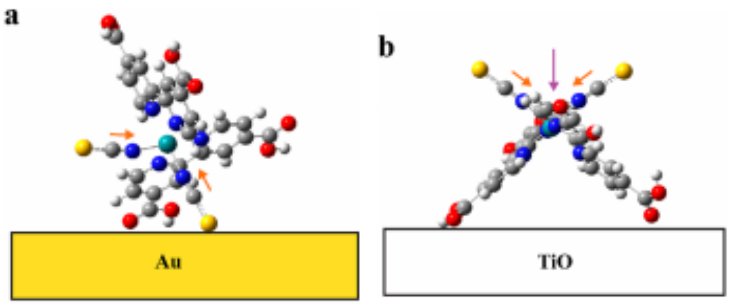

Figure 6.3: Schematic to show the absorption geometry of N3 on Au (a) and TiO_2 (b) surface. White = hydrogen, grey = carbon, red = oxygen, blue = nitrogen, yellow = sulfur, and teal = ruthenium. Taken from reference.[65]

Ruthenium bis-bipyridine complexes with thiol-functionalised anchor units have previously been synthesised and shown to attached to AuNP.[59, 67] The nanoprobe has been demonstrated to adopt the photophysical properties of the molecular probes (Figure 6.4).

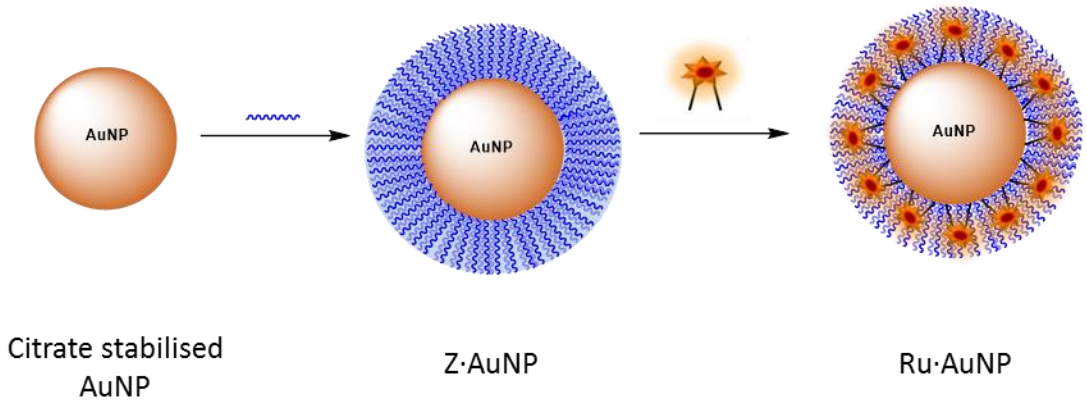

Figure 6.4: Schematic to show the attachment of surfactant and ruthenium complex to AuNP.

6.1.1 Chapter summary

In this chapter, ruthenium coated AuNP have been investigated for applications in DSCs. AuNP have been demonstrated in the literature to lead to enhancements in efficiency. In addition, using AuNP allows for use of a sulfur linker on the ruthenium sensitizer. The widely used carboxylate-TiO_2 bond has been shown to be weak, leading to poor lifetime of the solar cells, whereas the Au-S bond is known to be strong. The efficiency and stability of carboxylate and thiocyanate free ruthenium sensitizers attached to AuNP for use in DSCs were investigated. Through using previously characterised nanoprobes (thiol functionalised

ruthenium complexes attached to AuNP) improvements to the efficiency and lifetime were attempted. Four complexes: RuS1; RuS12; RuphenS12 and RuSconj (Figure 6.5), previously synthesised and characterised attached to AuNP were incorporated into a TiO_2 electrode and characterised. The efficiency was monitored through current – voltage experiments, both in the presence and absence of gold, and reported.

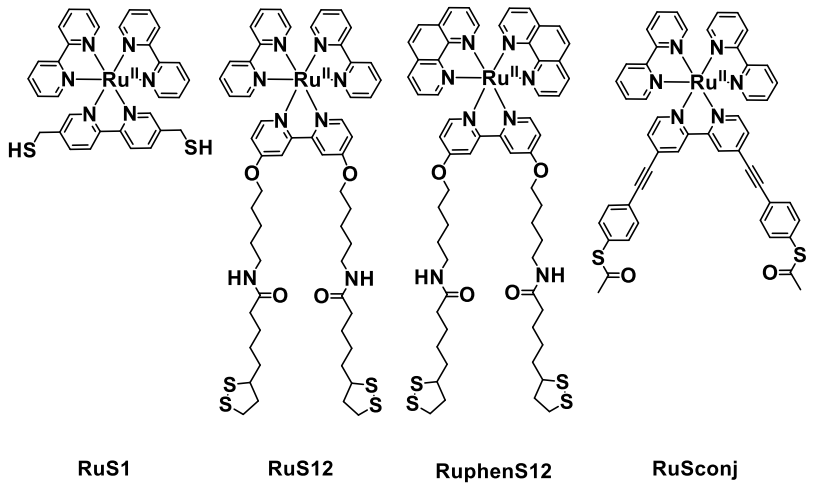

Figure 6.5: Schematic to show the structures of RuS1, RuS12, RuphenS12 and RuSconj.

6.2 Results and discussion

6.2.1 Preparation of titania electrodes

The titania electrodes (@TiO_2) were used as the anode in the solar cell for comparison of the dyes and different gold coated systems. They were prepared through the doctor blading technique; titania paste was coated onto fluorine doped tin oxide (FTO) conductive glass, followed by sintering at 500 °C. To incorporate the gold, two methods were taken from the literature; a 5 nm Au layer evaporated on the surface (@Au+TiO_2) and AuNP13 dried on the surface (@AuNP13+TiO_2).[17] The electrodes were characterised using scanning electron microscopy (SEM), transmission electron microscopy (TEM) and solid state absorption.

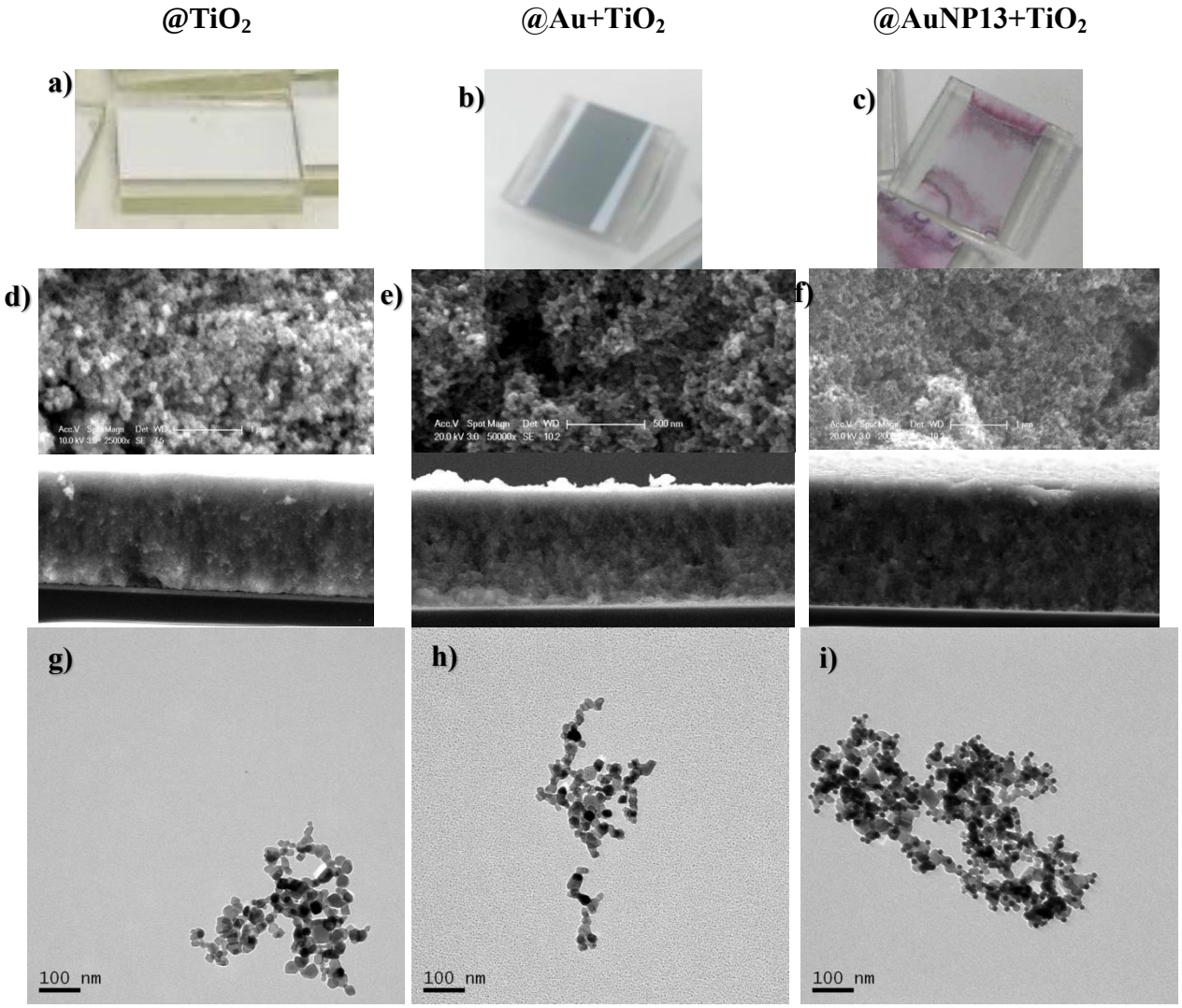

Figure 6.6: Images of the electrodes @TiO_2 (a), @Au+TiO_2 (b) and @AuNP13+TiO_2 (c). SEM images of the electrode surface (top) and cross section (bottom) for @TiO_2 (d), @Au+TiO_2 (e) and @AuNP13+TiO_2 (f). TEM images of the electrode particles of @TiO_2 (g), @Au+TiO_2 (h) and @AuNP13+TiO_2 (i).

Visually the electrodes are different; @TiO_2 appears as a white surface, @Au+TiO_2 (the 5 nm evaporated gold layer) has a metallic grey colour and the AuNP surface through evaporation (@AuNP13+TiO_2) appears pink (Figure 6.6.a-c).

From the SEM images, it is apparent that there is a rough surface, which is seen in the literature (Figure 6.6.d-f).[68, 69] These images however do not show a clear difference between the three electrodes, so the gold coating cannot be characterised through this method. This is due to both the low resolution of the instrument and the high eV beam penetrating through the 5 nm Au layer. The cross section shows the thickness of the surfaces to be around 15 µm.

From the TEM, the differences in the surfaces are clearer (Figure 6.6.g-i). The TEM samples were prepared through dissolving Degussa P-25 TiO_2NPs in water with (@AuNP13+TiO_2) and without (@TiO_2 and @Au+TiO_2) 1 nM AuNP13, and drying them onto a copper grid. @Au+TiO_2 was then taken and a 5 nm Au layer was evaporated onto the surface. The @TiO_2 TEM image (Figure 6.6.g) is similar to the SEM of TiO_2 NPs (Figure 6.19), showing a large clump of smaller NPs of different sizes and shapes. This can be seen for both @Au+TiO_2 and @AuNP13+TiO_2. @Au+TiO_2 (Figure 6.6.h) has the addition of small NPs (< 5 nm) covering the whole sample. This shows that the 5 nm Au layer formed by evaporation is not a continuous layer, but a collection of small NPs. For the image of @AuNP13+TiO_2, AuNP13 can be seen only in association with the TiO_2NPs, showing that they bond to the TiO_2.

To analyse the gold coating of the electrodes, solid state absorption in the form of percentage reflectance (%R) was performed (Figure 6.7). The @TiO_2 electrode has a gradual increase in reflectance (decrease in absorption) from 800 – 400 nm where there is a large drop in reflectance (peak in absorption) at 350 nm. This is similar to what is seen in the literature.[32, 68, 70] For both of the gold coated surfaces, a peak between 500 – 600 nm is seen, which is in correlation with the AuNP SPR (Section 3.2.2). @Au+TiO_2 has a slight blue shift due to being formed of smaller AuNP (< 5 nm).[71] The peak intensities are similar, showing similar gold coverage of the TiO_2 electrodes.

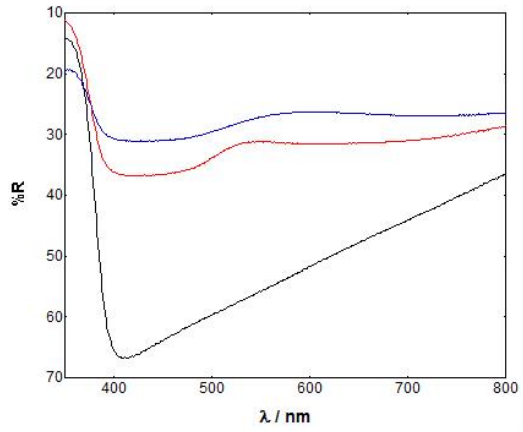

Figure 6.7: Solid state absorption of @TiO_2 (black), @Au+TiO_2 (red) and @AuNP13+TiO_2 (blue).

6.2.2 Choosing ruthenium dyes for use in Dye Sensitized Solar Cells

RuS1, RuS12, RuSconj and RuphenS12 were used because their photophysics have been previously studied attached to AuNP (Section 3.2.1.2 and 4.2.3). RuS1 (short) and RuS12 (long) were chosen to investigate the distance dependence between the photoactive ruthenium centre and the gold surface on the efficiency of the cell. RuSconj and RuphenS12 were chosen to investigate the effect of conjugation of the ligand and the use of a bis-phenanthroline system respectively on the efficiency.

6.2.3 Ruthenium dye coating of gold-titania electrodes

Four ruthenium dyes (RuS1, RuS12, RuphenS12 and RuSconj) were attached to a TiO_2 electrode coated in gold. The electrodes were soaked in the dyes for 24 hours for complete surface coverage. The surface coverage was characterised using solid state absorption and X-ray Photoelectron Spectroscopy (XPS) and the performance in solar cells was determined by the efficiency of the cell (which was characterised through current – voltage graphs). Each cell was run on the solar simulator three times to create an average result. Three cells for each dye were tested and the values reported are the averages from the three electrodes.

The efficiency is calculated from the current – voltage graphs. The voltage (V) is varied between -1.0 and 1.5 V and the current (J) is measured (Figure 6.8). The open-circuit voltage (V_{OC}) and short-circuit current (J_{SC}) are the values from the intercept of the graph at the x and y axis respectively, where the current and voltage are maximum. The maximum power (P_{max}) is calculated from the maximum voltage (V_{max}) and current (J_{max}) (Equation 6.1). V_{max} and J_{max} are the values that lead to the maximum power. The overall efficiency of the system (η) is calculated as the percentage of output energy (P_{max}) to input energy (P_s) (Equation 6.2).[72] The fill factor (FF) is also calculated (Equation 6.3) and represents the losses from the cell.

$$P_{max} = J_{max}\, x\, V_{max} \qquad \textbf{Equation 6.1}$$

$$\eta = \frac{P_{max}}{P_S} \text{ x } 100 \qquad \textbf{Equation 6.2}$$

$$FF = \frac{P_{max}}{Jsc\, x\, Voc} \qquad \textbf{Equation 6.3}$$

N719 was used as a standard to compare these systems with the literature as it has been greatly studied.[15, 32, 73-75] Efficiencies of 2 – 8% have been seen for the N719@TiO_2 system in the literature. This N719@TiO_2 system has an efficiency of 3.3% and the N719@Au+TiO_2 and N719@AuNP13+TiO_2 have efficiencies of 3.5 and 3.1% respectively (Figure 6.8, Table 6.1). This is on the lower end of what is seen in the literature as optimisation of cell assembly was not performed.

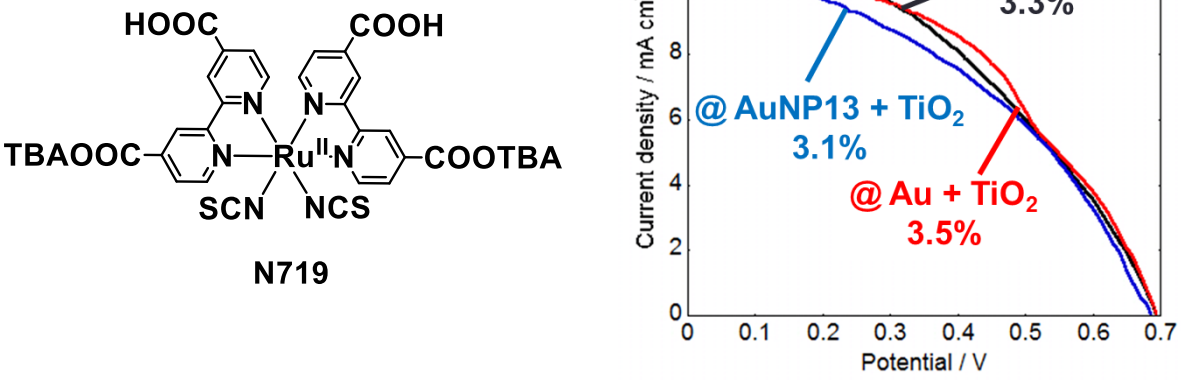

Figure 6.8: Schematic to show structure of N719 (left) and current – voltage graph of N719@TiO_2 (black), N719@Au+TiO_2 (red) and N719@AuNP13+TiO_2 (blue) (right). Electrodes were run on the Solar simulator, illuminated at 1 Sun (100 mW cm^{-2}), AM 1.5 illumination.

Table 6.1: Measured current (J_{SC}) and voltage (V_{OC}) and calculated maximum power (P_{max}), fill factor (FF) and efficiency (η) for N719@TiO_2, N719@Au+TiO_2 and N719@AuNP13+TiO_2.

	J_{SC} / mA cm^{-2}	V_{OC} / V	P_{max} / mW cm^{-2}	FF	η / %
N719@TiO_2	11.29	0.69	3.25	0.42	3.25
N719@Au+TiO_2	11.23	0.69	3.50	0.45	3.50
N719@AuNP13+TiO_2	11.16	0.68	3.05	0.40	3.05

The current, voltage and efficiency for N719@Au+TiO_2 and N719@AuNP13+TiO_2 are similar, showing that there is no difference on the effect between the @Au+TiO_2 and @AuNP13+TiO_2 surfaces. The gold coated surfaces have similar properties to the N719@TiO_2 surface, showing that the presence of the gold has no effect on the efficiency. There are examples in the literature of AuNP leading to enhancements in efficiency due to plasmonic enhancement and electron transfer, however this is not seen in this system and all three electrodes (N719@TiO_2, N719@Au+TiO_2 and N719@AuNP13+TiO_2) lead to similar efficiencies (Figure 6.8, Table 6.1).

The absorption spectra for N719 in solution, N719@TiO_2 and N719@Au+TiO_2 were recorded (Figure 6.9). In solution, N719 has two maximum absorptions at 370 and 500 nm. Upon attachment to the surface, these maxima red-shift by 30 nm (400 and 530 nm). This agrees with literature and can be attributed to the interaction of N719 with the TiO_2.[76, 77] This large shift arises from the photoactive ruthenium centre being close to the surface. There is no shift seen between the maximum in N719@TiO_2 and N719@Au+TiO_2.

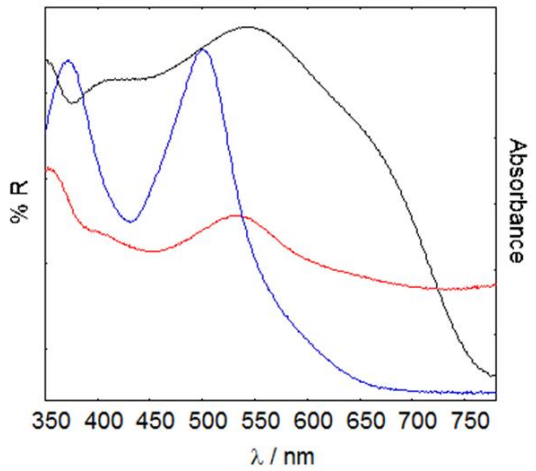

Figure 6.9: Absorption of N719 in MeOH (blue), N719@TiO_2 (black) and N719@Au+TiO_2 (red).

RuphenS12@Au+TiO_2, RuSconj@Au+TiO_2, RuSi@TiO_2, @Au+TiO_2, @AuNP13+TiO_2, RuS1@Au+TiO_2 and RuS12@Au+TiO_2 were prepared and absorption (Figure 6.10), XPS and current – voltage (Figure 6.12) data was taken.

As for N719, a small red-shift can be seen for the dyes when attached to the electrodes, compared to in solution (Figure 6.10). The level of dye coating can be estimated from the ratio of the dye absorbance (450 nm) to the TiO_2 absorbance (350 nm). RuS12 appears to have the highest coating, with the singlet MLCT peak of RuS12 approximately the same as the TiO_2 absorbance. RuphenS12 in comparison appears to have the lowest coating, with a very small singlet MLCT peak.

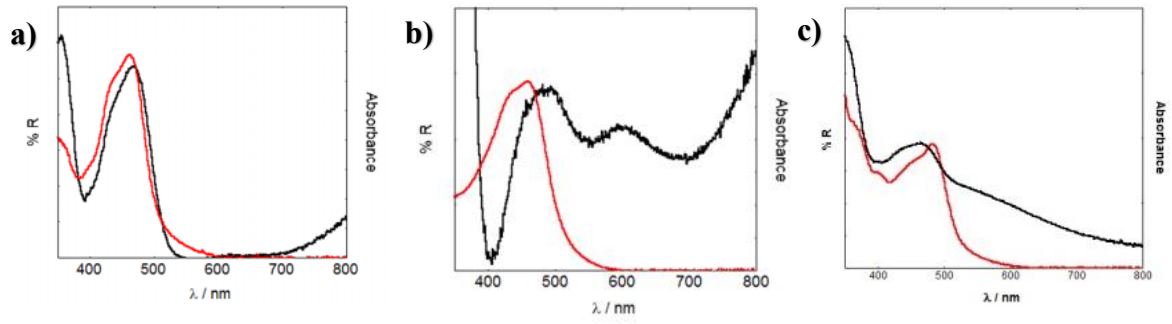

Figure 6.10: Absorption of RuS12 (a), RuphenS12 (b) and RuSconj (c) in solution (red) and attached to @Au+TiO_2 (black).

XPS was used to characterise the surface of the electrodes to show the presence of the gold and ruthenium attached to the TiO_2 surface (Table 6.2). The DSC surfaces were examined for the presence of gold, ruthenium, sulfur and titanium.

Table 6.2: XPS data for @Au+TiO_2, RuphenS12@Au+TiO_2 and RuphenS12@AuNP13+TiO_2.

	Literature / eV	@Au+TiO_2 / eV	RuphenS12 @Au+TiO_2 / eV	RuphenS12 @AuNP13+TiO_2 / eV
Au 4f 7/2	84	84.0	84.0	84.0
Au 4f 5/2	88	87.7	87.8	87.7
S 2p 3/2	164	X	162.3	161.8
S 2p 1/2	165	X	163.5	163.0
Ru 3d 5/2	280	X	280.8	280.9
Ru 3d 3/2	284	X	284.9	285.0
C 1s	285	285.0	285.1	285.1
Ti 2p 3/2	454	454.0	454.0	453.9
Ru 3p 3/2	461	X	458.2	459.3
Ti 2p 1/2	460	460.0	460.2	460.2
Ru 3p 1/2	483	X	X	X

For all electrodes, the peaks are slightly shifted from the literature values which can be caused by the oxidation state of the element and the local chemical and physical environment (Figure 6.11).[78, 79] All of the electrodes show the presence of Ti with peaks at 460 and 454 for the Ti

2p 3/2 and 1/2 respectively (Figure 6.11.d) and the peaks for Au 4f 7/2 and 5/2 at 84 and 88 eV respectively (Figure 6.11.a). It is difficult to characterise the presence of ruthenium due to the peak at 284 eV for Ru 3d 3/2 being over-shadowed by a large peak for C 1s (Figure 6.11.c) and the peak at 461 eV for Ru 3p 3/2 being over-shadowed by a large peak for Ti 2p 1/2 (Figure 6.11.d). There is however a small peak at 280 eV seen for Ru 3d 5/2, although it is not conclusive for the presence of ruthenium attached to the surface. The absorption data above does however confirm the presence of the ruthenium. The peak at 162 eV for S 2p 3/2 shows the presence of a sulphide atom, suggesting the ruthenium complex is chemisorbed to the gold surface.[80, 81]

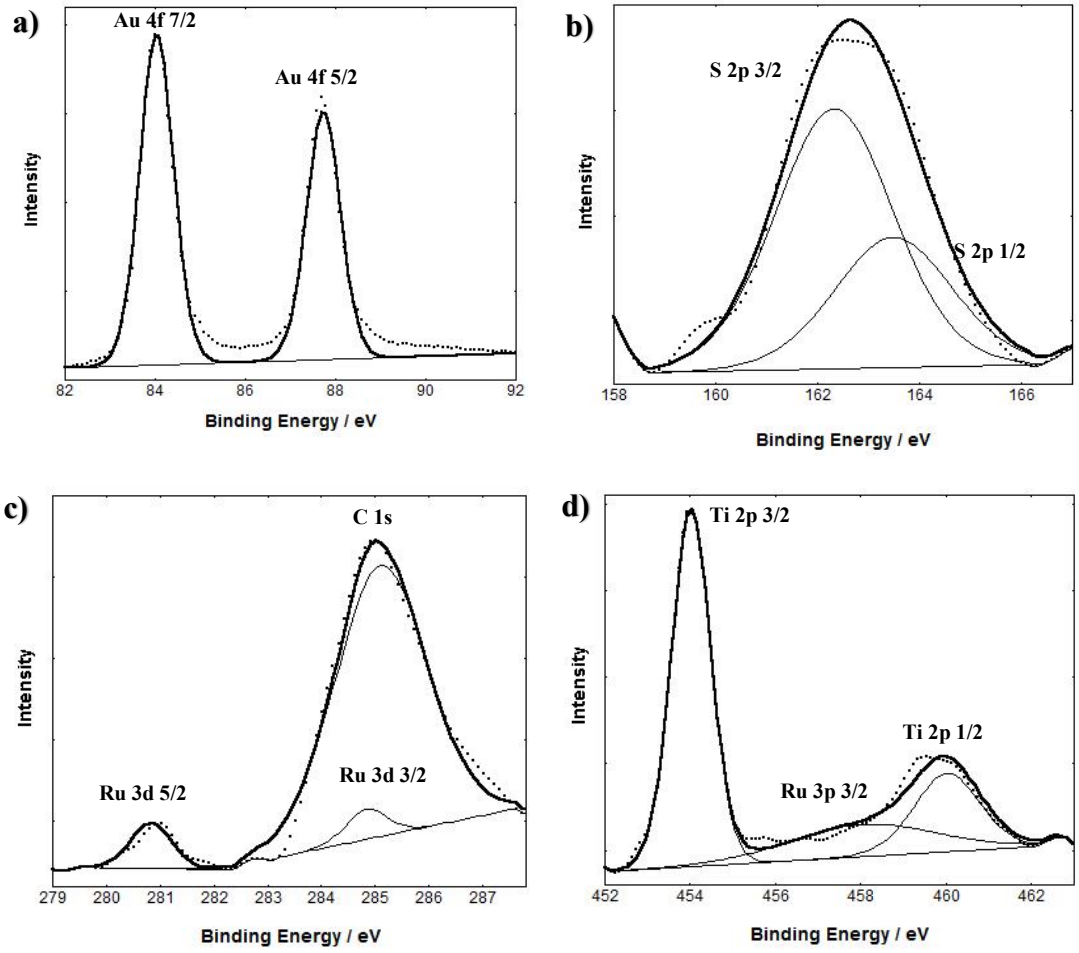

Figure 6.11: XPS binding energy showing the regions of Au 4f (a), S 2p (b), Ru 3d (c) and Ru 3p (d) for RuphenS12@Au+TiO_2.

The ruthenium sensitized gold-titania electrodes were run on the Solar Simulator and the current, voltage, fill factor and efficiency were calculated (Equation 6.1-6.3). The current – voltage graphs show that RuphenS12@Au+TiO_2 has the highest efficiency at 1.0%, with all the other electrodes having an efficiency in the range 0.3 – 0.5% (Figure 6.12, Table 6.3).

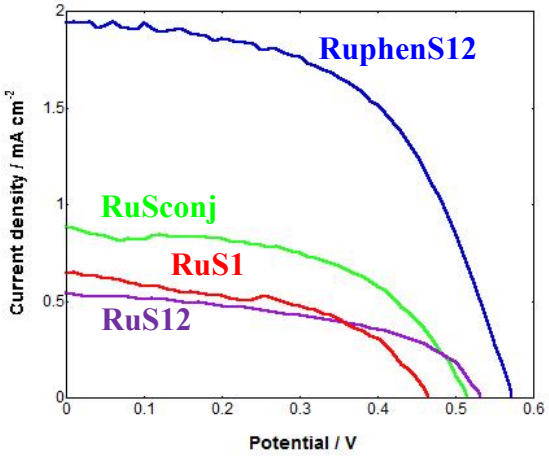

Figure 6.12: Current – Voltage graphs for electrodes RuphenS12@Au+TiO_2 (blue), RuSconj@Au+TiO_2 (green), RuS1@Au+TiO_2 (red) and RuS12@Au+TiO_2 (purple). Electrodes were run on the Solar simulator, illuminated at 1 Sun (100 mW cm^{-2}), AM 1.5 illumination.

Table 6.3: Measured current (J_{SC}) and voltage (V_{OC}) and calculated maximum power (P_{max}), fill factor (FF) and efficiency (η) for RuS1@Au+TiO_2, RuS12@Au+TiO_2, RuphenS12@Au+TiO_2 and RuSconj@Au+TiO_2.

	J_{SC} / mA cm^{-2}	V_{OC} / V	P_{max} / mW cm^{-2}	FF	η / %
RuS1@Au+TiO_2	0.64	0.46	0.15	0.49	0.15
RuS12@Au+TiO_2	0.54	0.53	0.14	0.50	0.14
RuphenS12@Au+TiO_2	3.3	0.6	1.0	0.5	1.0
RuSconj@Au+TiO_2	0.89	0.51	0.24	0.53	0.24

This enhanced efficiency suggests that there is faster electron transfer between the photoactive ruthenium centre of RuphenS12 and the TiO_2 electrode, compared to the other dyes. This was confirmed through time – resolved studies of the electrodes (Figure 6.13).

RuS12 and RuphenS12 both see a large quenching of lifetime when attached to @TiO_2, showing electron transfer from the photoactive centre to the electrode (Figure 6.13.c). For

both complexes, a tri-exponential lifetime is seen. The first lifetime has a small contribution (< 10%) and is attributed to scattering, so only the longer lived lifetimes are reported. RuS12@TiO_2 has a long and short lifetime of 50 (38%) and 15 ns (55%) respectively. This is a six times decrease when compared to the solid state properties. RuphenS12@TiO_2 has a long and short lifetime of 20 (42%) and 5 ns (48%) respectively. This is a thirty times decrease when compared to the solid state properties. This shows that the quenching of RuphenS12 lifetime, and thus rate of electron transfer by @TiO_2 is five times more efficient than for RuS12, leading to a greater DSC efficiency.

In the solid state absorption, there is a peak between 400 – 500 nm belonging to the singlet MLCT for both complexes (Figure 6.13.a&b). The excitation at 650 nm mirrors the absorption, showing that the luminescent properties measured belong to the ruthenium dyes. The emission maximum for RuS12@TiO_2 is approximately the same as for the molecular probe, however for RuphenS12@TiO_2 it has red-shifted by 40 nm (670 nm). This is due to the TiO_2 interacting with the probe and causing a change in the energy levels.

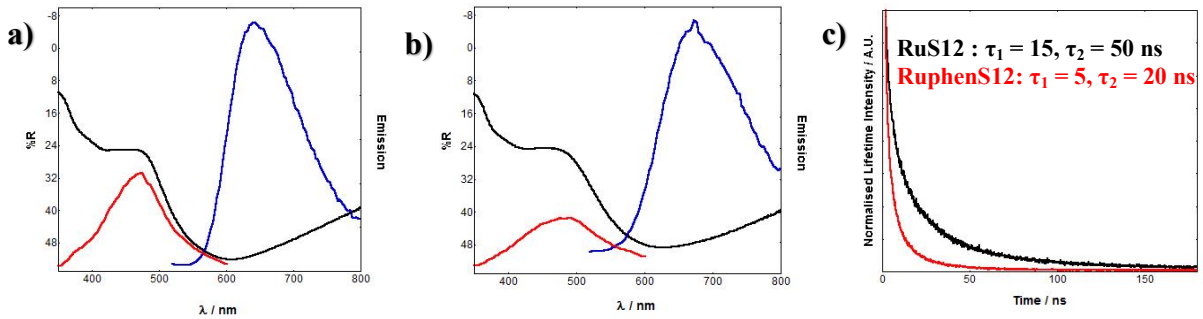

Figure 6.13: Solid state absorption (black), luminescence emission (blue) and excitation (red) data of RuS12@TiO_2 (a) and RuphenS12@TiO_2. Luminescent lifetime of RuS12@TiO_2 (black) and RuphenS12@TiO_2 (red) (c). λ_{exc} = 445 nm and λ_{det} = 650 nm. X^2 was fitted between 1.0 and 1.2 for both lifetimes.

It was expected that RuSconj@Au+TiO_2 would have a greater efficiency due to its high conjugation and larger molar absorptivity (21000 M^{-1} cm^{-1}). It has been shown that increasing the molar absorptivity increases the efficiency of DSCs.[75] Although its efficiency is slightly higher than RuS1@Au+TiO_2 and RuS12@Au+TiO_2, the improvement is insignificant (Figure

6.14). This may be due to the rigid legs which cause lower packing (Section 4.2.5); however the packing by absorbance does not seem to be different compared to the other dyes (Figure 6.10, Table 6.3). As the conjugation is located on the binding legs, it may be causing slow electron transfer from the photoactive ruthenium centre and TiO_2 electrode.

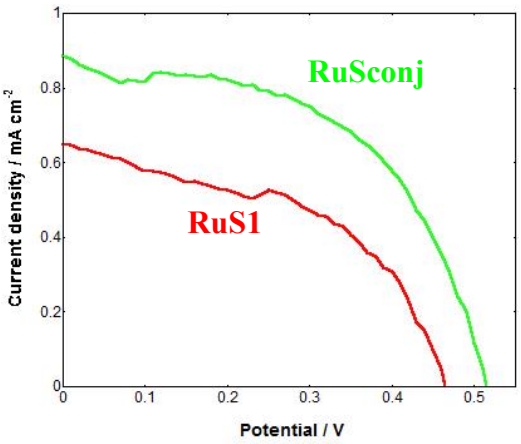

Figure 6.14: Current – Voltage graphs for electrodes RuSconj@Au+TiO_2 (green) and RuS1@Au+TiO_2 (red). Electrodes were run on the Solar simulator, illuminated at 1 Sun (100 mW cm^{-2}), AM 1.5 illumination.

RuS1@Au+TiO_2 and RuS12@Au+TiO_2 were tested to compare the effect of distance on the efficiency. It has been shown that RuS1 (short) has a larger quenching by AuNP when compared to RuS12 (long) due to the short distance from the gold surface and therefore more efficient quenching.[67] A hypothesis was that RuS1 would be a better sensitizer and have a greater efficiency due to the closer distance to the TiO_2 electrode surface, which allows for faster electron transfer through the system. This is not seen and there are minimal differences in efficiency between RuS1@Au+TiO_2 and RuS12@Au+TiO_2. What is seen however is that RuS1@Au+TiO_2 has a larger J_{max} and RuS12@Au+TiO_2 has a larger V_{max}, suggesting that differences are seen due to the change in distance, but these differences even out to give the same efficiency (Figure 6.15, Table 6.3). A larger J_{max} can arise from either an increase in molar absorptivity of the dye (η_{LH}) or faster electron injection into the TiO_2 electrode (η_{INJ}).[43] As both RuS1 and RuS12 have a similar molar absorptivity, this increase seen for RuS1@Au+TiO_2 is more likely due to more efficient electron injection (η_{INJ}) which can be

attributed to the decreased distance between the photoactive ruthenium centre and TiO_2 surface.

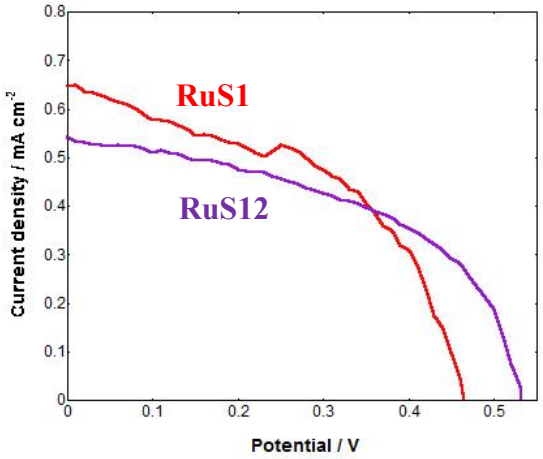

Figure 6.15: Current – Voltage graphs for electrodes RuS1@Au+TiO_2 (red) and RuS12@Au+TiO_2 (purple). Electrodes were run on the Solar simulator, illuminated at 1 Sun (100 mW cm^{-2}), AM 1.5 illumination.

As seen previously, the @Au+TiO_2 and @AuNP13+TiO_2 have similar properties, however what is interesting, is that the efficiency of the uncoated @Au+TiO_2 and @AuNP13+TiO_2 are also similar, if not improved, compared to the sensitizer coated surfaces (RuS1@Au+TiO_2 and RuS12@Au+TiO_2) (Figure 6.16, Table 6.4). This suggests that the RuS1 and RuS12 dye are having little effect on the efficiency and are not acting as sensitizers.

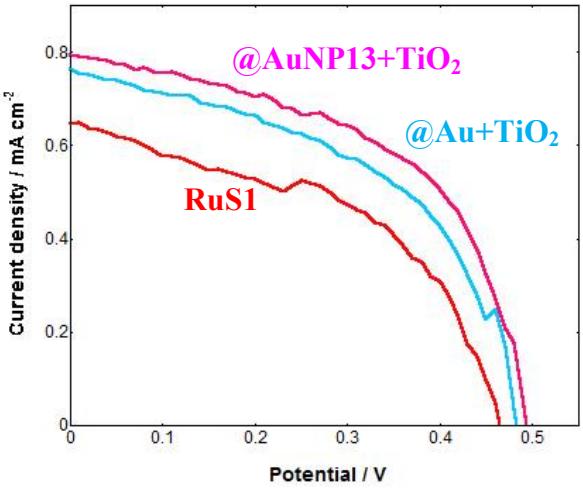

Figure 6.16: Current – Voltage graphs for electrodes RuS1@Au+TiO_2 (red), @Au+TiO_2 (pink) and @AuNP13+TiO_2 (light blue). Electrodes were run on the Solar simulator, illuminated at 1 Sun (100 mW cm^{-2}), AM 1.5 illumination.

Table 6.4: Measured current (J_{SC}) and voltage (V_{OC}) and calculated maximum power (P_{max}), fill factor (FF) and efficiency (η) for RuS1@Au+TiO_2, @Au+TiO_2 and @AuNP13+TiO_2.

	J_{SC} / mA cm^{-2}	V_{OC} / V	P_{max} / mW cm^{-2}	FF	η / %
RuS1@Au+TiO_2	0.64	0.46	0.15	0.49	0.15
@Au+TiO_2	0.78	0.50	0.21	0.53	0.21
@AuNP13+TiO_2	0.76	0.48	0.18	0.50	0.18

This data shows that RuphenS12 is acting as a sensitizer in RuphenS12@Au+TiO_2 but none of the other dyes appear to sensitize the TiO_2. It also shows that neither of the gold layers have an effect on the efficiency.

6.2.4 Comparison of ruthenium dye coating of titania electrodes without gold

RuSi was synthesised and characterised as a comparison ligand for direct attachment to the TiO_2 surface with no gold present (Figure 6.17).[39, 52, 82]

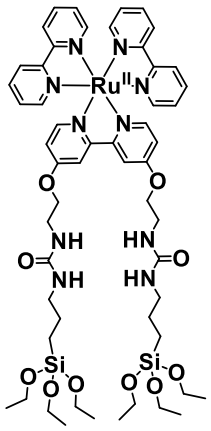

RuSi

Figure 6.17: Schematic to show the structure of RuSi.

6.2.4.1 Synthesis and photophysical characterisation of RuSi

RuSi was synthesised and characterised by ^{1}H NMR, ^{13}C NMR and ES^{+} MS. The synthesis is based on a method that was adapted from a previously published method in the Pikramenou group.[83] The ligand was synthesised through a Williamson ether reaction of N-(Boc)ethanolamine with 4,4'-dihydroxy-2,2'-bipyridine followed by complexation with

$Ru(bpy)_2Cl_2$ and formation of a urea bond with 3-(triethoxysilyl)propylisocyanate (Scheme 6.1). The complex was isolated as a chloride ion through washing with hexane and toluene to remove and unreacted material.

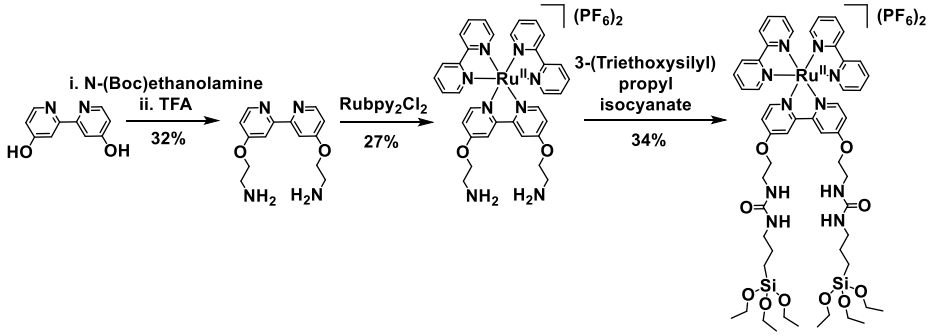

Scheme 6.1: Synthetic scheme for synthesis of RuSi.

The ^1H and ^{13}C spectrum of RuSi agrees with published material (Appendix).[83] The ES^+ MS has a peak with a characteristic ruthenium isotope pattern at 1327.8 m/z for the $[M\text{-}PF_6]^+$.

The absorption, steady state emission and excitation were taken for RuSi as a 6 µM solution in aerated methanol (Figure 6.18). The absorbance shows the singlet Metal to Ligand Charge Transfer (MLCT) (d - π*) between 400 – 500 nm with the maximum at 460 nm and molar absorptivity approximately 14000 M^{-1} cm^{-1}, which is similar to previously synthesised dyes (Section 3.2.1.2 and 4.2.3). The sharp Ligand Centre (LC) state (π - π*) is present at 290 nm with absorptions also seen at 430 and 240 nm assigned to the Metal Centre (MC) (d - d) and singlet MLCT (d - π*) respectively.[84] The emission shows the triplet MLCT broad band between 550 - 800 nm with the maximum at 650 nm. The excitation spectrum mirrors the absorbance, with the singlet MLCT between 400 – 500 nm and the LC at 290 nm. There is a decreased contribution of the LC excitation compared to the absorbance, which is seen for the other complexes (Section 3.2.1.2 and 4.2.3).

RuSi has a luminescent lifetime and quantum yield of 130 ns and 1% respectively. These are lower than $Ru(bpy)_3Cl_2$ (τ = 480 ns, Φ = 2.8%) and RuS12 (τ = 280 ns, Φ = 2%).[85] This can

be attributed to either internal quenching from the urea bond or quenching from residual ammonia from the last synthetic step which could not be removed.[86] Zhang *et al*. found a 14-fold decrease in luminescence lifetime of $[Ru(bpy)_3]^{2+}$ when NH_2 was attached to the bipyridine ring (1150 to 84 ns).[87]

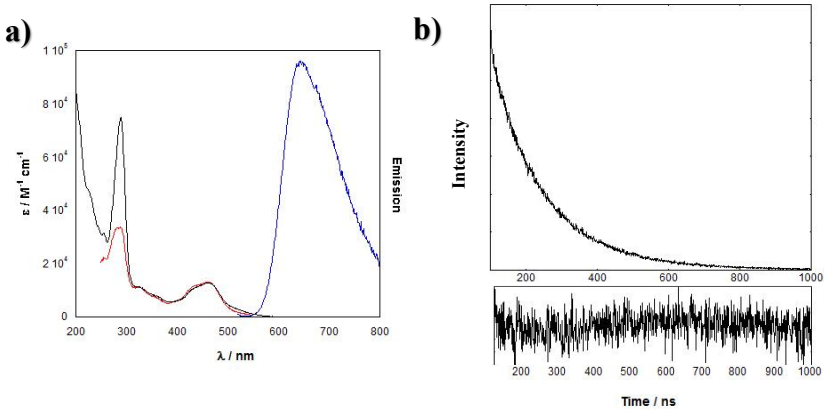

Figure 6.18: Absorption (black), luminescence emission (blue) and excitation (red) data (a), luminescent lifetime (top) and lifetime fit (bottom) (b) of 6 μM RuSi in aerated methanol. λ_{exc} = 445 nm and λ_{det} = 650 nm. X^2 is fitted between 1.0 and 1.2.

RuSi was attached to commercially available 200 nm TiO_2NPs, to form RuSi•TiO_2NP, and characterised. The TiO_2 NPs are 21 nm p25 Degussa, but from the TEM and dynamic light scattering (DLS) it is clear that the particles sinter together, creating larger non-spherical 200 nm particles, and are unaffected upon addition of RuSi (Figure 6.19).

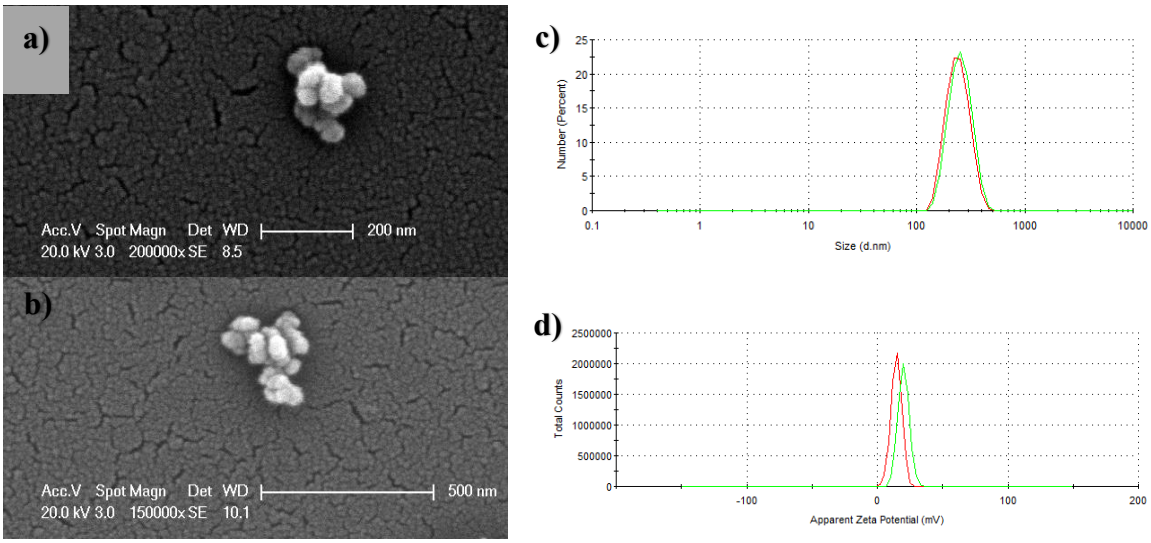

Figure 6.19: TEM of TiO_2 NP (a) and RuSi•TiO_2 NP (b) and DLS sizing number (c) and zeta potential (d) for TiO_2 NP (red) and RuSi•TiO_2 NP (green).

Absorption and steady state and time-resolved emission spectroscopy was performed on RuSi•TiO_2NP in water. The emission maximum is the same as for the molecular probe (650 nm). For the solid state absorption there is the singlet MLCT (d - π*) between 400 – 600 nm with maximum at 470 nm and the LC at 290 nm, which is similar to RuSi in methanol. The excitation at 650 nm mirrors the absorption of the molecular probe however there is no contribution from the LC to the triplet MLCT emission. This shows that when attached to TiO_2NP, the LC contribution to the emission is negligible. There is a slight red shift for the solid state absorption maximum, however it is know that solid state photophysical properties shift due to rigidity of the complex.

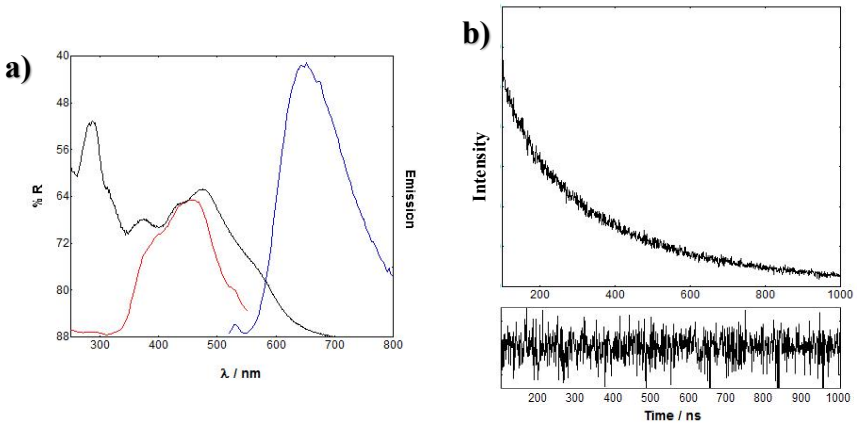

Figure 6.20: Absorption (black), luminescence emission (blue) and excitation (red) data (a), luminescent lifetime (top) and lifetime fit (bottom) (b) of RuSi•TiO_2NP in aerated water. λ_{exc} = 445 nm and λ_{det} = 650 nm. X^2 is fitted between 1.0 and 1.2.

It has been shown that the lifetime of ruthenium probes are quenched when attached to TiO_2 however this is not seen here.[88] There is a 2.5 times increase in luminescent lifetime of RuSi•TiO_2NP compared to the molecular probe (130 → 300 ns). This increase is most likely due to a reduction in dye – solvent interactions and therefore a decrease in quenching from ammonia.

6.2.4.2 Surface characterisation of RuSi•TiO_2NP

RuSi was attached to the TiO_2 electrode and characterised using solid state absorption, XPS and current – voltage graphs. The electrode was soaked in a solution of RuSi for 24 hours for complete surface coverage.

As for the other dyes, a small red-shift can be seen in the absorption of RuSi when attached to the electrode, compared to in solution (Figure 6.21). RuSi appears to have a similar level of dye coating of the electrode compared to RuS12 (Figure 6.10).

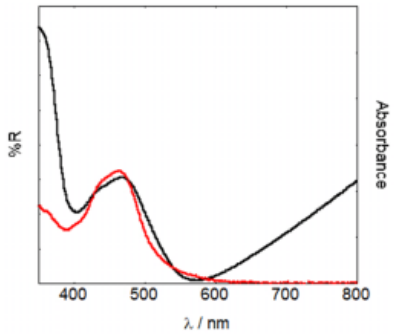

Figure 6.21: Absorption of RuSi in solution (red) and RuSi@TiO_2 (black).

XPS was used to characterise the surface of the electrodes to show the presence of the ruthenium attached to the TiO_2 surface (Table 6.5).

Table 6.5: XPS data of RuSi@TiO_2.

	Literature / eV	RuSi@TiO_2 / eV
Ru 3d 5/2	280	281.7
Ru 3d 3/2	284	285.7
C 1s	285	284.9
Ti 2p 3/2	454	254.0
Ru 3p 3/2	461	455.4
Ti 2p 1/2	460	460.0
Ru 3p 1/2	483	X

The peaks for the elements in RuSi@TiO_2 are slightly shifted from the literature values, which can be caused by the oxidation state of the element and the local chemical and physical environment (Figure 6.22).[78, 79] The presence of Ti is seen with peaks at 454 and 460 for the Ti 2p 3/2 and 1/2 respectively (Figure 6.22.b). As for the other electrodes, it is difficult to characterised the presence of ruthenium due to the peak at 284 eV for Ru 3d 3/2 being over-

shadowed by a large peak for C 1s (Figure 6.22.a) and the peak at 461 eV for Ru 3p 3/2 being over-shadowed by a large peak for Ti 2p 1/2 (Figure 6.22.b). There is however a small peak at 280 eV seen for Ru 3d 5/2, although it is not conclusive for the presence of ruthenium attached to the surface. The absorption data above does however confirm the presence of the ruthenium.

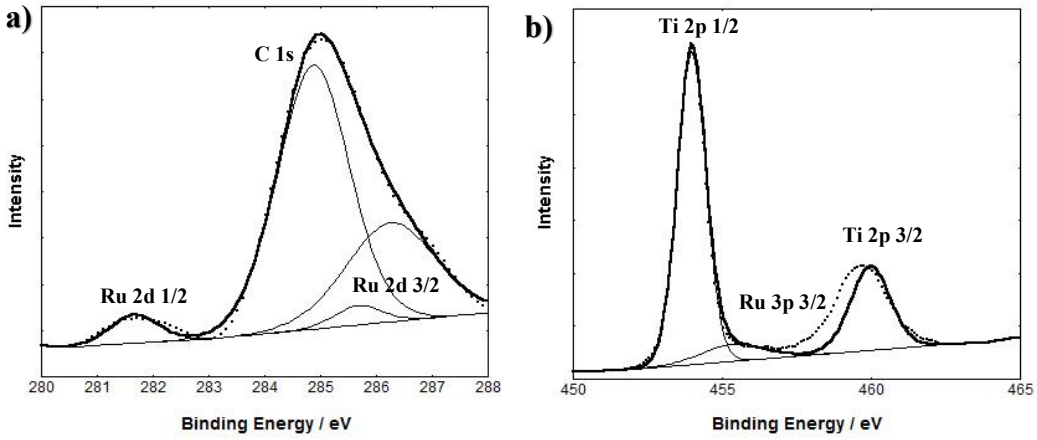

Figure 6.22: XPS binding energy showing the regions of Ru 3d (a) and Ru 3p (b) for RuSi@TiO_2.

RuSi@TiO_2 was run on the Solar Simulator and the current and voltage was measured and the maximum power, fill factor and efficiency were calculated (Equation 6.1-6.3). It was tested to compare the properties of the gold coated electrodes with just the TiO_2 surface (Figure 6.23, Table 6.6). RuSi has a similar structure to RuS12, but has the silyl groups for bonding to the TiO_2 surface, so a gold surface for attachment is not required. The efficiency for RuSi@TiO_2 and RuS12@Au+TiO_2 are similar, agreeing with previous data suggesting that the gold is not leading to an enhancement in efficiency (Section 6.3.3).

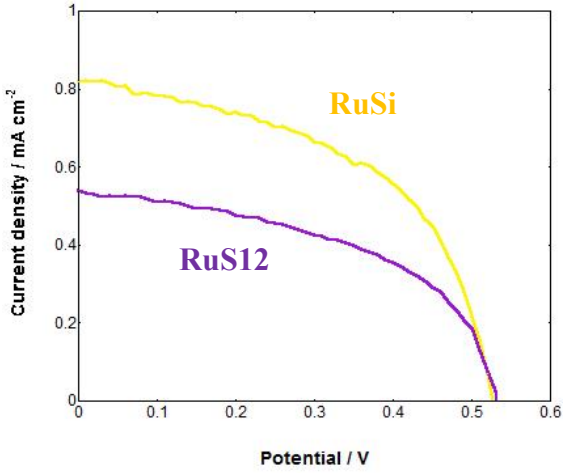

Figure 6.23: Current – Voltage graphs for electrodes RuSi@TiO_2 (yellow) and RuS12@Au+TiO_2 (purple). Electrodes were run on the Solar simulator, illuminated at 1 Sun (100 mW cm^{-2}), AM 1.5 illumination.

Table 6.6: Measured current (J_{SC}) and voltage (V_{OC}) and calculated maximum power (P_{max}), fill factor (FF) and efficiency (η) for RuSi@TiO_2 and RuS12@Au+TiO_2.

	J_{SC} / mA cm^{-2}	V_{OC} / V	P_{max} / mW cm^{-2}	FF	η / %
RuSi@TiO_2	0.82	0.52	0.22	0.52	0.22
RuS12@Au+TiO_2	0.54	0.53	0.14	0.50	0.14

6.2.5 Sustainability of electrodes

In addition to the fact that the gold layer has no effect on the efficiency, it was noticed that once the electrodes had been run in the cell there was a change in colour. It was suspected that this change in colour was caused by the gold being removed from the surface. As this colour change only occurs after the electrode has been assembled in a cell, it was attributed to interference of the iodide - iodine electrolyte. Gold coated electrodes were taken and soaked in iodide - iodine electrolyte for 30 seconds and washed with methanol. They were analysed before and after the wash both visually and by solid state absorption to confirm removal of the gold (Figure 6.24).

It is clear visually that the metallic grey colour belonging to the 5 nm Au layer has gone both after the electrolyte wash (Figure 6.24.b) and after the electrode was run in a cell (Figure

6.24.c). In the absorbance the same pattern is seen; before the electrolyte wash there is a peak between 500 – 600 nm for the gold SPR, however this peak is not seen after the electrolyte wash, and the absorbance reflects the TiO_2 surface only (Figure 6.7).

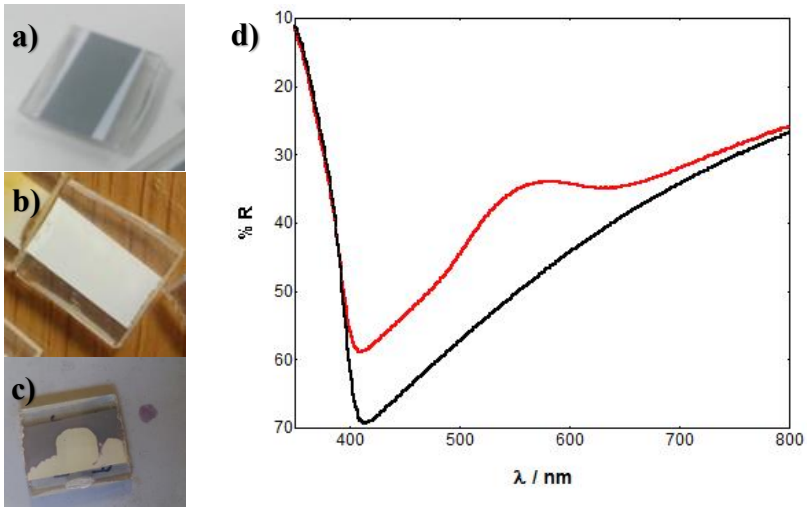

Figure 6.24: Photograph of @Au+TiO_2 before electrolyte wash (a), after electrolyte wash (b) and after run in a cell on the Solar Simulator (c). Solid state absorption of @Au+TiO_2 before electrolyte wash (red) and after (black) (d).

This was repeated with a ruthenium coated surface, RuphenS12@Au+TiO_2, to investigate if the dye was providing any protection of the gold. It is clear visually that after the electrolyte wash the metallic grey colour belonging to the 5 nm Au layer has gone, leaving behind a yellow colour of the ruthenium dye (Figure 6.25.a). This is also seen for the absorbance; before the electrolyte wash the electrode has a peak between 400 – 500 nm for the singlet MLCT of RuphenS12 and a shoulder around 600 nm for the gold SPR, whereas after the electrolyte wash, the gold SPR has disappeared and only the peak between 400 – 500 nm for the RuphenS12 is present (Figure 6.25.b).

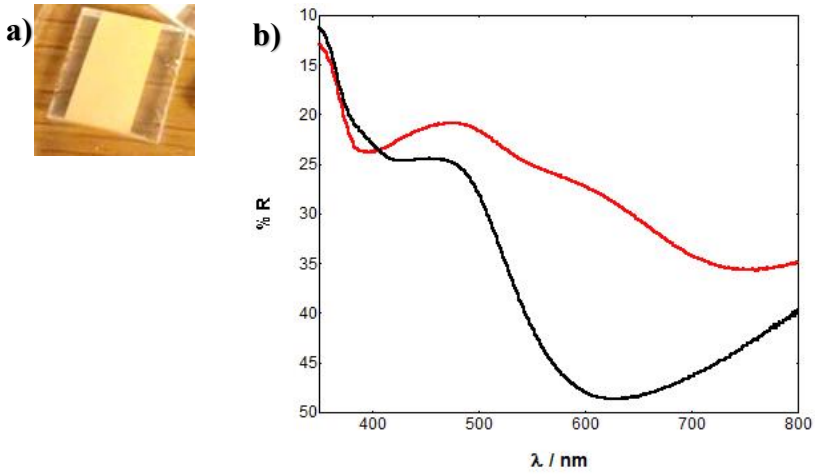

Figure 6.25: Photograph of RuphenS12@Au+TiO_2 after electrolyte wash (a) and solid state absorption before electrolyte wash (red) and after (black) (b).

This would suggest that the gold is being removed from the surface of the electrode by the electrolyte. Previous investigations have shown that iodide – iodine solutions of a certain concentration and pH can efficiently dissolve metallic gold, forming AuI_2^- (Equation 6.4 – 6.6).[89-92] Wang *et al*. demonstrated that extracting gold from its ore could be performed using iodide – iodine electrolyte rather than the environmentally unfriendly cyanide.[93] They found gold leaching rates of 85% at 25 °C.

Anodic:	$\mathbf{Au + 2I^- \rightarrow AuI_2^- + e^-}$	**Equation 6.4**
Cathodic:	$\mathbf{I_3^- + 2e^- \rightarrow 3I^-}$	**Equation 6.5**
Overall:	$\mathbf{2Au + I^- + I_3^- \rightarrow 2AuI_2^-}$	**Equation 6.6**

If this is the case, then it suggests that the ruthenium dye that is left behind is bonded to the TiO_2 surface. It has been shown that sulfur can bond to TiO_2 surfaces by sitting in oxygen vacancies.[94-99] You *et al.* has shown that SO_2 can be removed from flue gas using photocatalytic TiO_2 immobilised on glass beads.[100]

Further investigations were performed to characterise this dissolving of the gold. TEM images show the disappearance of AuNP13 after washing TiO_2NP with electrolyte (Figure 6.26). The

AuNP13 can be clearly seen in the first image interacting with the TiO_2NP but are not present after washing with electrolyte.

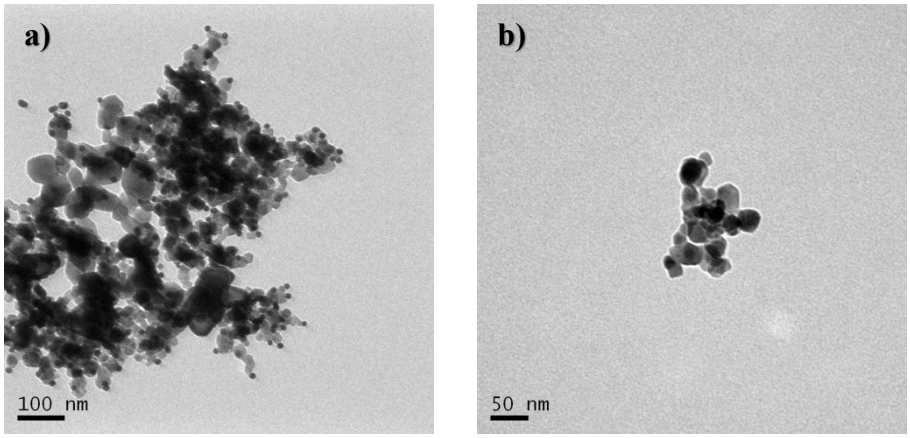

Figure 6.26: TEM image of @AuNP13+TiO_2 before (a) and after (b) wash with electrolyte.

Inductively Coupled Plasma Mass Spectrometry (ICP-MS) was performed on the electrodes before and after washing with electrolyte to monitor the gold content. A 0.5 cm^2 area was scrapped off the surface of the electrode and digested with ultra-pure aqua-regia. It was centrifuged for 30 minutes at 13000 G and the supernatant was tested. After washing the electrode with electrolyte the gold ion count decreased to similar levels to the @TiO_2 surface without gold (Table 6.7). The gold concentration in @Au+TiO_2 decreases from 510 to 7 ppb after electrolyte wash.

Table 6.7: ICP-MS results showing the Au ions for electrodes before and after electrolyte wash.

	Au ions before wash / ppb	Au ions after wash / ppb
RuS12@TiO_2	13	28
RuS12@Au+TiO_2	240	20
RuS12@AuNP13+TiO_2	190	5
@Au+TiO_2	510	7
@AuNP13+TiO_2	215	6

ICP-MS was also performed on the supernatant of an aqueous solution of AuNP13 with and without electrolyte present (Table 6.8). There is a 3-fold increase in concentration of gold ions in the supernatant when 50 µL of electrolyte is added (470 → 1500 ppb) and a 4-fold increase with 100 µL electrolyte (470 → 2200 ppb). This shows the production of gold ions upon

addition of electrolyte, confirming the theory of dissolving of gold into the electrolyte (Equation 6.4 – 6.6).

Table 6.8: ICP-MS results showing the Au ions for solutions of AuNP13 with and without iodide – iodine electrolyte.

	Au ions / ppb
AuNP13	470
AuNP13 + 50 µL electrolyte	1500
AuNP13 + 100 µL electrolyte	2200
50 µL electrolyte	140

An absorption titration of iodide – iodine into AuNP100 was performed. 400 µL of electrolyte was added in 20 µL increments into a 20 pM aqueous suspension of AuNP100. As the concentration of electrolyte increased, the SPR of the AuNP100 decreased, showing a decrease in AuNP concentration (Figure 6.27).

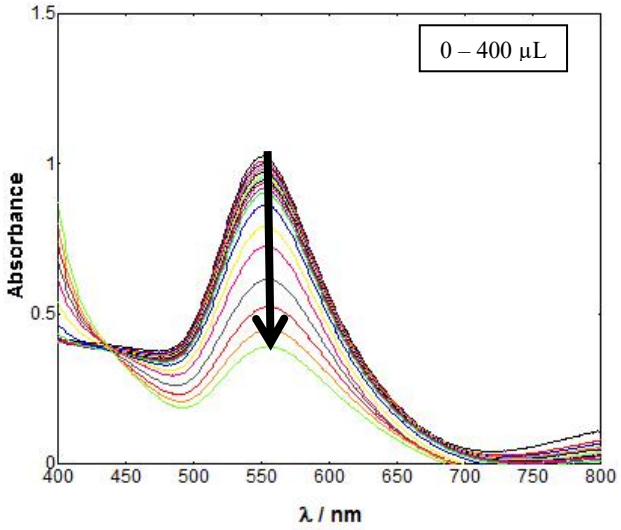

Figure 6.27: UV-vis titration of iodide – iodine electrolyte (0 – 400 µL) into 20 pM AuNP100.

MS was performed on the supernatant of the starting and finishing sample from the titration. It shows the presence of a gold species at 331 m/z, $[Au + 2MeCN + 3NH_3 + H]^+$, in the AuNP13 sample mixed with electrolyte, but this species is not seen in the AuNP13 or electrolyte solutions individually (Appendix). This also shows the production of gold ions upon addition of electrolyte, confirming the theory of dissolving of gold into the electrolyte (Equation 6.4 – 6.6).

To try and overcome this issue with the gold layer dissolving, two new TiO_2 surfaces were attempted; AuNP13 mixed with the TiO_2 paste (@AuNP13/TiO_2) and a paste prepared from mesoporous TiO_2 (@AuNP13/m-TiO_2).

It has been shown that mixing AuNP into the TiO_2 paste leads to enhancements in efficiency by up to 20%, compared to using the N719 dye alone.[19, 20] Komarala *et al.* demonstrate a 20% increase when the AuNP concentration is 0.25 wt%.[32] It was thought that by mixing the AuNP into the TiO_2 paste an enhancement would be seen, which is present in the literature, and the gold would be more protected from the electrolyte, so dissolution would not occur.

Different concentration of AuNP13 (0.3, 0.6, 0.9 and 1.2 wt%) were mixed with TiO_2NP and turned into a paste for the doctor blading technique, to produce electrodes. These were then washed with iodide – iodine electrolyte and the effect was measured visually and by absorption (Figure 6.28). As the concentration of AuNP13 increases, the pink colour (belonging to AuNP13) becomes more dominant (Figure 6.28.a). It is clear that the pink colour has disappeared for all electrodes after washing with electrolyte and as the concentration of AuNP13 increases, the washed electrode has increased flaking. These unstable surfaces are caused by inefficient packing of TiO_2 due to too high concentration of AuNP13. The removal of gold is also seen in the absorbance; before the electrolyte wash, all the electrodes have a peak between 500 – 600 nm for the gold SPR, whereas after the electrolyte wash, the gold SPR has disappeared (Figure 6.28.b). As the concentration of AuNP13 increases, the intensity of the SPR peak increases.

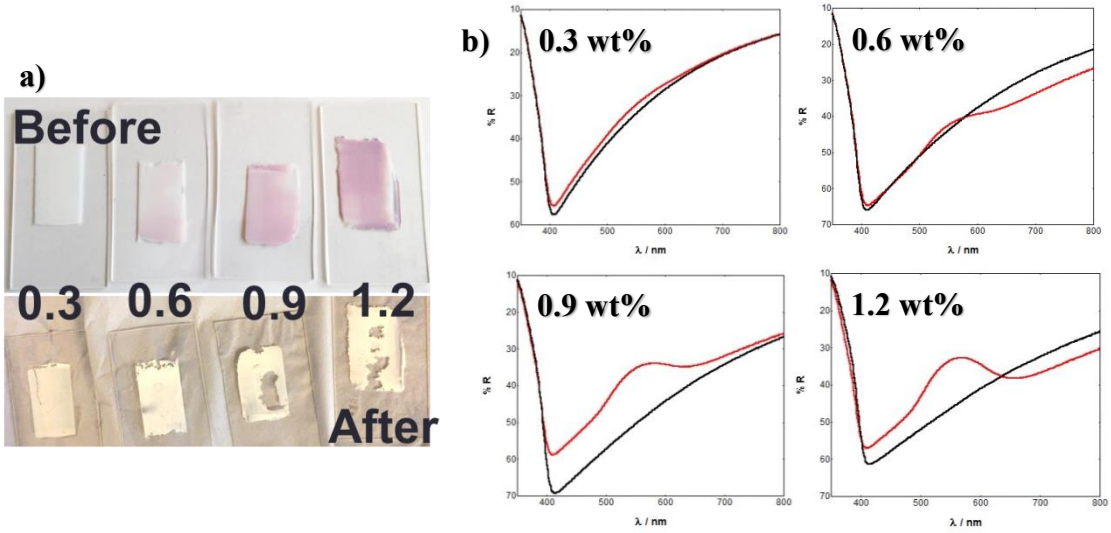

Figure 6.28: Photograph (a) and solid state absorption (b) of the different concentration mixed AuNP and TiO_2 electrodes (@AuNP13/TiO_2) before (red) and after (black) wash with iodide – iodine electrolyte.

It has been shown that mesoporous TiO_2 can lead to advanced photoactive properties due to the increase in surface area.[101-105] Caruso *et al.* demonstrate a 10% increase in efficiency when using 1 µm mesoporous TiO_2 with 12 nm pores [106] and Dai *et al.* show a 15% increase.[107] It was thought that by using mesoporous TiO_2 with the AuNP, the AuNP would sit in the pores of the TiO_2 and it would provide protection from the electrolyte, as well as the enhancement that has been seen in the literature.

Mesoporous TiO_2NPs (m-TiO_2NP) were synthesised as previously explained,[107] producing 2 µm particles with 10 nm pores. The size was measured by SEM and DLS sizing and the pore size was measured by nitrogen sorption (Figure 6.29).

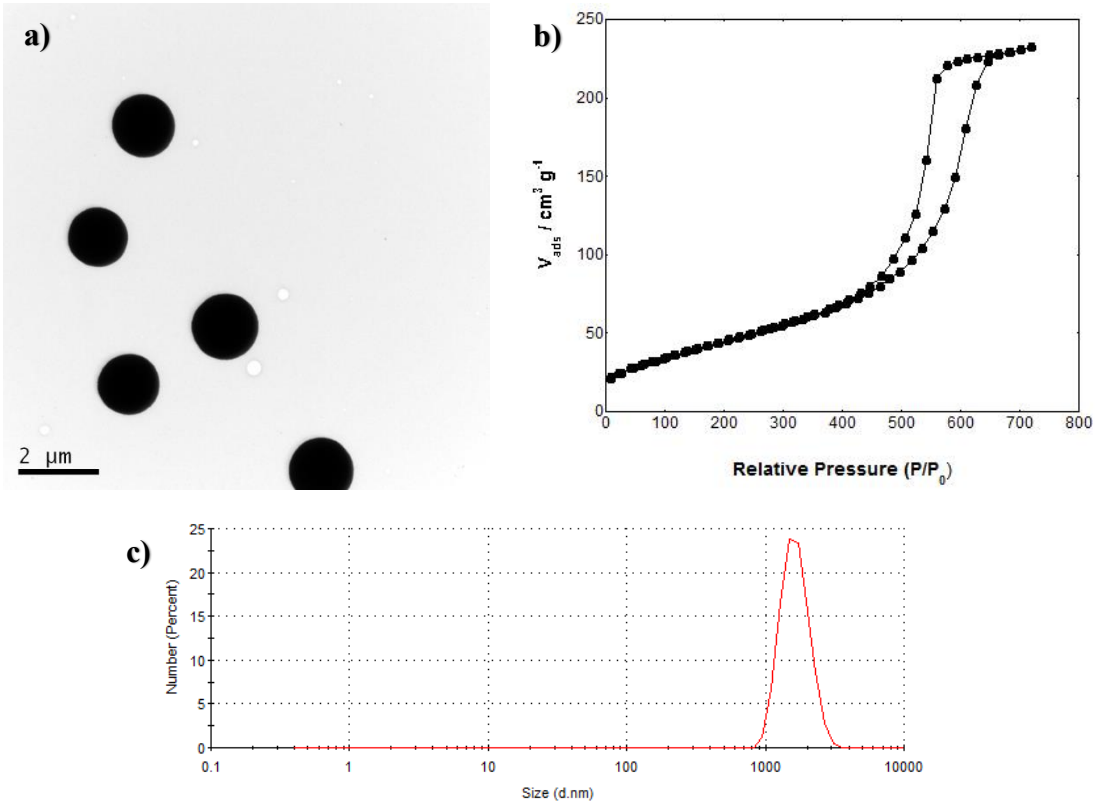

Figure 6.29: SEM (a), nitrogen sorption (b) and DLS number distribution (c) of m-TiO_2 NP.

These m-TiO_2NP were mixed with AuNP13 and turned into a paste for the doctor blading technique, to produce electrodes. These were then washed with iodide – iodine electrolyte and measured visually and by absorption (Figure 6.30). It is clear that the pink colour (belonging to the AuNP13) has gone after washing with electrolyte (Figure 6.30.b). This is also seen for the absorbance; before the electrolyte wash the electrode has a peak between 500 – 600 nm for the gold SPR, whereas after the electrolyte wash, the gold SPR has disappeared (Figure 6.30.c).

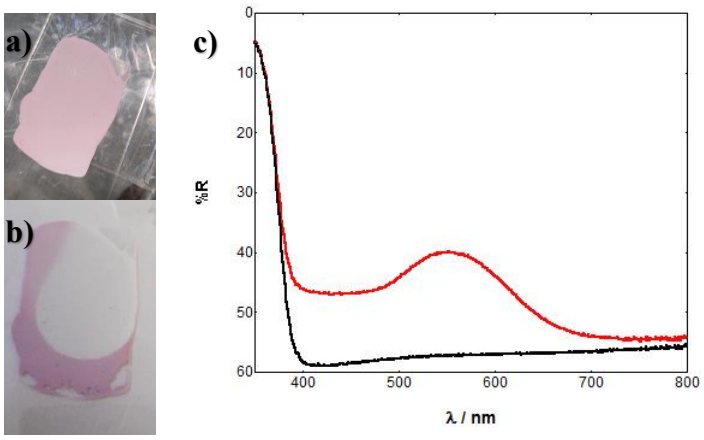

Figure 6.30: Photograph of m-TiO_2 before (a) and after (b) wash with iodide – iodine electrolyte. Solid state absorption of m-TiO_2 before (red) and after (black) electrolyte wash (c).

There is no improvement for the new electrodes; both TiO_2 surfaces (@AuNP13/TiO_2 and @AuNP13/m-TiO_2) appear to have removal of the gold through dissolution into the iodide – iodine electrolyte.

It is clear that the gold layer is being dissolved by the iodide – iodine electrolyte in these cells, however some groups report enhancement of DSCs through the use of AuNP with this electrolyte.[17, 19, 20, 63, 108-112] A few examples use a scattering layer of TiO_2 on the surface of the gold layer which may create a protective layer, stopping the electrolyte reaching the AuNP.[32, 62, 113] Suh *et al.* demonstrate a 10% increase in efficiency when using 30 nm citrate stabilised AuNP and coated with a TiO_2 scattering layer.[62] There are, however, examples of enhancement without the scatter layer. Thotawatthage *et al.* have shown a 25% increase in efficiency through mixing 60 nm citrate stabilised AuNP with the TiO_2NP and using the iodide – iodine electrolyte[114] and Wang *et al.* have shown a 35% increase in efficiency when 50 – 200 nm citrate stabilised AuNP are evaporated onto the surface of the electrode.[115] There are studies saying that AuNP are stable in iodide – iodine electrolyte which is contrary to these studies, suggesting that there are other factors involved in the dissolving of the gold.[116, 117]

There is evidence to believe that the reason no change in DSC properties are seen with the gold coated surfaces compared to @TiO_2 is due to the iodide – iodine electrolyte dissolving the gold, leaving behind a dye coated TiO_2 surface. Although there is literature supporting this data, showing the electrolyte being used to dissolve gold ore, there is also literature which opposes this data, demonstrating enhancements in DSC efficiency when incorporating AuNP into the cell with an iodide - iodine electrolyte.

6.3 Conclusion and future research

Carboxylate and thiocyanate free ruthenium polypyridyl complexes with thiol-functionalised legs were successfully used as sensitizers in DSCs and shown to directly bond to the TiO_2 surface. Although the majority of the dyes showed poor sensitization (η = 0.3 – 0.5%), RuphenS12 showed potential with enhanced properties (η = 1%). This was demonstrated to arise from efficient electron transfer from the ruthenium photoactive centre to the TiO_2 surface. The gold layer, attached for enhancement, was found to be dissolved by the iodide – iodine electrolyte in all attempted surfaces. Potential to overcome this could arise from investigating different methods of attaching the AuNP to the cell that allow protection of the gold[33] or by using a different electrolyte.[16]

6.4 Summary of data

Table 6.9: Measured current (J_{SC}) and voltage (V_{OC}) and calculated maximum power (P_{max}), fill factor (FF) and efficiency (η) for N719@TiO_2, N719@Au+TiO_2, N719@AuNP13+TiO_2, RuS1@Au+TiO_2, RuS1@AuNP13+TiO_2, RuS12@Au+TiO_2, RuphenS12@Au+TiO_2, RuSconj@Au+TiO_2, @Au+TiO_2, @AuNP13+TiO_2 and RuSi@TiO_2.

	J_{SC} / mA cm^{-2}	V_{OC} / V	P_{max} / mW cm^{-2}	FF	η / %
N719@TiO_2	11.29	0.69	3.25	0.42	3.25
N719@Au+TiO_2	11.23	0.69	3.50	0.45	3.50
N719@AuNP13+TiO_2	11.16	0.68	3.05	0.40	3.05
RuS1@Au+TiO_2	0.64	0.46	0.15	0.49	0.15
RuS1@AuNP13+TiO_2	0.61	0.52	0.14	0.44	0.14
RuS12@Au+TiO_2	0.54	0.53	0.14	0.50	0.14
RuphenS12@Au+TiO_2	3.3	0.6	1.0	0.5	1.0
RuSconj@Au+TiO_2	0.89	0.51	0.24	0.53	0.24
@Au+TiO_2	0.78	0.50	0.21	0.53	0.21
@AuNP13+TiO_2	0.76	0.48	0.18	0.50	0.18
RuSi@TiO_2	0.82	0.52	0.22	0.52	0.22

6.5 Experimental

6.5.1 Materials

Starting materials were purchased from Sigma Aldrich or Fisher Scientific.

6.5.2 Ruthenium dyes

RuS1 and **RuS12** were synthesised as previously discussed (Section 3.5.3). **RuphenS12** and **RuSconj** were synthesised as previously discussed (Section 4.5.3).

6.5.2.1 Synthesis of RuSi

1-(Amino-N-Boc)-ethyl bromide[83] 1-Aminoethyl bromide.HBr (1.49 g, 7.4 mmol), tert-butyloxycarbonyl (4.5 mL, 2M in THF, 9 mmol) and triethylamine (2.5 mL, 18 mmol) were dissolved in THF (30 mL) and left to stir at room temperature for 24 hours. The solvent was removed *in vacuo*, ethyl acetate (100 mL) was added and the solution was washed with aqueous $NaHCO_3$ (25 mL) and brine (25 mL). The organic layer was dried with $MgSO_4$, filtered and the solvent removed *in vacuo* to produce a yellow oil (1.61 g, 7.2 mmol, 97%). δ_H (300 MHz; $CDCl_3$): 1.30 (9H, s, H5); 3.25-3.43 (4H, m, H1, H2); 5.40 (1H, bs, NH). Data agreed with previously published.

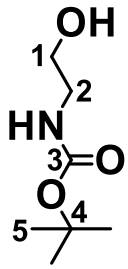

4,4'-Dihydroxy-2,2'-bipyridine was synthesised as previously discussed (Section 3.5.3.2).

4,4'-Ethoxyamino-N-boc-2,2'-bipyridine[83] 4,4'-Dihydroxy-2,2'-bipyridine (0.26 g, 1.4 mmol), 1-(amino-N-Boc)-ethyl bromide (1.13 g, 5.1 mmol) and potassium carbonate (0.69 g, 5.0 mmol) were dissolved in acetone (60 mL) with a catalytic amount of 18-crown-6 and stirred at 60 °C for 96 hours under N_2. The solvent was reduced *in vacuo* (10 mL) and cooled to 0 – 5 °C. The precipitate was filtered to give a white solid (0.21 g, 0.44 mmol, 32%). δ_H (300 MHz;

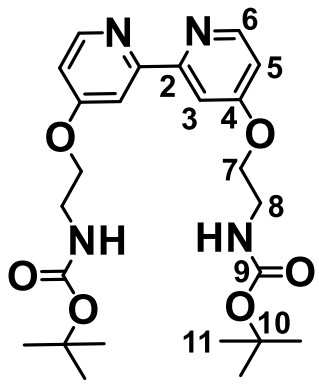

$CDCl_3$): 1.38 (18H, s, H11); 3.51 (4H, dd, *5.15, 10.48*, H8); 4.12 (4H, t, *5.15*, H7); 4.96 (2H, bt, NH); 6.77 (2H, dd, *2.50, 5.67*, H5); 7.89 (2H, d, *2.50*, H3); 8.40 (2H, d, *5.67*, H6). δ_C (100 MHz; $CDCl_3$): 28.4 (C11); 39.8 (C8); 67.3 (C7); 79.7 (C10); 107.0 (C5); 111.0 (C3); 150.3 (C6); 155.8 (C4); 157.7 (C2) 165.7 (C9). m/z (TOF MS ES^+) 475.3 ($[M+H]^+$). Data agreed with previously published.

4,4'-Ethoxyamine-2,2'-bipyridine[83] 4,4'-Ethoxyamino-N-boc-2,2'-bipyridine (127 mg, 269 mmol) was stirred in trifluoroacetic acid (5 mL) for 2 hours at rt. The solvent was removed *in vacuo* and the colourless oil was dissolved in sodium hydroxide (1 M, 50 mL) and extracted with chloroform (3 x 30 mL) and washed with ethyl acetate (30 mL). The solvent from the combined organic layers was removed *in vacuo* to form a white solid (94 mg, 343 mmol, quantitative). δ_H (300 MHz; d_6-DMSO): 2.85 (4H, t, *5.72*, H8); 4.02 (4H, t, *5.72*, H7); 6.97 (2H, dd, *2.55, 5.66*, H5); 7.86 (2H, d, *2.55*, H3); 8.42 (2H, d, *5.66*, H6). δ_C (100 MHz; d_6-DMSO): 40.6 (C8); 70.3 (C7); 106.4 (C3); 111.0 (C5); 150.5 (C6); 156.8 (C4); 165.6 (C2). m/z (TOF MS ES^+) 275.2 ($[M+H]^+$). Data agreed with previously published.

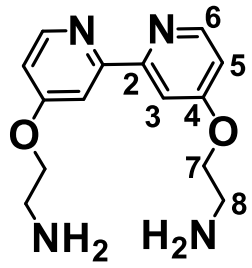

$Ru(bpy)_2Cl_2$ was synthesised as previously discussed (Section 3.5.3.1).

$RuNH_2$ Synthesis adapted from reference.[58] 4,4'-Ethoxyamine-2,2'-bipyridine (94.1 mg, 0.34 mmol) and $Ru(bpy)_2Cl_2$ (145 mg, 0.30 mmol) were heated to reflux under N_2 in ethanol (100 mL) for 24 hours. The solution was cooled to rt and the solvent was reduced in *vacuo* (25 mL). Water (35 mL) was added and the solution was filtered. A saturated solution of ammonium hexafluorophosphate (1g in 1 mL of MeOH) was added, forming a red precipitate, which was filtered and washed with ice cold water and diethyl ether to produce a red solid

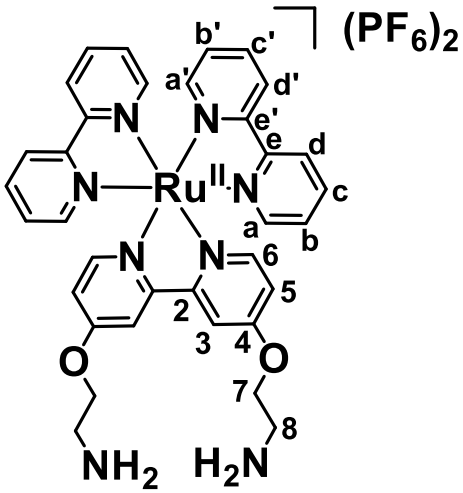

hexafluorophosphate salt (54.9 mg, 0.08 mmol, 27%). δ_H (300 MHz; CD_3CN): 3.25-3.45 (4H, t, *5.35*, H8); 3.59 (4H, t, *5.35*, H7); 5.82 (2H, bt, *5.33*, NH); 6.41 (2H, dd, *2.49, 6.55*, H5); 6.89 (2H, d, *6.55*, H6); 7.20-7.25 (2H, m, Hb); 7.30-7.40 (4H, m, Hb', H3); 7.62 (2H, d, *5.54*, Ha); 7.80-8.00 (6H, m, Hc, Hc', Ha'); 8.37 (4H, m, Hd, Hd'). δ_C (100 MHz; CD_3CN): 44.3 (C8); 59.5 (C7); 123.5 (Cd, Cd'); 123.6 (C5); 126.9 (Cb, Cb'); 127.0 (C3); 136.4 (Cc, Cc'); 136.8 (C6); 151.1 (Ca); 151.4 (Ca'); 154.6 (Ce, Ce'); 157.0 (C4); 157.2 (C2). Assignments from COSY and HSQC (Appendix). m/z (TOF MS ES^+) 344.1 ($[M\text{-}2PF_6]^{2+}$, 100%): 341.1 (30%); 341.6 (10%); 342.1 (15%); 342.6 (60%); 343.1 (70%); 343.6 (80%); 344.1 (100%); 344.6 (75%); 345.1 (85%); 345.6 (50%); 346.1 (10%).

RuSi Synthesis adapted from reference.[83] Triethylamine (21.3 µL, 0.086 mmol) and isocyanatopropyltriethoxysilane (6.3 µL, 0.086 mmol) were added to a solution of $RuNH_2$ (40.1 mg, 0.041 mmol) in dry THF and stirred at room temperature for 24 hours. The solvent was removed *in vacuo* and the solid was suspended in hexane (50 mL), filtered and washed through with toluene (50 mL) and diethyl ether (50 mL) to form a black solid hexafluorophosphate salt (20 mg, 0.014 mmol, 34%). δ_H (300 MHz; CD_3CN): 0.58 (4H, m, H12); 1.18 (18H, t, *7.0*, H14); 1.50 (4H, m, H11); 3.04 (4H, t, 7.2, H10); 3.50 (4H, m, H8); 3.79 (12H, q, *7.0*, H13); 4.31 (4H, t, *6.2*, H7); 5.23 (2H, t, *5.7*, NH); 5.30 (2H, t, *5.7*, NH'); 6.94 (2H, dd, *2.7, 6.5*, H5); 7.41 (6H, m, Hb, Hb', H3); 7.73 (2H, d, *5.6*, Ha'); 7.84 (2H, d, *5.6*, Ha); 8.05 (4H, dq, *1.5, 8.0*, Hc, Hc'); 8.50 (4H, d, *8.0*, Hd, Hd'); 8.50 (2H, m, H6). δ_C (100 MHz; CD_3CN): 8.2 (C12); 17.7 (C14); 23.5 (C11); 38.2 (C8); 42.5 (C10); 58.0 (C13); 68.5 (C7); 110.7 (C5); 115.4 (C3); 124.1 (Cd, Cd'); 127.4 (Cb, Cb'); 137.4 (Cc, Cc'); 151.6 (Ca, Ca'); 151.8 (C6); 157.1 (Ce, Ce'); 158.4 (C4); 166.6 (C2). Assignments from

COSY and HSQC (Appendix). m/z (TOF MS ES^+) 1327.8 ($[M\text{-}PF_6]^+$): 1321.8 (5%); 1322.8 (5%); 1323.8 (5%); 1324.8 (25%); 1325.8 (40%); 1326.8 (60%); 1327.8 (100%); 1328.8 (55%); 1329.8 (50%); 1330.8 (25%); 1331.8 (10%); 1332.8 (3%). All photophysical characterisation is performed as a 6 μM solution in methanol as the hexafluorophosphate salt. UV-VIS λ_{max} / nm (ε / $M^{-1}cm^{-1}$): 460 (14000), 430 (sh), 289 (80000), 230 (sh). Emission λ_{max}: 650 nm. τ: 130 ns. Φ: 1%.

6.5.3 Synthesis of nanoparticles

AuNP13 was synthesised as previously discussed (Section 3.5.2).

Mesoporous TiO_2 Titanium isopropoxide (0.9 mL) was added to a vigorously stirred solution of anhydrous acetone (22.4 mL) and transferred to a 40 mL autoclave. It was heated to 200 °C for 12 hours and centrifuged at 4500 G for 30 minutes. The supernatant was decanted and the pellet was redispersed in ethanol (30 mL). The process was repeated twice. Surface area / m_2g^{-1}: 151. Pore diameter / nm: 10. Diameter / μm: 1.8 ± 0.3 (DLS number distribution), 2.5 (TEM).

6.5.4 Preparation of electrodes and assembly of Dye Sensitized Solar Cell

6.5.4.1 Preparation of TiO_2 paste

Ethanol (10 mL) and α-terpiniol (3 mL) were added to a mixture of either Degussa p25 21 nm (purchased by Sigma Aldrich) or 2.5 μm mesoporous TiO_2 particles (synthesised) (1 g) and ethyl cellulose (0.5 g). The mixture was ground by hand in a pestle and mortar for 30 minutes to produce the paste which is used as is. When preparing the AuNP13 and TiO_2 mixed pastes, AuNP13 suspended in ethanol (10 mL) with varying concentrations depending on the Au loading and α-terpiniol (3 mL) were added to a mixture of either Degussa p25 21 nm or 2.5 μm mesoporous TiO_2 particles (1 g) and ethyl cellulose (0.5 g). The mixture was ground by hand in a pestle and mortar for 30 minutes.

6.5.4.2 Preparation of electrodes

2 x 2 cm FTO glass sheets (purchased from Sigma Aldrich) were sonicated for 15 mins in acetone followed by IPA. They were sonicated in $TiCl_4$ (0.5 % in water) for 15 mins and then placed in the oven at 70 °C for 30 mins. The glass sheets were washed with water twice, dried and heated to 450 °C for 30 mins. TiO_2 paste was coated on the conductive side of the glass through the doctor blading technique and the electrodes were left to dry for 30 mins. They were then heated to 100 °C for 30 mins, 450 °C for 45 mins and 500 °C for 15 mins. The white electrodes were suspended in $TiCl_4$ (0.5% in water) and heated to 60 °C for 30 mins. The electrodes were dried and heated to 450 °C for 30 mins.

6.5.4.3 Coating of TiO_2 electrodes with gold layer

AuNP13 layer The TiO_2 electrode was soaked in a 9 nM solution of AuNP13 and heated to 80 °C for 30 minutes until the nanoparticles were dried on to the electrode surface.

5 nm Au layer The TiO_2 electrode was coated with a 5 nm layer of Au using a metal evaporator.

6.5.4.4 Preparation of dye solution

N719 N719 (5 mg, 4.2 mmol) was dissolved in 10 mL ethanol to form a 0.4 mM solution.

RuS1 RuS1 solution (1 mL, 1.2 mM in MeOH) was diluted to 10 mL in methanol to form a 0.1 mM solution.

RuS12 RuS12 (2 mg, 1.4 mmol) was dissolved in 10 mL acetonitrile to form a 0.1 mM solution.

RuSconj RuSconj (2 mg, 1.7 mmol) was dissolved in 10 mL acetonitrile to form a 0.2 mM solution.

RuphenS12 RuphenS12 (2 mg, 1.6 mmol) was dissolved in 10 mL methanol to form a 0.2 mM solution.

RuSi RuSi solution (1 mL, 1.1 mM in MeOH) was diluted to 10 mL in methanol to form a 0.1 mM solution.

6.5.4.5 Assembly of DSC

The electrode was soaked in the dye solution for 24 hours and washed with methanol and dried with nitrogen. A Sellotape spacer with 0.25 cm^2 square open area was attached. The counter electrode was prepared through coating a 2 x 2 cm FTO glass sheet with platinum *via* a metal sputterer. Silver paint was added to the edge of the electrodes. The two electrodes were clipped together and iodine-iodide electrolyte (0.1 M LiI, 0.05 M I_2, 0.5 M 4-tertbutylpyridine, 0.6 M 1-methyl-3-propylimidazolium) was pipetted in the middle.

6.6 References

1. M. Eskandari, V. Ahmadi, M. Yousefi rad and S. Kohnehpoushi, *Physica E Low Dimens Syst Nanostruct*, 2015, 68, 202-209.
2. X. Li, K. Suzuki, T. Toda, S. Yasuda and K. Murakoshi, *J. Phys. Chem. C*, 2015, 119, 22092-22101.
3. P. V. Kamat, J. A. Christians and J. G. Radich, *Langmuir*, 2014, 30, 5716-5725.
4. Z. Xu, Y. Lin, M. Yin, H. Zhang, C. Cheng, L. Lu, X. Xue, H. J. Fan, X. Chen and D. Li, *Adv. Mater. Interfaces*, 2015, 2, 1500169.
5. S. Ng, X. Lu, N. Ding, C. L. Wu and C. Lee, *Sol Energy*, 2014, 99, 115-125.
6. X. Dang, J. Qi, M. T. Klug, P. Y. Chen, D. S. Yun, N. X. Fang, P. T. Hammond and A. M. Belcher, *Nano Lett.*, 2013, 13, 637-642.
7. Z. Lu, X. Pan, Y. Ma, Y. Li, L. Zheng, D. Zhang, Q. Xu, Z. Chen, S. Wang, B. Qu, F. Liu, Y. Huang, L. Xiao and Q. Gong, *RSC Adv.*, 2015, 5, 11175-11179.
8. S. D. Standridge, G. C. Schatz and J. T. Hupp, *J. Am. Chem. Soc.*, 2009, 131, 8407-8409.
9. Tanvi, A. Mahajan, R. K. Bedi, S. Kumar, V. Saxena and D. K. Aswal, *J. Appl. Phys.*, 2015, 117, 083111.
10. S. Pillai, K. R. Catchpole, T. Trupke and M. A. Green, *J. Appl. Phys.*, 2007, 101, 093105.
11. X. Li, W. C. H. Choy, L. Huo, F. Xie, W. E. I. Sha, B. Ding, X. Guo, Y. Li, J. Hou, J. You and Y. Yang, *Adv. Mater.*, 2012, 24, 3046-3052.
12. A. J. Morfa, K. L. Rowlen, T. H. Reilly, M. J. Romero and J. Lagemaat, *Appl. Phys. Lett.*, 2008, 92, 013504.
13. W. Zhang, M. Saliba, S. D. Stranks, Y. Sun, X. Shi, U. Wiesner and H. J. Snaith, *Nano Lett.*, 2013, 13, 4505-4510.

14. P. K. Jain, K. S. Lee, I. H. El-Sayed and M. A. El-Sayed, *J. Phys. Chem. B*, 2006, 110, 7238-7248.

15. Y. Bai, T. Butburee, H. Yu, Z. Li, R. Amal, G. Q. Lu and L. Wang, *J. Colloid Interface Sci.*, 2015, 449, 246-251.

16. Y. H. Su, Y. F. Ke, S. L. Cai and Q. Y. Yao, *Light Sci Appl*, 2012, 1, e14.

17. W. Hou, P. Pavaskar, Z. Liu, J. Theiss, M. Aykol and S. B. Cronin, *Energ Environ Sci*, 2011, 4, 4650-4655.

18. M. Al-Azawi, N. Bidin, A. Ali and M. Bououdina, *J. Mater. Sci.: Mater. Electron.*, 2015, 26, 6276-6284.

19. N. Chander, P. Singh, A. F. Khan, V. Dutta and V. K. Komarala, *Thin Solid Films*, 2014, 568, 74-80.

20. H. Chen, C. Hong, C. Kung, C. Mou, K. C. W. Wu and K. Ho, *J. Power Sources*, 2015, 288, 221-228.

21. T. Meen, J. Tsai, S. Chao, Y. Lin, T. Wu, T. Chang, L. Ji, W. Water, W. Chen, I. T. Tang and C. Huang, *Nanoscale Res. Lett.*, 2013, 8, 450-450.

22. H. Choi, W. T. Chen and P. V. Kamat, *ACS Nano*, 2012, 6, 4418-4427.

23. E. S. Arinze, B. Qiu, G. Nyirjesy and S. M. Thon, *ACS Photonics*, 2016, 3, 158-173.

24. W. H. Lai, Y. H. Su, L. G. Teoh and M. H. Hon, *J. Photochem. Photobiol. A*, 2008, 195, 307-313.

25. E. Thimsen, F. Le Formal, M. Grätzel and S. C. Warren, *Nano Lett.*, 2011, 11, 35-43.

26. P. Reineck, G. P. Lee, D. Brick, M. Karg, P. Mulvaney and U. Bach, *Adv. Mater.*, 2012, 24, 4750-4755.

27. V. Subramanian, E. E. Wolf and P. V. Kamat, *J. Am. Chem. Soc.*, 2004, 126, 4943-4950.

28. I. Carmeli, I. Lieberman, L. Kraversky, Z. Fan, A. O. Govorov, G. Markovich and S. Richter, *Nano Lett.*, 2010, 10, 2069-2074.

29. H. A. Atwater and A. Polman, *Nat. Mater.*, 2010, 9, 205-213.

30. M. D. Brown, T. Suteewong, R. S. S. Kumar, V. D'Innocenzo, A. Petrozza, M. M. Lee, U. Wiesner and H. J. Snaith, *Nano Lett.*, 2011, 11, 438-445.

31. N. C. Jeong, C. Prasittichai and J. T. Hupp, *Langmuir*, 2011, 27, 14609-14614.

32. N. Chander, A. F. Khan, E. Thouti, S. K. Sardana, P. S. Chandrasekhar, V. Dutta and V. K. Komarala, *Sol Energy*, 2014, 109, 11-23.

33. C. Bauer, J. Abid and H. H. Girault, *Chem. Phys.*, 2005, 319, 409-421.

34. A. Dawson and P. V. Kamat, *J. Phys. Chem. B*, 2001, 105, 960-966.

35. L. Amidani, A. Naldoni, M. Malvestuto, M. Marelli, P. Glatzel, V. Dal Santo and F. Boscherini, *Angew. Chem., Int. Ed.*, 2015, 54, 5413-5416.

36. Y. Liu and L. Juang, *Langmuir*, 2004, 20, 6951-6955.

37. Y. Konishi, I. Tanabe and T. Tatsuma, *Dalton Trans.*, 2013, 42, 15937-15940.

38. A. Furube, L. Du, K. Hara, R. Katoh and M. Tachiya, *J. Am. Chem. Soc.*, 2007, 129, 14852-14853.

39. T. Luitel and F. P. Zamborini, *Langmuir*, 2013, 29, 13582-13594.

40. L. Zedler, F. Theil, A. Csaki, W. Fritzsche, S. Rau, M. Schmitt, J. Popp and B. Dietzek, *RSC Adv.*, 2012, 2, 4463-4471.

41. T. Bora, H. H. Kyaw, S. Sarkar, S. K. Pal and a. J. Dutta, *Beilstein J. Nanotechnol.*, 2011, 2, 681–690.

42. J. Mao, N. He, Z. Ning, Q. Zhang, F. Guo, L. Chen, W. Wu, J. Hua and H. Tian, *Angew. Chem., Int. Ed.*, 2012, 51, 9873-9876.

43. Y. Guo, G. Xue, T. Yu, J. Guan, X. Yu, J. Zhang, J. Liu and Z. Zou, *Int. J. Electrochem. Sci.*, 2012, 1496-1511.

44. H. Uam, Y. Jung, Y. Jun and K. Kim, *J. Photochem. Photobiol. A*, 2010, 212, 122-128.

45. Y. Chen, K. Wang and L. Lou, *J. Photochem. Photobiol. A*, 2004, 163, 281-287.

46. H. Pettersson and T. Gruszecki, *Sol. Energy Mater. Sol. Cells*, 2001, 70, 203-212.

47. Y. Ooyama, S. Inoue, T. Nagano, K. Kushimoto, J. Ohshita, I. Imae, K. Komaguchi and Y. Harima, *Angew. Chem., Int. Ed.*, 2011, 50, 7429-7433.

48. I. López-Duarte, M. Wang, R. Humphry-Baker, M. Ince, M. V. Martínez-Díaz, M. K. Nazeeruddin, T. Torres and M. Grätzel, *Angew. Chem., Int. Ed.*, 2012, 51, 1895-1898.

49. D. F. Zigler, Z. A. Morseth, L. Wang, D. L. Ashford, M. K. Brennaman, E. M. Grumstrup, E. C. Brigham, M. K. Gish, R. J. Dillon, L. Alibabaei, G. J. Meyer, T. J. Meyer and J. M. Papanikolas, *J. Am. Chem. Soc.*, 2016, 138, 4426-4438.

50. H. He, A. Gurung and L. Si, *Chem. Commun.*, 2012, 48, 5910-5912.

51. N. Iguchi, C. Cady, R. Snoeberger, B. Hunter, E. Sproviero, C. Schmuttenmaer, R. Crabtree, G. Brudvig and V. Batista, *Physical Chemistry of Interfaces and Nanomaterials VII*, 2008, DOI: 10.1117/12.798938.

52. L. Gamble, L. S. Jung and C. T. Campbell, *Langmuir*, 1995, 11, 4505-4514.

53. Y. Dong, S. Abaci, C. Shannon and M. J. Bozack, *Langmuir*, 2003, 19, 8922-8926.

54. T. Burgi, *Nanoscale*, 2015, 7, 15553-15567.

55. E. Pensa, E. Cortés, G. Corthey, P. Carro, C. Vericat, M. H. Fonticelli, G. Benítez, A. A. Rubert and R. C. Salvarezza, *Acc. Chem. Res.*, 2012, 45, 1183-1192.

56. Y. Xue, X. Li, H. Li and W. Zhang, *Nature Communications*, 2014, 5, 4348.

57. D. Grasseschi, A. L. A. Parussulo, V. M. Zamarion, R. R. Guimarães, K. Araki and H. E. Toma, *Int. J. of Nanotechnology*, 2015, 12, 263 - 274.

58. S. J. Adams, D. J. Lewis, J. A. Preece and Z. Pikramenou, *ACS Appl. Mater. Interfaces*, 2014, 6, 11598-11608.

59. N. J. Rogers, S. Claire, R. M. Harris, S. Farabi, G. Zikeli, I. B. Styles, N. J. Hodges and Z. Pikramenou, *Chem. Commun.*, 2014, 50, 617-619.

60. M. Jebb, P. K. Sudeep, P. Pramod, K. G. Thomas and P. V. Kamat, *J. Phys. Chem. B*, 2007, 111, 6839-6844.

61. O. Kedem, W. Wohlleben and I. Rubinstein, *Nanoscale*, 2014, 6, 15134-15143.

62. H. Kim, D. H. Song, H. Yoon and J. S. Suh, *RSC Adv.*, 2015, 5, 27464-27469.

63. C. Andrei, E. Lestini, S. Crosbie, C. Frein, T. O'Reilly and D. Zerulla, *PLoS One*, 2014, 9.

64. M. G. Lobello, F. De Angelis and S. Fantacci, *Polyhedron*, 2014, 82, 88-103.

65. C. C. Rich, M. A. Mattson and A. T. Krummel, *J. Phys. Chem. C*, 2016, 120, 6601-6611.

66. F. Theil, L. Zedler, A. März, W. Xie, A. Csáki, W. Fritzsche, D. Cialla, M. Schmitt, J. Popp and B. Dietzek, *J. Phys. Chem. C*, 2013, 117, 1121-1129.

67. S. A. M. Osborne and Z. Pikramenou, *Farad. Discuss.*, 2015, 185, 219-231.

68. S. Lin, K. Lee, J. Wu and J. Wu, *Sol Energy*, 2012, 86, 2600-2605.

69. M. Grätzel, *J. Photochem. Photobiol., C*, 2003, 4, 145-153.

70. G. Cheng, M. S. Akhtar, O. B. Yang and F. J. Stadler, *ACS Appl. Mater. Interfaces*, 2013, 5, 6635-6642.

71. N. G. Bastús, J. Comenge and V. Puntes, *Langmuir*, 2011, 27, 11098-11105.

72. J. Nelson, *The Physics of Solar Cells*, 2003, Imperial College Press, London.

73. C. Li, C. Su, H. Wang, P. Kumaresan, C. Hsu, I. T. Lee, W. Chang, Y. S. Tingare, T. Li, C. Lin and W. Li, *Dyes Pigm.*, 2014, 100, 57-65.

74. H. Oh, J. Kim, S. H. Yun, J. Lee, B. Park, J. Tak and B. H. Kim, *Synth. Met.*, 2014, 198, 260-266.

75. P. G. Bomben, K. C. D. Robson, B. D. Koivisto and C. P. Berlinguette, *Coord. Chem. Rev.*, 2012, 256, 1438-1450.

76. F. Gao, Y. Wang, D. Shi, J. Zhang, M. Wang, X. Jing, R. Humphry-Baker, P. Wang, S. M. Zakeeruddin and M. Grätzel, *J. Am. Chem. Soc.*, 2008, 130, 10720-10728.

77. D. D. Babu, R. Su, A. El-Shafei and A. V. Adhikari, *Electrochim. Acta*, 2016, 198, 10-21.

78. A. V. Naumkin, A. KrautVass, S. W. Gaarenstroom and C. J. Powell, *NIST Standard Reference Database 20, Version 4.1* 2012.

79. F. C. Krebs, *Polymer Photovoltaics: A Practical Approach*, 2008, In: K. Norrman; S. Cros; R. Bettignies; M. Firon; F. C. Krebs,. *Lifetime and Stability Studies*, SPIE, Washington.

80. C. Battocchio, F. Porcaro, S. Mukherjee, E. Magnano, S. Nappini, I. Fratoddi, M. Quintiliani, M. V. Russo and G. Polzonetti, *J. Phys. Chem. C*, 2014, 118, 8159-8168.

81. D. Grumelli, C. Vericat, G. Benitez, M. E. Vela, R. C. Salvarezza, L. J. Giovanetti, J. M. Ramallo-López, F. G. Requejo, A. F. Craievich and Y. S. Shon, *J. Phys. Chem. C*, 2007, 111, 7179-7184.

82. K. Szpakolski, K. Latham, C. Rix, R. A. Rani and K. Kalantar-zadeh, *Polyhedron*, 2013, 52, 719-732.

83. D. J. Lewis, V. Dore, N. J. Rogers, T. K. Mole, G. B. Nash, P. Angeli and Z. Pikramenou, *Langmuir*, 2013, 29, 14701-14708.

84. A. Juris, V. Balzani, F. Barigelletti, S. Campagna, P. Belser and A. Von Zelewsky, *Coord. Chem. Rev.*, 1988, 84, 85-277.

85. B. Durham, J. V. Caspar, J. K. Nagle and T. J. Meyer, *J. Am. Chem. Soc.*, 1982, 104, 4803-4810.

86. A. Fojtik and A. Henglein, *Chem. Phys. Lett.*, 1994, 221, 363-367.

87. Y. Hou, P. Xie, K. Wu, J. Wang, B. Zhang and Y. Cao, *Sol. Energy Mater. Sol. Cells*, 2001, 70, 131-139.

88. S. Meng, J. Ren and E. Kaxiras, *Nano Lett.*, 2008, 8, 3266-3272.

89. P. H. Qi and J. B. Hiskey, *Hydrometallurgy*, 1993, 32, 161-179.

90. T. N. Angelidis, K. A. Kydros and K. A. Matis, *Hydrometallurgy*, 1993, 34, 49-64.

91. P. H. Qi and J. B. Hiskey, *Hydrometallurgy*, 1991, 27, 47-62.

92. A. Davis and T. Tran, *Hydrometallurgy*, 1991, 26, 163-177.

93. H. Wang, C. Sun, S. Li, P. Fu, Y. Song, L. Li and W. Xie, *Int. J. Min. Met. Mater.*, 2013, 20, 323-328.

94. N. Somasundaram and C. Srinivasan, *J. Photochem. Photobiol. A*, 1996, 99, 67-70.

95. D. I. Sayago, P. Serrano, O. Böhme, A. Goldoni, G. Paolucci, E. Román and J. A. Martín-Gago, *Surf. Sci.*, 2001, 482–485, Part 1, 9-14.

96. J. A. Rodriguez, J. Hrbek, Z. Chang, J. Dvorak, T. Jirsak and A. Maiti, *Phys. Rev. B*, 2002, 65, 235414.

97. W. Langel, *Surf. Sci.*, 2006, 600, 1884-1890.

98. L. Benz, A. Park, J. R. Corey, M. P. Mezher and V. C. Park, *Langmuir*, 2012, 28, 10209-10216.

99. A. V. Vorontsov, *J. Struct. Chem.*, 2015, 56, 813-822.

100. H. Wang and C. You, *Chem. Eng. J. (Lausanne)*, 2016, 292, 199-206.

101. M. A. Abdolahi Sadatlu and N. Mozaffari, *Sol Energy*, 2016, 133, 24-34.

102. H. Li, Z. Bian, J. Zhu, D. Zhang, G. Li, Y. Huo, H. Li and Y. Lu, *J. Am. Chem. Soc.*, 2007, 129, 8406-8407.

103. M. Meire, S. W. Verbruggen, S. Lenaerts, P. Lommens, P. Van Der Voort and I. Van Driessche, *J. Mater. Sci.*, 2016, 51, 9822-9829.

104. M. Zukalová, A. Zukal, L. Kavan, M. K. Nazeeruddin, P. Liska and M. Grätzel, *Nano Lett.*, 2005, 5, 1789-1792.

105. N. Tasić, Z. Marinković Stanojević, Z. Branković, U. Lačnjevac, V. Ribić, M. Žunić, T. Novaković, M. Podlogar and G. Branković, *Electrochim. Acta*, 2016, 210, 606-614.

106. D. Chen, F. Huang, Y.-B. Cheng and R. A. Caruso, *Adv. Mater.*, 2009, 21, 2206-2210.

107. Z. Li, Y. Que, L. E. Mo, W. Chen, Y. Ding, Y. Ma, L. Jiang, L. Hu and S. Dai, *ACS Appl. Mater. Interfaces*, 2015, 7, 10928-10934.

108. A. A. Shah, A. A. Umar and M. M. Salleh, *Electrochim. Acta*, 2016, 195, 134-142.

109. S. P. Lim, A. Pandikumar, H. N. Lim and N. M. Huang, *Sol Energy*, 2016, 125, 135-145.

110. M. A. Al-Azawi, N. Bidin, M. Bououdina and S. M. Mohammad, *Sol Energy*, 2016, 126, 93-104.

111. J. Villanueva-Cab, J. L. Montaño-Priede and U. Pal, *J. Phys. Chem. C*, 2016, 120, 10129-10136.

112. M. A. Al-Azawi, N. Bidin, A. K. Ali and M. Bououdina, *J. Mater. Sci.: Mater. Electron.*, 2015, 26, 6276-6284.

113. H. Elbohy, M. R. Kim, A. Dubey, K. M. Reza, D. Ma, J. Zai, X. Qian and Q. Qiao, *J. Mater. Chem. A.*, 2016, 4, 545-551.

114. M. A. K. L. Dissanayake, J. M. K. W. Kumari, G. K. R. Senadeera and C. A. Thotawatthage, *J. Appl. Electrochem.*, 2016, 46, 47-58.

115. L. Zhang and Z. Wang, *J. Mater. Chem. C.*, 2016, 4, 3614-3620.

116. H. K. Jun, M. A. Careem and A. K. Arof, *Materials Today: Proceedings*, 2016, 3, Supplement 1, S73-S79.

117. M. A. Abbas, T. Kim, S. U. Lee, Y. S. Kang and J. H. Bang, *J. Am. Chem. Soc.*, 2016, 138, 390-401.

7 General conclusion

Numerous luminescent thiol functionalised ruthenium(II) polypryidyl complexes were synthesised and characterised with NMR, MS and FTIR. They were attached to aqueously dispersed gold nanoparticles, producing luminescent nanoprobes. The molecular probes and nanoprobes were characterised by absorption and steady state and time resolved emission, both as an aqueous solution and in the solid state. These probes were employed in applications in Dye Sensitized Solar Cells through attaching to a TiO_2 electrode and investigating the photo produced current and voltage in a circuit. The electrodes were characterised using solid state absorption and XPS.

From these investigations it was found that the nanoprobes show enhanced photophysical properties compared to the molecular probes due to enhancement from the electromagnetic field of the nanoparticle. The size of the nanoparticle does not have an effect on the photophysical properties of the nanoprobe. A further enhancement is seen with increasing distance between the photoactive ruthenium centre and the surface of the nanoparticle. The presence of the Zonyl fluorosurfactant is important for the enhancement and stability of the nanoprobe. Further research must be taken to adopt these nanoprobes into applications.

Through design of new ruthenium probes, it was discovered that there is internal quenching when the probe contains an oxygen adjacent to the bipyridine ring. Enhancements to photophysical properties by 2-fold have been seen through removing the oxygen. Enhancements were also seen through increasing the conjugation of the system and through the replacement of the 2,2'-bipyridine ligand with 1,10-phenanthroline.

The molecular probes and nanoprobes were employed into Dye Sensitized Solar Cells. The most promising dye was the 1,10-phenanthroline derivative, RuphenS12, giving an efficiency of 1%. The presence of the gold nanoparticles did not lead to enhancement of the efficiency,

unlike in the literature, and follow up research determined that the gold nanoparticles were being dissolved by the iodide - iodine electrolyte. Experiments to protect the gold nanoparticles from the electrolyte were unsuccessful and further research in this area needs to be completed, such as using a different electrolyte.

8 Appendix

8.1 Summary of complexes photophysics

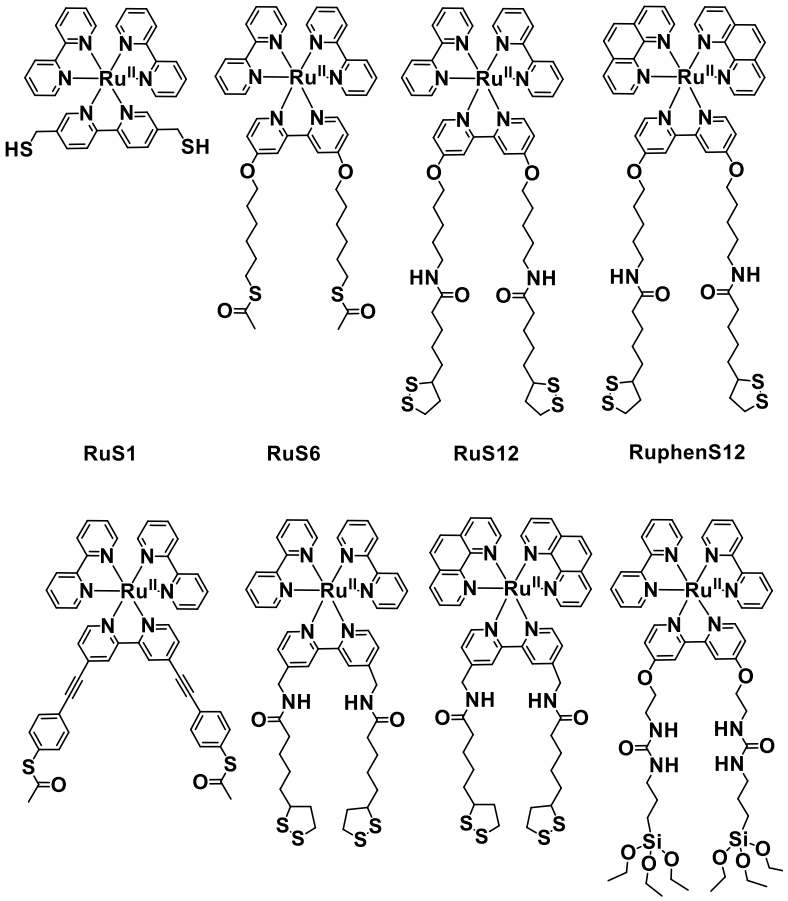

Figure 8.1: Schematic to show the structure of RuS1, RuS6, RuS12, RuphenS12, RuSconj, RuS8, RuphenS8 and RuSi.

Table 8.1: Absorption (ε), emission (λ_{max}), lifetime (τ) and quantum yield (Φ) of ruthenium complexes in solution, with Zonyl FSA surfactant (+Z) and in the solid state (ss). The absorbance is displayed in nm and the molar absorptivity is shown in brackets as M^{-1} cm^{-1}. The emission is displayed in nm. The lifetime is displayed in ns and the percentage contribution of the lifetime is shown in brackets. The quantum yield is displayed as %.

	RuS1	**RuS6**	**RuS12**	**RuphenS12**	**RuSconj**	**RuS8**	**RuphenS8**	**RuSi**
ε	451 (13000), 430 (sh), 288 (82000), 244 (41000)	463 (14000), 430 (sh), 287 (75000), 253 (30000)	460 (13000), 430 (sh), 280 (70000), 230 (sh)	457 (15000), 430 (sh), 263 (88000), 222 (88000)	481 (21000), 320 (sh), 288 (87000), 260 (60000)	456 (13000), 430 (sh), 287 (72000), 244 (26000)	452 (16000), 420 (sh), 380(sh), 286 (42000), 263 (82000), 230 (sh)	460 (14000), 430 (sh), 288 (80000), 230 (sh)
ε (+Z)	451 (13000), 430 (sh), 288 (82000), 244 (sh)	464 (14000), 430 (sh), 288 (75000), 253 (sh)	460 (13000), 430 (sh), 280 (70000), 230 (sh)	455 (15000), 264 (88000)	481 (21000), 320 (sh), 288 (87000)	465 (13000), 430 (sh), 288 (72000)	450 (16000), 420 (sh), 380 (sh), 285 (44000), 263 (70000)	-
λmax	645	645	645	630	670	635	625	650
λmax (+Z)	645	645	645	635	680	635	615	-
λmax ss	670	650	640	630	640	620	630	-
τ	420	240	280	550	440	430	500	130
τ (+Z)	420	400	350	750	500	600	700	-
τ ss	16 (20%), 50 (53%), 260 (27%)	30 (6%), 150 (37%), 500 (57%)	30 (5%), 120 (30%), 300 (65%)	45 (3%), 210 (21%), 580 (76%)	30 (1%), 170 (15%), 480 (84%)	20 (1%), 160 (14%), 650 (85%)	30 (2%), 150 (24%), 570 (74%)	-
Φ	2	2	2	3	3	4	4	1
Φ (+Z)	1	3	2	4	3	5	4	-
Φ ss	1	3	2	3	3	5	4	-

Table 8.2: Absorption (SPR), emission (λ_{max}), lifetime (τ), quantum yield (Φ), dynamic light scattering size and zeta and number of complexes per particles determined by inductively coupled plasma mass spectrometry (ICPMS) of ruthenium complexes attached to AuNP13 in solution and in the solid state (ss). The absorbance and emission is displayed in nm. The lifetime is displayed in ns and the percentage contribution of the lifetime is shown in brackets. The quantum yield is displayed as %. The DLS size is displayed in nm and the DLS zeta is displayed in mV.

	RuS1.AuNP13	**RuS6.AuNP13**	**RuS12.AuNP13**	**RuphenS12.AuNP13**	**RuSconj.AuNP13**	**RuS8.AuNP13**	**RuphenS8.AuNP13**
SPR	521	522	520	521	521	518	520
λmax	650	650	650	635	680	635	620
λmax ss	655	650	630	630	655	610	620
τ	470	340	480	1700	370	850	1100
τ ss	20 (7%), 100 (27%), 470 (66%)	30 (8%), 170 (48%), 500 (43%)	25 (2%), 160 (15%), 730 (84%)	20 (3%), 100 (7%), 840 (80%)	30 (3%), 160 (12%), 800 (85%)	10 (1%), 100 (8%), 710 (80%)	10 (4%), 75 (20%), 475 (76%)
Φ	2	6	8	30	5	10	20
Φ ss	1	5	12	13	10	8	7
Size	15 ± 6	24 ± 8	18 ± 6	17 ± 5	20 ± 7	21 ± 6	20 ± 7
Zeta	- 48 ± 11	- 62 ± 15	- 42 ± 13	- 42 ± 7	- 40 ± 8	- 51 ± 7	- 47 ± 6
ICPMS	550	550	680	550	400	550	680

8.2 Chapter 3: Highly luminescent gold nanoparticles effect of ruthenium distance for nanoprobes with enhanced lifetimes

8.2.1 Synthesis: NMR and MS

8.2.1.1 RuS1

5,5'-Dimethylbromide-2,2'-bipyridine

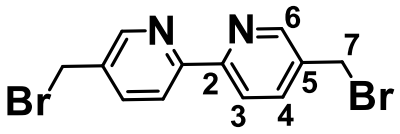

Figure 8.2: Structure of 5,5'-dimethylbromide-2,2'-bipyridine.

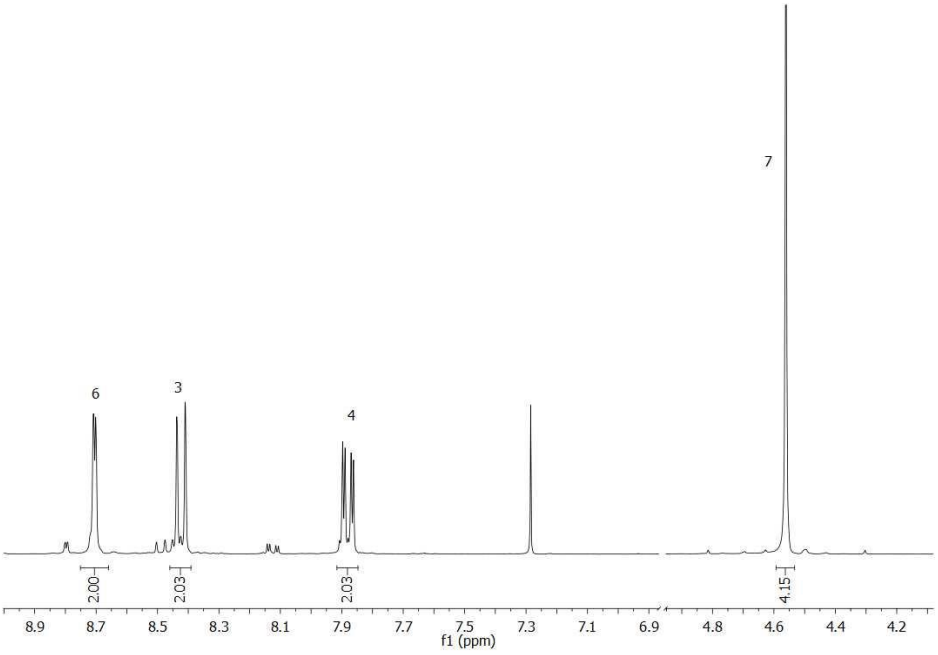

Figure 8.3: ^{1}H NMR 5,5'-dimethylbromide-2,2'-bipyridine. ($CDCl_3$).

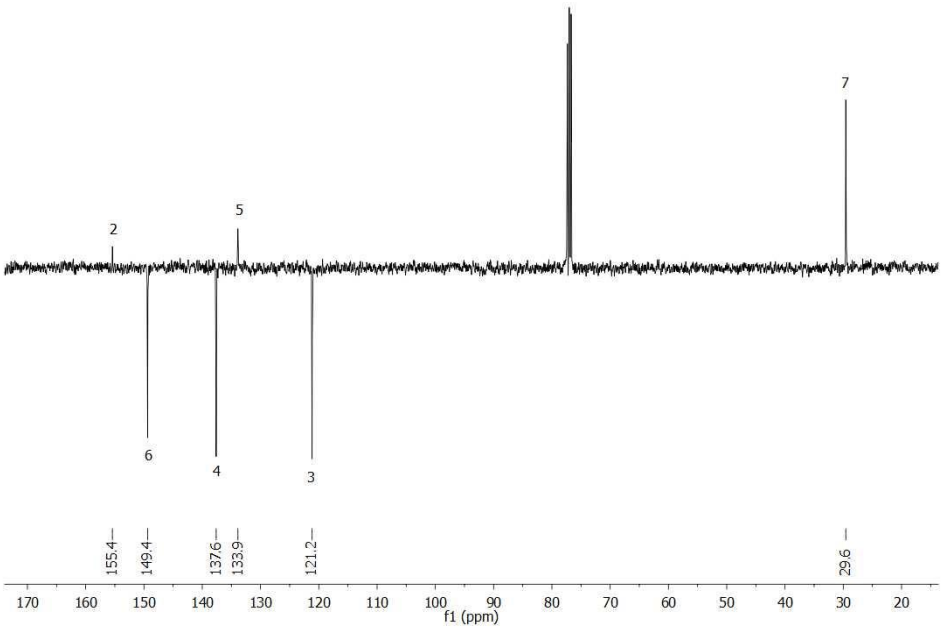

Figure 8.4: ^{13}C NMR 5,5'-dimethylbromide-2,2'-bipyridine. ($CDCl_3$).

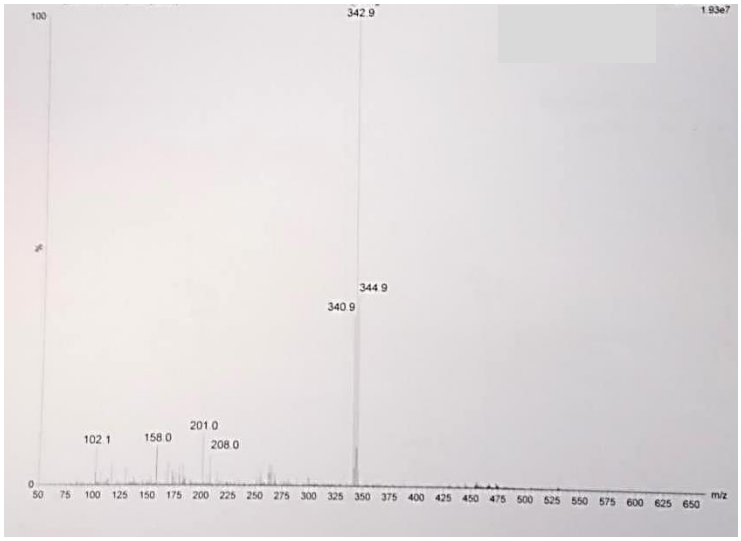

Figure 8.5: 5,5'-dimethylbromide-2,2'-bipyridine MS.

5,5’-Dimethylthiol-2,2’-bipyridine

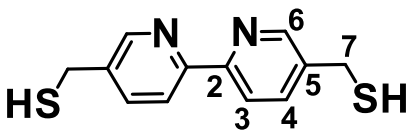

Figure 8.6: Structure of 5,5’-dimethylthiol-2,2’-bipyridine.

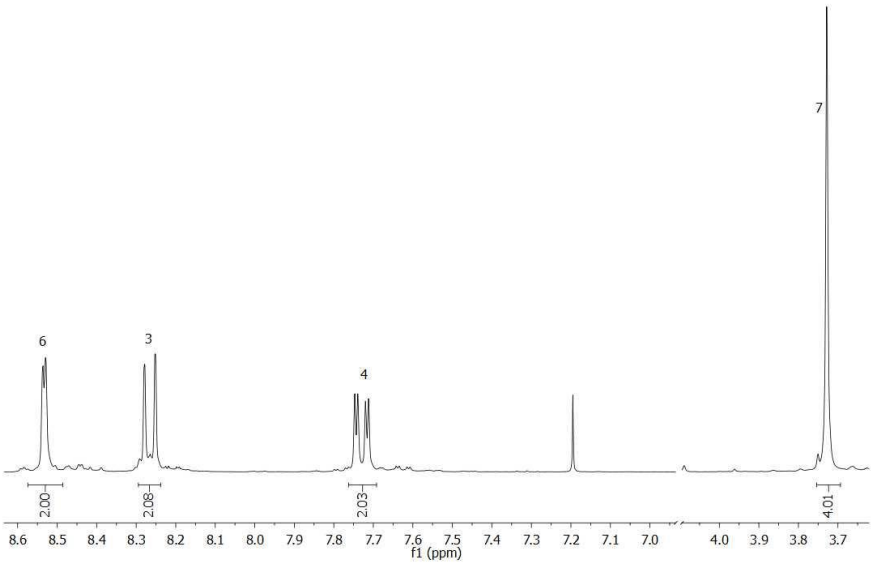

Figure 8.7: ^{1}H NMR 5,5’-dimethylthiol-2,2’-bipyridine. ($CDCl_3$).

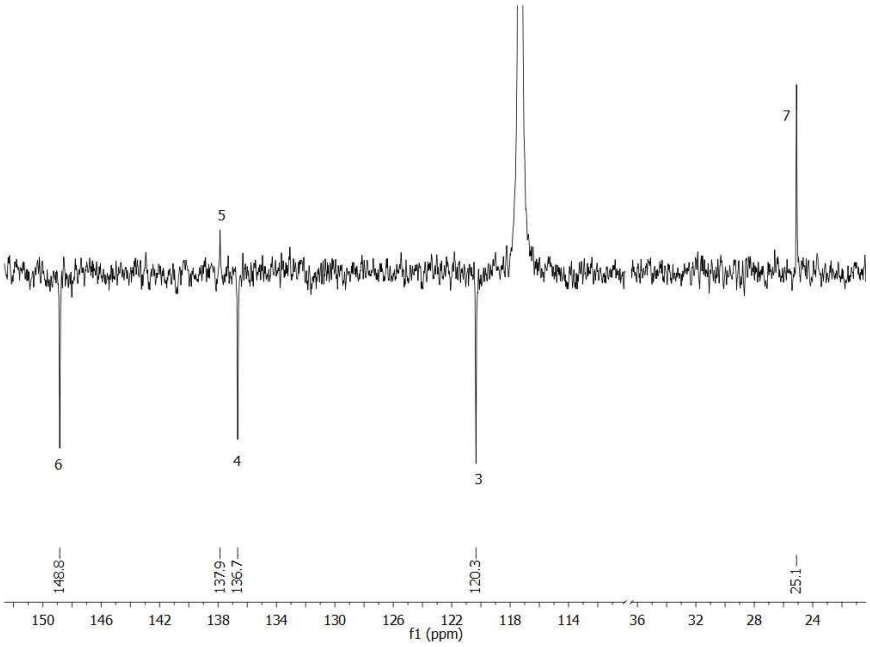

Figure 8.8: ^{13}C NMR 5,5'-dimethylthiol-2,2'-bipyridine. ($CDCl_3$).

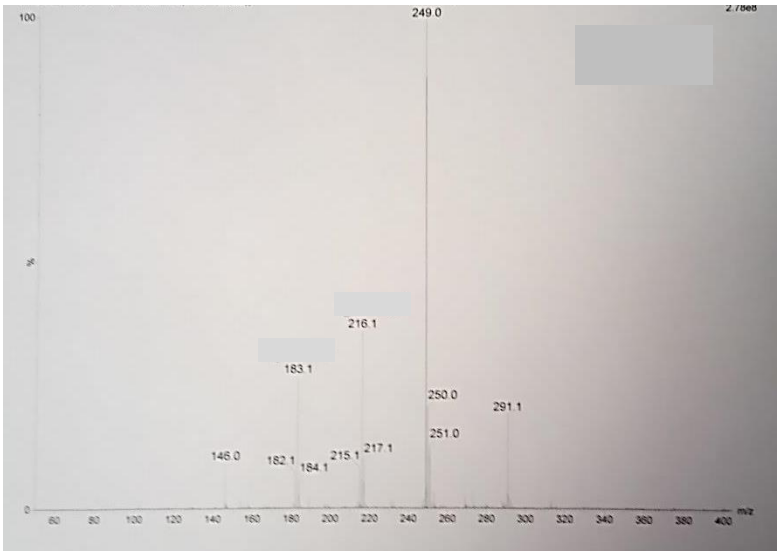

Figure 8.9: 5,5'-dimethylthiol-2,2'-bipyridine MS.

$Ru(bpy)_2Cl_2$

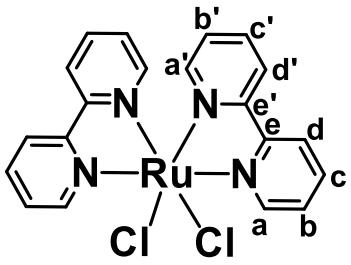

Figure 8.10: Structure of $Ru(bpy)_2Cl_2$.

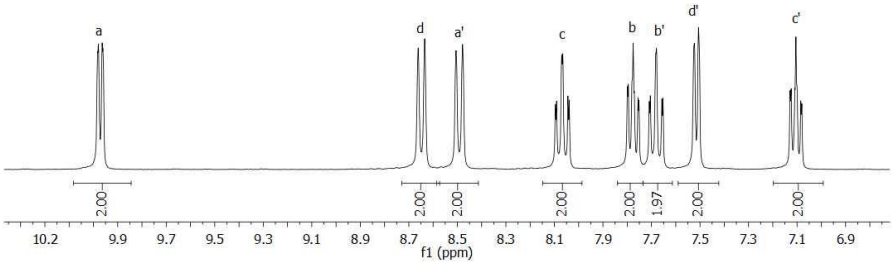

Figure 8.11: ^1H NMR $Ru(bpy)_2Cl_2$. (d_6-DMSO).

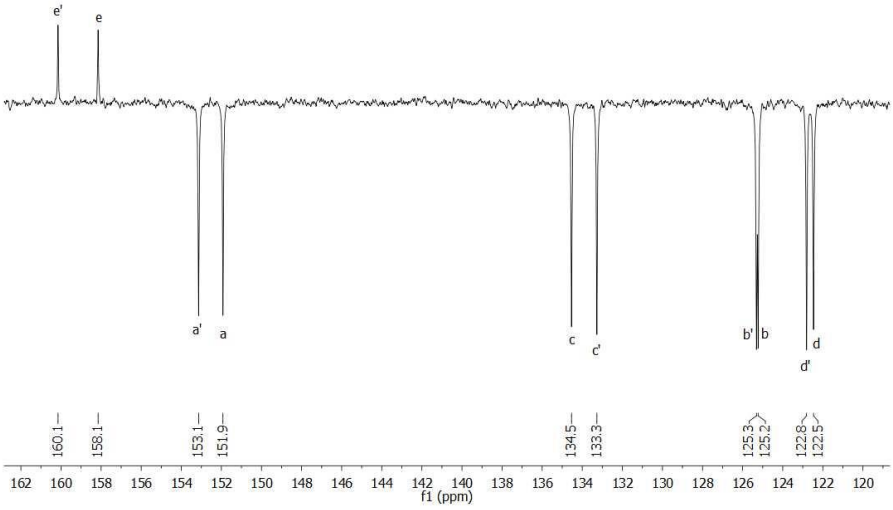

Figure 8.12: ^{13}C NMR $Ru(bpy)_2Cl_2$. (d_6-DMSO).

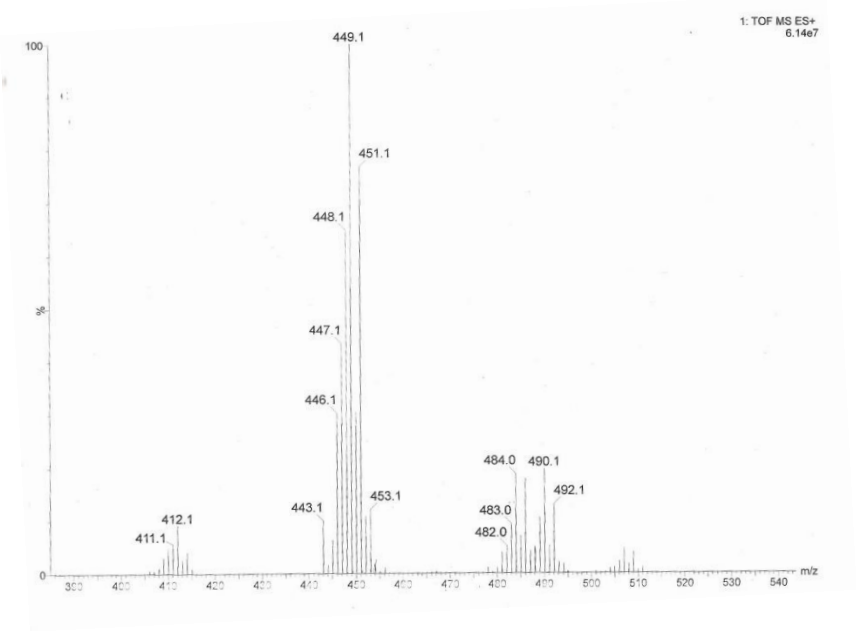

Figure 8.13: $Ru(bpy)_2Cl_2$ MS.

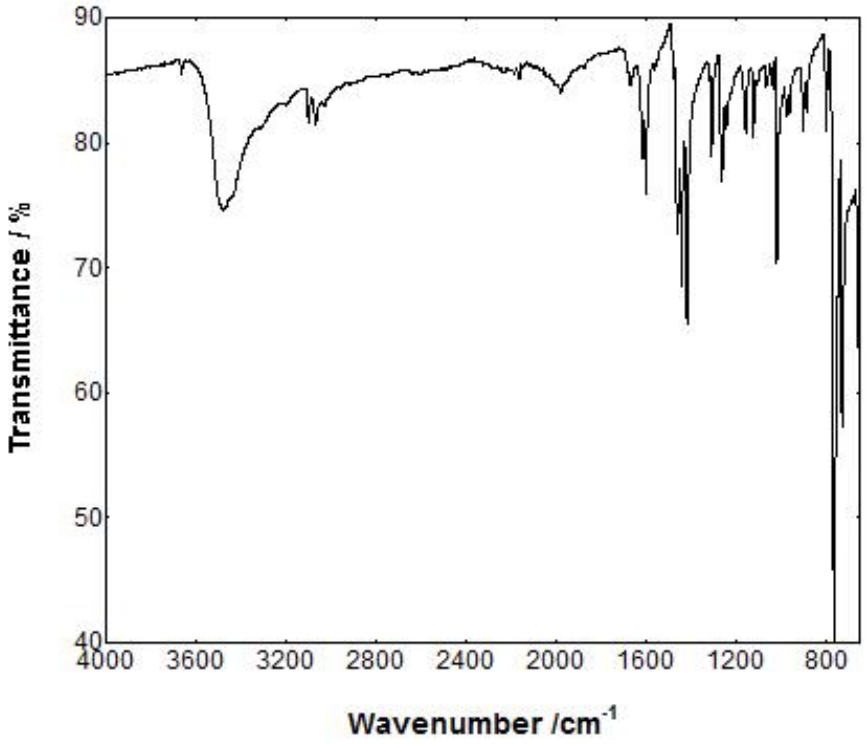

Figure 8.14: $Ru(bpy)_2Cl_2$ FTIR.

RuS1

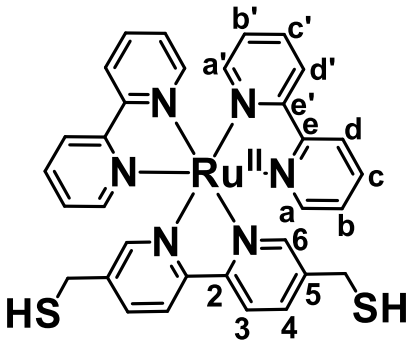

Figure 8.15: Structure of RuS1.

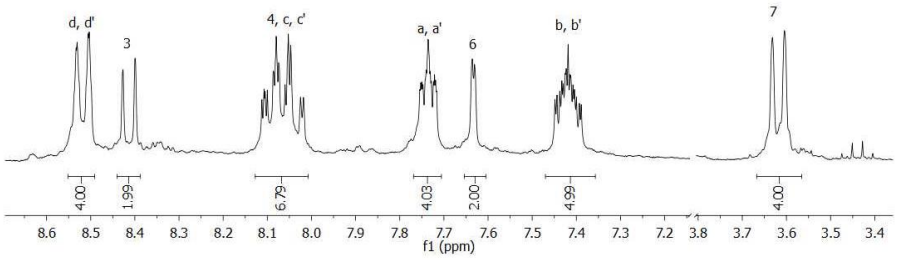

Figure 8.16: ^{1}H NMR RuS1. (CD_3CN).

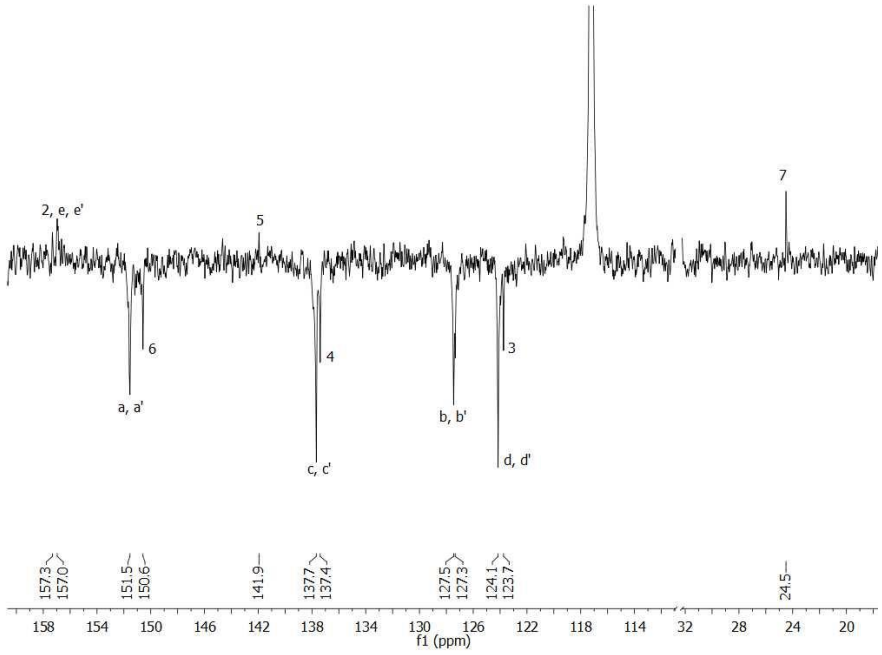

Figure 8.17: ^{13}C NMR RuS1. (CD_3CN).

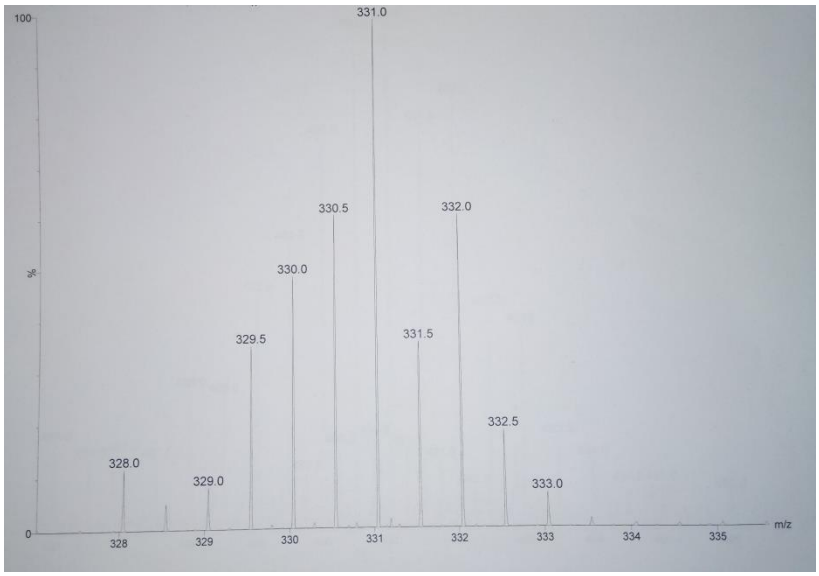

Figure 8.18: RuS1 MS.

8.2.1.2 RuS6

4,4-Dihydroxy-2,2’-bipyridine

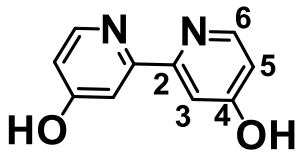

Figure 8.19: Structure of 4,4’-dihydroxy-2,2’-bipyridine.

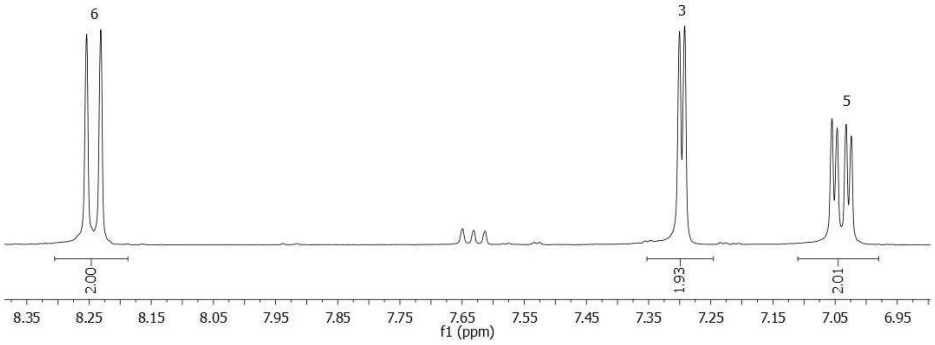

Figure 8.20: ^{1}H NMR 4,4’-dihydroxy-2,2’-bipyridine. (D_2O).

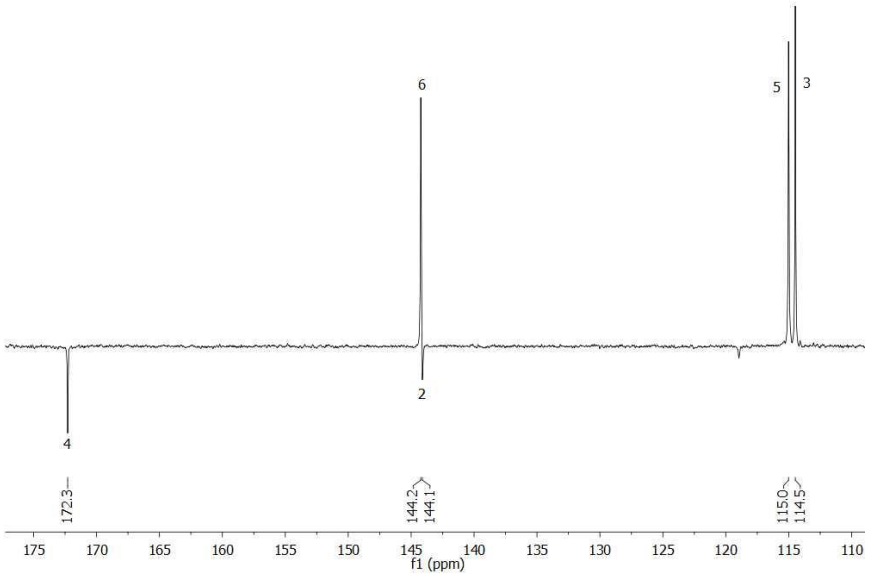

Figure 8.21: ^{13}C NMR 4,4’-dihydroxy-2,2’-bipyridine. (D_2O).

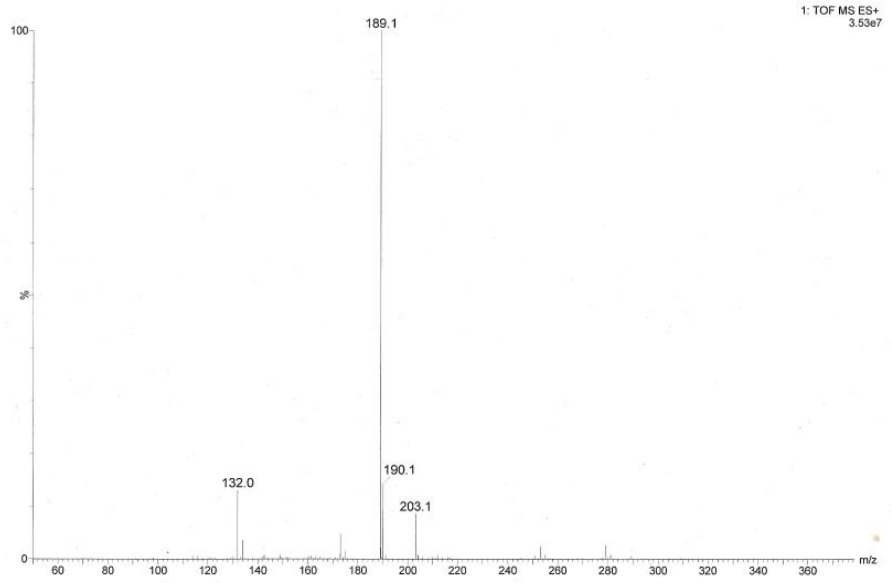

Figure 8.22: 4,4’-Dihydroxy-2,2’-bipyridine MS.

4,4’-Bis(5-hexen-1-yloxy)-2,2’-bipyridine

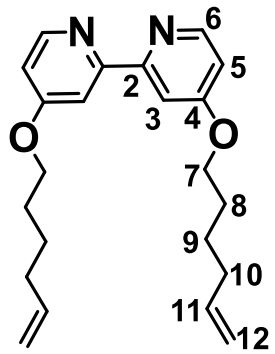

Figure 8.23: Structure of 4,4’-bis(5-hexen-1-yloxy)-2,2’-bipyridine.

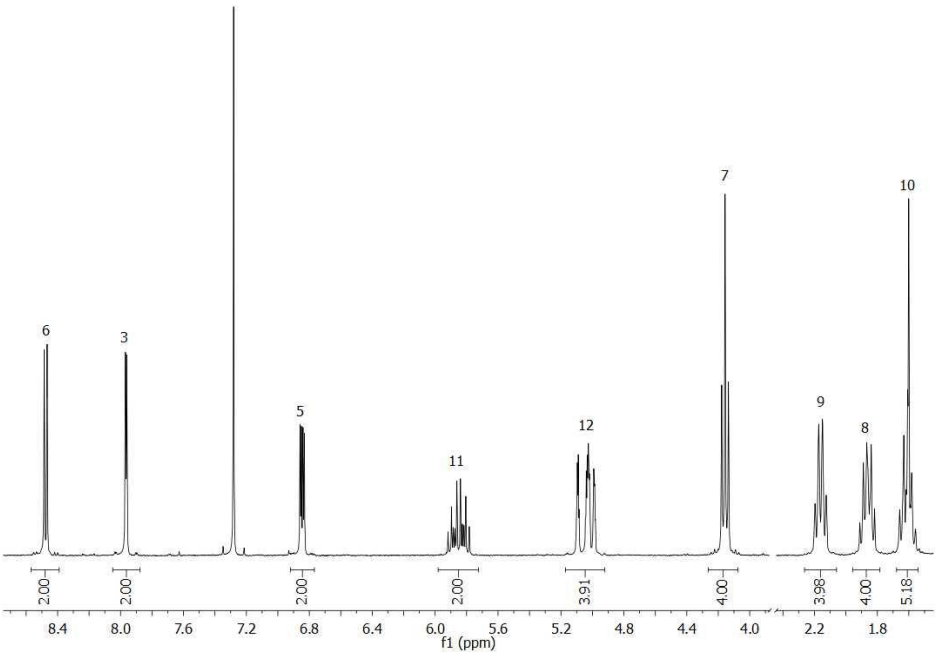

Figure 8.24: ^{1}H NMR 4,4’-bis(5-hexen-1-yloxy)-2,2’-bipyridine. ($CDCl_3$).

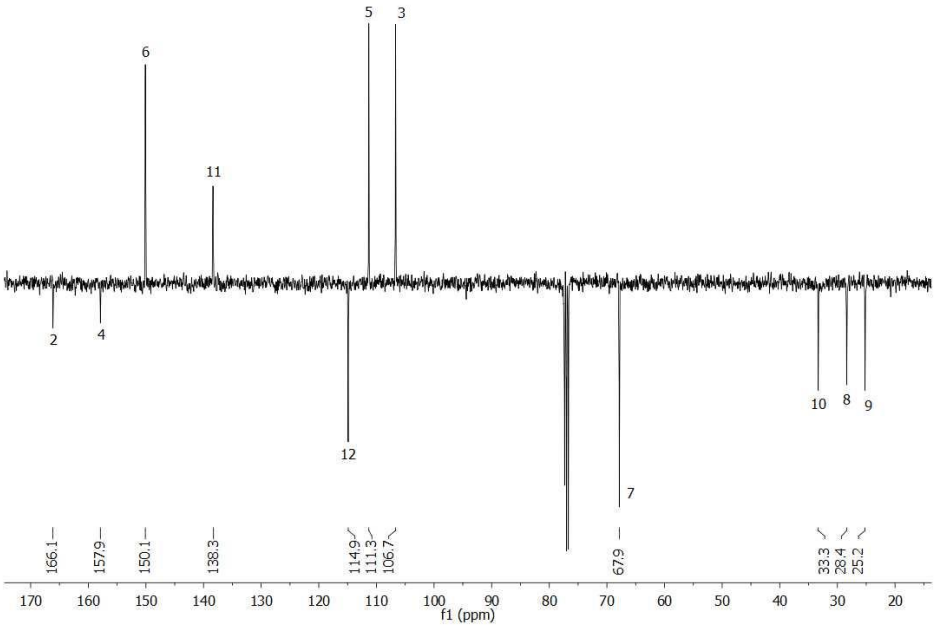

Figure 8.25: ^{13}C NMR 4,4'-bis(5-hexen-1-yloxy)-2,2'-bipyridine. ($CDCl_3$).

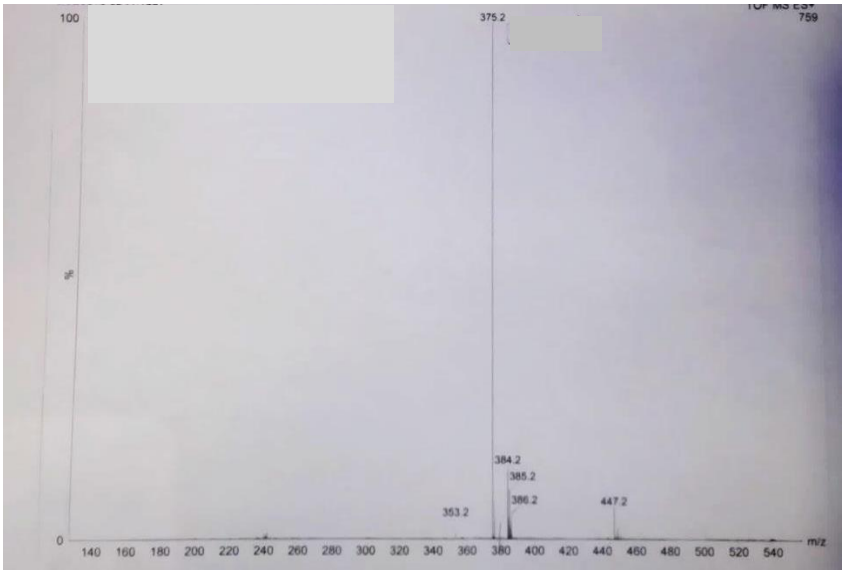

Figure 8.26: 4,4'-bis(5-hexen-1-yloxy)-2,2'-bipyridine MS.

Rubpyhex

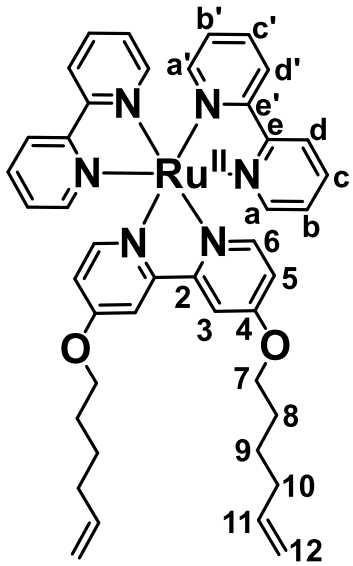

Figure 8.27: Structure of Rubpyhex.

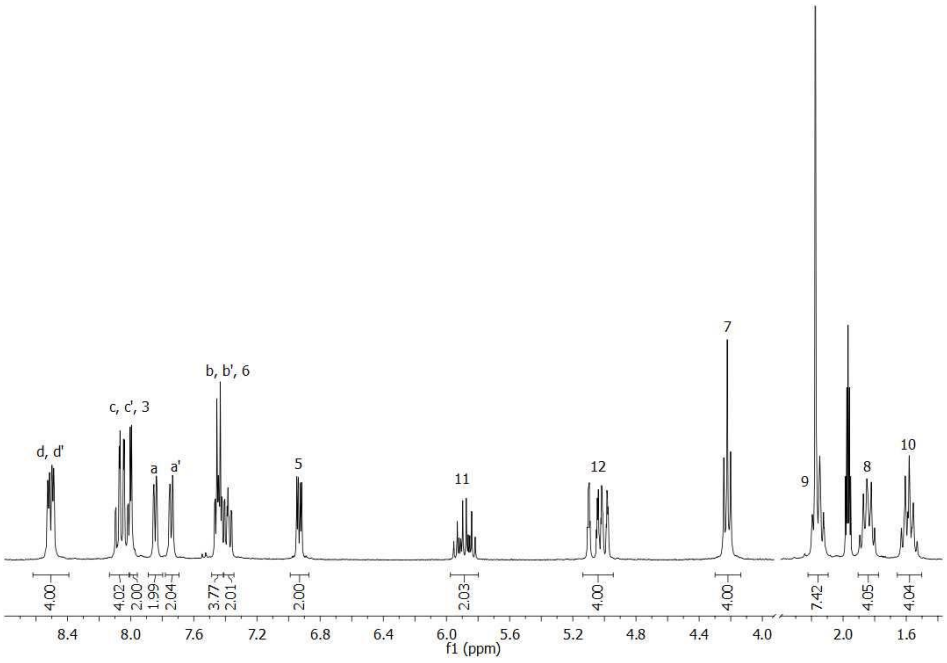

Figure 8.28: ^{1}H NMR Rubpyhex. (CD_3CN).

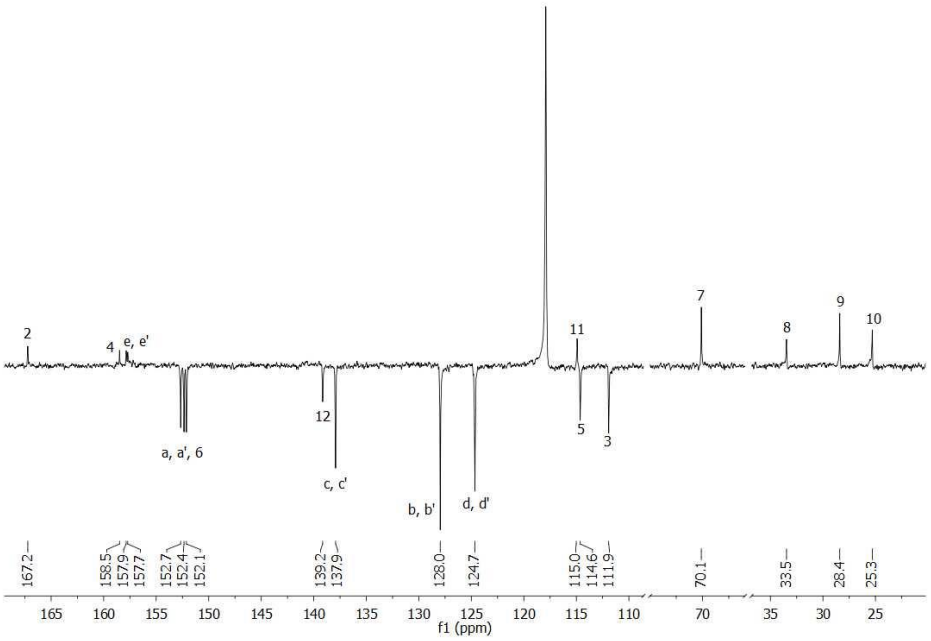

Figure 8.29: ^{13}C NMR Rubpyhex. (CD_3CN).

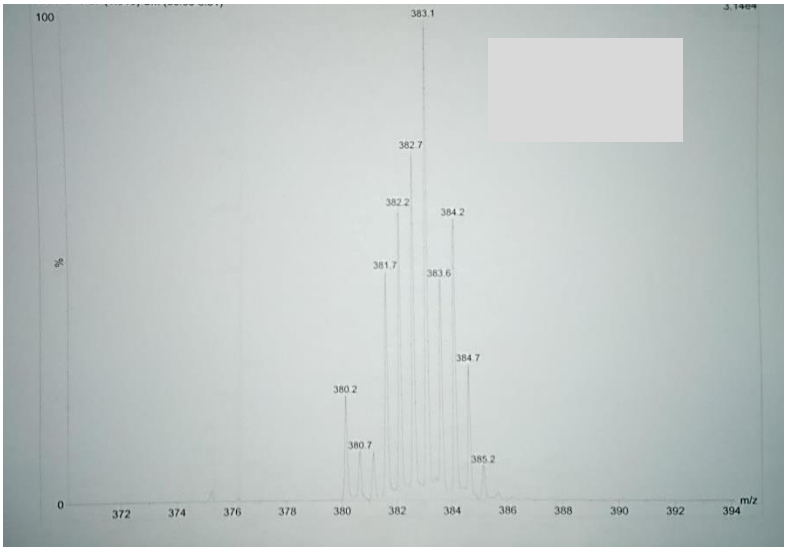

Figure 8.30: Rubpyhex MS.

RuS6

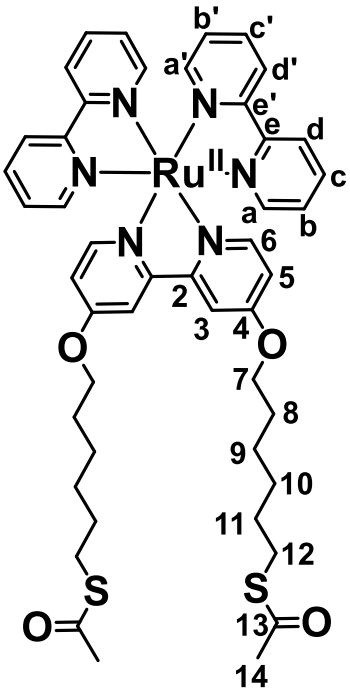

Figure 8.31: Structure of RuS6.

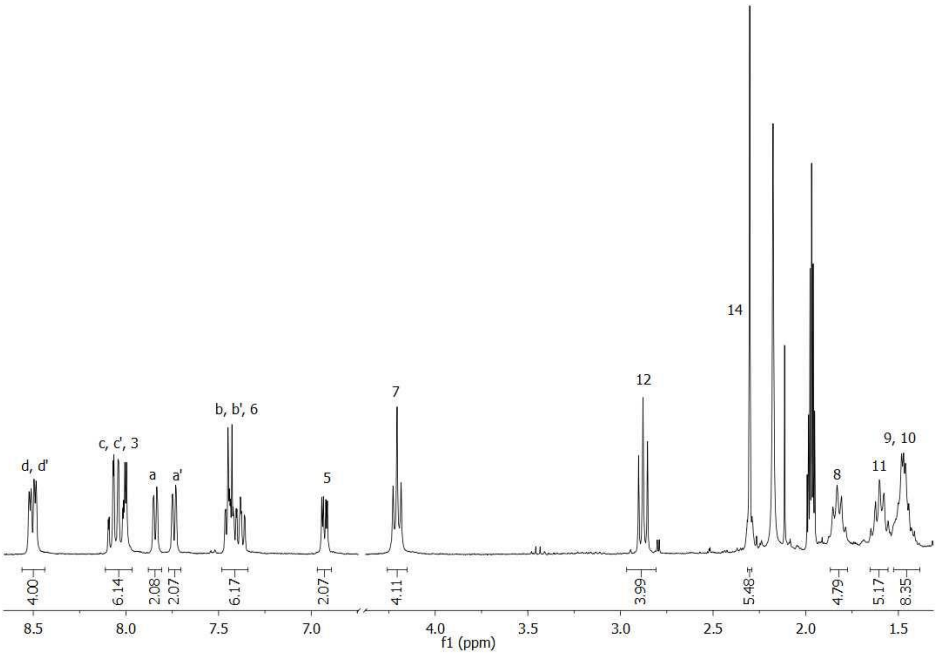

Figure 8.32: ^{1}H NMR RuS6. (CD_3CN).

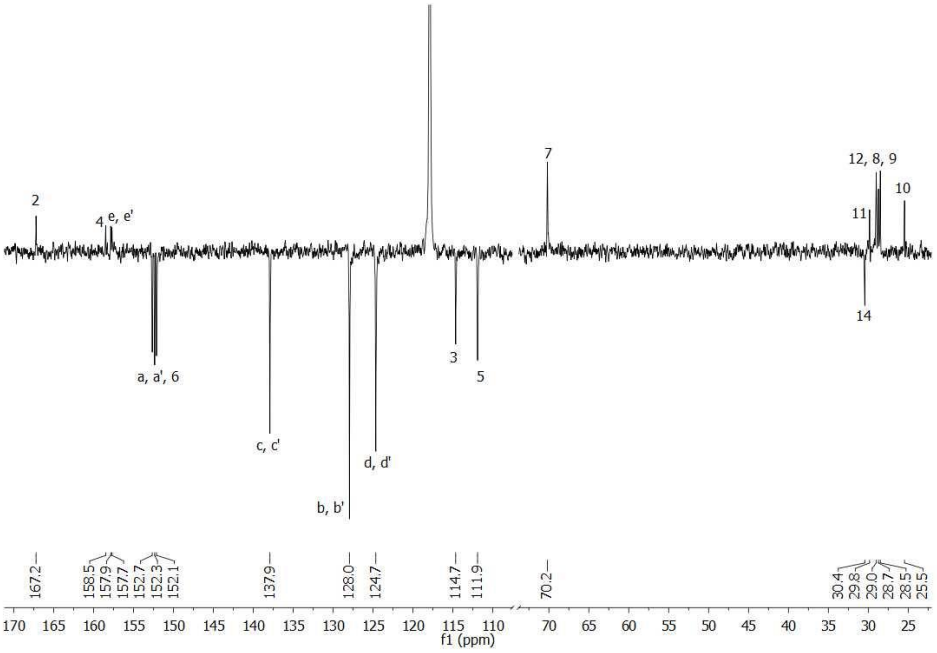

Figure 8.33: ^{13}C NMR RuS6. (CD_3CN).

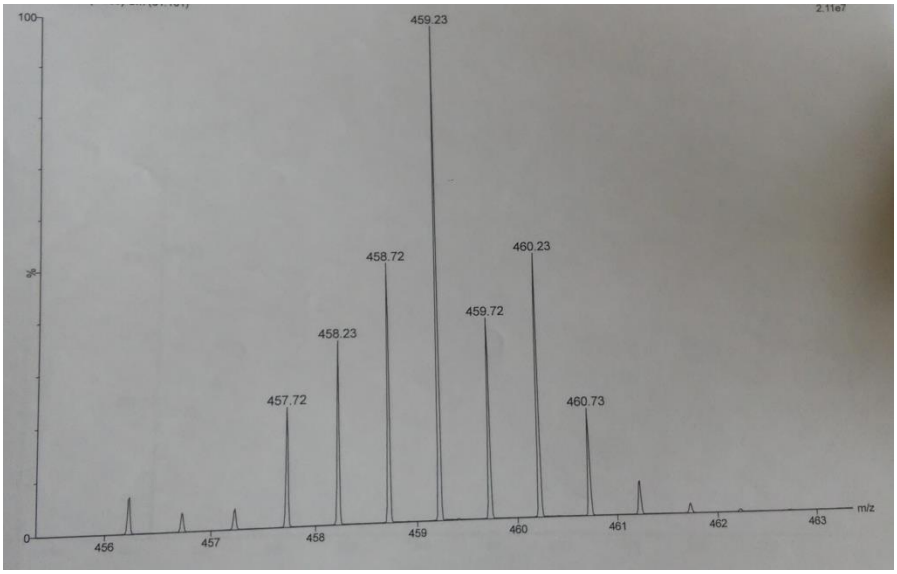

Figure 8.34: RuS6 MS.

8.2.1.3 RuS12

N-Boc-5-amino-1-pentanol

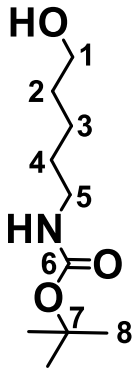

Figure 8.35: Structure of N-Boc-5-amino-1-pentanol.

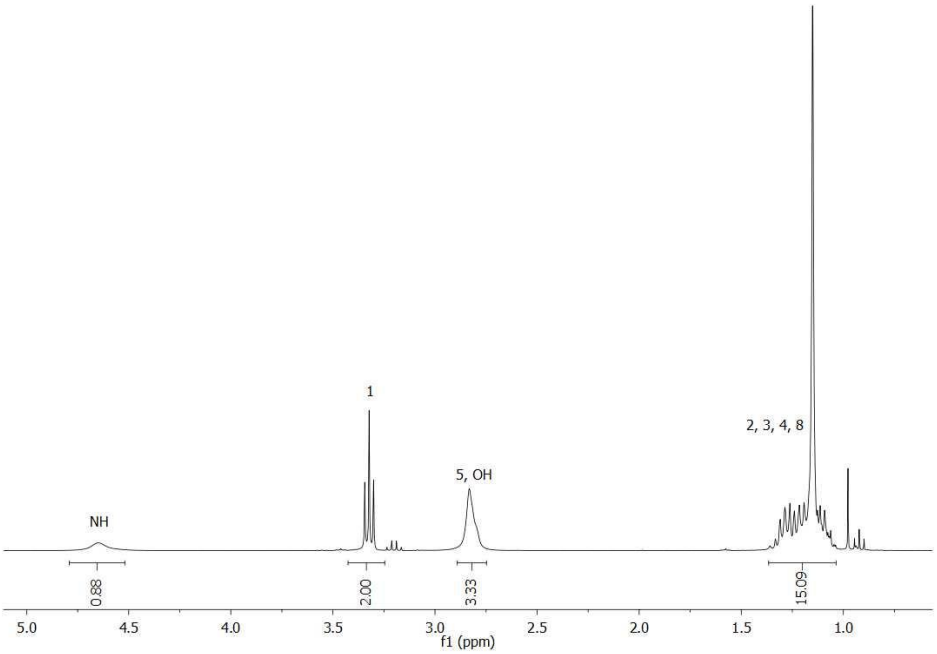

Figure 8.36: ^{1}H NMR N-Boc-5-amino-1-pentanol. ($CDCl_3$).

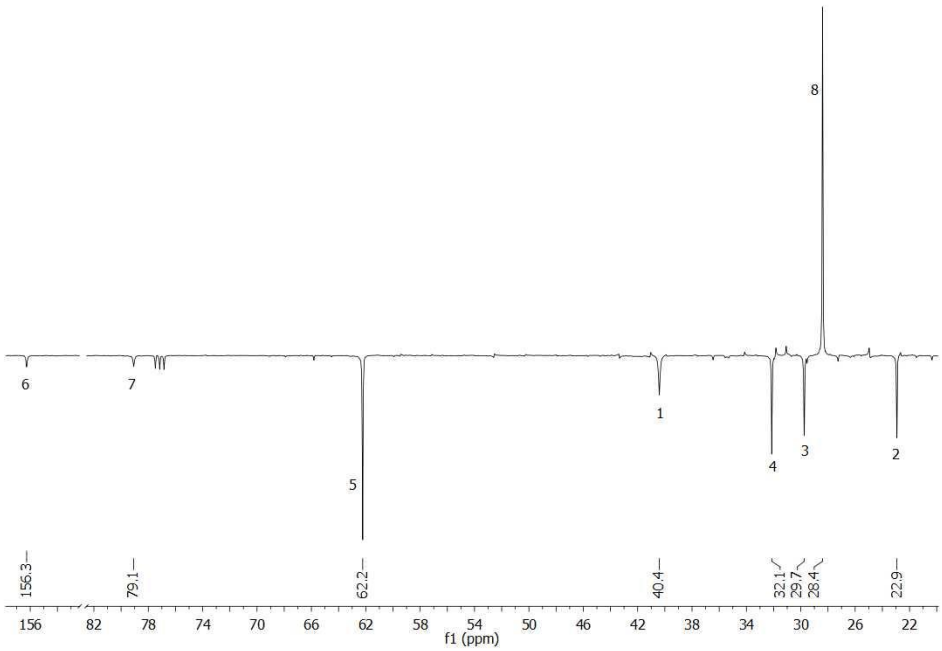

Figure 8.37: ^{13}C NMR N-Boc-5-amino-1-pentanol. ($CDCl_3$).

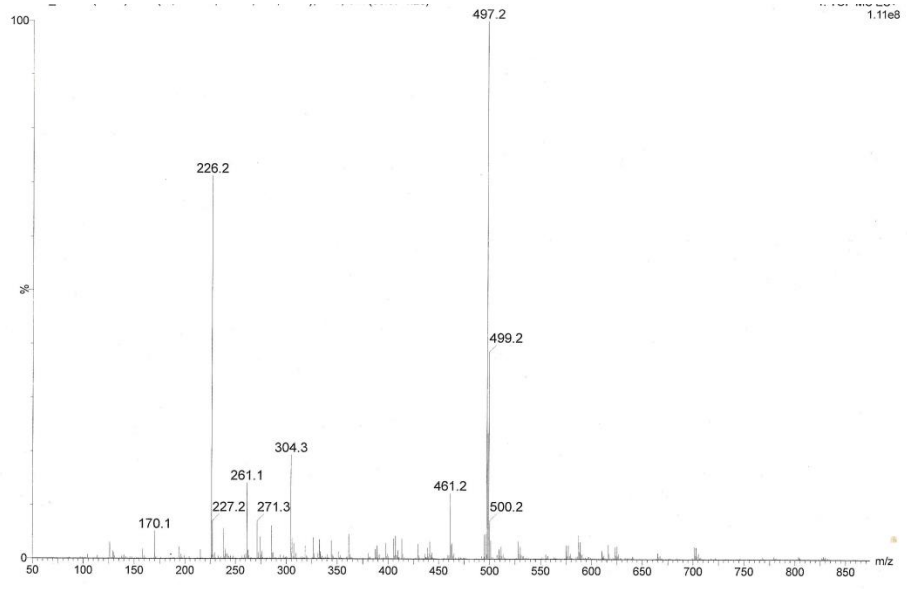

Figure 8.38: N-Boc-5-amino-1-pentanol MS.

N-Boc-5-amino-1-tosylpentane

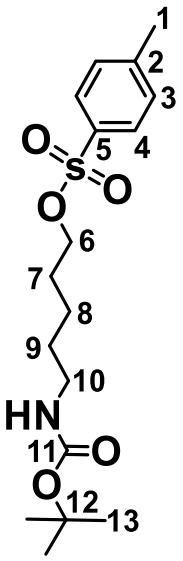

Figure 8.39: Structure of N-Boc-5-amino-1-tosylpentane.

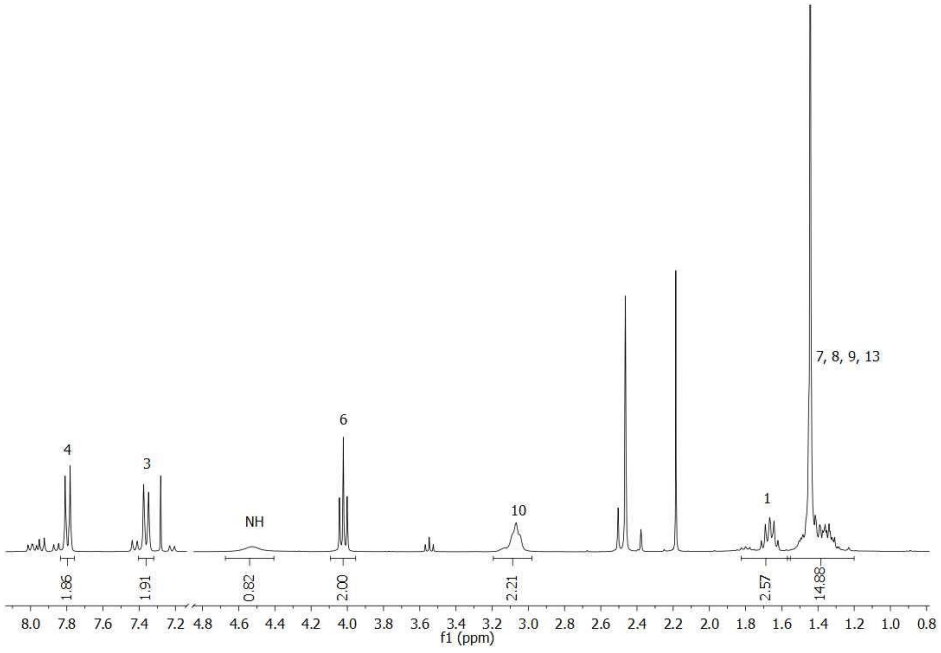

Figure 8.40: ^{1}H NMR N-Boc-5-amino-1-tosylpentane. ($CDCl_3$).

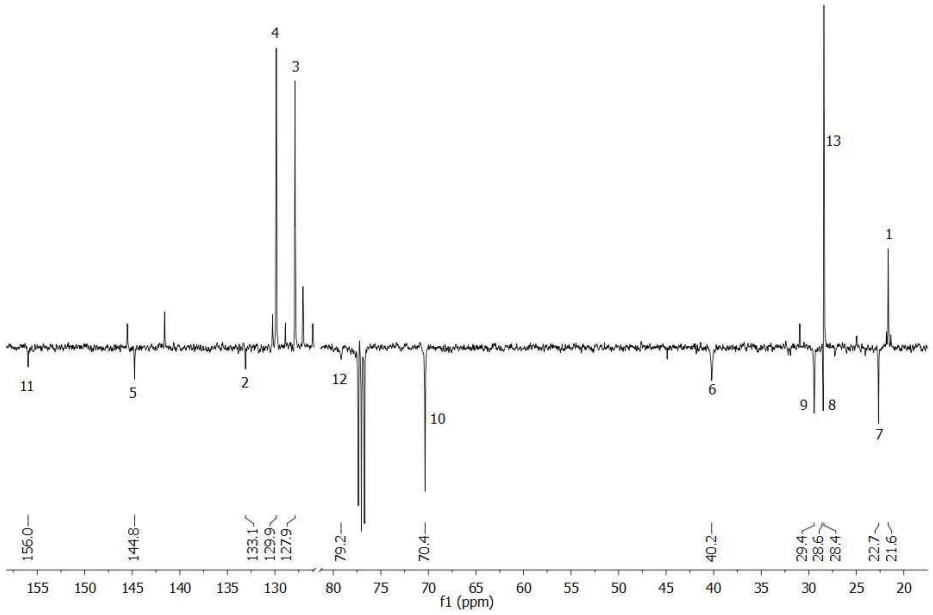

Figure 8.41: ^{13}C NMR N-Boc-5-amino-1-tosylpentane. ($CDCl_3$).

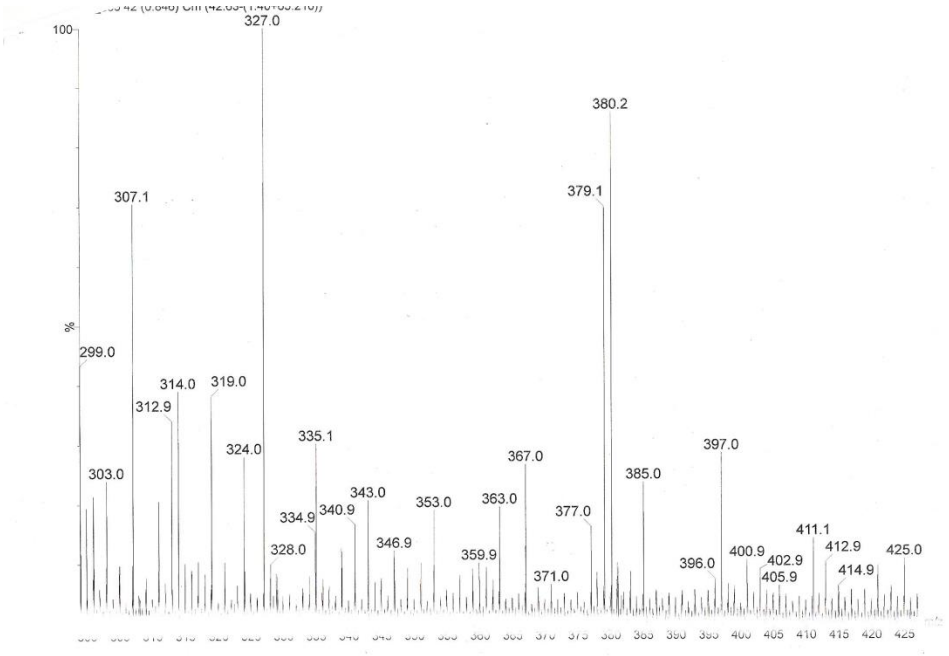

Figure 8.42: N-Boc-5-amino-1-tosylpentane MS.

4,4’-Di-(N-boc-5-amino-1-pentoxy)-2,2’-bipyridine

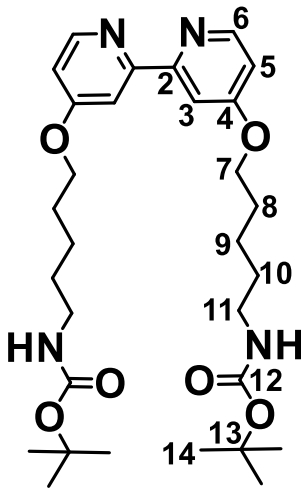

Figure 8.43: Structure of 4,4’-di-(N-boc-5-amino-1-pentoxy)-2,2’-bipyridine.

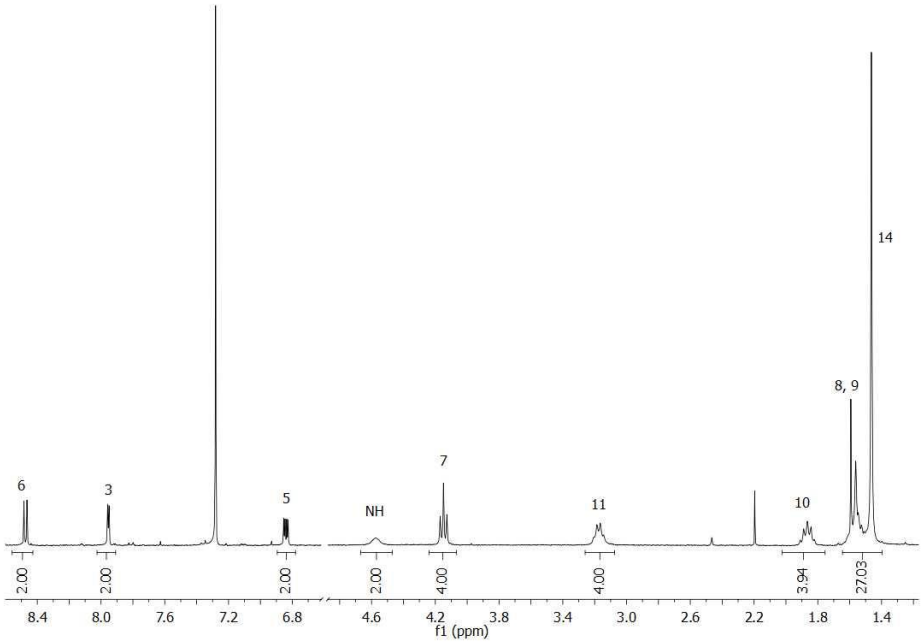

Figure 8.44: ^{1}H NMR 4,4’-di-(N-boc-5-amino-1-pentoxy)-2,2’-bipyridine. ($CDCl_3$).

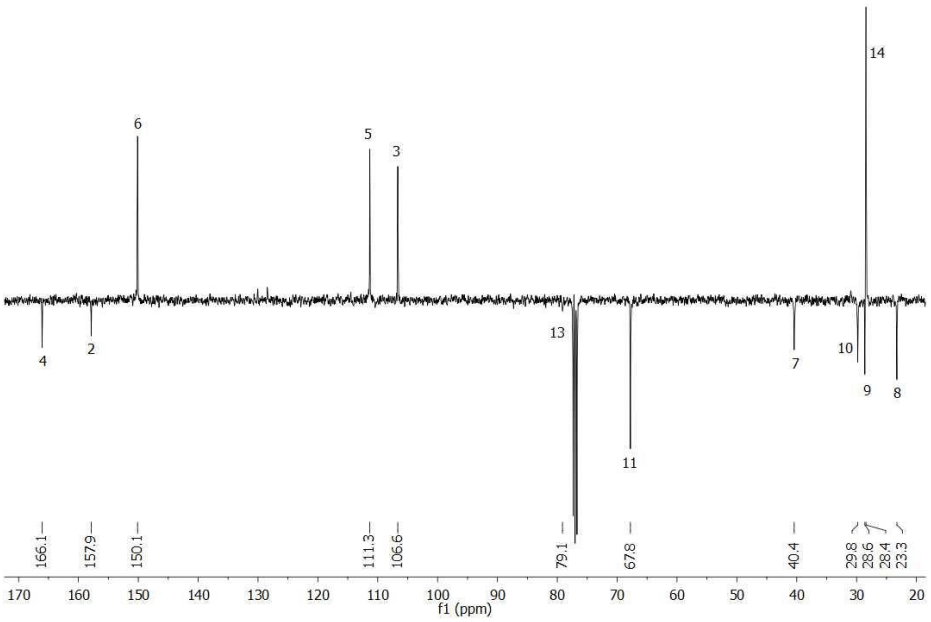

Figure 8.45: ^{13}C NMR 4,4'-di-(N-boc-5-amino-1-pentoxy)-2,2'-bipyridine. ($CDCl_3$).

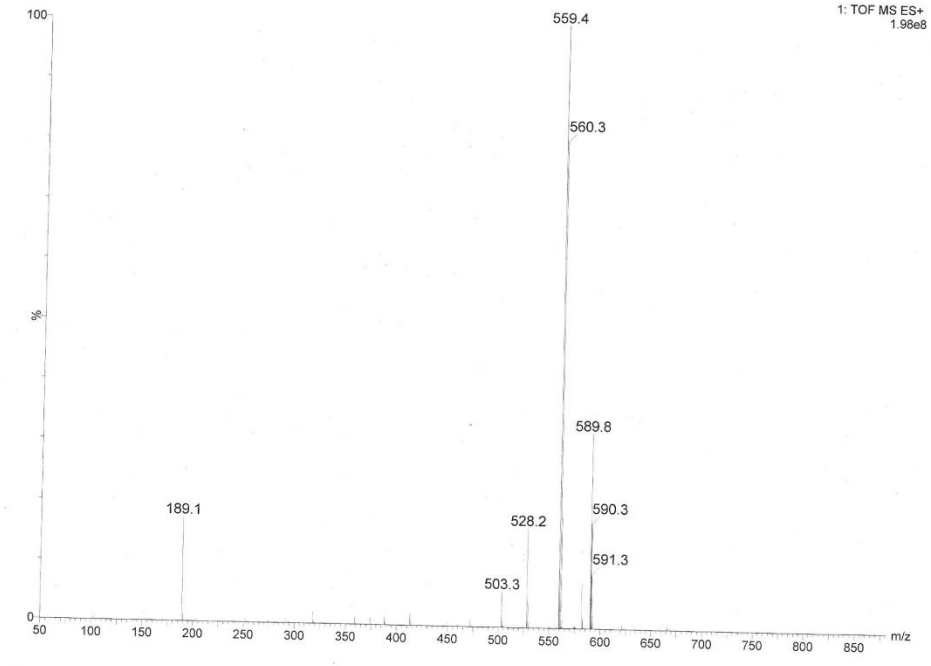

Figure 8.46: 4,4'-di-(N-boc-5-amino-1-pentoxy)-2,2'-bipyridine MS.

4,4’-Di-(5-amino-1-pentoxy)-2,2’-bipyridine

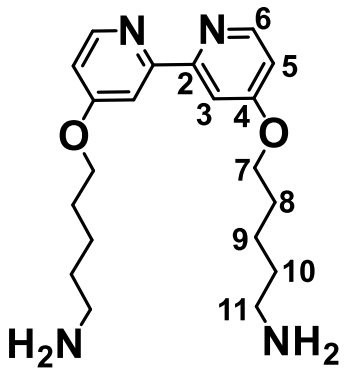

Figure 8.47: Structure of 4,4’-di-(5-amino-1-pentoxy)-2,2’-bipyridine.

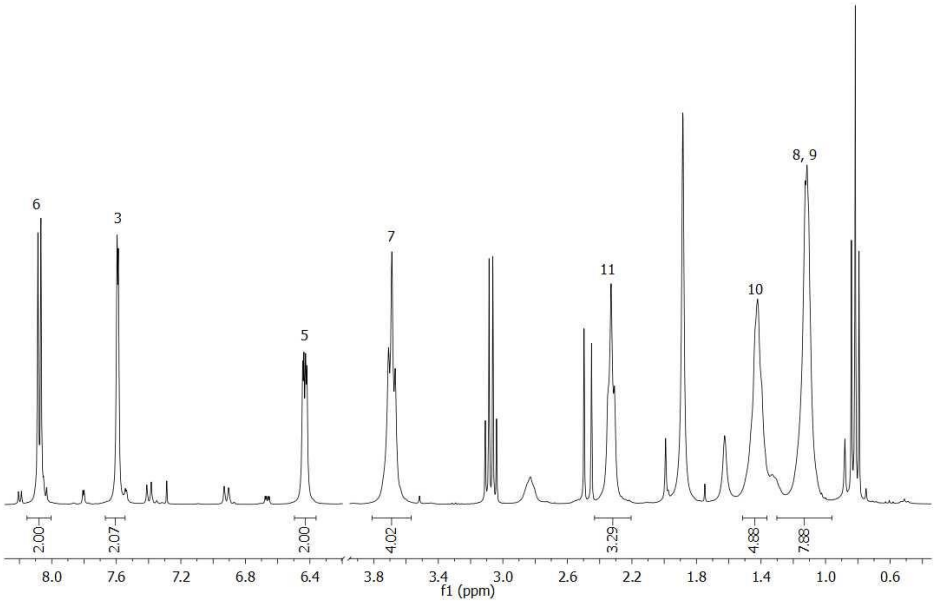

Figure 8.48: ^{1}H NMR 4,4’-di-(5-amino-1-pentoxy)-2,2’-bipyridine. ($CDCl_3$).

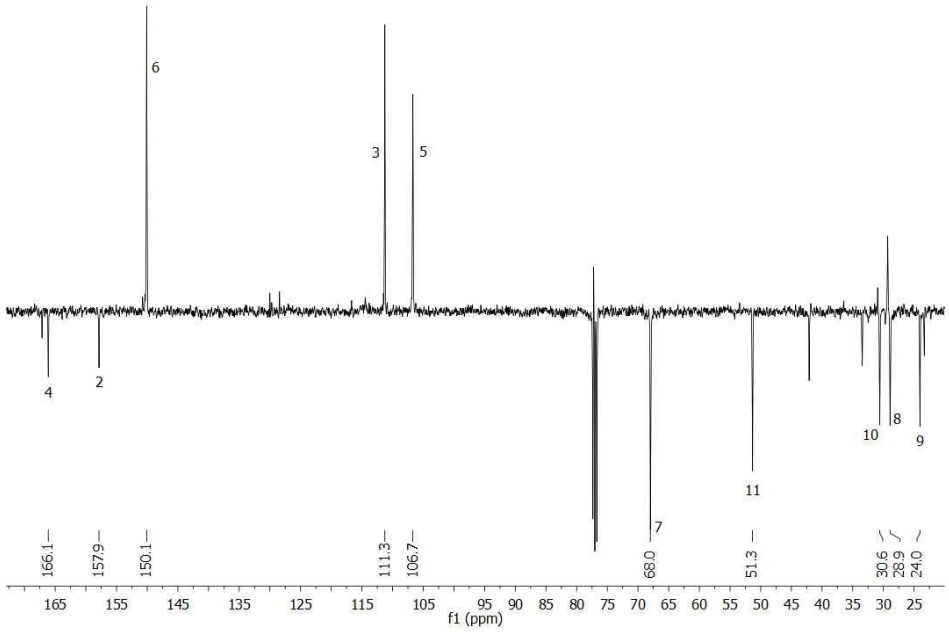

Figure 8.49: ^{13}C MS 4,4'-di-(5-amino-1-pentoxy)-2,2'-bipyridine. ($CDCl_3$).

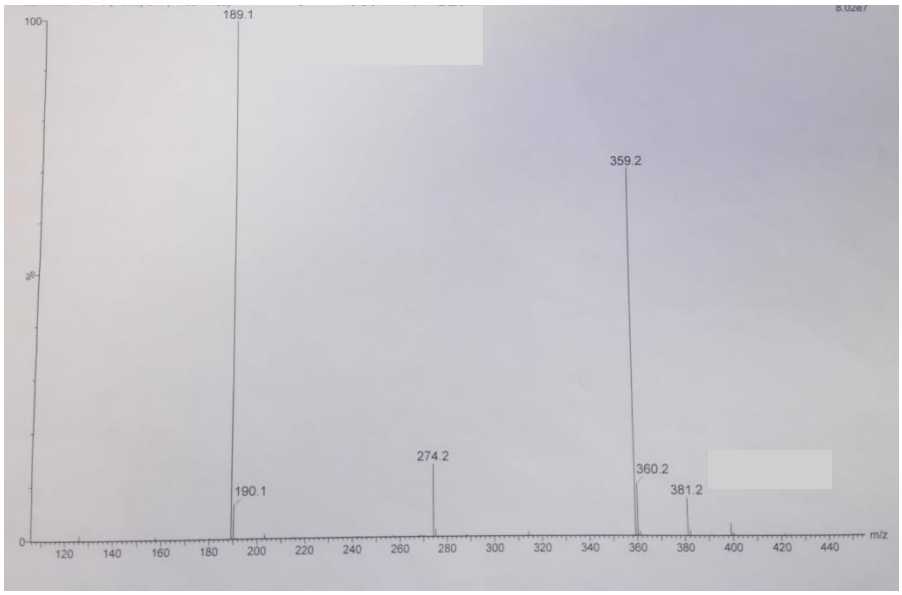

Figure 8.50: 4,4'-di-(5-amino-1-pentoxy)-2,2'-bipyridine MS.

4,4’-Di-(5-lipoamide-1-pentoxy)-2,2’-bipyridine

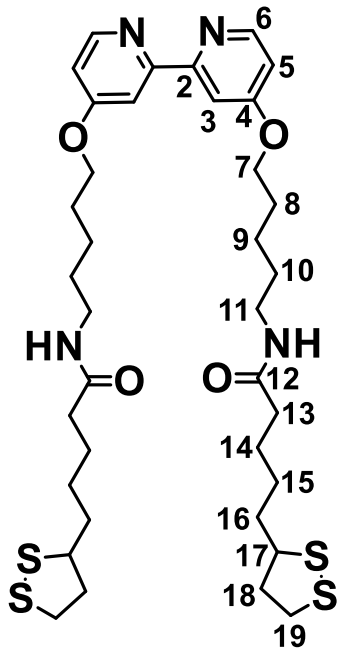

Figure 8.51: Structure of 4,4’-di-(5-lipoamide-1-pentoxy)-2,2’-bipyridine.

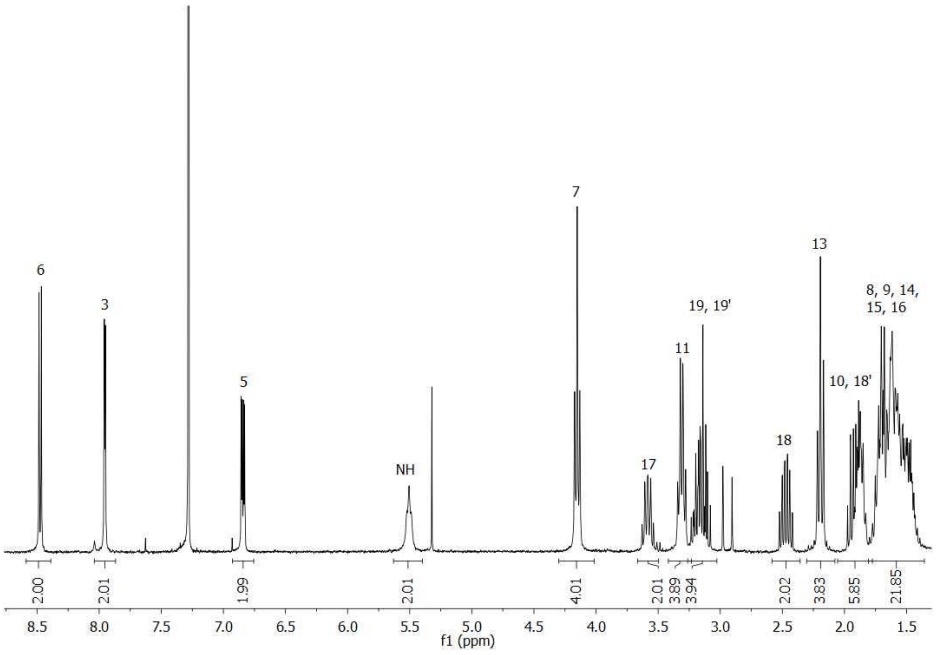

Figure 8.52: ^{1}H NMR 4,4’-di-(5-lipoamide-1-pentoxy)-2,2’-bipyridine. ($CDCl_3$).

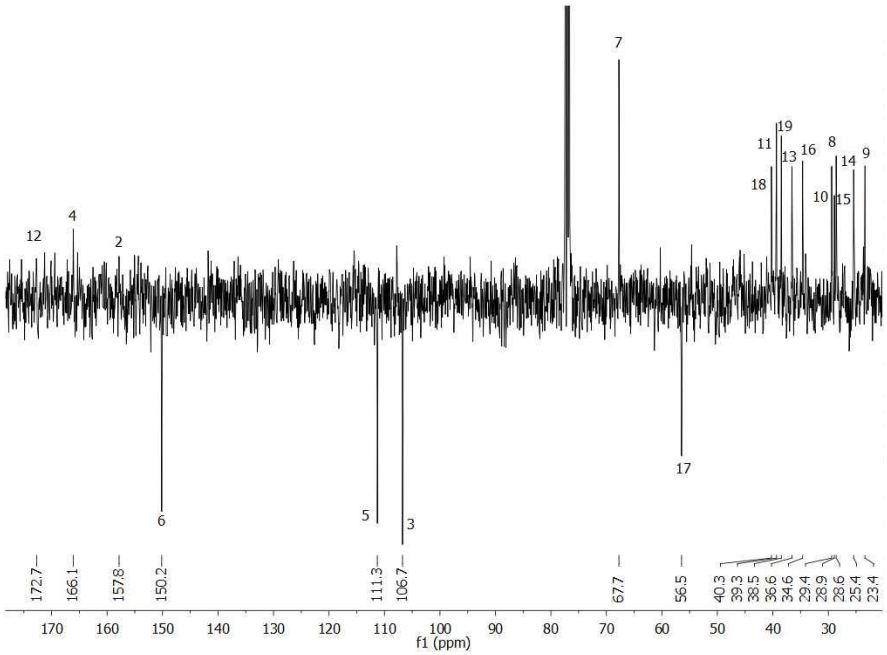

Figure 8.53: ^{13}C NMR 4,4'-di-(5-lipoamide-1-pentoxy)-2,2'-bipyridine. ($CDCl_3$).

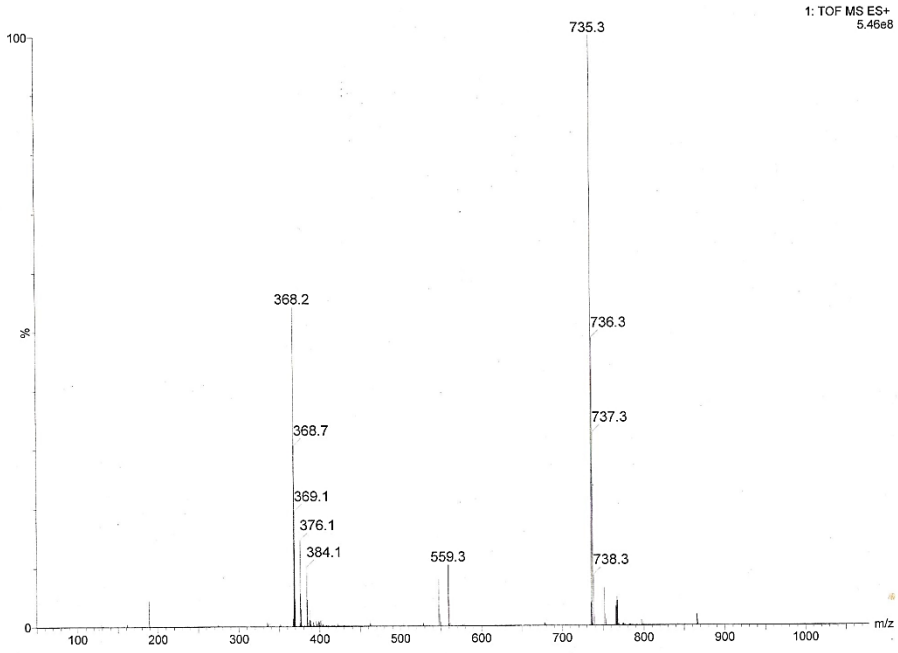

Figure 8.54: 4,4'-di-(5-lipoamide-1-pentoxy)-2,2'-bipyridine MS.

RuS12

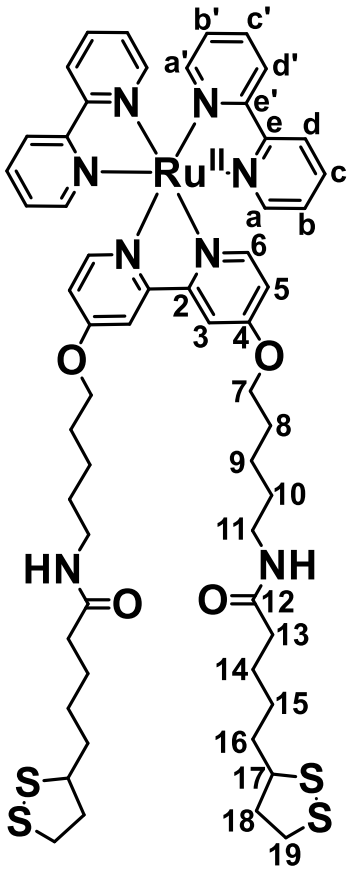

Figure 8.55: Structure of RuS12.

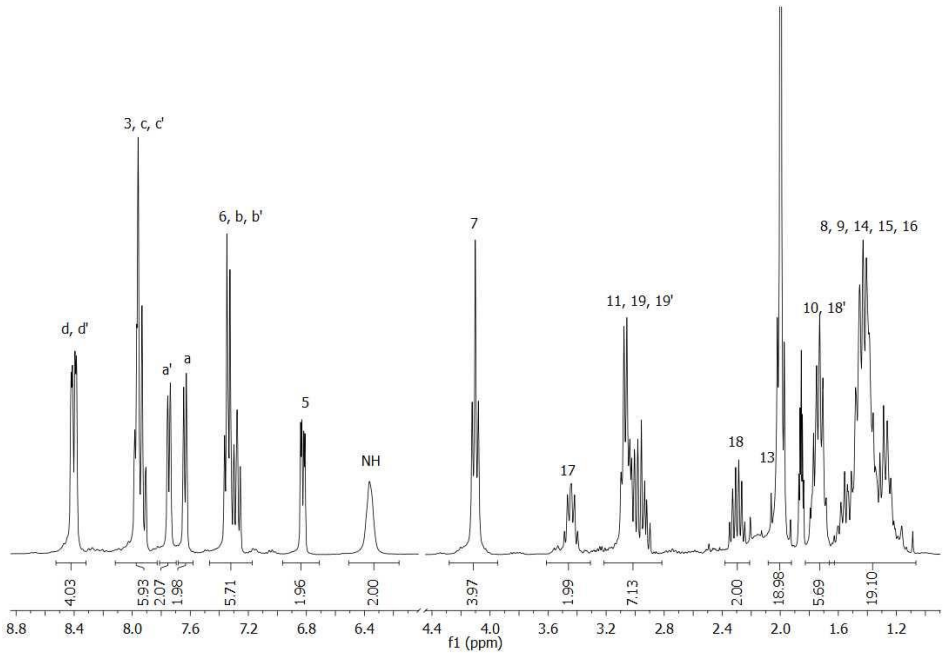

Figure 8.56: ^{1}H NMR RuS12. (CD_3CN).

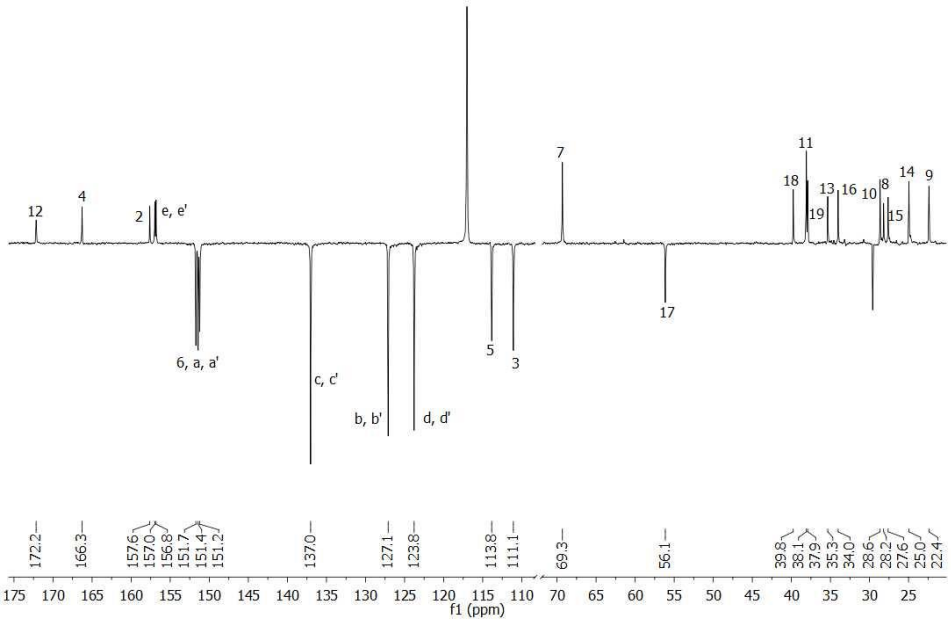

Figure 8.57: ^{13}C NMR RuS12. (CD_3CN).

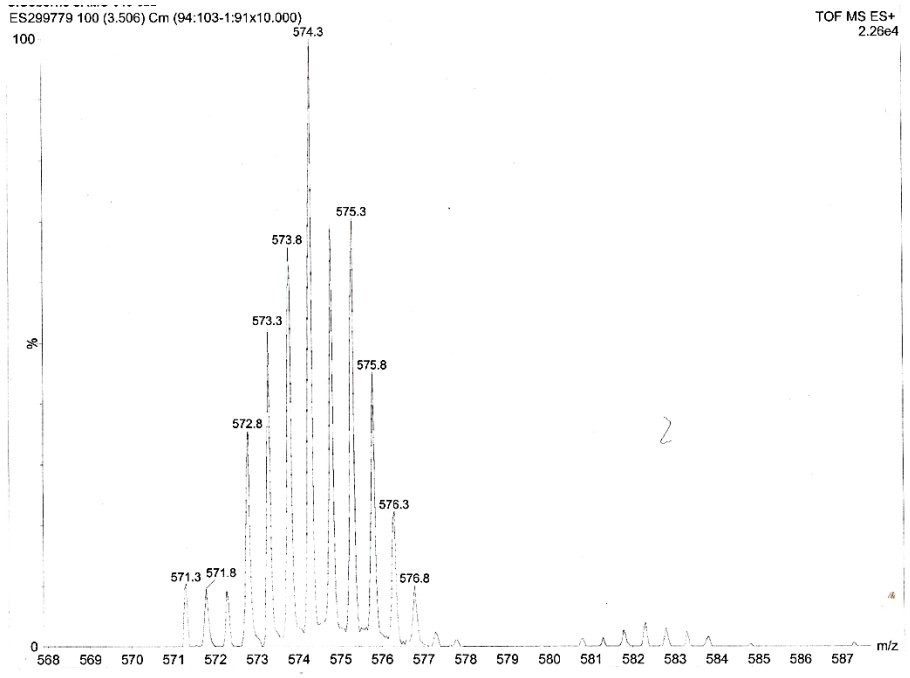

Figure 8.58: RuS12 MS.

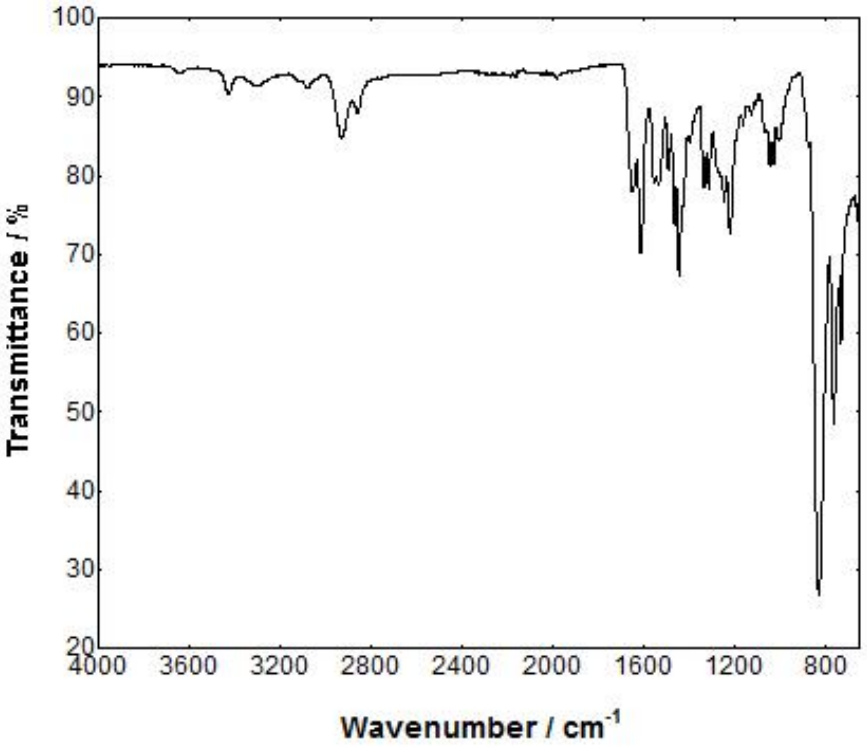

Figure 8.59: RuS12 FTIR.

8.2.2 XPS of ruthenium coated AuNP

8.2.2.1 RuS1•AuNP13

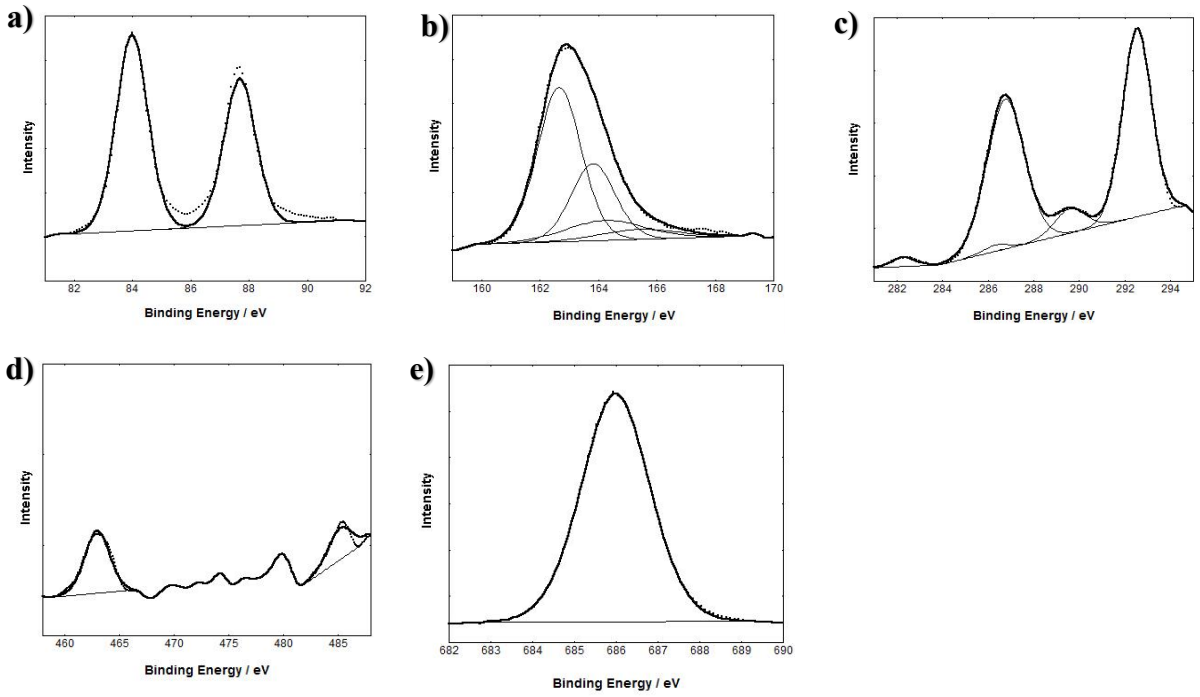

Figure 8.60: XPS binding energy showing the regions of Au 4f (a), S 2p (b), Ru 3d (c), Ru 3p (d) and F 1s (e) for RuS1•AuNP13.

8.2.2.2 RuS6•AuNP13

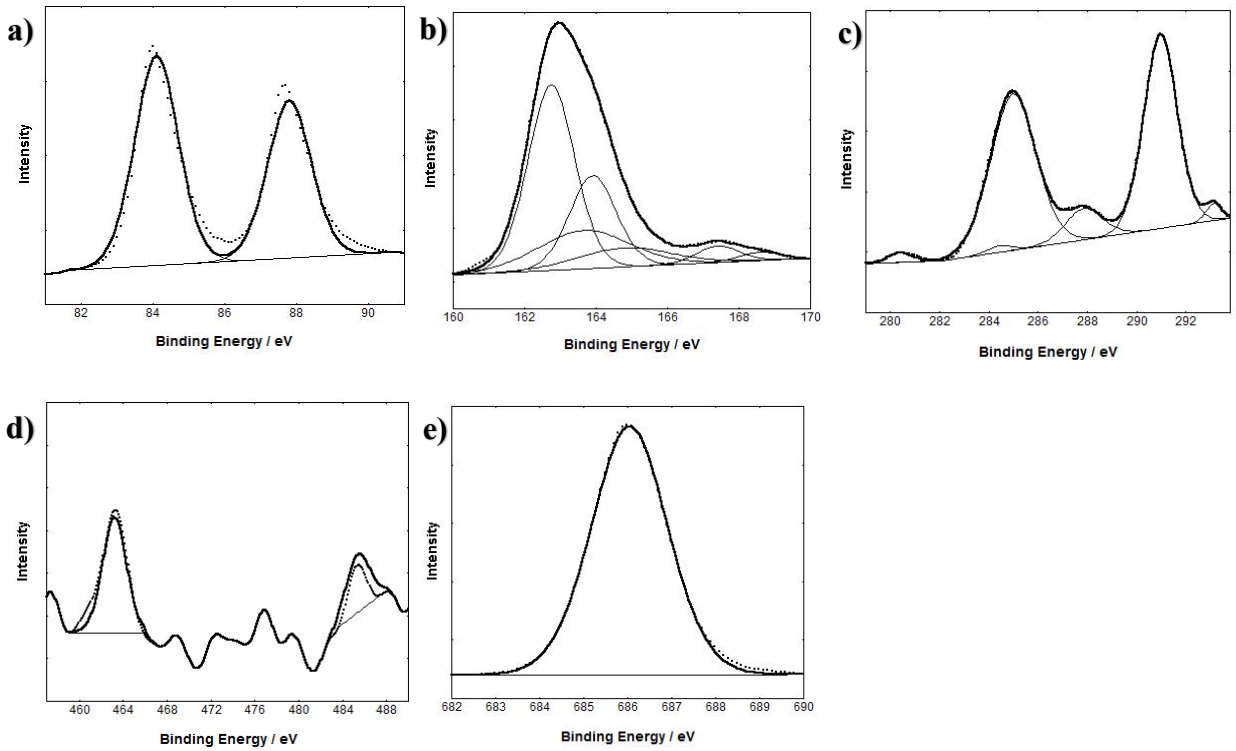

Figure 8.61: XPS binding energy showing the regions of Au 4f (a), S 2p (b), Ru 3d (c), Ru 3p (d) and F 1s (e) for RuS6•AuNP13.

8.3 Chapter 4: Improving the photophysical properties of ruthenium complexes with 2,2'-bipyridine-4,4' sulphur ligands

8.3.1 Synthesis: NMR and MS

8.3.1.1 RuphenS12

$Ru(phen)_2Cl_2$

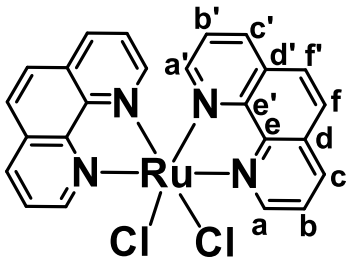

Figure 8.62: Structure of $Ru(phen)_2Cl_2$.

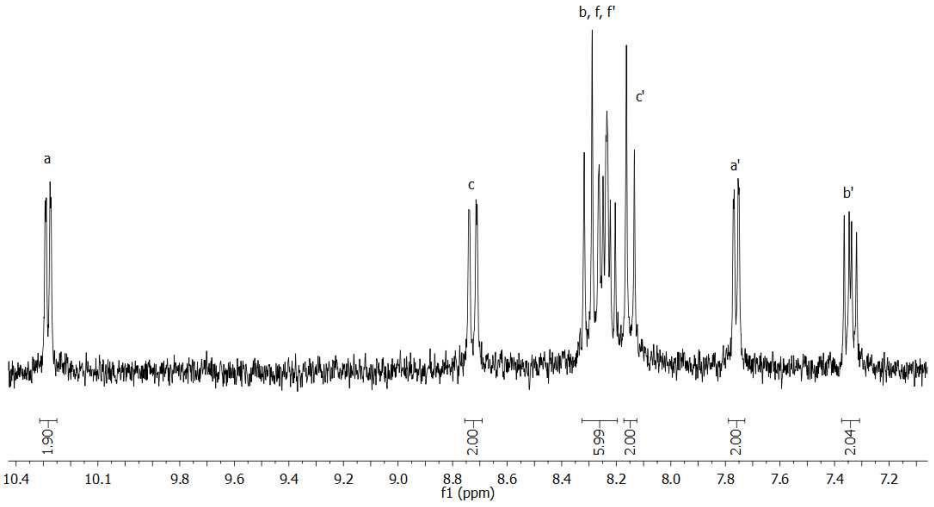

Figure 8.63: ^1H NMR $Ru(phen)_2Cl_2$. (d_6-DMSO).

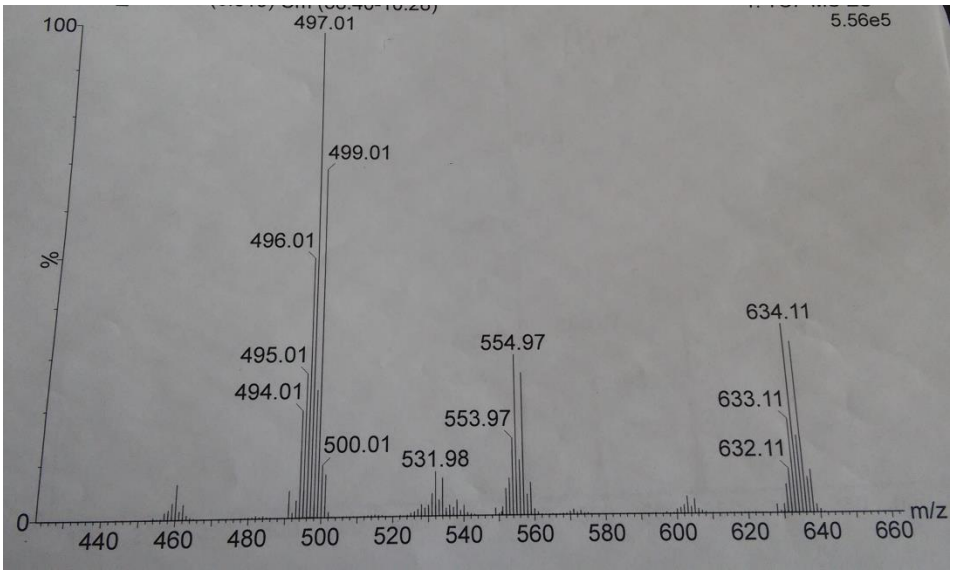

Figure 8.64: $Ru(phen)_2Cl_2$ MS.

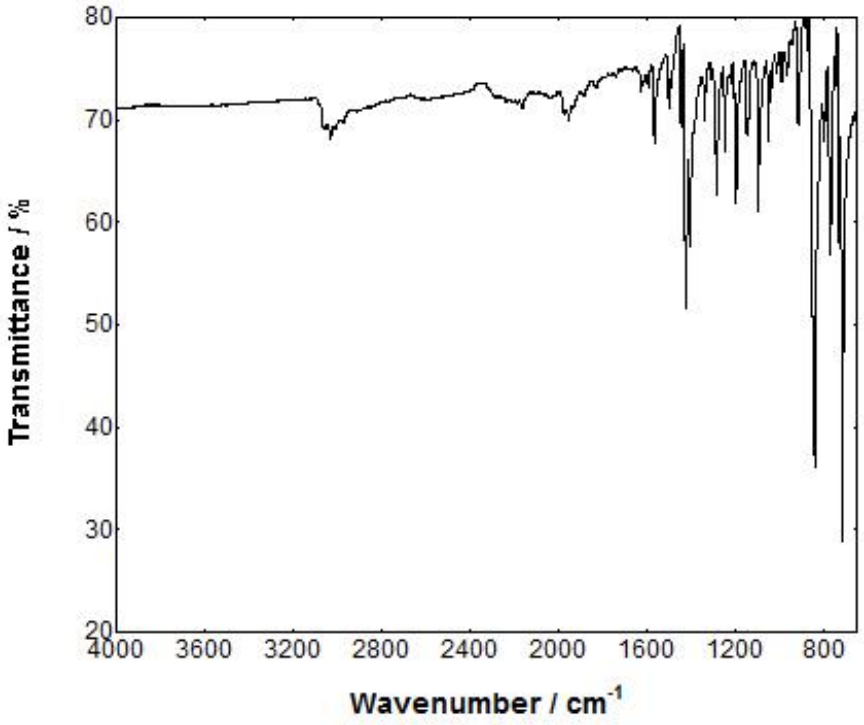

Figure 8.65: $Ru(phen)_2Cl_2$ FTIR.

RuphenS12

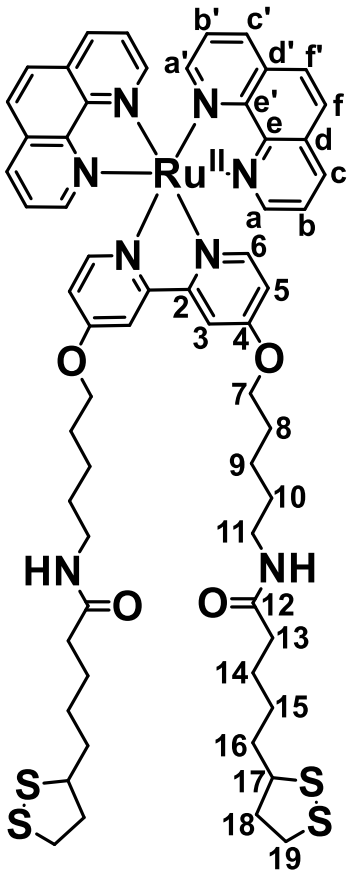

Figure 8.66: Structure of RuphenS12.

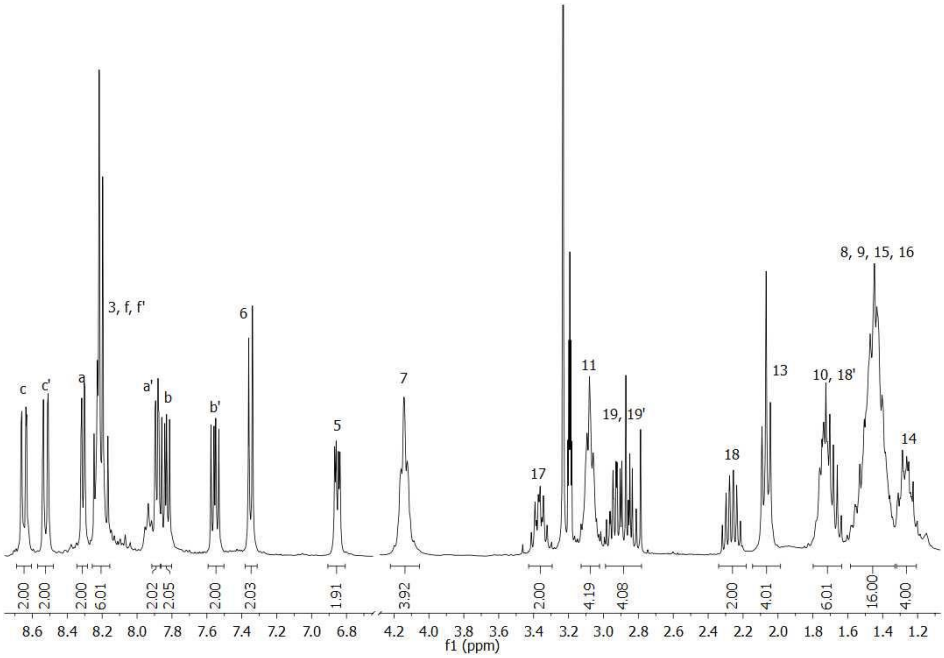

Figure 8.67: ^{1}H NMR RuphenS12. (d_4-MeOD).

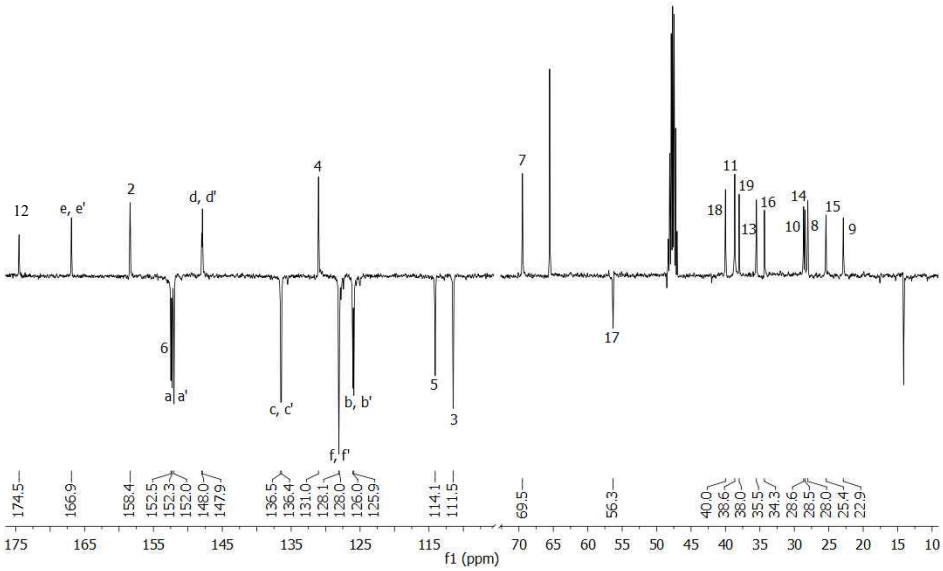

Figure 8.68: ^{13}C NMR RuphenS12. (d_4-MeOD).

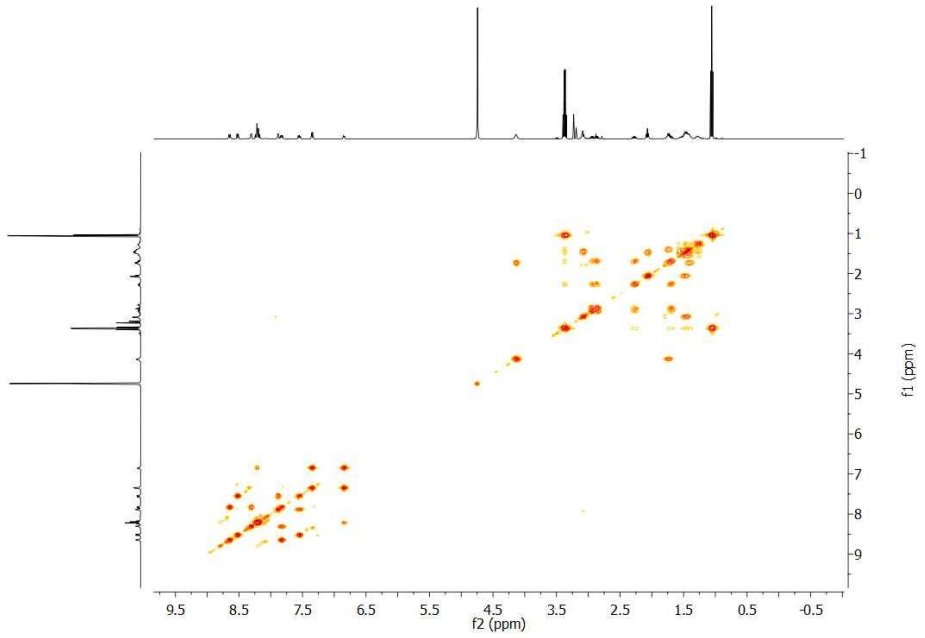

Figure 8.69: RuphenS12 COSY NMR. (d_4-MeOD).

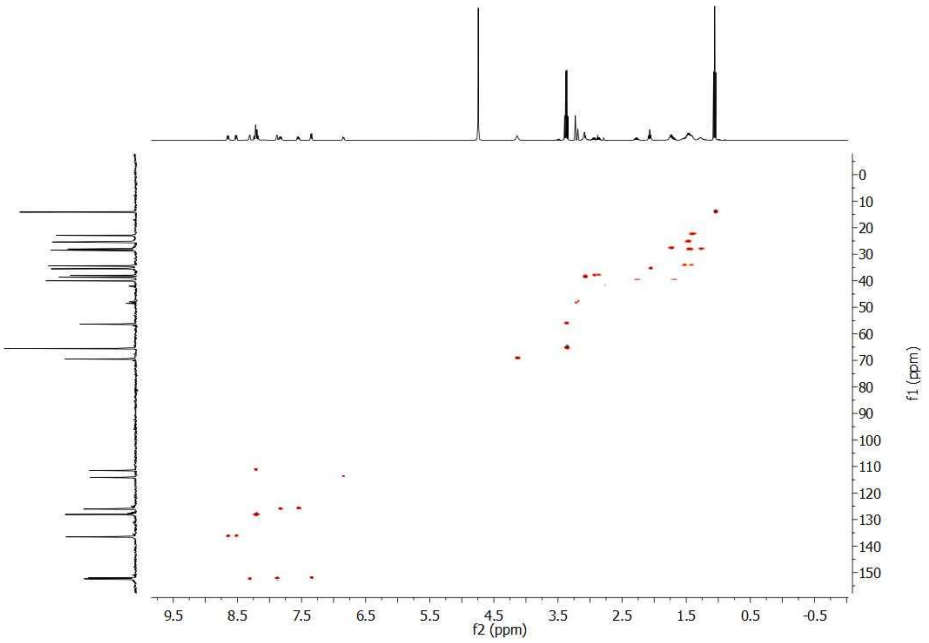

Figure 8.70: RuphenS12 HSQC NMR. (d_4-MeOD).

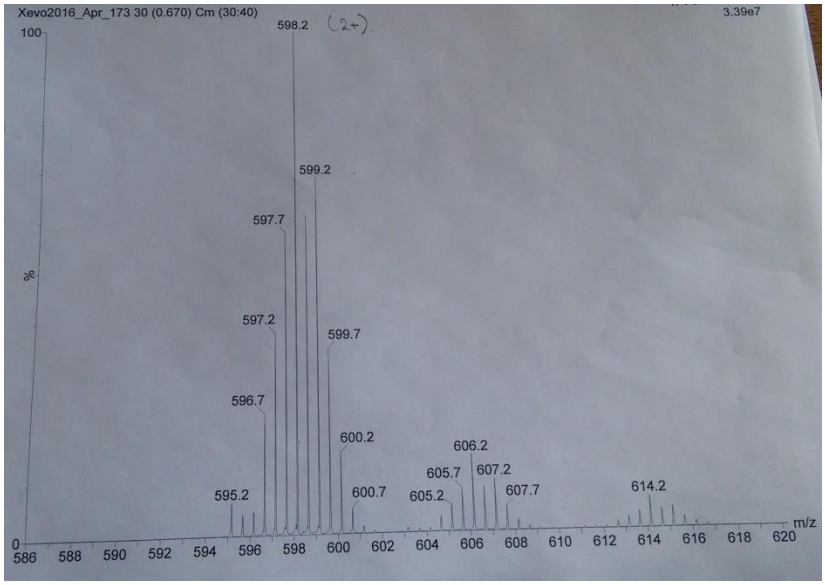

Figure 8.71: RuphenS12 MS.

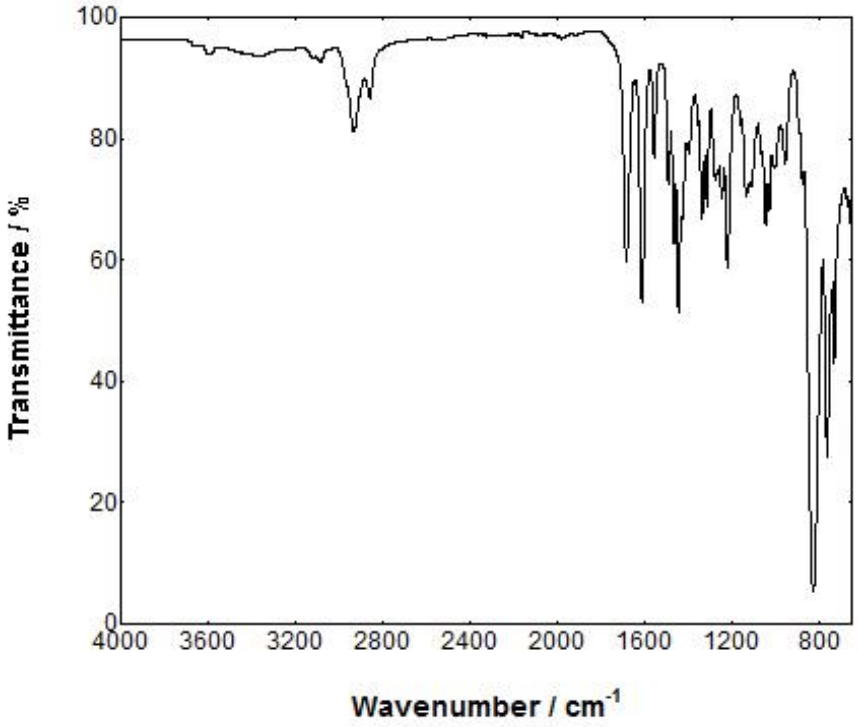

Figure 8.72: RuphenS12 FTIR.

8.3.1.2 RuSconj

4,4'-Diacetylene-2,2'-bipyridine

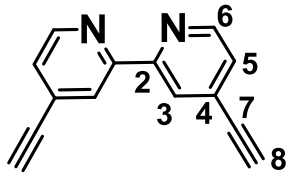

Figure 8.73: Structure of 4,4'-diacetylene-2,2'-bipyridine.

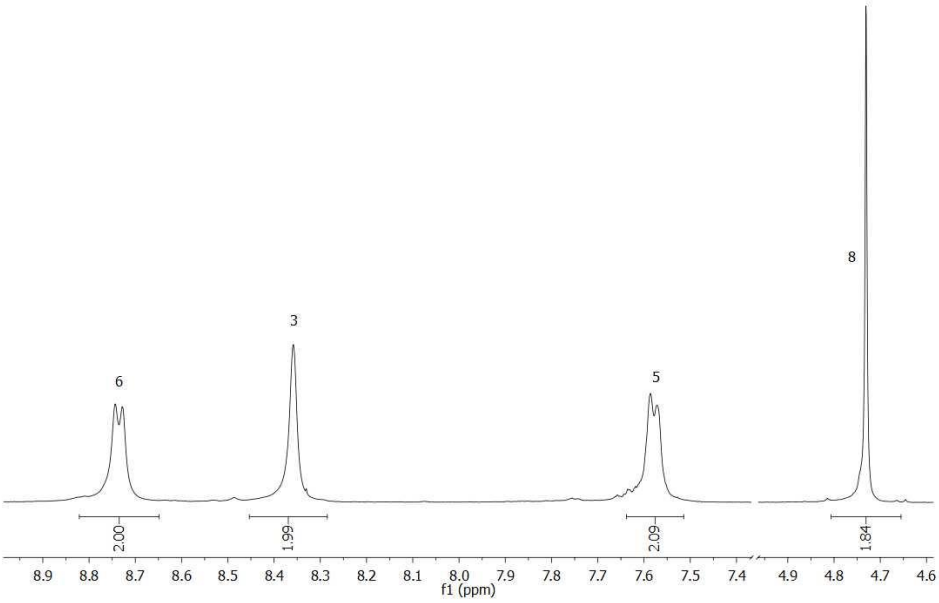

Figure 8.74: ^{1}H NMR 4,4'-diacetylene-2,2'-bipyridine. (d_6-DMSO).

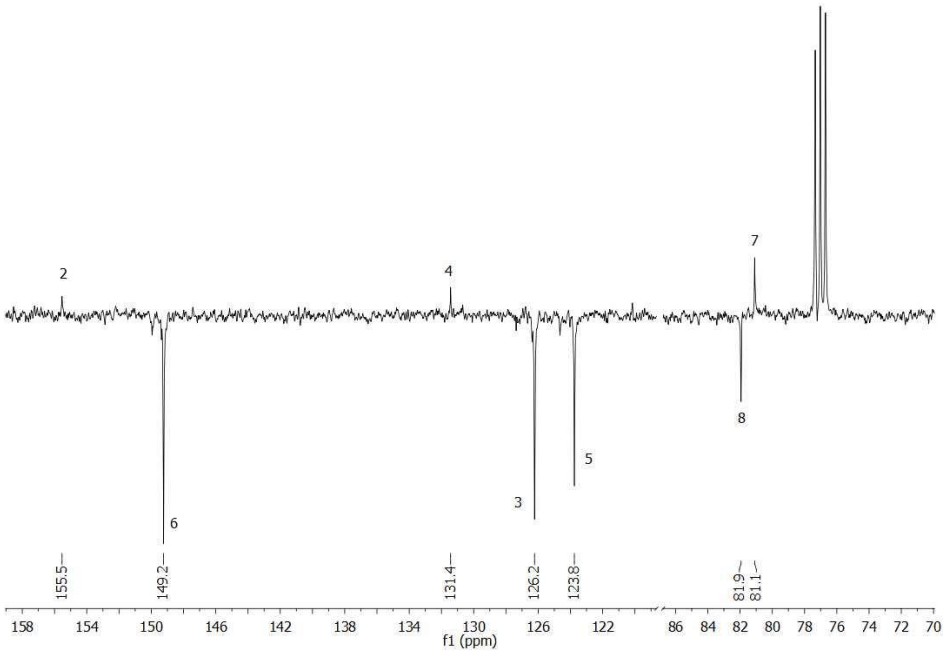

Figure 8.75: ^{13}C NMR 4,4'-diacetylene-2,2'-bipyridine. (d_6-DMSO).

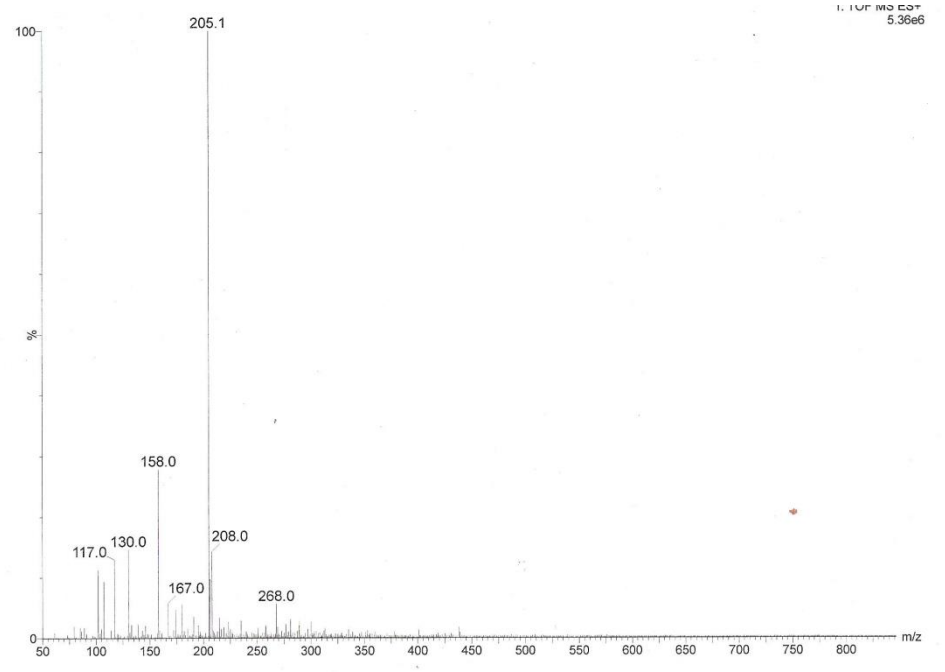

Figure 8.76: 4,4'-diacetylene-2,2'-bipyridine MS.

4-Iodo-1-thioacetate benzene

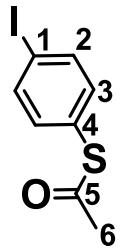

Figure 8.77: Structure of 4-iodo-1-thioacetate benzene.

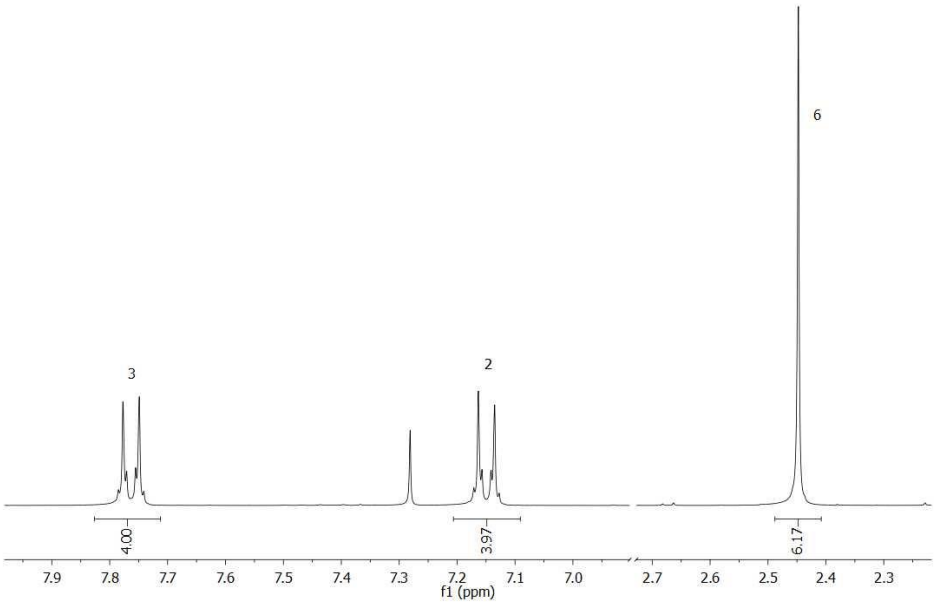

Figure 8.78: ^{1}H NMR 4-iodo-1-thioacetate benzene. ($CDCl_3$).

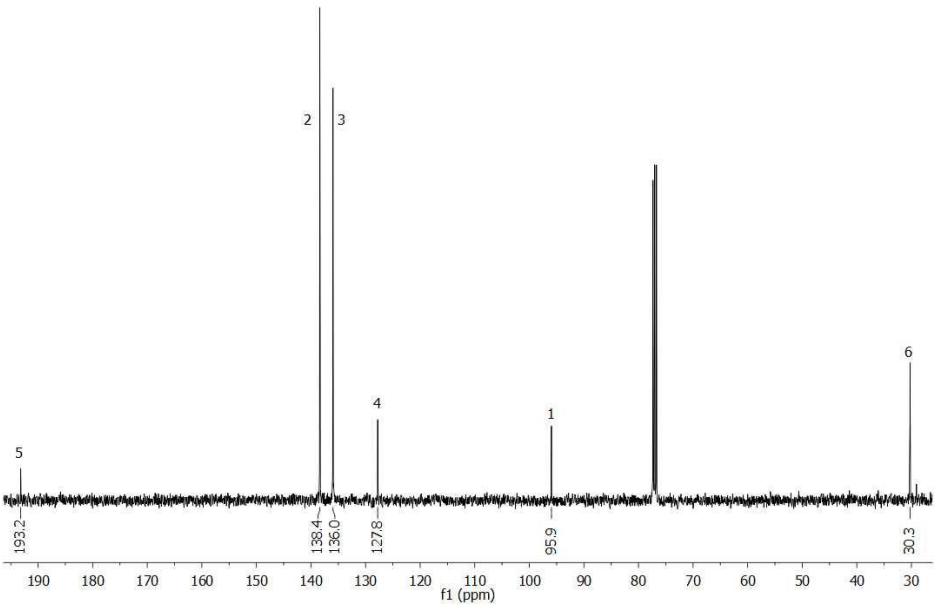

Figure 8.79: ^{13}C NMR 4-iodo-1-thioacetate benzene. ($CDCl_3$).

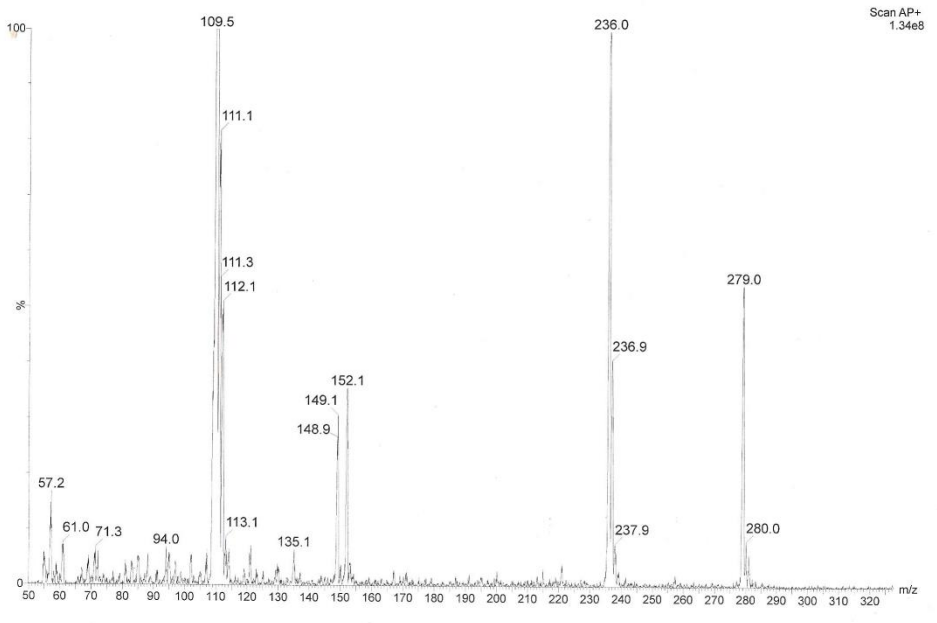

Figure 8.80: 4-Iodo-1-thioacetate benzene MS.

4,4’-Di(4-acetylene-1-thioacetatephenyl)-2,2’-bipyridine

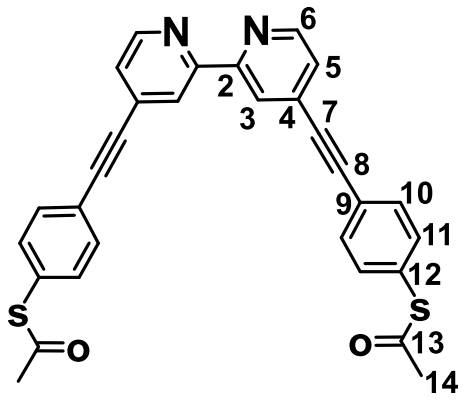

Figure 8.81: Structure of 4,4’-di(4-acetylene-1-thioacetatephenyl)-2,2’-bipyridine.

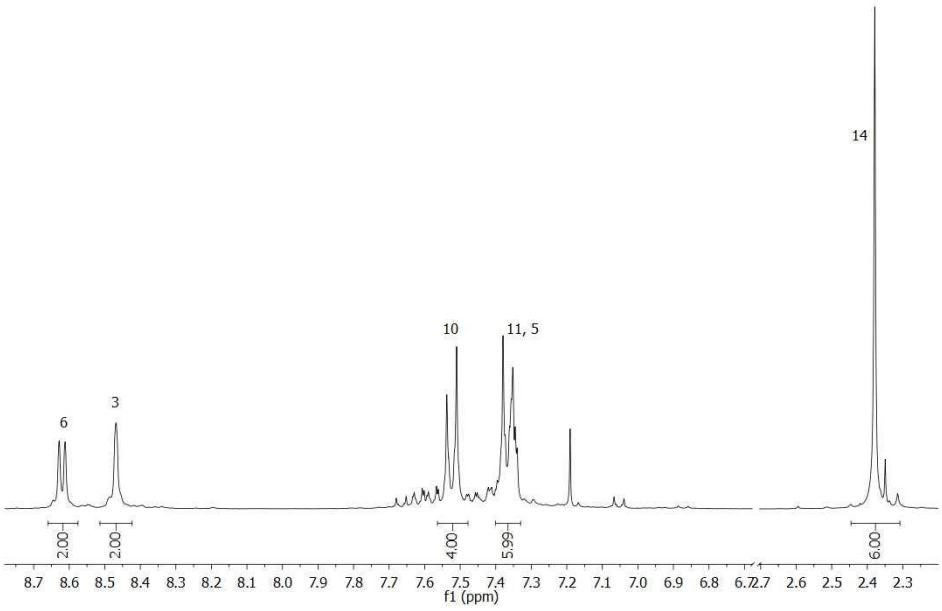

Figure 8.82: ^{1}H NMR 4,4’-di(4-acetylene-1-thioacetatephenyl)-2,2’-bipyridine. ($CDCl_3$).

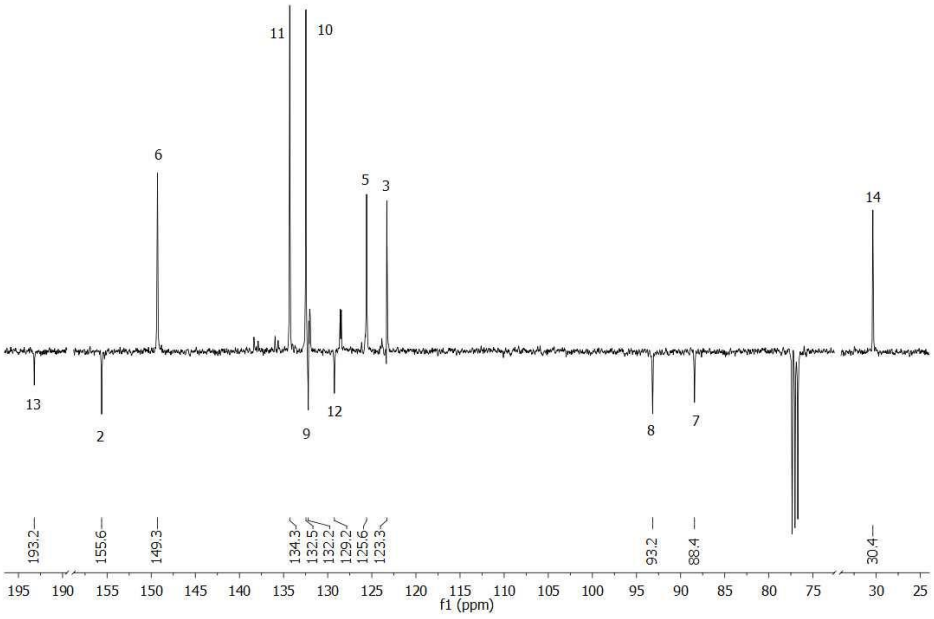

Figure 8.83: ^{13}C NMR 4,4'-di(4-acetylene-1-thioacetatephenyl)-2,2'-bipyridine. ($CDCl_3$).

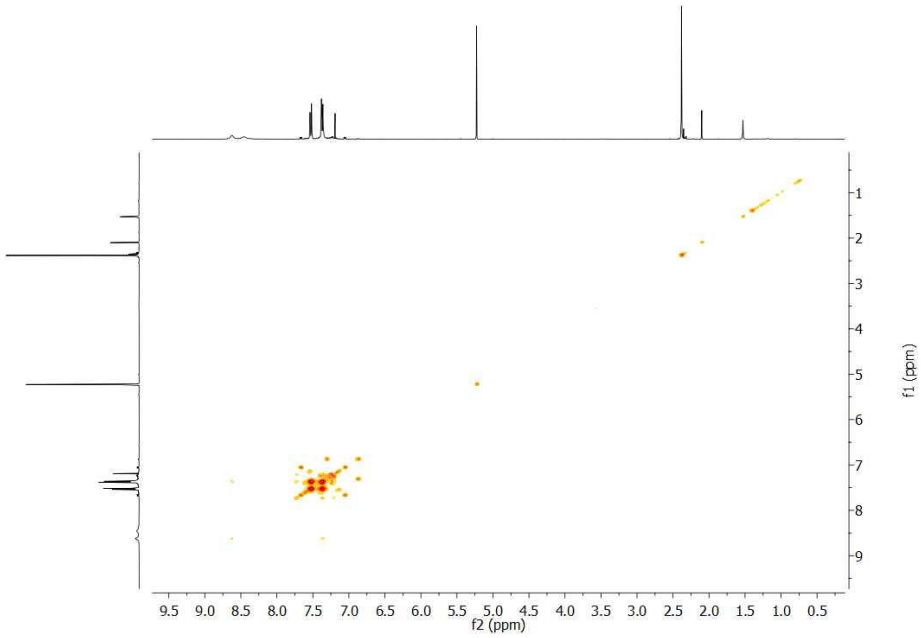

Figure 8.84: 4,4'-Di(4-acetylene-1-thioacetatephenyl)-2,2'-bipyridine COSY NMR. ($CDCl_3$).

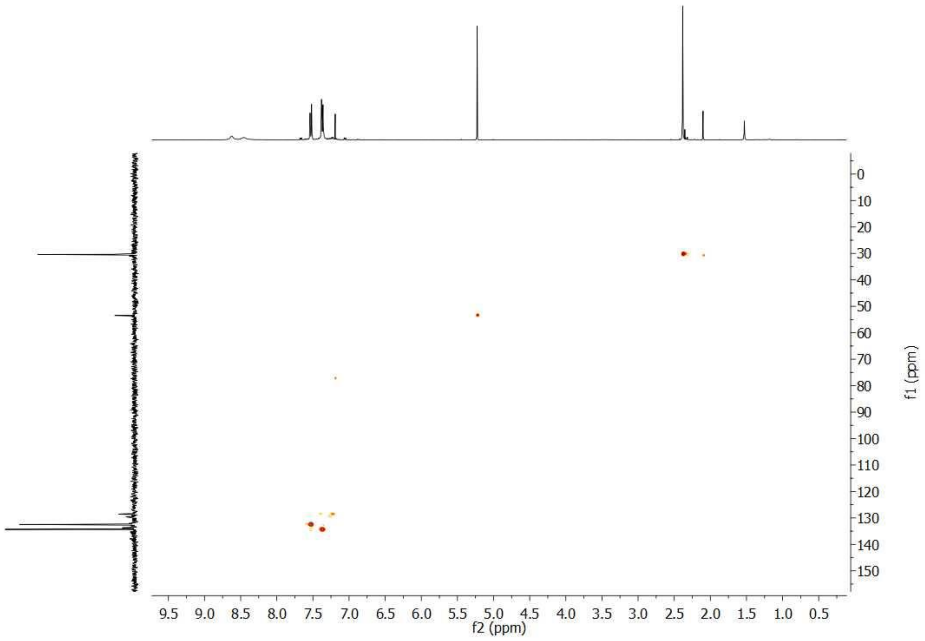

Figure 8.85: 4,4'-Di(4-acetylene-1-thioacetatephenyl)-2,2'-bipyridine HSQC NMR. ($CDCl_3$).

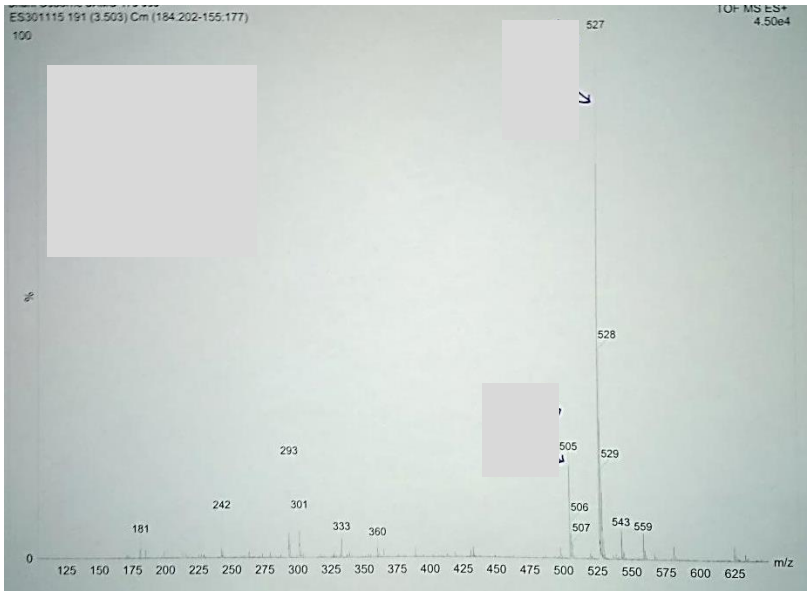

Figure 8.86: 4,4'-Di(4-acetylene-1-thioacetatephenyl)-2,2'-bipyridine MS.

RuSconj

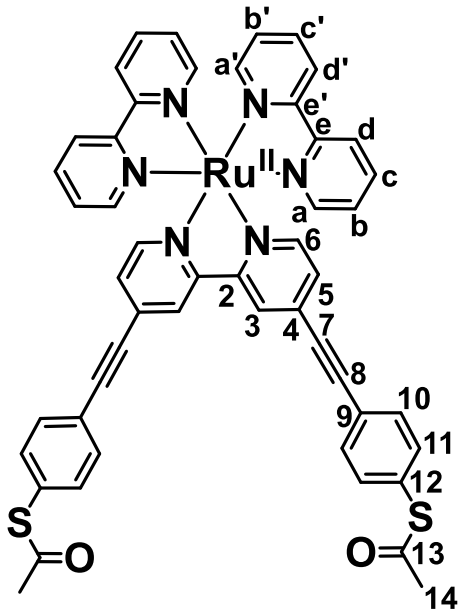

Figure 8.87: Structure of RuSconj.

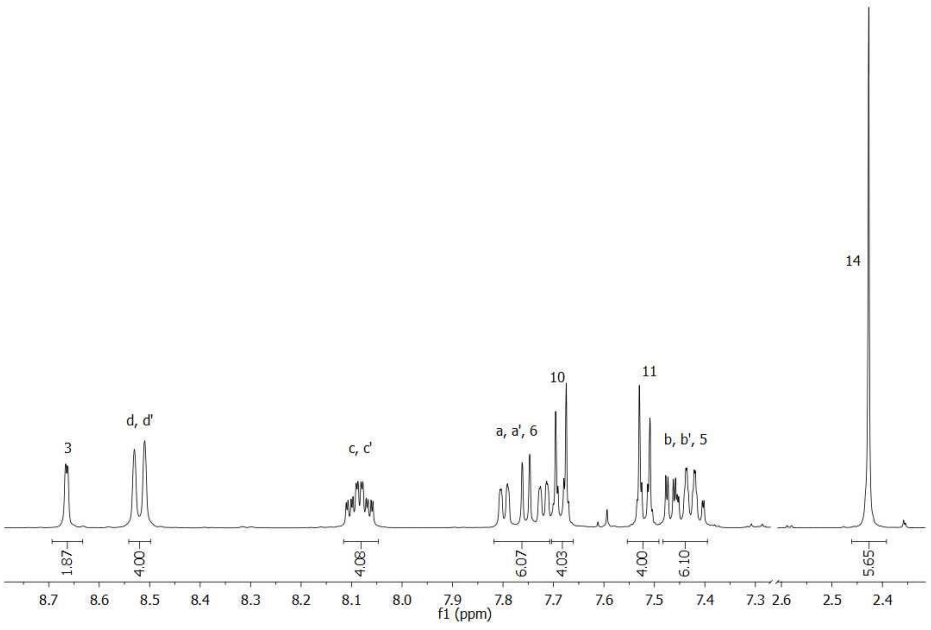

Figure 8.88: ^{1}H NMR RuSconj. (CD_3CN).

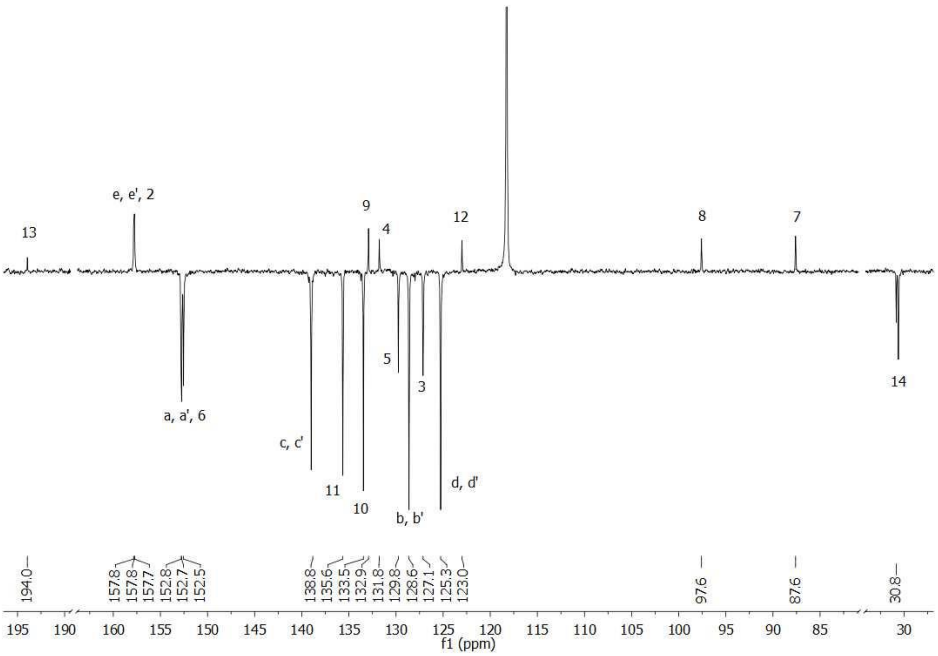

Figure 8.89: ^{13}C NMR RuSconj. (CD_3CN).

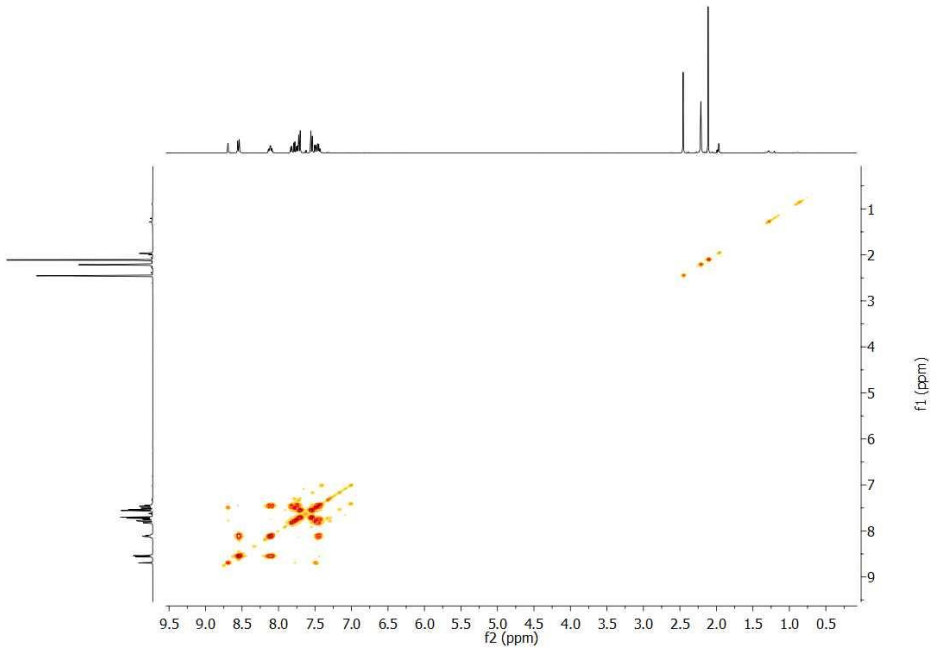

Figure 8.90: RuSconj COSY NMR. (CD_3CN).

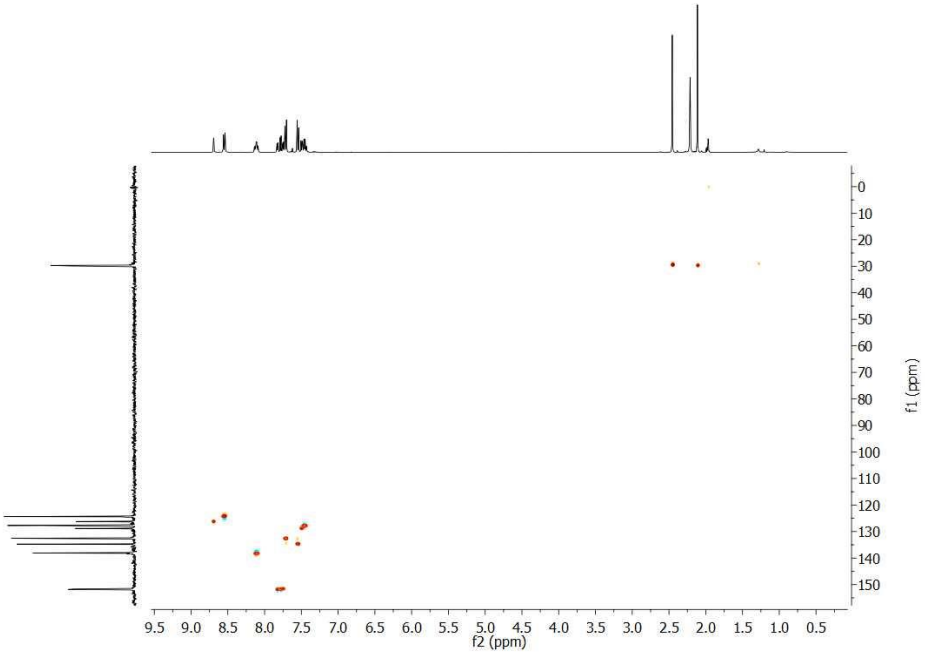

Figure 8.91: RuSconj HSQC NMR. (CD_3CN).

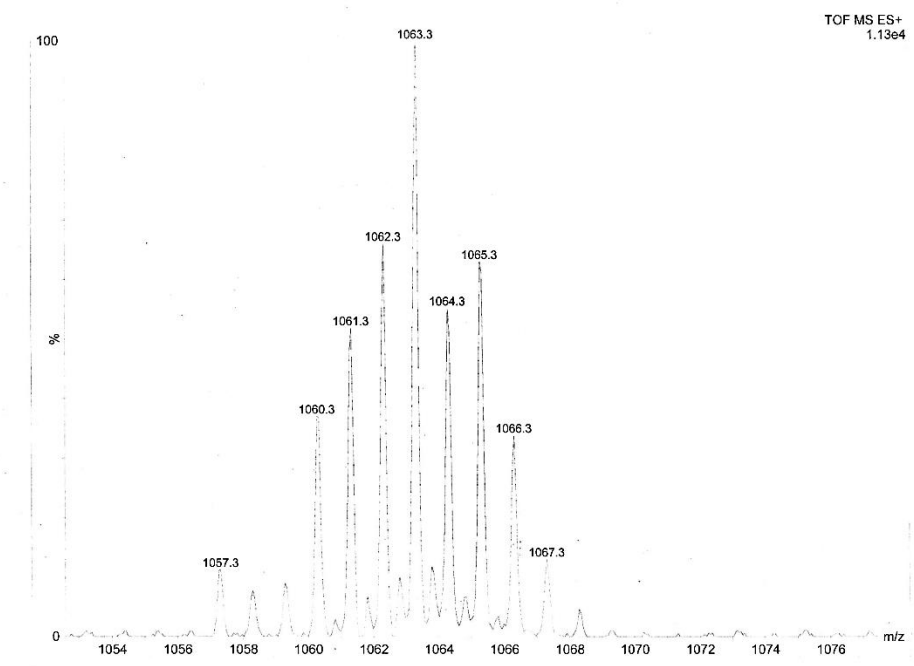

Figure 8.92: RuSconj MS.

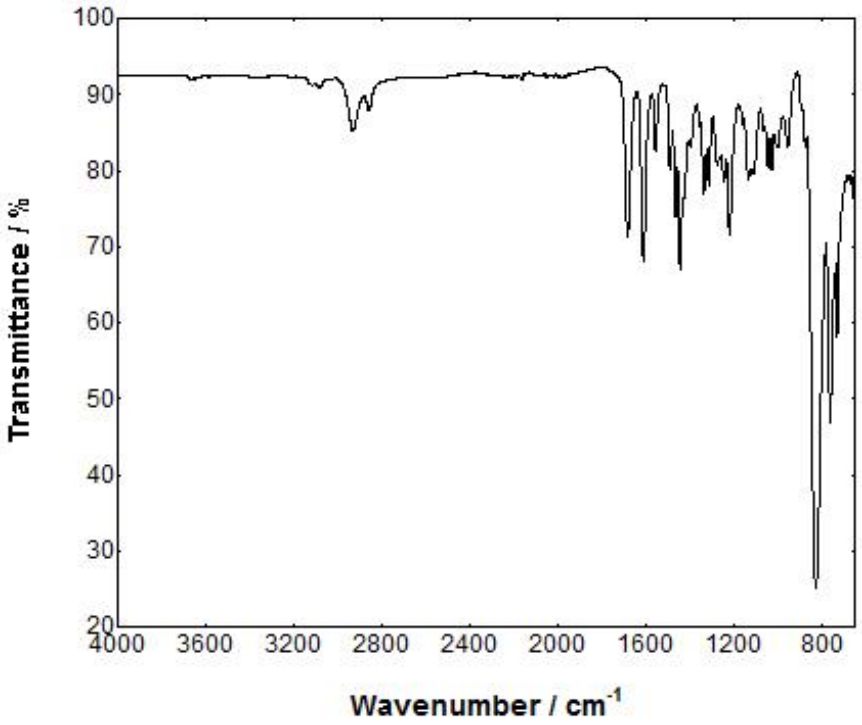

Figure 8.93: RuSconj FTIR.

8.3.1.3 RuS8

4,4’-Dimethylester-2,2’-bipyridine

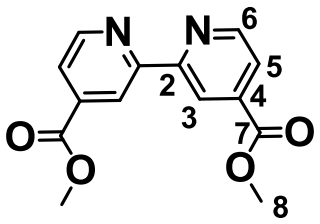

Figure 8.94: Structure of 4,4’-dimethylester-2,2’-bipyridine.

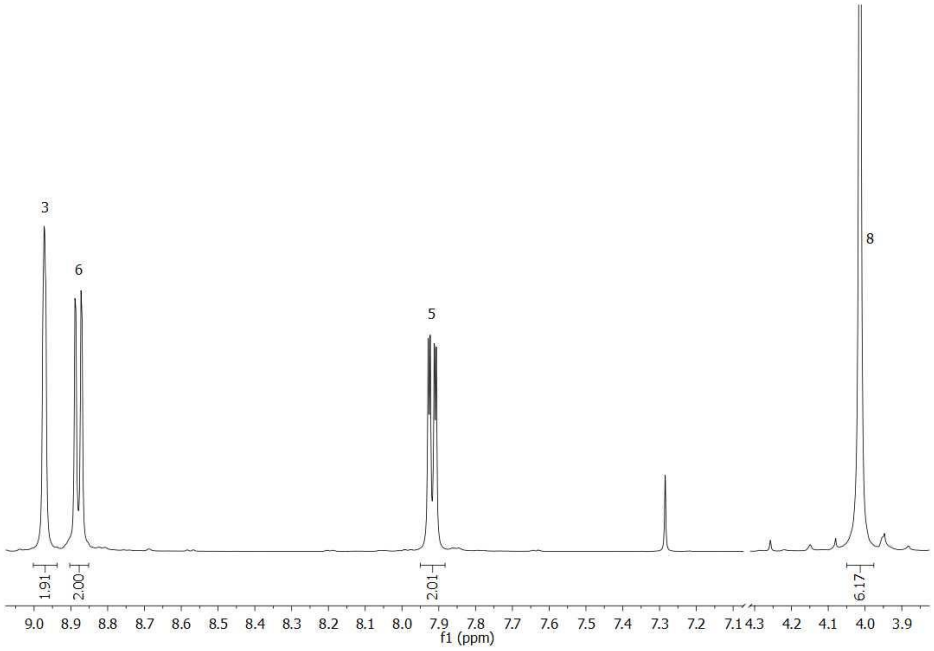

Figure 8.95: ^{1}H NMR 4,4’-dimethylester-2,2’-bipyridine. ($CDCl_3$).

4,4’-Dimethylalcohol-2,2’-bipyridine

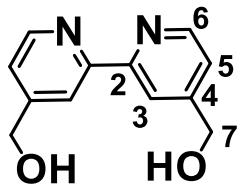

Figure 8.96: Structure of 4,4’-dimethylalcohol-2,2’-bipyridine.

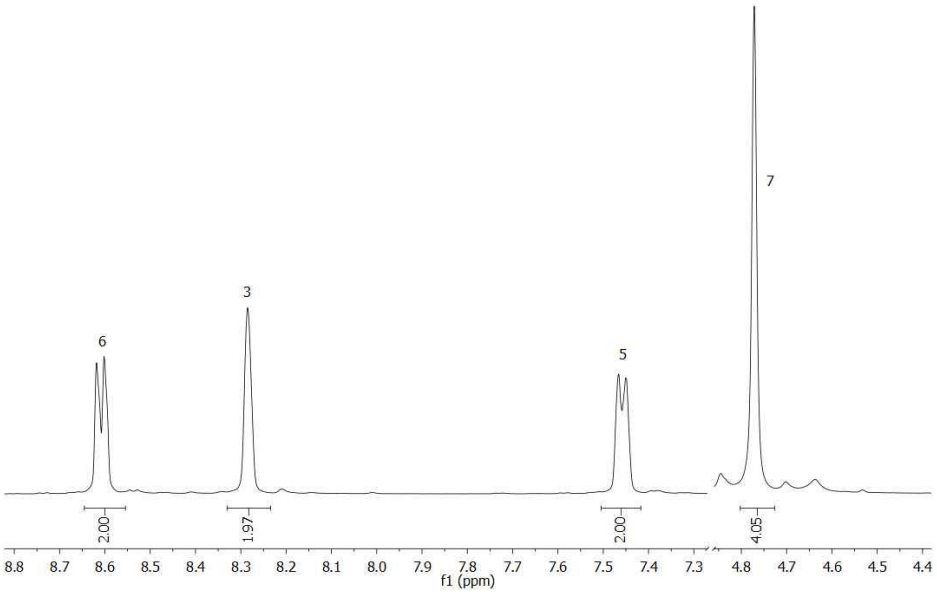

Figure 8.97: ^{1}H NMR 4,4’-dimethylalcohol-2,2’-bipyridine. ($CDCl_3$).

4,4’-Dimethylbromine-2,2’-bipyridine

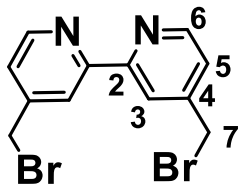

Figure 8.98: Structure of 4,4’-dimethylbromine-2,2’-bipyridine.

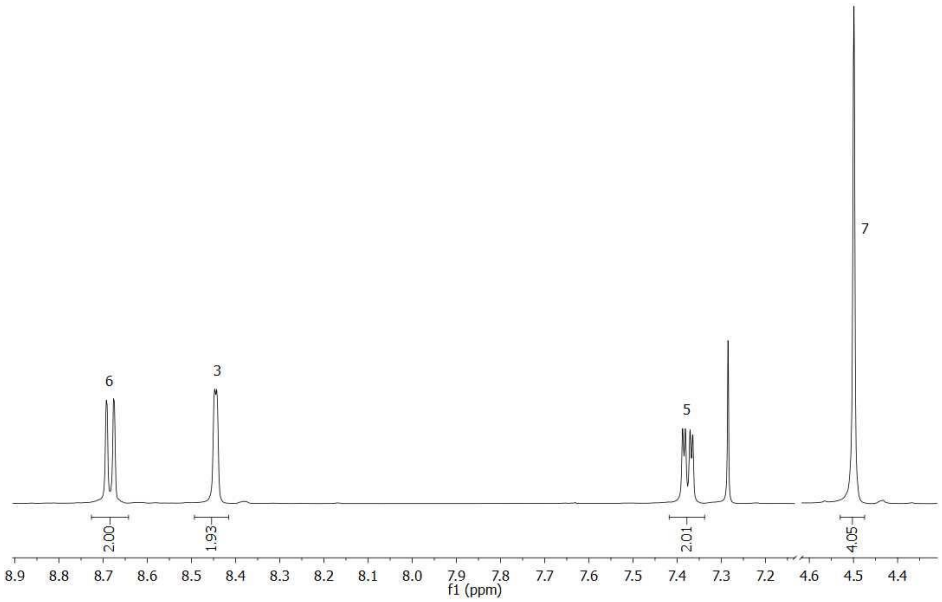

Figure 8.99: ^{1}H NMR 4,4’-dimethylbromine-2,2’-bipyridine. ($CDCl_3$).

4,4’-Dimethylazide-2,2’-bipyridine

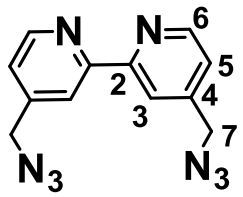

Figure 8.100: Structure of 4,4’-dimethylazide-2,2’-bipyridine.

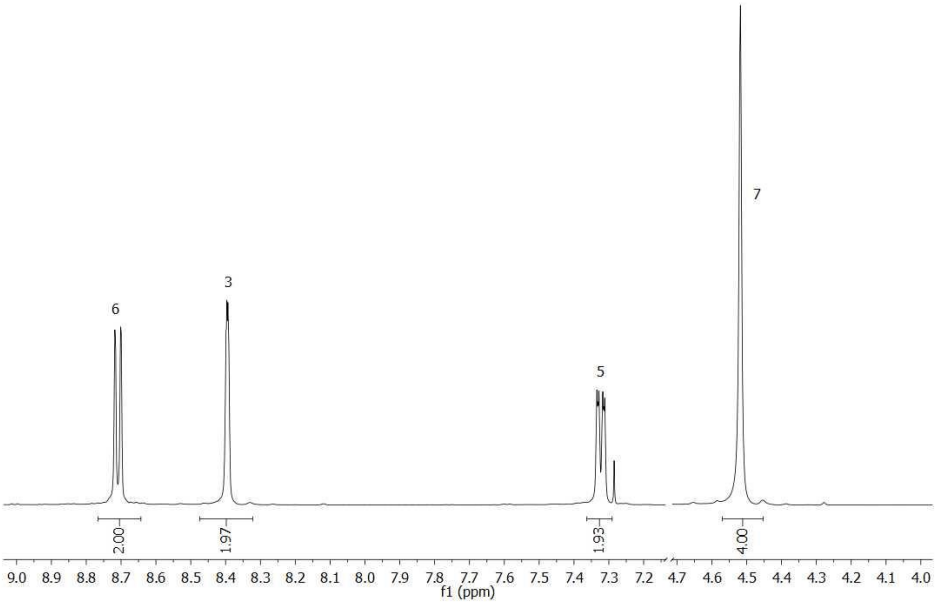

Figure 8.101: ^{1}H NMR 4,4’-dimethylazide-2,2’-bipyridine. ($CDCl_3$).

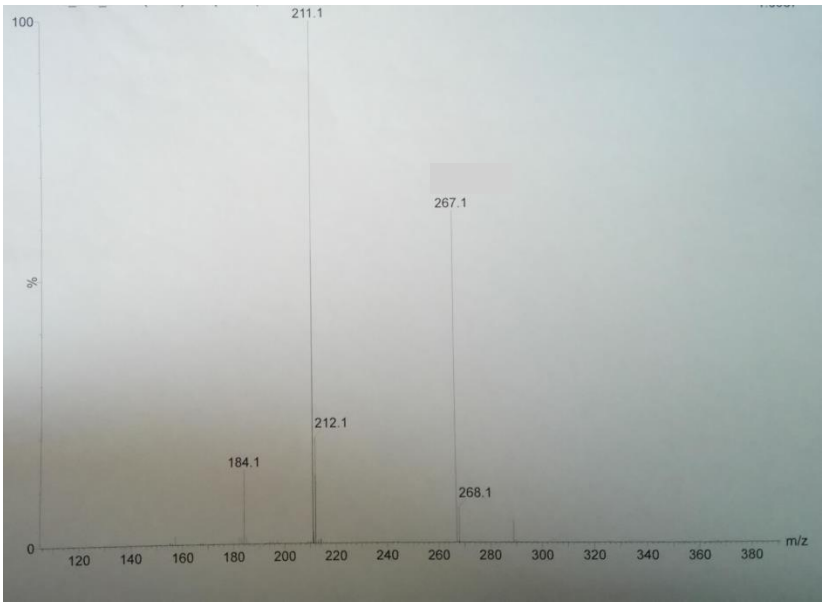

Figure 8.102: 4,4’-Dimethylazide-2,2’-bipyridine MS.

4,4’-Dimethylamine-2,2’-bipyridine

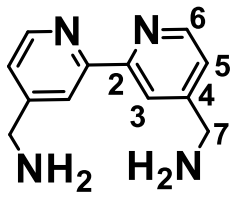

Figure 8.103: Structure of 4,4’-dimethylamine-2,2’-bipyridine.

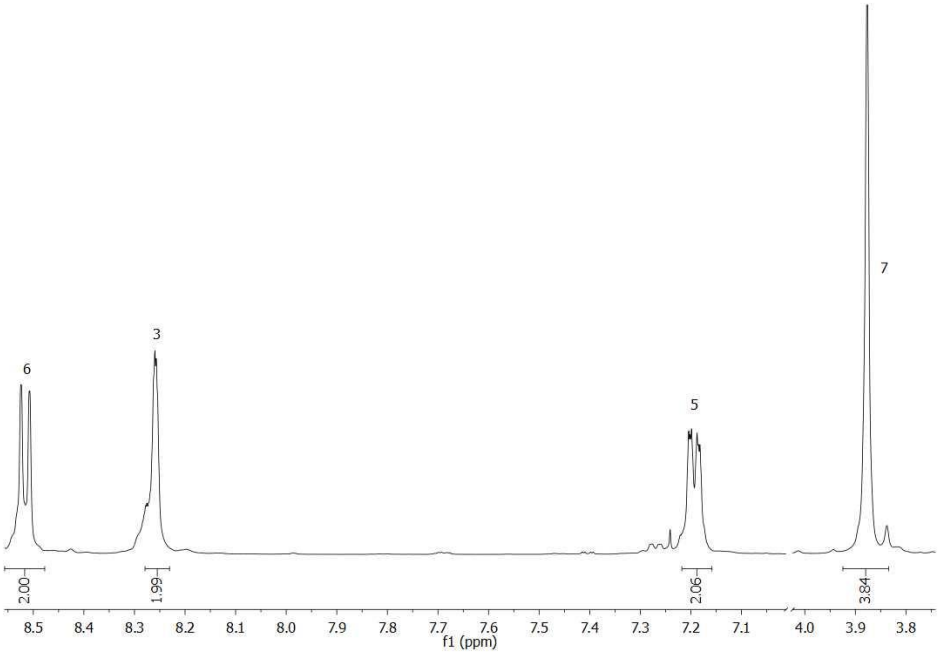

Figure 8.104: ^{1}H NMR 4,4’-dimethylamine-2,2’-bipyridine. ($CDCl_3$).

4,4-Dimethyllipoamide 2,2-bipyridine

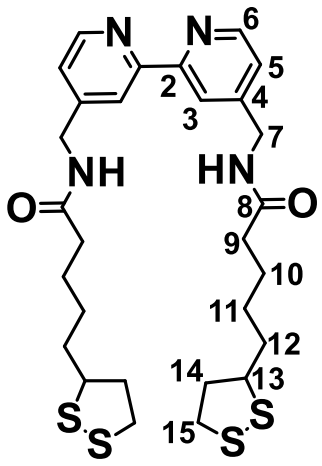

Figure 8.105: Structure of 4,4'-dimethyllipoamide-2,2'-bipyridine.

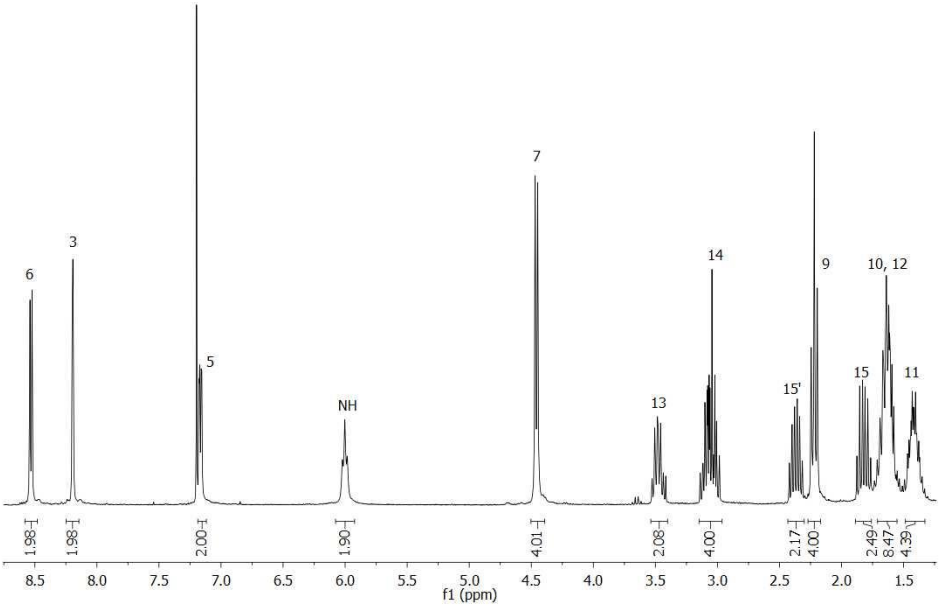

Figure 8.106: ^{1}H NMR 4,4'-dimethyllipoamide-2,2'-bipyridine. ($CDCl_3$).

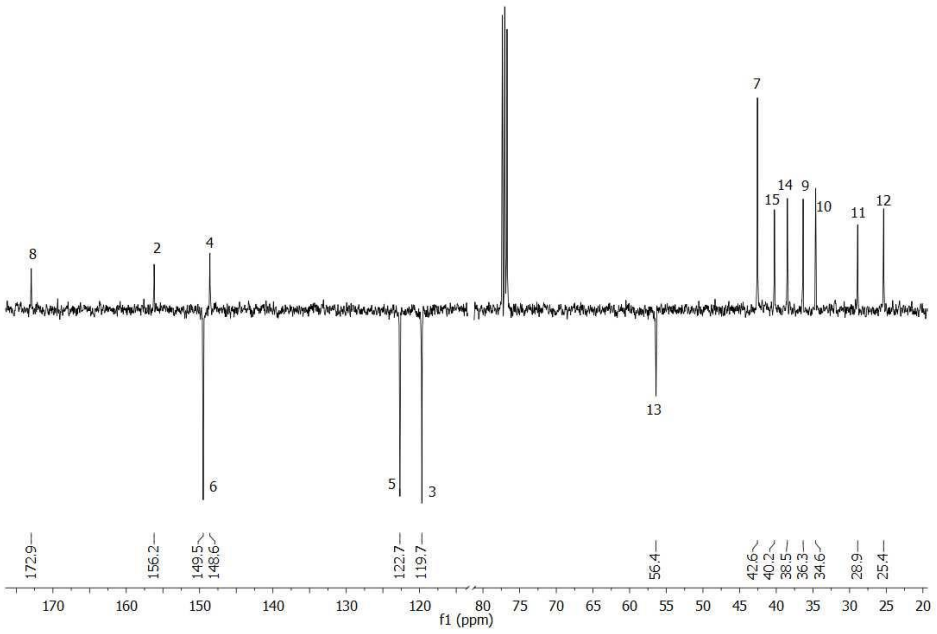

Figure 8.107: ^{13}C NMR 4,4'-dimethyllipoamide-2,2'-bipyridine. ($CDCl_3$).

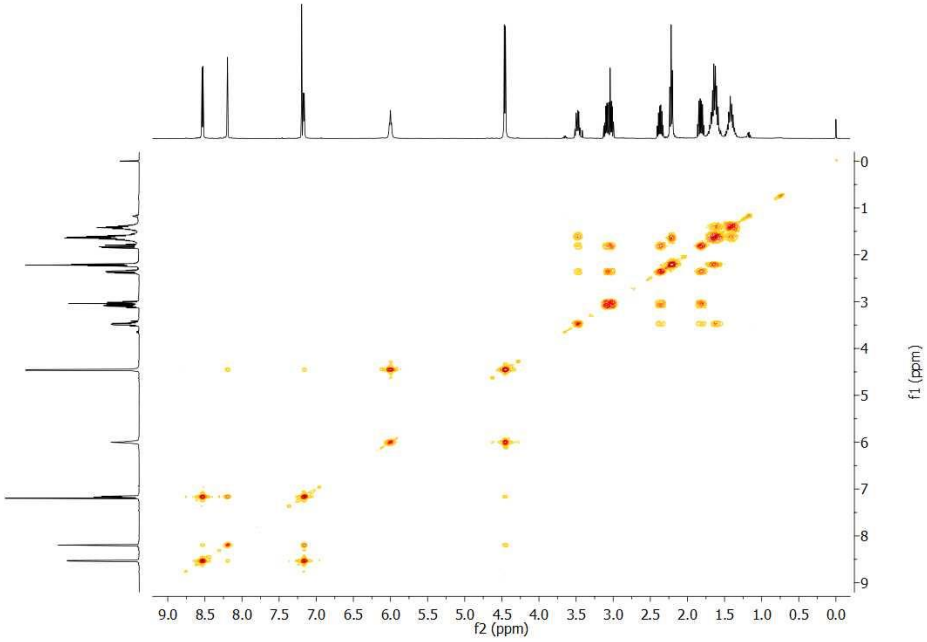

Figure 8.108: 4,4'-Dimethyllipoamide-2,2'-bipyridine COSY NMR. ($CDCl_3$).

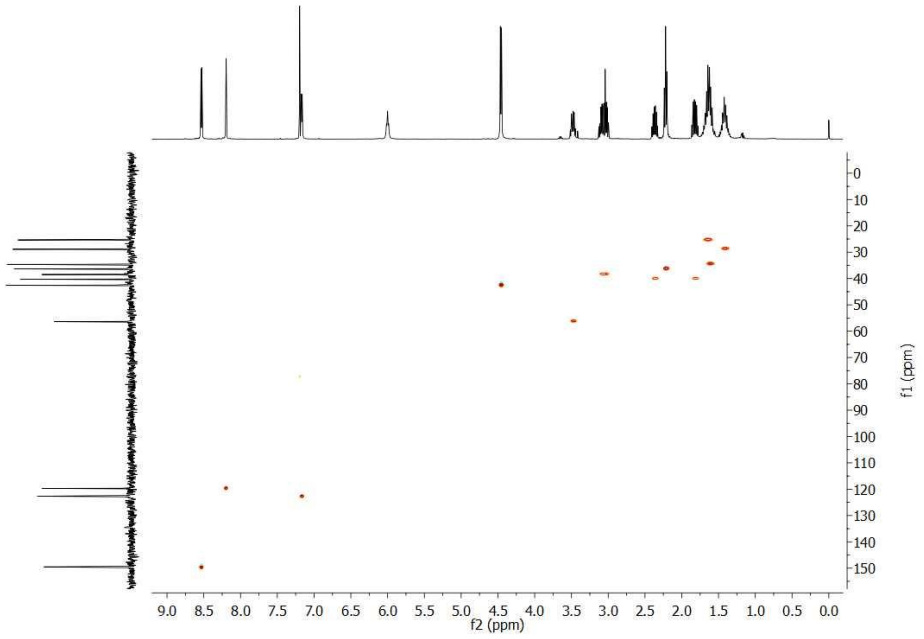

Figure 8.109: 4,4'-Dimethyllipoamide-2,2'-bipyridine HSQC NMR. ($CDCl_3$).

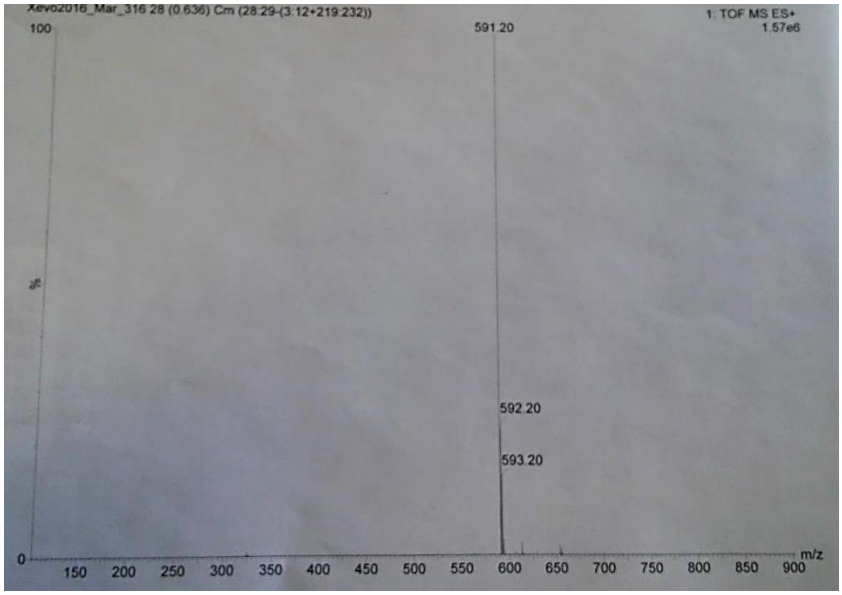

Figure 8.110: 4,4'-Dimethyllipoamide-2,2'-bipyridine MS.

RuS8

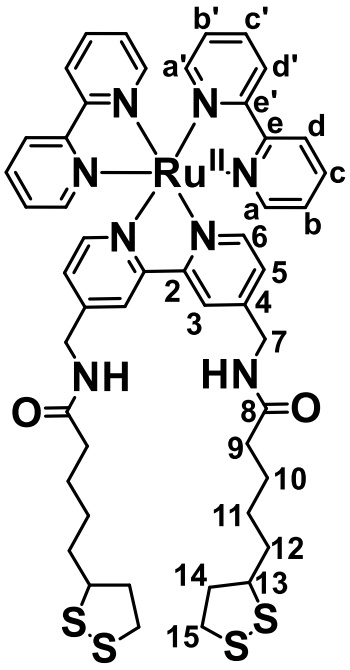

Figure 8.111: Structure of RuS8.

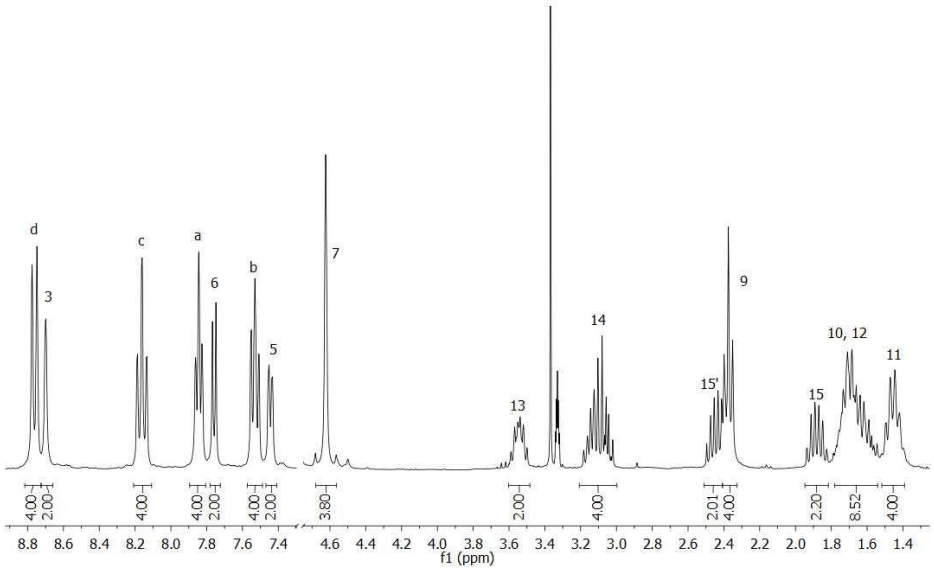

Figure 8.112: ^{1}H NMR RuS8. (d_4-MeOD).

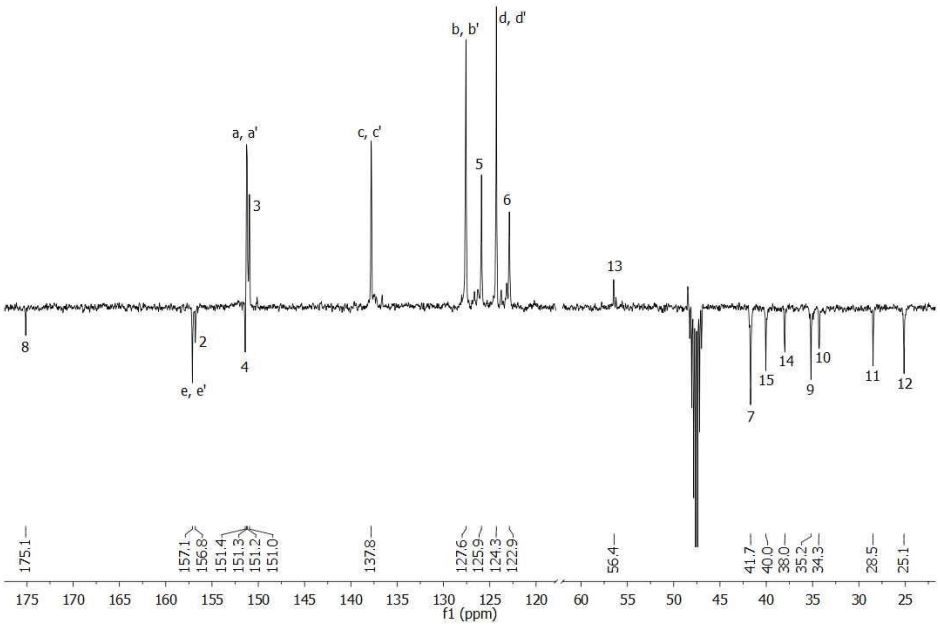

Figure 8.113: ^{13}C NMR RuS8. (d_4-MeOD).

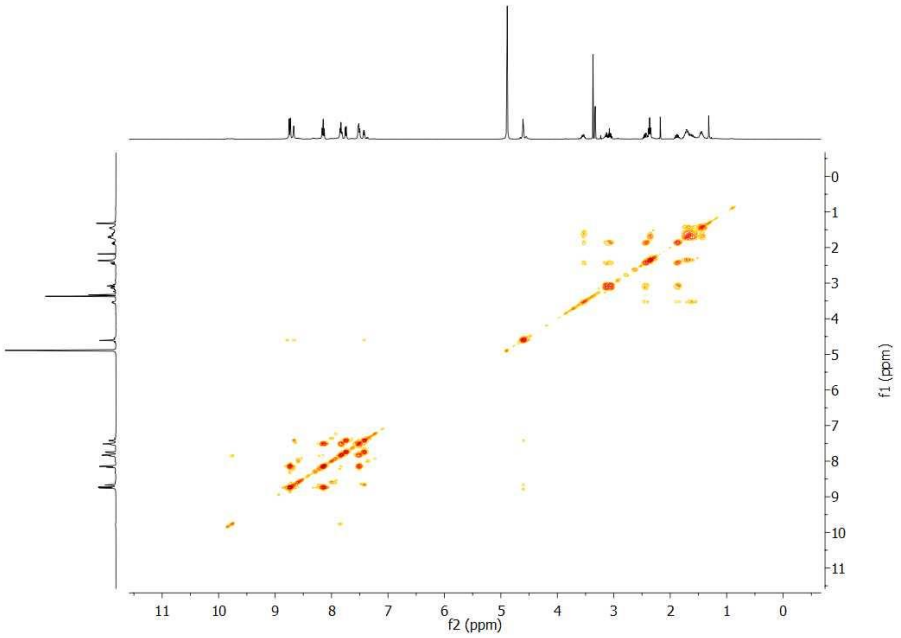

Figure 8.114: RuS8 COSY NMR. (d_4-MeOD).

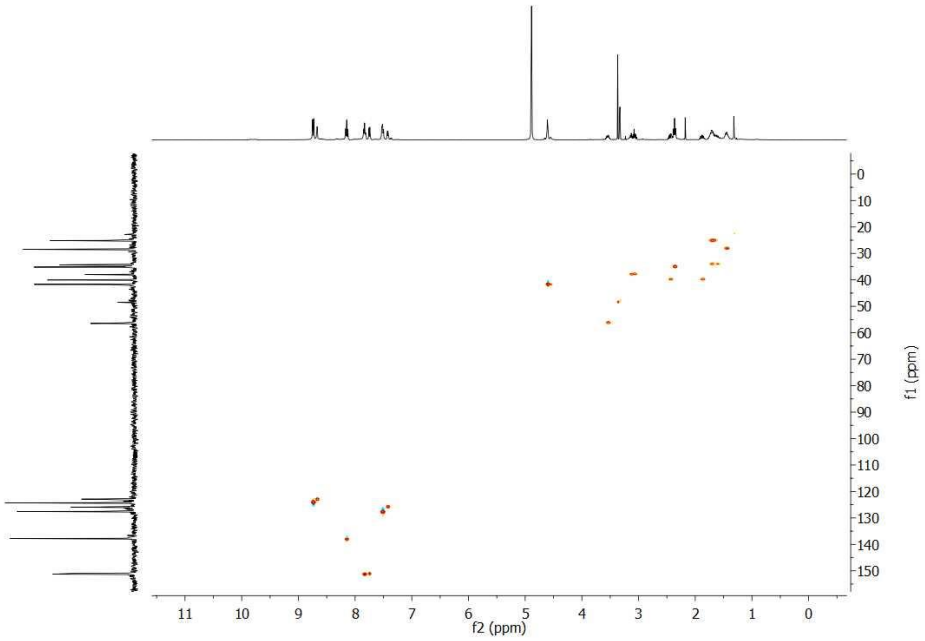

Figure 8.115: RuS8 HSQC NMR. (d_4-MeOD).

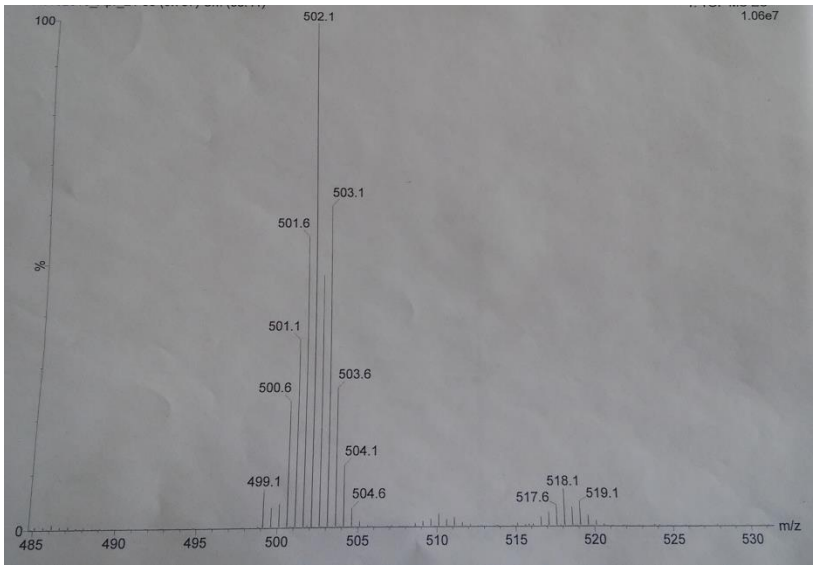

Figure 8.116: RuS8 MS.

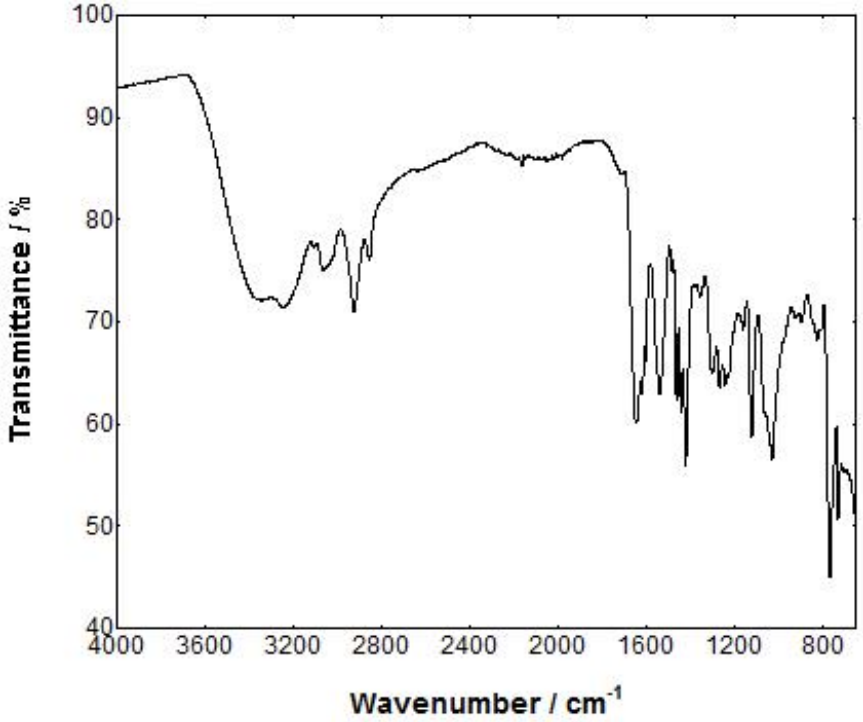

Figure 8.117: RuS8 FTIR.

8.3.1.4 RuphenS8

RuphenS8

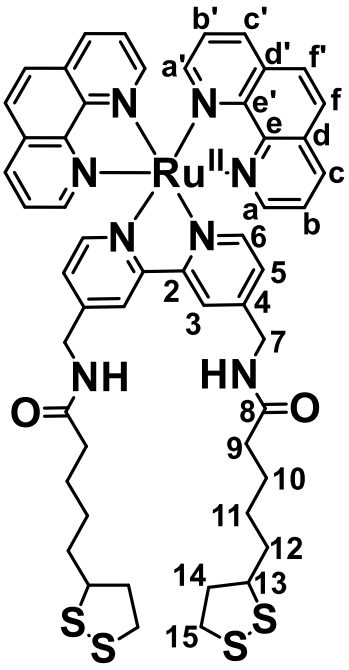

Figure 8.118: Structure of RuphenS8.

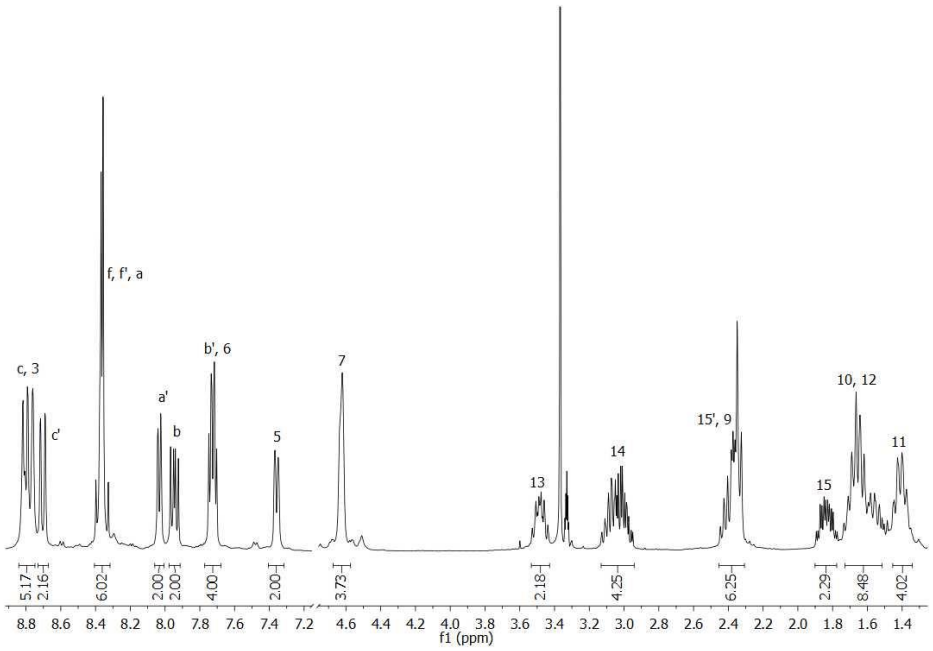

Figure 8.119: ^{1}H NMR RuphenS8. (d_4-MeOD).

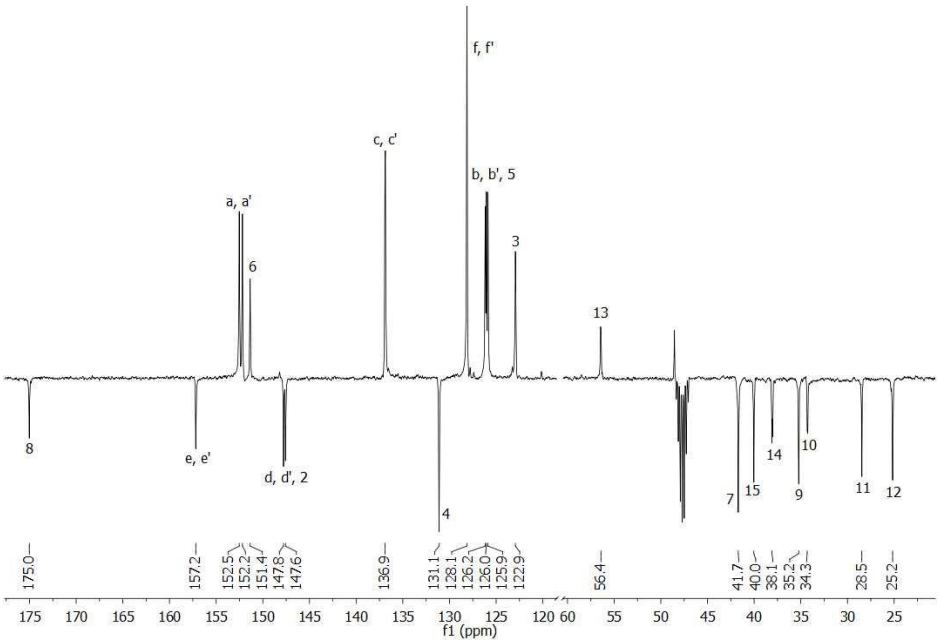

Figure 8.120: ^{13}C NMR RuphenS8. (d_4-MeOD).

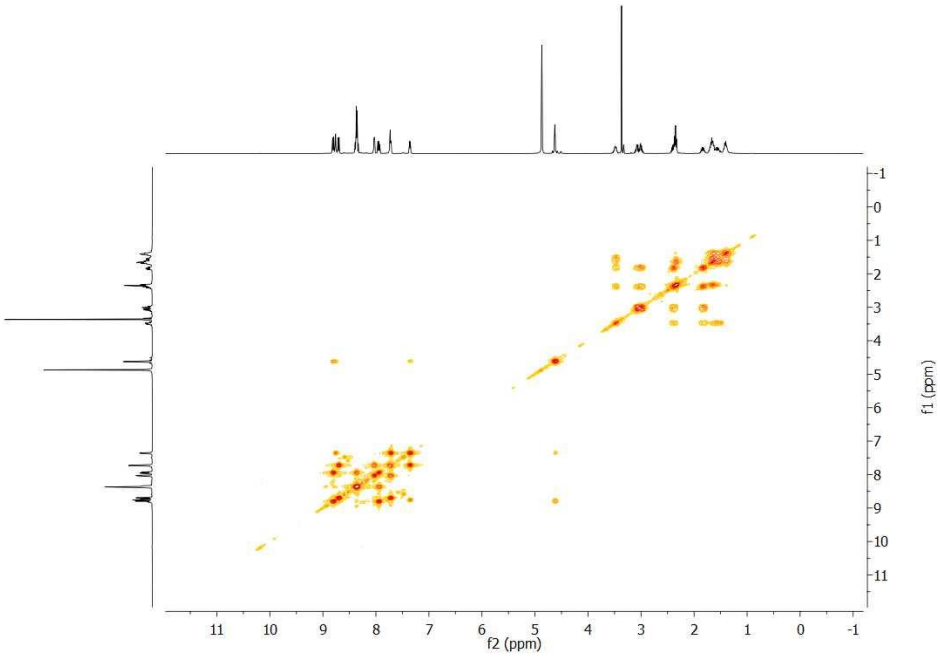

Figure 8.121: RuphenS8 COSY NMR. (d_4-MeOD).

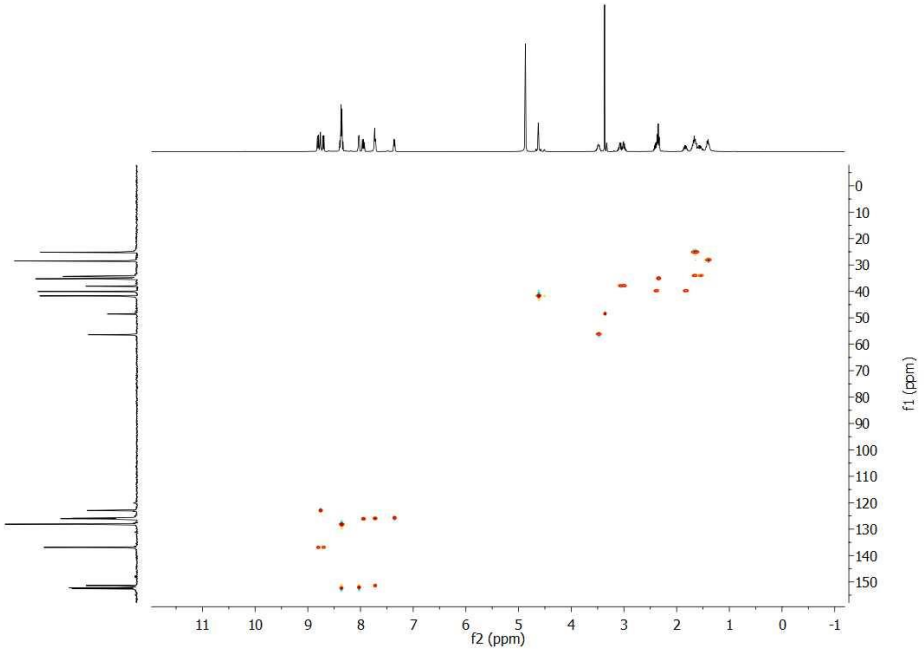

Figure 8.122: RuphenS8 HSQC NMR. (d_4-MeOD).

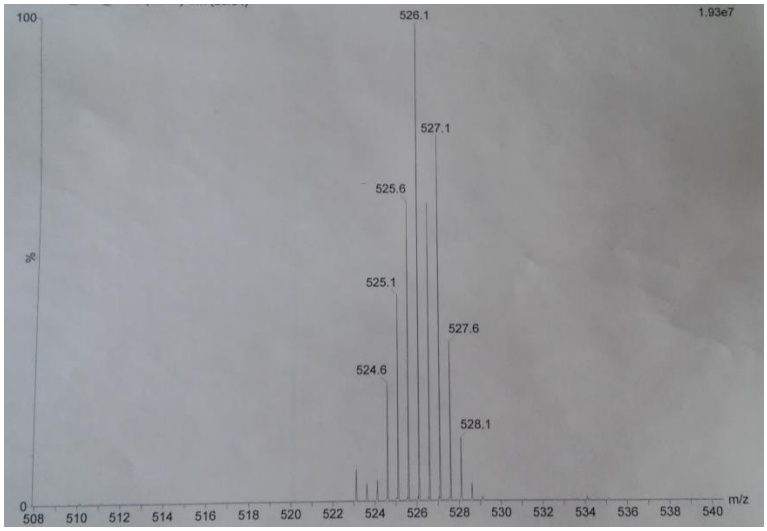

Figure 8.123: RuphenS8 MS.

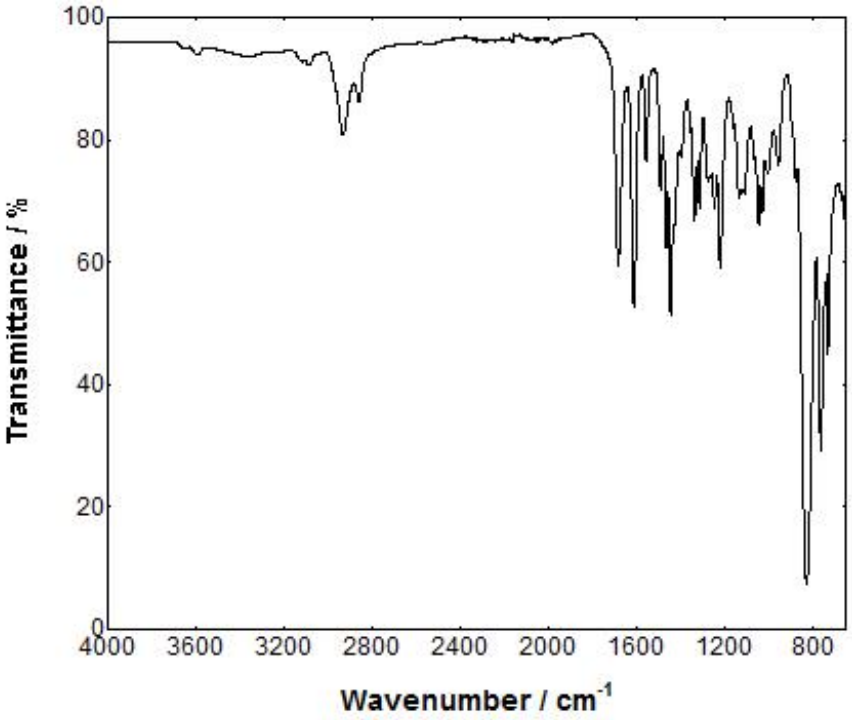

Figure 8.124: RuphenS8 FTIR.

8.3.2 Gold nanoparticle solution concentration calculations

Mass of $HAuCl_4$ (48 % Au by assay) = 0.0085 g

Mass (Au) = 0.48 x 0.0085 = 0.00408 g

Moles (Au) = 0.00408 / 197 = 2.0711 x 10^{-5} moles.

[Au] = 2.0711 x 10^{-5} moles / 0.125 dm^3 = 1.657 x 10^{-4} M.

Number of Au atoms per 13 nm nanoparticle = $(6.5 \times 10^{-9})^3$ / $(140 \times 10^{-12})^3$ = 106,802 (assuming that the particles are spherical and estimated atomic radius of gold = 140 pm).

Concentration of AuNP13 = 1.657 x 10^{-4} M / 100,082 = 1.7 nM

During the first growth step, 30 mL of the AuNP13 seeds are diluted in 80 mL. Assuming no new seeds are formed, the concentration of the AuNP25 formed = 0.8 nM.

In the second growth step 8 mL of the AuNP25 seeds are diluted to 80 mL. Assuming no new seeds are formed, the concentration of the AuNP50 formed = 80 pM.

In the final growth step, 40 mL of the AuNP50 are diluted to 80 mL, rendering AuNP100 at 40 pM.

8.3.3 Ruthenium AuNP13 coverage calculations

Table 8.3: Ruthenium coverage on AuNP13 calculations. Au atoms per AuNP13 = 100082.

	Ru:Au	Complexes per AuNP13
RuS1•AuNP13	1:180	550
RuS6•AuNP13	1:180	550
RuS12•AuNP13	1:150	680
RuphenS12•AuNP13	1:150	680
RuSconj•AuNP13	1:250	400
RuS8•AuNP13	1:180	550
RuphenS8•AuNP13	1:150	680

8.3.4 XPS of ruthenium coated AuNP

8.3.4.1 RuphenS12•AuNP13

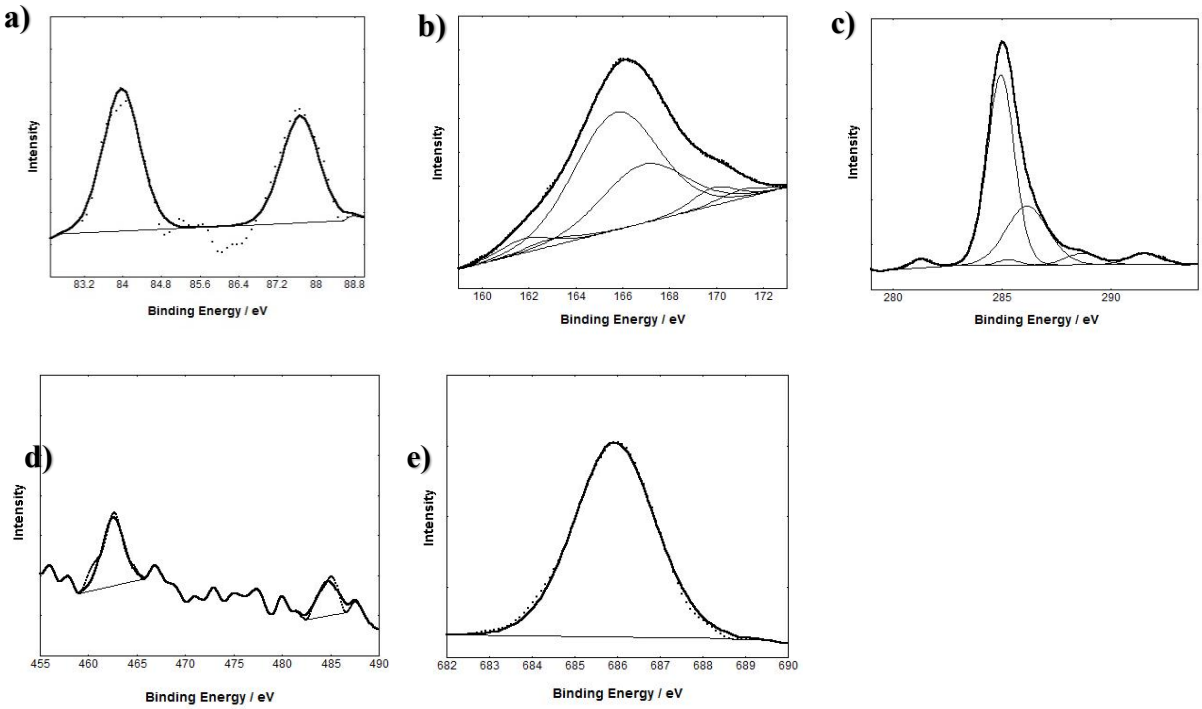

Figure 8.125: XPS binding energy showing the regions of Au 4f (a), S 2p (b), Ru 3d (c), Ru 3p (d) and F 1s (e) for RuphenS12•AuNP13.

8.3.4.2 RuSconj•AuNP13

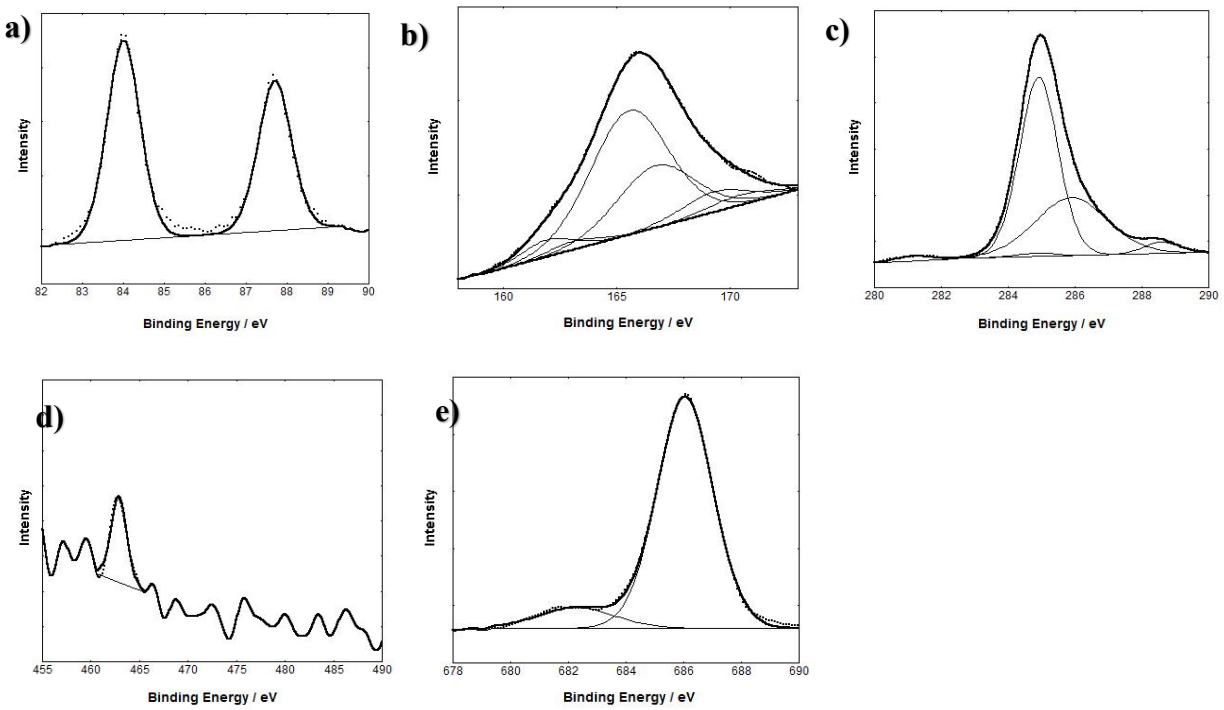

Figure 8.126: XPS binding energy showing the regions of Au 4f (a), S 2p (b), Ru 3d (c), Ru 3p (d) and F 1s (e) for RuSconj•AuNP13.

8.3.4.3 RuS8•AuNP13

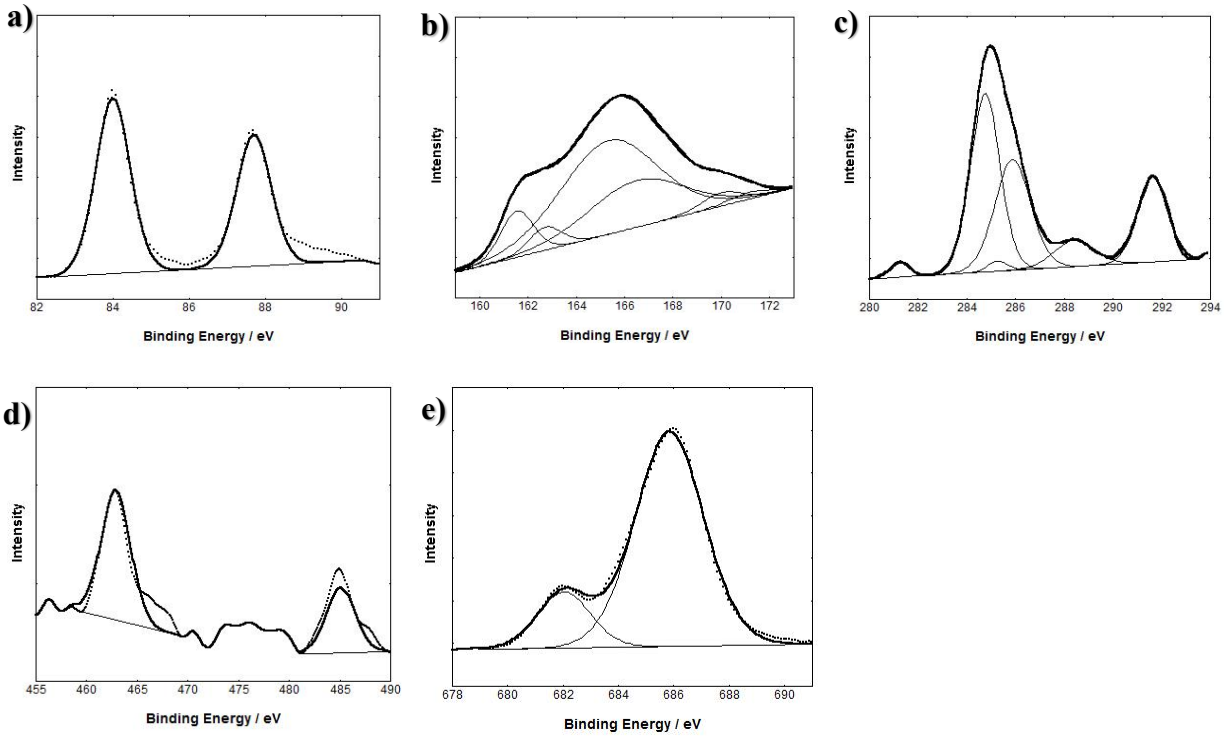

Figure 8.127: XPS binding energy showing the regions of Au 4f (a), S 2p (b), Ru 3d (c), Ru 3p (d) and F 1s (e) for RuS8•AuNP13.

8.3.4.4 RuphenS8•AuNP13

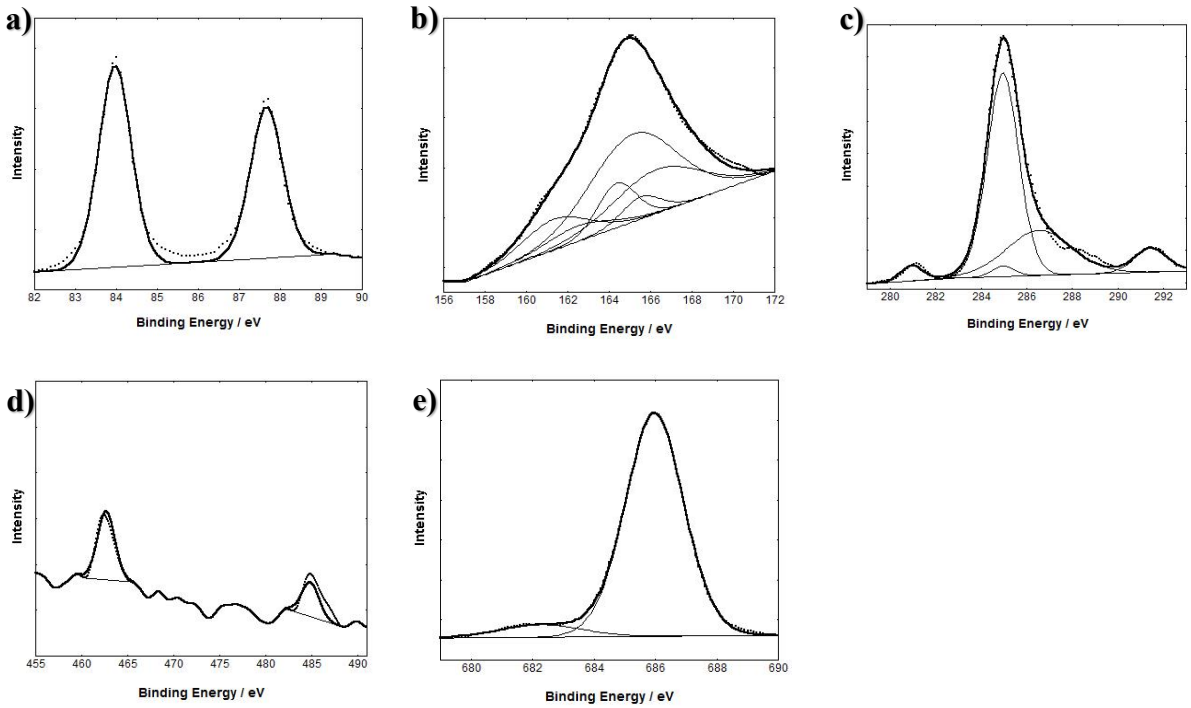

Figure 8.128: XPS binding energy showing the regions of Au 4f (a), S 2p (b), Ru 3d (c), Ru 3p (d) and F 1s (e) for RuphenS8•AuNP13.

8.4 Chapter 6: Using AuNPs to aid the properties of Ruthenium complexes in Dye Sensitized Solar Cells

8.4.1 Synthesis: NMR and MS

8.4.1.1 RuSi

1-(Amino-N-Boc)-ethyl bromide

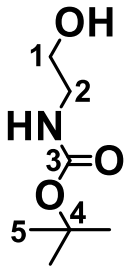

Figure 8.129: Structure of 1-(amino-N-Boc)-ethyl bromide.

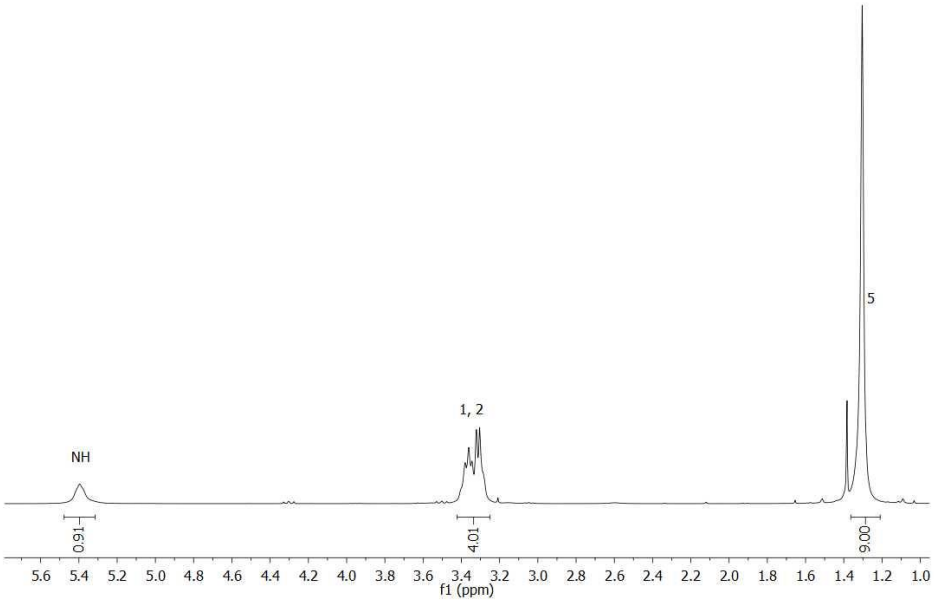

Figure 8.130: ^{1}H NMR 1-(amino-N-Boc)-ethyl bromide. ($CDCl_3$).

4,4’-Ethoxyamino-N-boc-2,2’-bipyridine

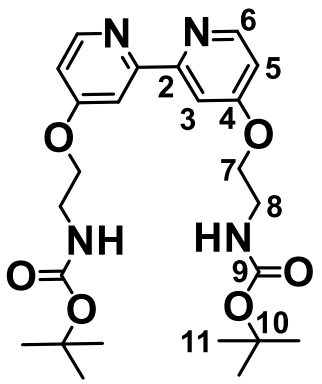

Figure 8.131: Structure of 4,4’-ethoxyamino-N-boc-2,2’-bipyridine.

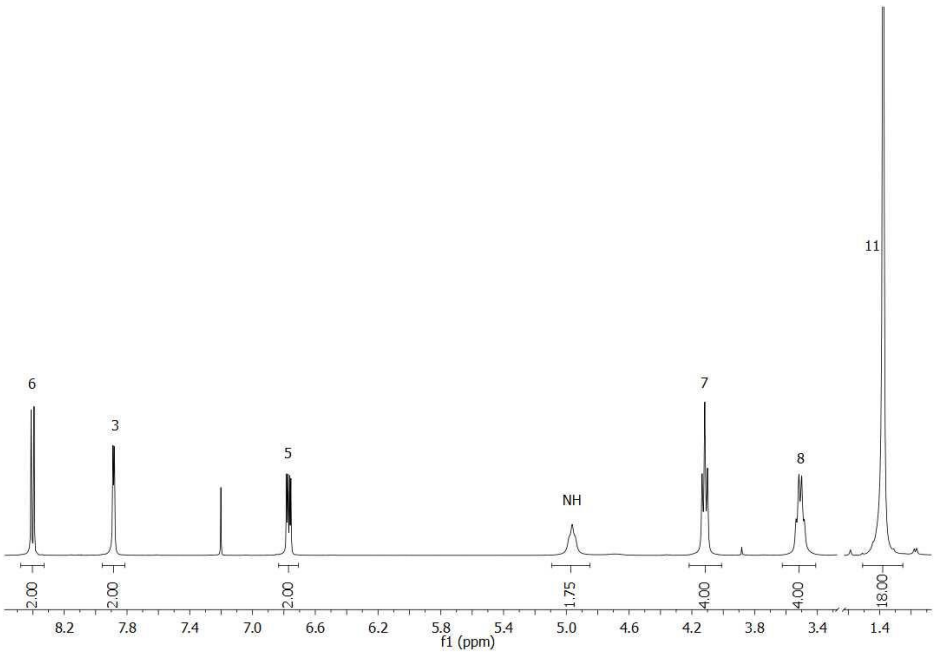

Figure 8.132: ^{1}H NMR 4,4’-ethoxyamino-N-boc-2,2’-bipyridine. ($CDCl_3$).

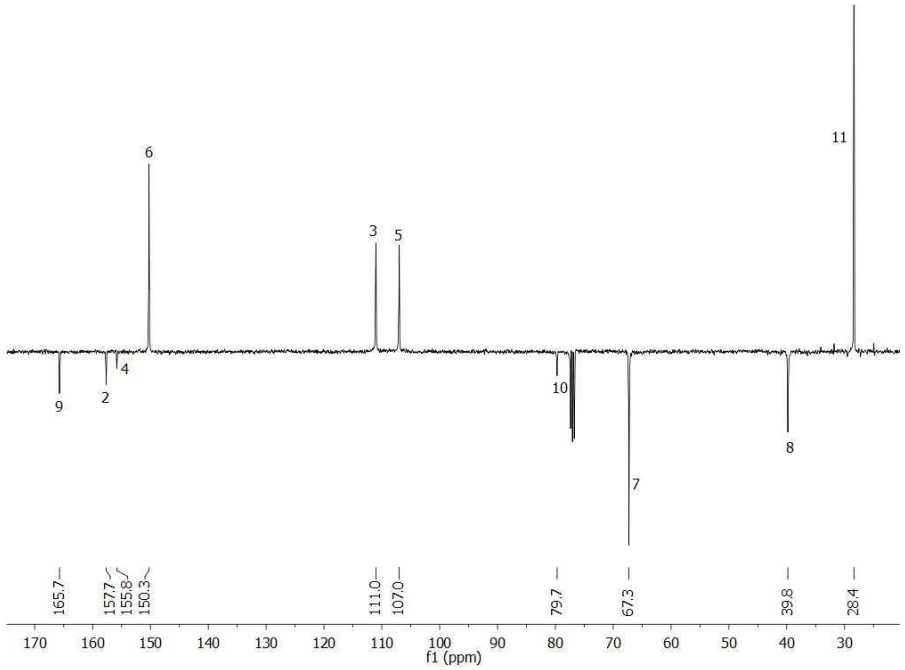

Figure 8.133: ^{13}C NMR 4,4'-ethoxyamino-N-boc-2,2'-bipyridine. ($CDCl_3$).

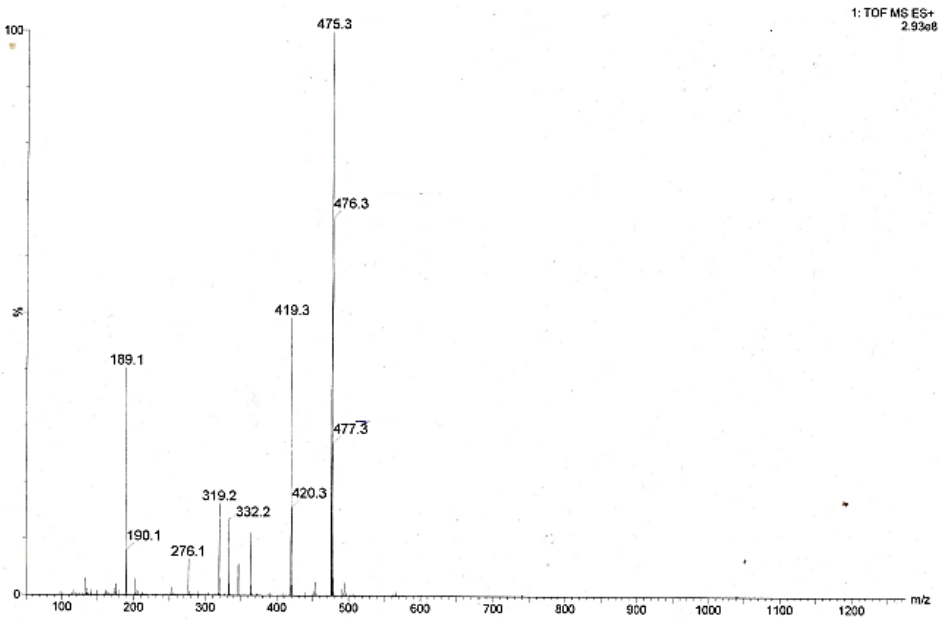

Figure 8.134: 4,4'-Ethoxyamino-N-boc-2,2'-bipyridine MS.

4,4’-Ethoxyamine-2,2’-bipyridine

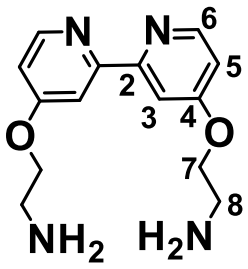

Figure 8.135: Structure of 4,4’-ethoxyamine-2,2’-bipyridine.

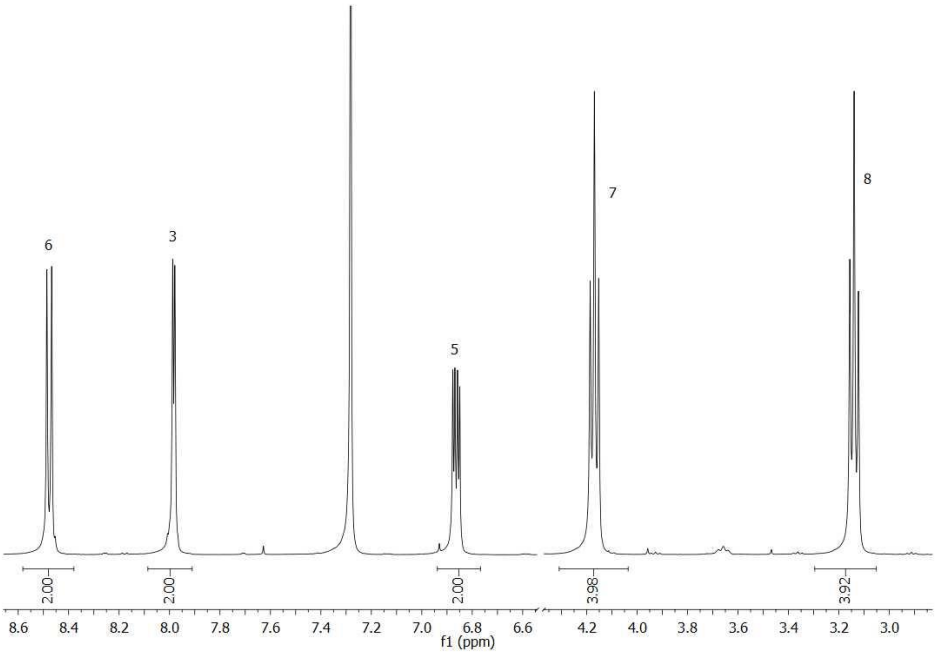

Figure 8.136: ^{1}H NMR 4,4’-ethoxyamine-2,2’-bipyridine. (d_6-DMSO).

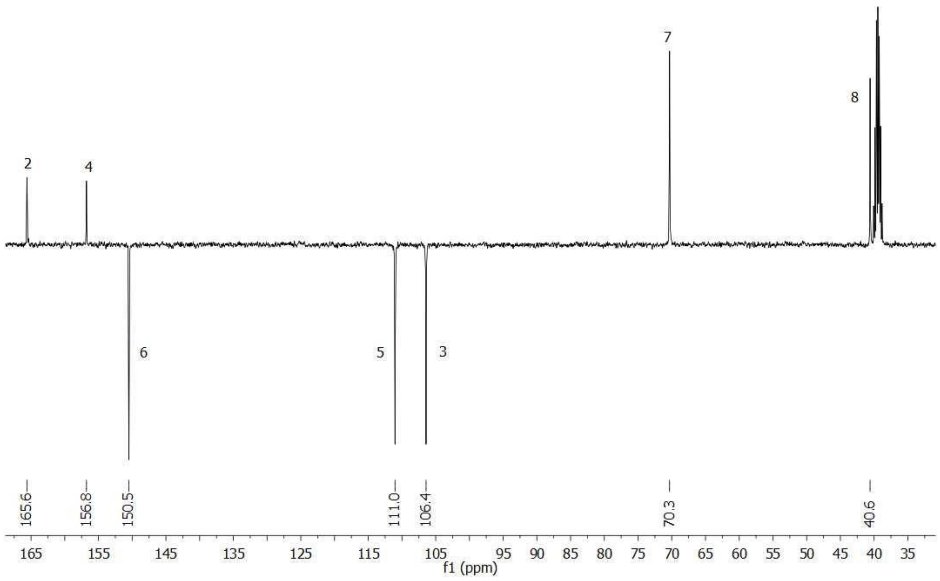

Figure 8.137: ^{13}C NMR 4,4'-ethoxyamine-2,2'-bipyridine. (d_6-DMSO).

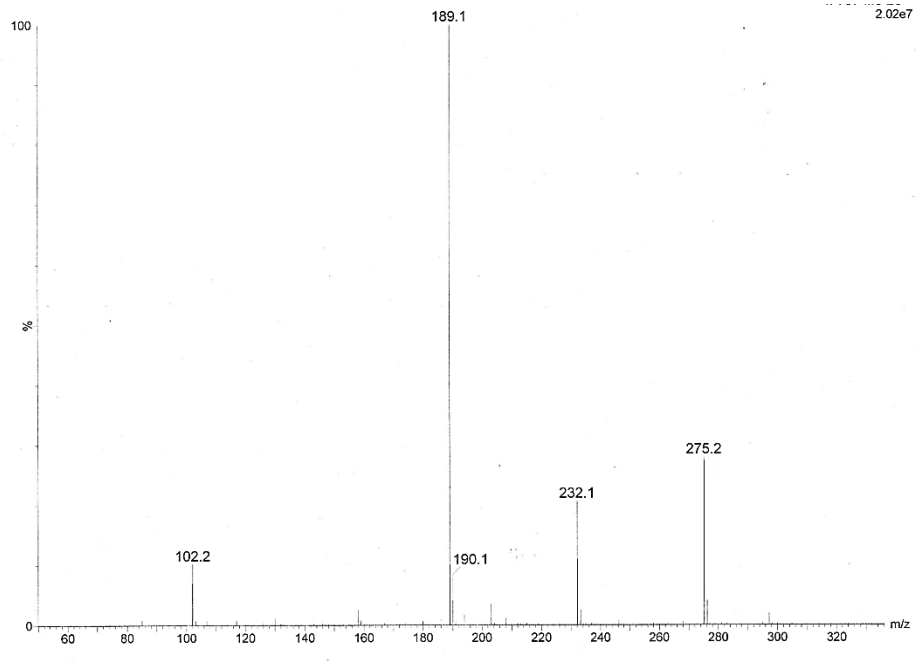

Figure 8.138: 4,4'-Ethoxyamine-2,2'-bipyridine MS.

$RuNH_2$

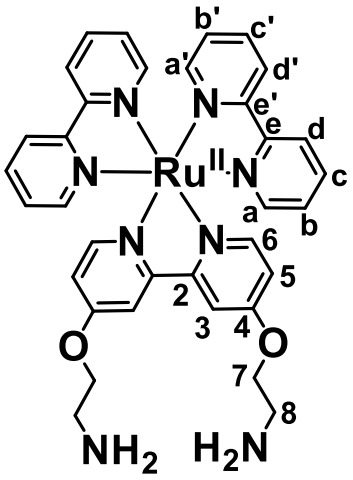

Figure 8.139: Structure of $RuNH_2$.

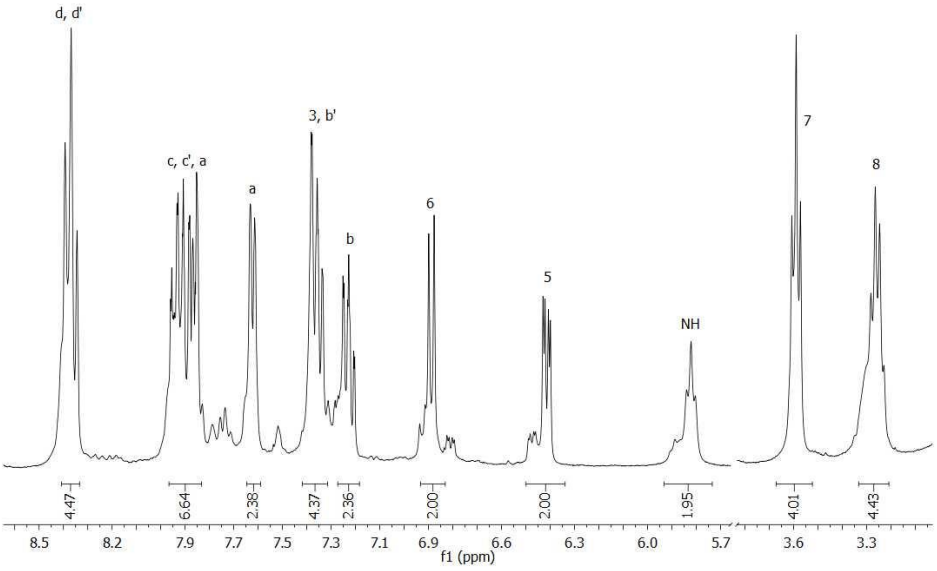

Figure 8.140: ^1H NMR $RuNH_2$. (CD_3CN).

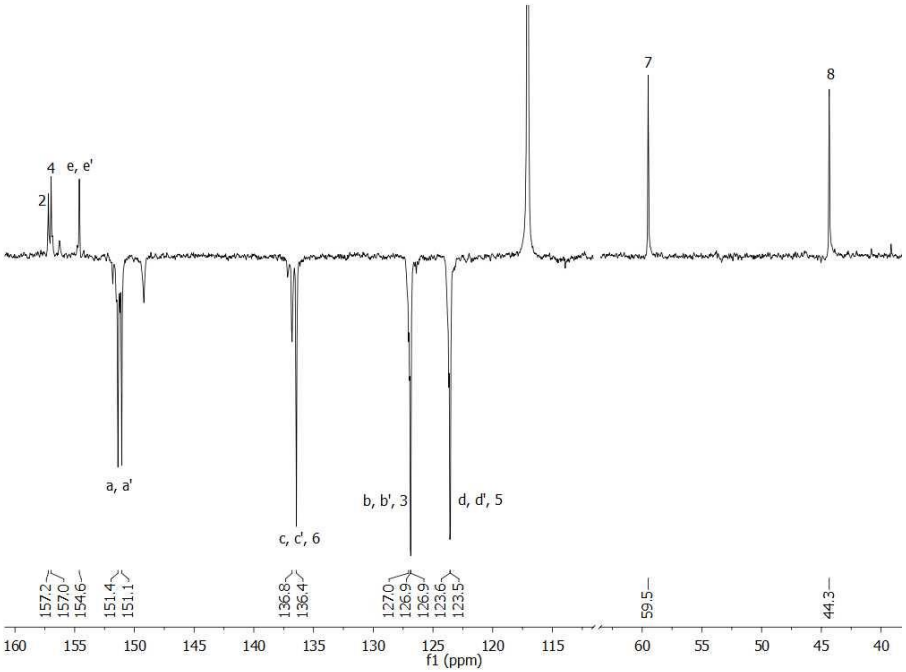

Figure 8.141: ^{13}C NMR $RuNH_2$. (CD_3CN).

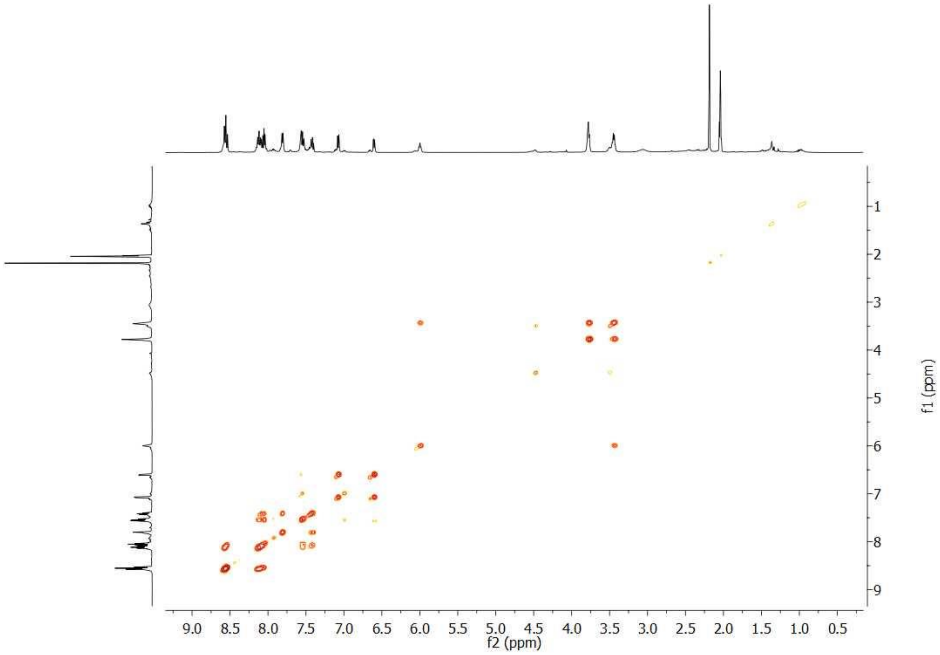

Figure 8.142: $RuNH_2$ COSY NMR. (CD_3CN).

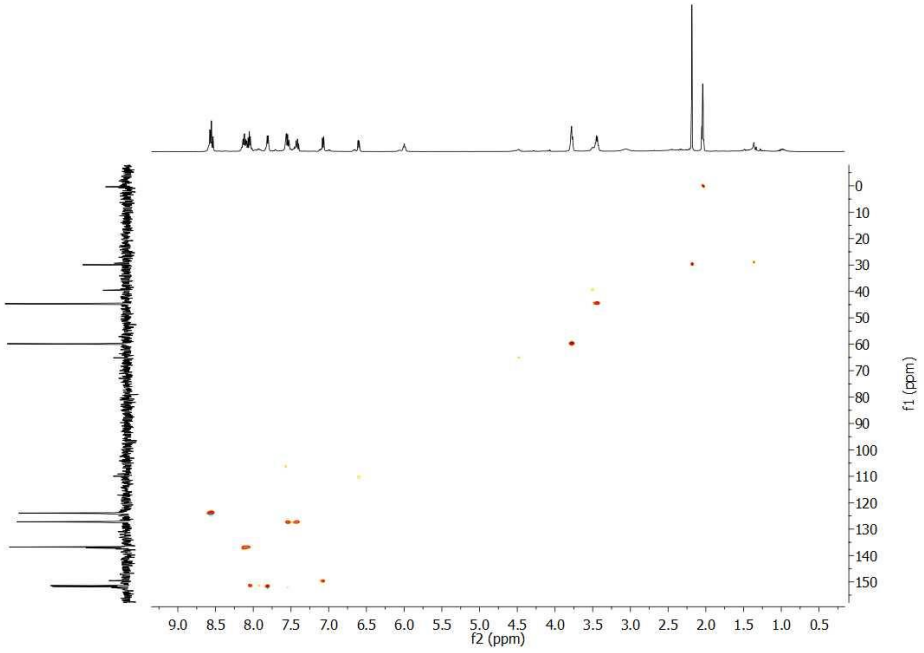

Figure 8.143: $RuNH_2$ HSQC NMR. (CD_3CN).

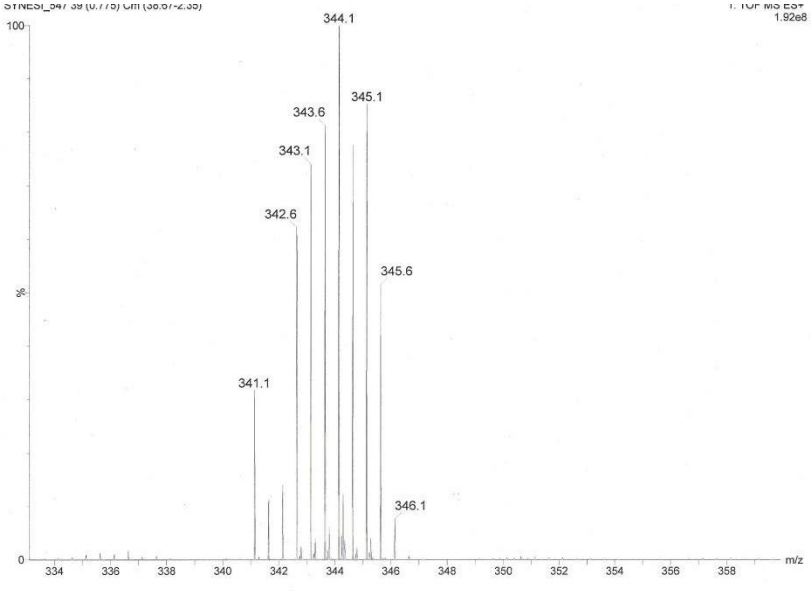

Figure 8.144: $RuNH_2$ MS.

RuSi

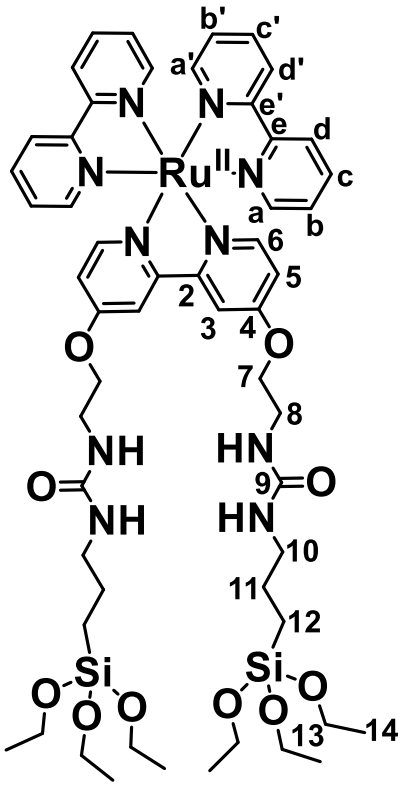

Figure 8.145: Structure of RuSi.

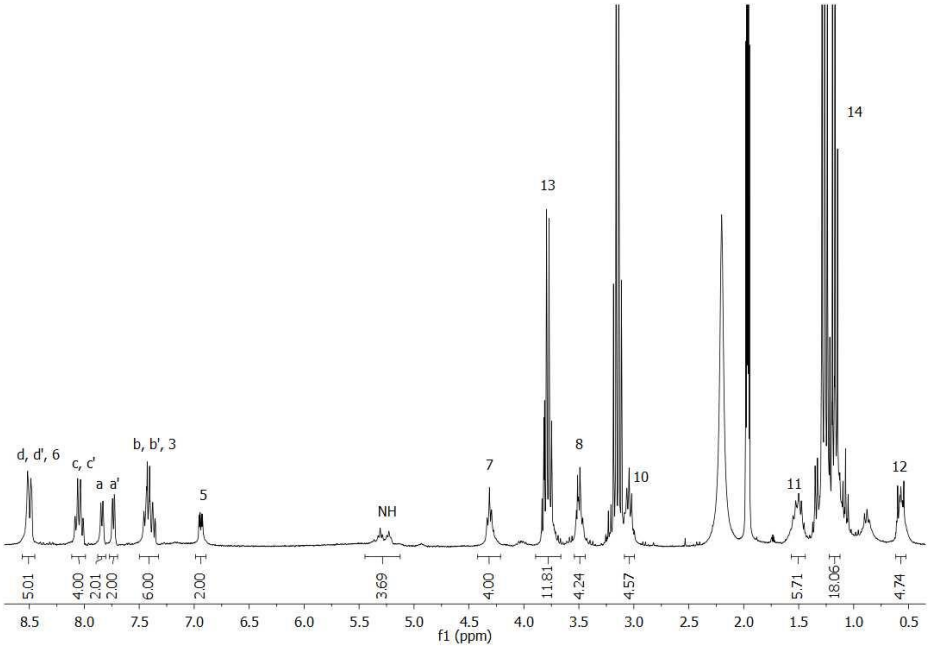

Figure 8.146: ^{1}H NMR RuSi. (CD_3CN).

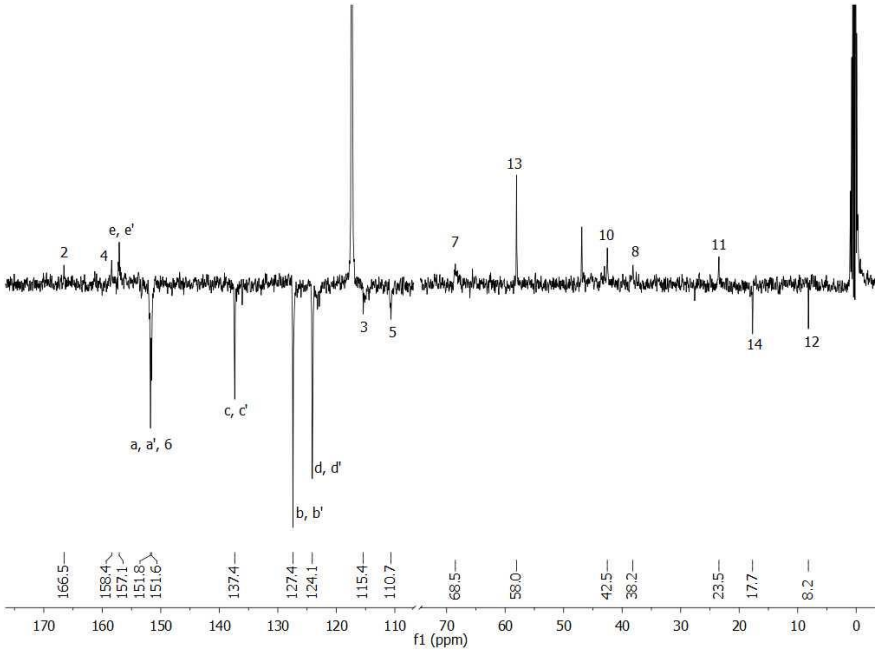

Figure 8.147: ^{13}C NMR RuSi. (CD_3CN).

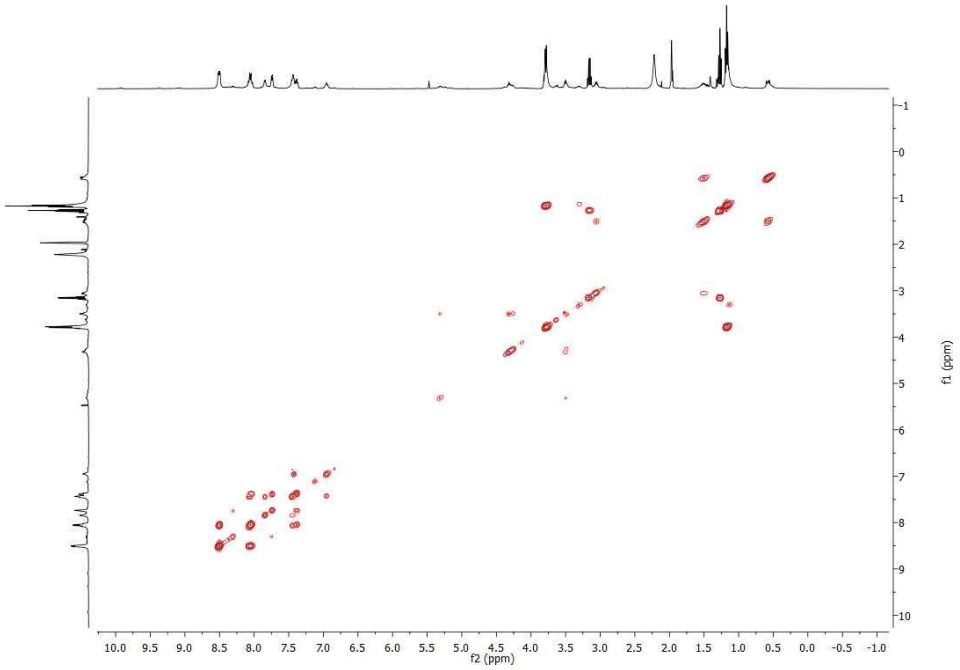

Figure 8.148: RuSi COSY NMR. (CD_3CN).

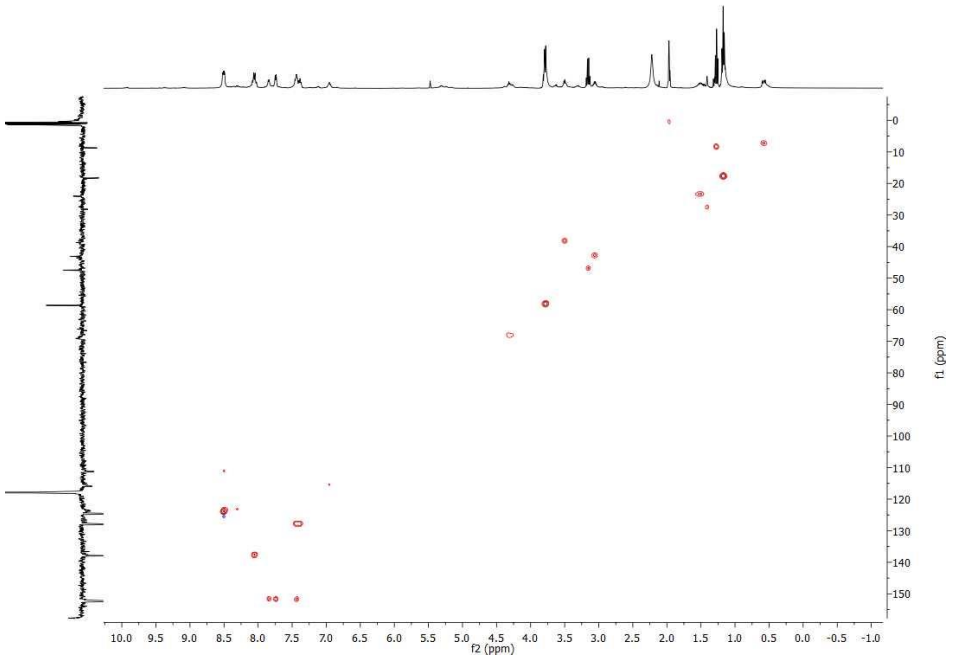

Figure 8.149: RuSi HSQC NMR. (CD_3CN).

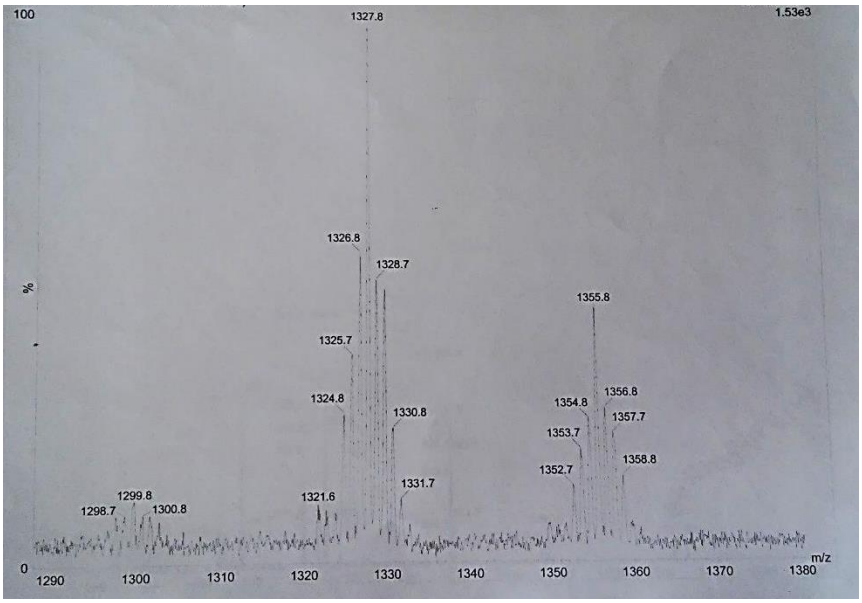

Figure 8.150: RuSi MS.

8.4.2 XPS of electrodes

8.4.2.1 @Au+TiO_2

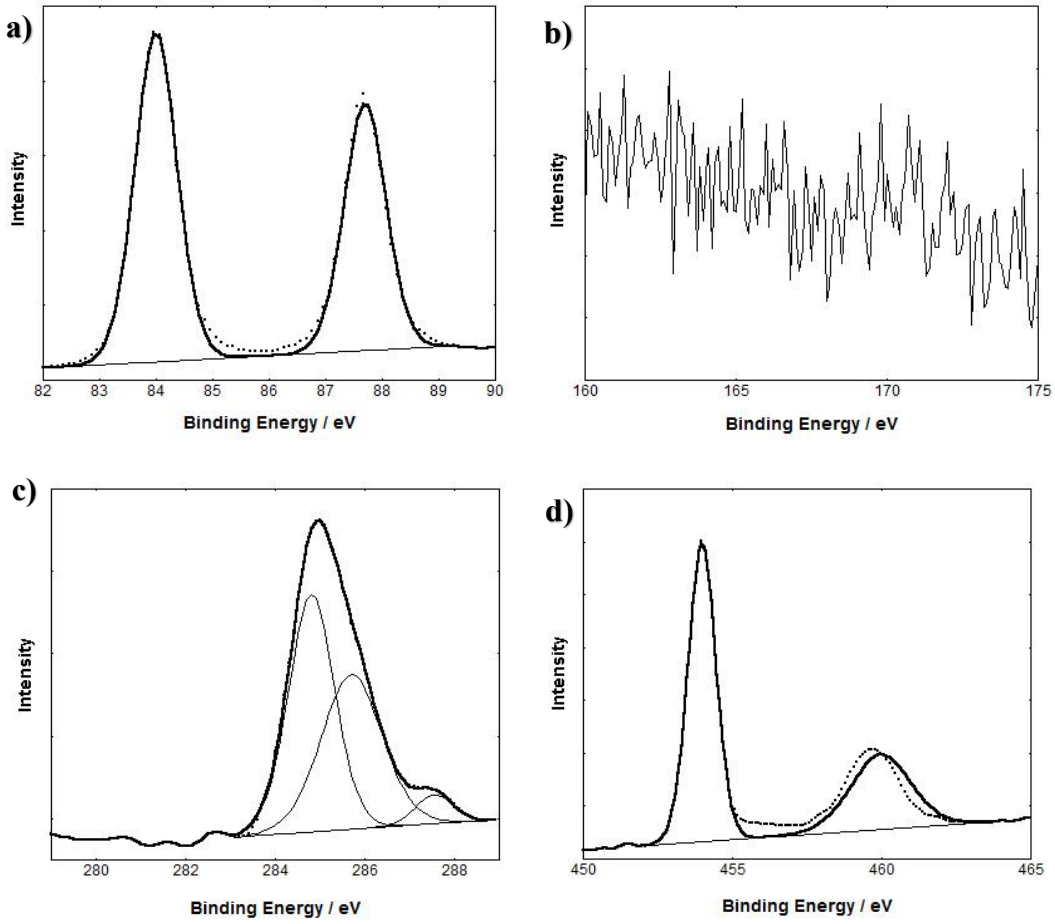

Figure 8.151: XPS binding energy showing the regions of Au 4f (a), S 2p (b), Ru 3d (c) and Ru 3p (d) for @Au+TiO_2.

8.4.2.2 RuphenS12@AuNP13+TiO_2

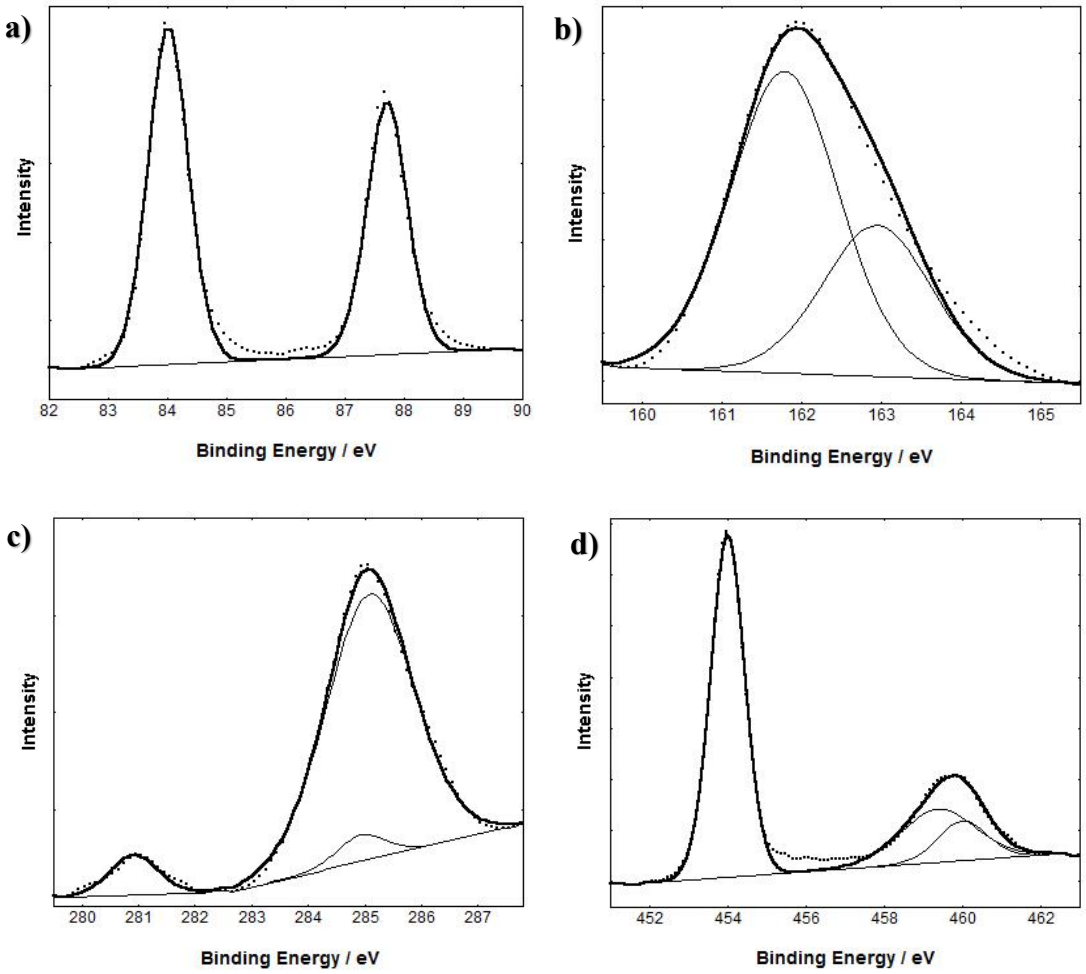

Figure 8.152: XPS binding energy showing the regions of Au 4f (a), S 2p (b), Ru 3d (c) and Ru 3p (d) for RuphenS12@AuNP13+TiO_2.

8.4.3 Iodide-iodine reaction with gold coated titania electrodes

8.4.3.1 MS of supernatant of AuNP and electrolyte

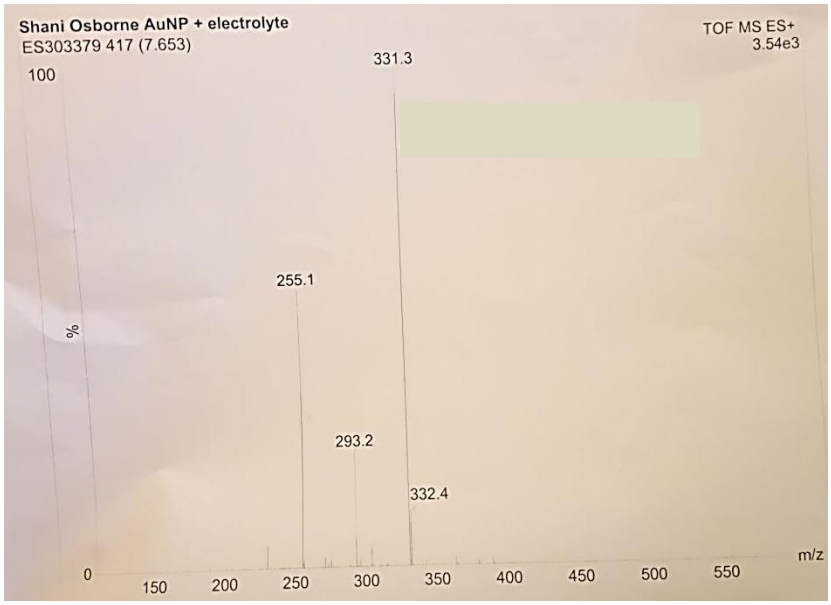

Figure 8.153: MS of the supernatant of the mixture of AuNP13 and iodide – iodine electrolyte.

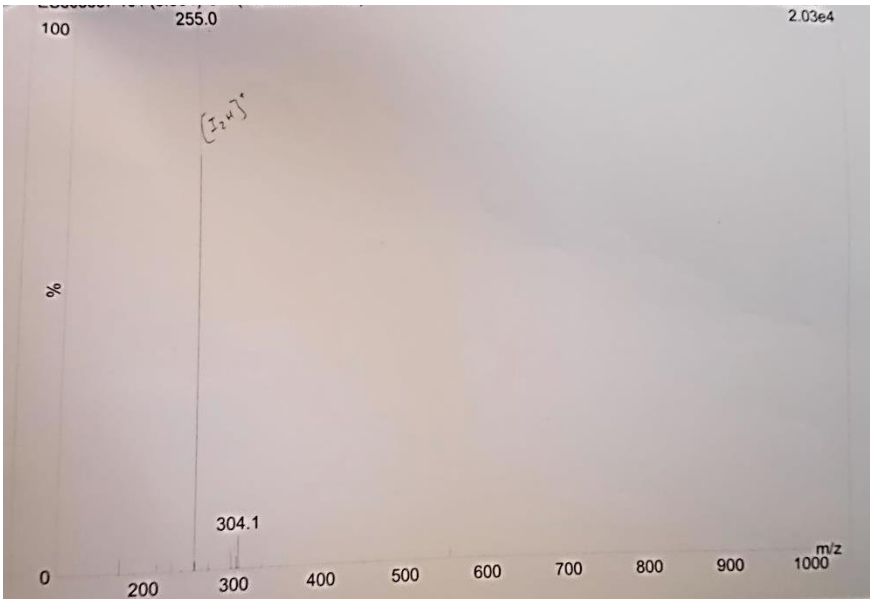

Figure 8.154: MS of the iodide – iodine electrolyte .

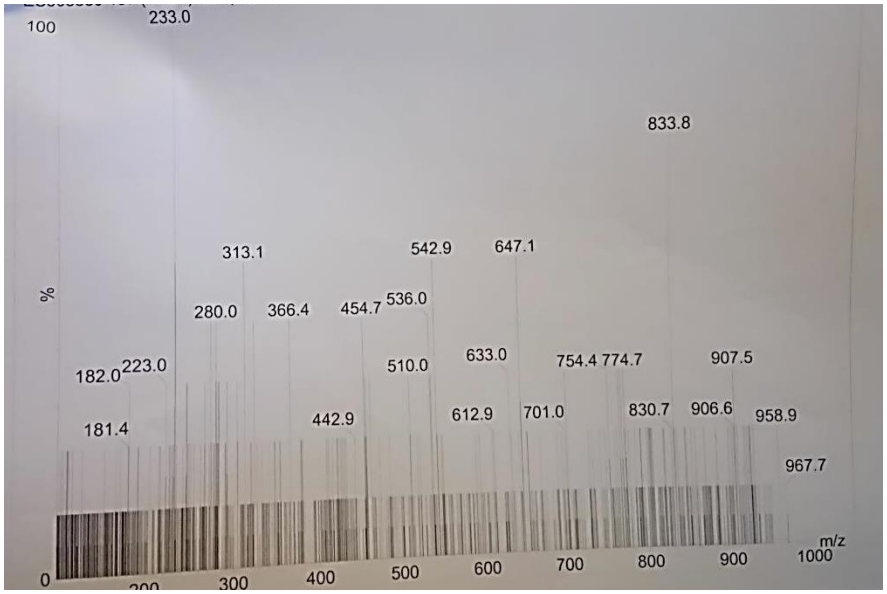

Figure 8.155: MS of the supernatant of AuNP13.

8.5 Publications and Conferences

8.5.1 Conferences Attended 2013-2016

1st RSC Nanosymposium, December 2013, University of Birmingham, UK.

RSC Next Generation Materials for Solar Photovoltaics, January 2014, London, UK.

Poster Presentation: **Supramolecular Systems for Applications in Dye Sensitized Solar Cells.** 3rd RSC Younger Member Symposium, June 2014, University of Birmingham, UK.

Poster Presentation: **Supramolecular Systems for Applications in Dye Sensitized Solar Cells.** 2nd RSC Nanosymposium, December 2014, University of Birmingham, UK.

Poster and Flash Presentation: **Supramolecular Systems for Applications in Dye Sensitized Solar Cells.** RSC Early Career Sector Chemists Symposium, February 2015, Derby, UK.

Oral Presentation: **Effect of probe design on luminescent properties of coated gold nanoparticles.** 10th Berliner Chemie Symposium, April 2015, Berlin, Germany.

Oral Presentation: **Effect of probe design on luminescent properties of coated gold nanoparticles.** RSC Photochemistry Meeting, June 2015, University of Newcastle, UK.

Poster and Flash Presentation: **Luminescent ruthenium probes for coating nanoparticles: effect of probe design on luminescent properties.** Birmingham Postgraduate Symposium, July 2015, University of Birmingham, UK.

Oral Presentation: **Effect of probe design on luminescent properties of coated gold nanoparticles.** Dalton Young Members Event, September 2015, University of Leeds, UK.

Oral Presentation, Panel Discussion and Paper Submitted: **Highly luminescent gold nanoparticles: effect of ruthenium distance for nanoprobes with enhanced lifetimes.**

Supramolecular Photochemistry: Faraday Discussion, September 2015, Cambridge University, UK.

Oral Presentation: **Highly luminescent gold nanoparticles: effect of ruthenium distance for nanoprobes with enhanced lifetimes.** 3rd RSC Nanosymposium, December 2015, University of Birmingham, UK.

Oral Presentation: **Ruthenium coated gold nanoparticles for dye sensitized solar cells.** Birmingham Postgraduate Symposium, July 2016, University of Birmingham, UK.

8.5.2 Osborne, S. A. M.; Pikramenou, Z., Highly luminescent gold nanoparticles: effect of ruthenium distance for nanoprobes with enhanced lifetimes. Farad. Discuss. 2015, 185 (0), 218-231.